

GETTING A GRIP ON TREE FROG ATTACHMENT:

Structures,
mechanisms, and
biomimetic
potential



Julian K.A. Schöning-Langowski

Propositions

1. The digital pads of tree frogs should be termed friction pads rather than adhesion pads.
(this thesis)
2. Tree frogs use pad-intrinsic smooth muscle fibres to modulate their attachment.
(this thesis)
3. The tubercles on the flippers of humpback whales increase the manoeuvrability of these animals by reducing spanwise cross-flow.
4. Not citing relevant literature that is old or non-English hampers scientific progress.
5. Tight supervision is counteractive in training PhD candidates to become independent scientists.
6. The sensitivity of a baby to modulations in the emotional content of its parent's voice renders story telling an excellent rhetorical training for the parent.
7. Work pressure during a PhD project is like wind during sailing.

The propositions belong to the thesis, entitled

**GETTING A GRIP
ON TREE FROG ATTACHMENT:
Structures, mechanisms, and biomimetic potential**

Julian K.A. Schöning-Langowski
Wageningen, 4 June 2019

**GETTING A GRIP
ON TREE FROG ATTACHMENT:**

Structures, mechanisms, and biomimetic potential

Julian K.A. Schöning-Langowski

Thesis committee

Promotor

Prof. Dr Johan L. van Leeuwen
Professor of Experimental Zoology
Wageningen University & Research

Co-promotors

Dr Dimitra Dodou
Associate Professor, Biomechanical Engineering
Delft University of Technology

Prof. Dr Marleen Kamperman
Professor of Polymer Science
University of Groningen

Other members

Prof. Dr Erik van der Linden, Wageningen University & Research
Prof. Dr Thomas Speck, University of Freiburg, Germany
Prof. Dr Peter H. Niewiarowski, The University of Akron, USA
Prof. Dr Patrick Flammang, University of Mons, Belgium

This research was conducted under the auspices of the Graduate School of the Wageningen Institute of Animal Sciences (WIAS)

**GETTING A GRIP
ON TREE FROG ATTACHMENT:**

Structures, mechanisms, and biomimetic potential

Thesis

submitted in fulfilment of the requirements for the degree of doctor at
Wageningen University

by the authority of the Rector Magnificus

Prof. Dr A.P.J. Mol,

in the presence of the

Thesis Committee appointed by the Academic Board

to be defended in public

on Tuesday 4 June 2019

at 4 p.m. in the Aula.

Julian K.A. Schöning-Langowski
Getting a grip on tree frog attachment:
Structures, mechanisms, and biomimetic potential,
244 pages.

PhD thesis, Wageningen University, Wageningen, the Netherlands (2019)
With references, with summaries in English, German, and Dutch

ISBN 978-94-6343-185-9
DOI 10.18174/471878

Für Annika und Sophie.

Table of Contents

Chapter 1	General introduction	9	1
Chapter 2	Tree frog attachment: Mechanisms, challenges, and perspectives	19	2
Chapter 3	Force-transmitting structures in the digital pads of the tree frog <i>Hyla cinerea</i>: a functional interpretation	65	3
Chapter 4	Comparative and functional analysis of the digital mucus glands and secretions of tree frogs	103	4
Chapter 5	Estimating the maximum attachment performance of tree frogs on rough substrates	143	5
Chapter 6	General discussion	175	6
Declarations		195	D
	Authorship statements	195	
	Ethical statements	198	
	Funding	199	
	Competing interests	199	
	Availability of data and materials	199	
References		201	R
Summaries		219	S
	Summary (English)	220	
	Samenvatting (Dutch)	223	
	Zusammenfassung (German)	226	
Acknowledgements		231	A
Personalia		237	P
	Curriculum vitae	237	
	Publications	239	
	Training and supervision plan	241	



Admiranda tibi levium spectacula rerum.

A.J. Rösel von Rosenhof, 1758

CHAPTER 1

General introduction

Next to the move from water to land, and from land to air, the exploration of arboreal habitats and the accompanying development of climbing abilities were important drivers of evolution (Sustaita *et al.*, 2013). Compared to a terrestrial lifestyle, climbing offers many advantages, from the avoidance of ground-dwelling predators, over the exploration of arboreal habitats and food sources, to an increased dispersal range (Cartmill, 1985). To move through arboreal habitats, and to avoid falling and a resulting injury or an increased exposure to predators (Cartmill, 1985), animal species from various clades have developed a wide range of attachment apparatuses. These attachment systems involve differing physical and chemical principles to generate adhesive and frictional attachment forces on diverse natural substrates (von Byern & Grunwald, 2010; Gorb, 2008; Smith, 2016). For example, tree frogs are versatile climbers that can attach with their adhesive digital pads to various substrates (Crawford *et al.*, 2016). The analysis of the adhesive pads of tree frogs helps to elucidate the fundamentals of (bio-)adhesion, gives insight into the ecology and evolution of these animals, and facilitates the design of biomimetic adhesives. Therefore, I present in this thesis a study of some of the structures and mechanisms involved in the attachment of tree frogs, and explore the biomimetic potential of the digital adhesive pads of tree frogs.

1.1 Bioadhesion

The evolution of a biological attachment system required for climbing is driven by multiple functional requirements. Among others, climbing animals have to (i) generate strong, reversible, and repeatable attachment to various substrates under challenging conditions, and (ii) control their attachment (Peattie, 2009). Moreover, the internal morphology of the attachment organs has to (iii) withstand the mechanical loads arising during attachment.

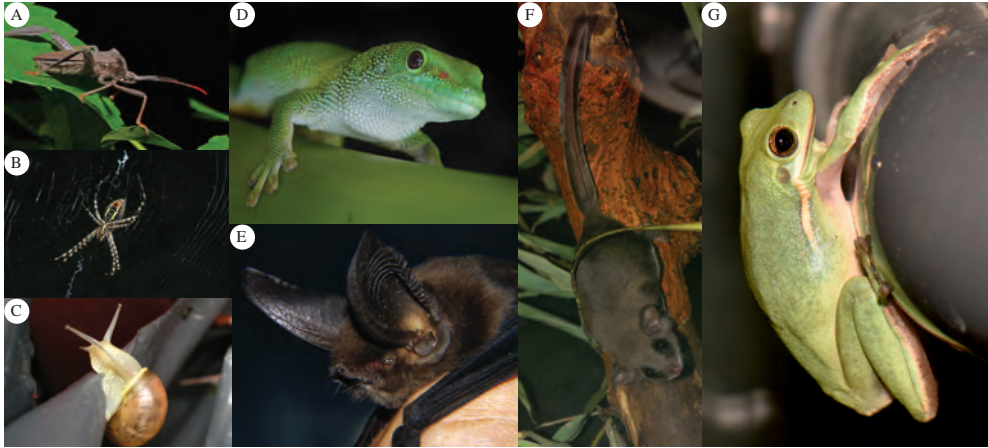


Figure 1.1 Example species for the diversity of attachment solutions in animals. (A) Insecta, *Acanthocephala terminalis* (Credit: Insects Unlocked), (B) Arachnida, Araneidae (Credit: Sarefo), (C) Gastropoda, *Cornu aspersum* (Credit: H. Svenson), (D) Reptilia, *Phelsuma madagascariensis* (Credit: B. Spragg), (E) Mammalia, Myzopodidae (Credit: I. Marinho), (F) Mammalia, *Acrobates pygmaeus* (Credit: E. Neideck), (G) Amphibia, *Hyla cinerea*. Figures A–F were taken from commons.wikimedia.org. For details see main text.

A variety of attachment solutions have developed in nature that cope with these requirements (Fig. 1.1). There is a virtually infinite list of insect species with adaptations towards climbing, such as—presumably independently evolved—hairy attachment pads in coleopterans (beetles), dermapterans (earwigs), and dipterans (flies), and smooth pads in ensiferans (crickets), hymenopterans (e.g. bees and ants), and mecopterans (scorpionflies), as well as suction discs and claws in various insect clades (e.g. Beutel & Gorb, 2001, 2006; Gorb, 2001; Gorb & Beutel, 2001; Gorb, 2008). Similarly, arachnids (among others spiders, mites, and scorpions) developed claws as well as smooth and hairy attachment pads (Wolff & Gorb, 2016). Gastropods (slugs and snails) use adhesive mucus in locomotion and attachment (Smith, 2010, 2016). Geckos developed hairy dry digital pads for the generation of van der Waals (vdW) forces (Autumn *et al.*, 2000, 2002), which allow these animals to climb vertical walls even in an upside-down orientation (Aristotle, 350 B.C.E., 1918). Various climbing adaptations are also found in other vertebrate clades, for example bats (Riskin & Racey, 2010), marsupials (Rosenberg & Rose, 1999), and amphibians, such as the wet smooth digital pads of tree frogs (Gatesby, 1743; Hanna & Barnes, 1991; Rösel von Rosenhof, 1758).

Studies on the attachment solutions found in nature are clustered under the term ‘bioadhesion’, which is an interdisciplinary research field with contributions from biology, physics, chemistry, and related disciplines. The attachment forces generated by bioadhesive organs can be separated into adhesion and friction. Throughout this thesis, I use ‘adhesion’ for attractive forces that act perpendicular to the interface between an adhesive and a substrate, whereas ‘friction’ refers to forces acting within the interfacial plane, and ‘attachment’ represents the combination of both forces.

Van der Waals forces

Attractive forces arising from interactions between molecules that are in close proximity (typically with an intermolecular distance $d < 5$ nm). Van der Waals forces can act between molecules with permanent dipoles (Keesom interactions), between molecules in which a permanent dipole induces a dipole in another non-polar molecule (Debye interactions), and between transient dipoles of nonpolar but polarisable molecules (London dispersion interactions; Parsegian, 2006). See CHAPTER 2 for details.



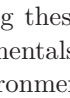
1.2 Tree frog attachment

Among amphibians with adhesive abilities, tree frogs are the most prominent group. The definition of a ‘tree frog’ can be based on an arboreal lifestyle (Manzano *et al.*, 2007), the microhabitat of a specific species or a higher-ranking taxon (Green & Simon, 1986; Manzano *et al.*, 2007), an enhanced attachment performance with respect to terrestrial species (Emerson & Diehl, 1980), or adaptations of the digital morphology towards arboreality (Green & Simon, 1986; Smith *et al.*, 2006b). Throughout this thesis, I use the term ‘tree frog’ in its widest sense, encompassing all of these definitions. Anyhow, tree frogs possess several remarkable traits among bioadhesive systems:

1. In contrast to other bioadhesive vertebrates such as geckos, the amphibian skin of tree frogs is continuously wetted with mucus. Despite this epicutaneous mucus layer, tree frogs can attach to various substrates (Blackwall, 1845; Federle *et al.*, 2006; Rösel von Rosenhof, 1758).
2. With a snout-vent-length ℓ_{sv} up to 13.5 cm and a body mass m up to 160 g (Endlein *et al.*, 2017; Tyler, 1968), tree frogs are the largest terrestrial organisms that have been proposed to utilise ‘wet adhesion’.
3. The adhesive ventral skin of the digital pads of tree frogs is covered with a hierarchical nano- to microscopic pillar-channel pattern formed by superficial epidermal cells and apical protrusions of these cells (Ernst, 1973a; Scholz *et al.*, 2009; Siedlecki, 1910). Detailed descriptions of the epidermal and internal pad morphology are given in CHAPTERS 2 and 3, respectively.
4. The surface structuring of the ventral pad epidermis has been described for various anuran families, hinting towards convergent evolution (Barnes *et al.*, 2013; Green, 1979) and an optimised morphology for attachment.
5. The pads have been reported to be among the softest structures found in nature (with a compressive effective elastic modulus of ca. 20–40 kPa; Barnes *et al.*, 2013, 2011).
6. As is commonly known, frogs jump (and land). Such highly dynamic manoeuvres come with considerable inertial loads of up to several body weights per digit acting on the whole locomotory apparatus including the adhesive system of tree frogs (Bijma *et al.*, 2016).

Wet adhesion

Adhesive contact forces that arise from the action of a liquid bridge between an object and the substrate. Wet adhesion comprises capillary adhesion, which is the result of the liquid's surface tension acting at the meniscus of the liquid bridge (Butt & Kappl, 2009; Popov, 2010), and hydrodynamic adhesion, which is caused by the viscous resistance against flow within the liquid bridge (Reynolds, 1886; Stefan, 1874). See CHAPTER 2 for details.

1  Considering these traits, tree frogs are fascinating model organisms for research on the fundamentals of bioadhesion, and for the development of biomimetic adhesives in a wet environment.

1.2.1 A short history of tree frog attachment

The remarkable attachment performance of tree frogs—in particular the ability to stick to smooth surfaces such as plant leaves or glass lenses—has been described already in the oldest scientific references mentioning these animals known to the author (Gatesby, 1743; Rösel von Rosenhof, 1758). During the 19th and early 20th century, accurate and detailed analyses of the (functional) anatomy of the digital pads of tree frogs were made (e.g. Dewitz, 1883; Leydig, 1868; Noble & Jaeckle, 1928; Schuberg, 1891; Siedlecki, 1909; v. Wittich, 1854). These early publications were rarely cited in later works, which may explain a partial loss of early gained insights into tree frog attachment.

The intensive use of electron microscopy in the 1970s and 1980s facilitated a new wave of publications, which focused on the morphological and phylogenetic characterisation of the ventral pad surface in numerous arboreal frog species (e.g. Emerson & Diehl, 1980; Ernst, 1973a; Green, 1979; Hertwig & Sinsch, 1992; Linnenbach, 1985; McAllister & Channing, 1983; Richards *et al.*, 1977; Welsch *et al.*, 1974). These address, among others, evolutionary, ecological, and functional aspects. In the 1980s, the first biomechanical models of the fundamental mechanisms of tree frog attachment were developed and experimentally tested (e.g. Emerson & Diehl, 1980; Green, 1981; Hanna & Barnes, 1991). The most prominent experimental setup for the validation of the hypothesised models is the so-called ‘rotation platform’, which allows the measurement of the adhesive and frictional attachment performance of whole tree frogs (see CHAPTER 5 for an updated rotation platform setup). Later, more sophisticated setups such as multi-dimensional force transducers were developed for the quantification of the attachment forces of individual digital pads (Barnes *et al.*, 2008; Crawford *et al.*, 2012; Federle *et al.*, 2006; Hanna & Barnes, 1991). Additional techniques such as white light interferometry and atomic force microscopy were applied to investigate the geometrical and material properties of the digital pad surface (Barnes *et al.*, 2013; Federle *et al.*, 2006; Kappl *et al.*, 2016).

Finally, the ventral surface patterning of the digital pads of tree frogs stimulated since around 2010 the design of a number of biomimetic and bioinspired micropatterned adhesives with an improved attachment performance compared to unpatterned adhe-

sives (e.g. Chen *et al.*, 2015; Drotlef *et al.*, 2013; Iturri *et al.*, 2015; Murarash *et al.*, 2011).

Biomimetics

The development of novel technical applications by the systematic analysis of the principles of the functioning of biological systems, and the transfer of these principles into technology (Lepora *et al.*, 2013; VDI-Department Biomimetics, 2012). Biomimetics is to be discerned from ‘biomimicry’, a philosophical approach to the solution of challenges related to (environmental, social, or economic) resilience inspired by nature, ‘bionics’, the replacement of biological functions with electronic/mechanical equivalents, and ‘bioinspired design’, a broad term describing all of the above (Fayemi *et al.*, 2014). Biomimetics is motivated by the assumption that the development of biological systems by natural selection during 3.8 billion years of evolution led to optimised solutions for a variety of problems that are also encountered in technology. In particular, convergent systems (i.e. systems with similar features that evolved independently in species of different lineages; Wehner & Gehring, 2007) are of interest for biomimetic research. Adhesion is a popular topic in biomimetics (Lepora *et al.*, 2013), with numerous biomimetic attachment designs inspired by the strong, reusable, and reversible adhesives found in nature (Bogue, 2008; von Byern & Grunwald, 2010; Favi *et al.*, 2014; Gorb, 2008).



1.2.2 Challenges and open questions

As shown by the diverse research history on tree frogs and their adhesive pads, a fundamental understanding of tree frog attachment (i.e. How do these animals attach and how did their pads evolve?) requires an interdisciplinary approach with contributions from morphology, evolutionary biology, ecology, material science, and mechanics (Fig. 1.2). The hypothesised interfacial mechanisms of tree frog attachment alone comprise a complex set of phenomena such as vdW forces, wet adhesion, mechanical interlocking, suction, drainage, and lubrication. These phenomena are affected by variations of substrate properties such as surface roughness, free surface energy, and stiffness, as well as by the properties of the liquid in the gap between digital pad and substrate (Dirks, 2014). Furthermore, the attachment performance is co-determined by the space around the interface, for example by the material properties and mechanics of subepidermal pad structures (Bartlett *et al.*, 2012b).

Some of the aforementioned factors determining the attachment performance of tree frogs have been already addressed in previous research. Especially the role of the surface geometry of the digital pads, and the common hypothesis of wet adhesion as primary adhesion mechanism have been in the focus of previous studies. However, neither has the function of the epidermal surface pattern been cleared conclusively, nor is there an unambiguous proof of a dominant role of wet adhesion in tree frog attachment (see our review in CHAPTER 2). CHAPTER 2 also shows that analyses of the internal morphology of the digital pads are largely missing. Consequently, the role of internal pad structures in tree frog attachment is virtually unknown. A lack of knowledge on the chemistry of the frog mucus secreted into the pad-substrate gap (and of the glands producing it) hinders a comprehensive discussion of mucus-related phenomena such as the hypothesised wet adhesion of tree frogs, or lubrication.

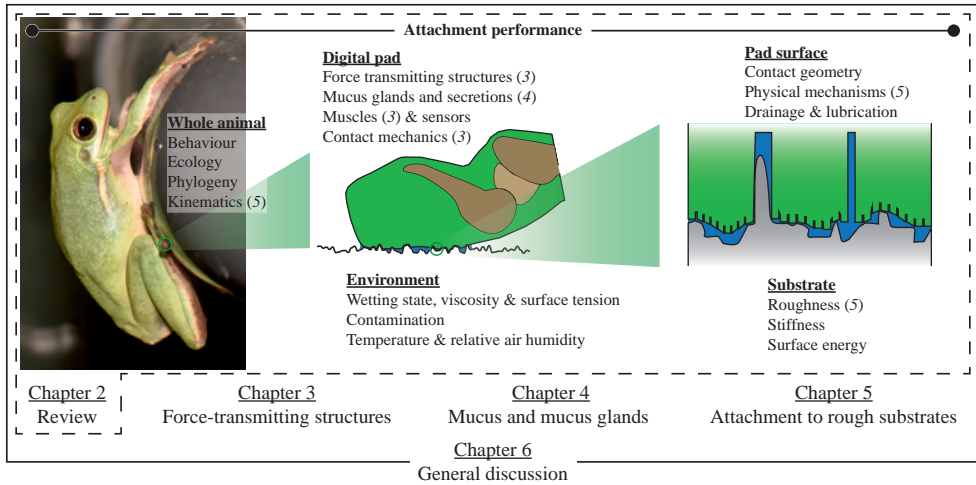


Figure 1.2 Schematic overview of the multidisciplinary aspects co-determining the attachment performance of tree frogs on the level of whole animals, individual digits, and the interface between digital epidermis and substrate. Aspects addressed in CHAPTERS 3 to 5 of this thesis are indicated with italic arabic numerals.

Finally, systematic analyses of the attachment performance of an adhesive system as a function of substrate properties such as roughness, free surface energy, or elastic modulus are a common approach in bioadhesion to test for the contribution of a specific attachment mechanism (e.g. Barnes *et al.*, 2002; Bullock & Federle, 2011; Klittich *et al.*, 2017; Stark *et al.*, 2013). Such studies are rare in the field of tree frog attachment, impeding a discussion of the contribution of the numerous hypothesised mechanisms that are possibly involved in tree frog attachment.

1.3 Aims and outline of this thesis

With this thesis, I aim to achieve two goals. First, I want to contribute to the fundamental understanding of the attachment of tree frogs, hence generating novel knowledge for the field of bioadhesion and for anuran biology. Second, I attempt to translate the findings on the fundamentals of tree frog attachment into insights useful for the design of biomimetic adhesives. The obtained insights are used in the interdisciplinary cooperative research project “Secure and gentle grip of delicate biological tissues” shared between the Experimental Zoology Group, Wageningen University & Research (NL), and the Department of BioMechanical Engineering, Delft University of Technology (NL), in which this thesis is embedded in. In this project, we aim for a deeper understanding of the attachment of soft objects, such as the adhesive digital pads of tree frogs, in a wet environment to inspire the development of novel biomimetic attachment solutions, for example in the context of minimally invasive surgery (Fig. 1.3). To obtain a fundamental understanding of tree frog attachment,

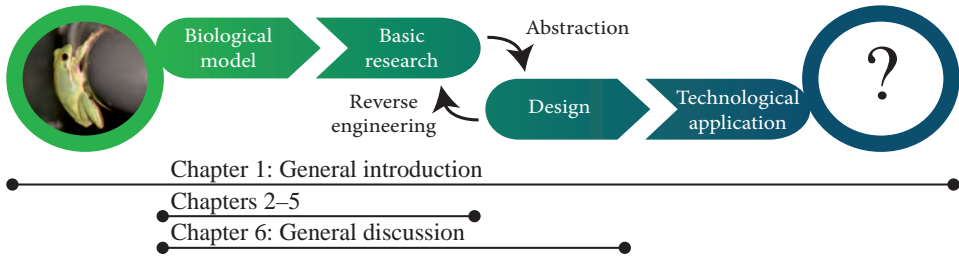


Figure 1.3 Placement of the thesis chapters in the biomimetic research project “Secure and gentle grip of delicate biological tissues”.

which is required for the design of biomimetic adhesives (VDI-Department Biomimetics, 2012), and hence to achieve my research goals, I followed an interdisciplinary approach (Fig. 1.2).

In CHAPTER 2, we review the field to identify the fundamental principles of tree frog attachment, or—where this was not possible—to highlight the crucial gaps of knowledge. The results of this study form the basis for the subsequent chapters. Among others, we show that the hypothesis of wet adhesion as primary mechanism of tree frog attachment (Barnes, 2012; Emerson & Diehl, 1980; Nachtigall, 1974; Smith *et al.*, 2006a) is not sufficiently supported by experimental data. VdW forces, which were for a long time believed to play only a minor role due to the presence of liquid in the pad-substrate gap (Emerson & Diehl, 1980), may well be involved in tree frog attachment. We also show that for a comprehensive understanding of tree frog attachment more knowledge is required about the internal morphology of the digital pads, the chemistry of the secreted mucus, and the attachment performance of tree frogs on various substrates as a function of the substrate’s surface properties.

The subsequent thesis chapters address these gaps of knowledge. In these chapters, I focus on the hylid frog species *Litoria caerulea* and *Hyla cinerea* (both Anura: Hylidae) for several scientific and practical reasons: (i) both species are among the most frequently studied tree frog species (e.g. Barnes *et al.*, 2011; Emerson & Diehl, 1980; Ernst, 1973a; Federle *et al.*, 2006; Green, 1981; Linnenbach, 1985; Scholz *et al.*, 2009), hence providing sufficient reference data for a discussion of results obtained in this thesis; (ii) the difference in snout-vent-length and body mass between the two species allows an assessment of the allometry of attachment performance parameters; (iii) both species are common pet animals, and thus relatively easy to obtain, inexpensive, and uncomplicated in handling and husbandry; (iv) both species are non-toxic, preventing safety measures for the experimenter during measurements.

In CHAPTER 3, we present a quantitative morphological analysis and functional interpretation of the internal morphology of the digital pads of *H. cinerea*. In particular, we aim to identify possible pathways for the transmission of adhesive and frictional forces from the ventral pad surface to the skeleton. Moreover, the low effective elastic modulus of frog pads—in combination with loads equivalent to several times the body weight acting on the pads (e.g. Bijma *et al.*, 2016)—raises the question how

the structures involved in the transmission of attachment forces are able to withstand substantial shear loads. Lastly, we investigate the presence of intrinsic muscular structures in the pads, which has been suggested in some historic references (Schuberg, 1891; Siedlecki, 1910). These aspects were examined by a 3D-analysis of the pad morphology, combining synchrotron micro-computer-tomography (μ -CT), histochemistry, and immunohistochemistry. A finite element model together with topological optimisation was used to provide a functional explanation of the distribution and orientation of the identified collagen fibre networks.

CHAPTER 4 addresses the mucus glands and their secretions in the digital pads of tree frogs. Despite their potentially central role in attachment, these components of the adhesive system are virtually undescribed in the current scientific literature. Using cryo-histochemistry combined with attenuated total reflectance-infrared spectroscopy (ATR-IR) and sum frequency generation spectroscopy (SFG), we characterised the general chemistry of digital tree frog mucus in *H. cinerea*. To test for a potential adaptation of the digital mucus chemistry towards attachment, we compared the mucus chemistry between different body locations for the tree frogs *H. cinerea* and *Osteopilus septentrionalis* (Anura: Hylidae), as well as between arboreal and non-arboreal (*Ceratophrys cranwelli*, Anura: Ceratophryidae; *Pyxicephalus adspersus*, Anura: Pyxicephalidae) frogs. Additionally, we quantified the gland morphology in *H. cinerea* using μ -CT to test for a modification of the ventral digital mucus glands compared to the dorsal ones, which would indicate attachment-related functional relevance. With the obtained 3D model of the mucus glands we also quantified the mucus volume available for attachment, and estimated the distribution of mucus present in the pad-substrate gap.

Finally, we studied in CHAPTER 5 the effects of variations in substrate roughness on the whole-animal attachment performance of the tree frogs *L. cinerea* and *H. cinerea*. By systematically varying the roughness of the test substrate, we elucidated the previously hypothesised contribution of mechanical interlocking (e.g. Cartmill, 1985; Crawford, 2016; Emerson & Diehl, 1980) to tree frog attachment. Parameters of adhesive and frictional performance were measured with an updated rotation platform. This setup allowed the dynamic measurement of the pad-substrate contact area, hence providing a more accurate estimate of the maximum attachment performance of tree frogs than obtained previously.

In the general discussion (CHAPTER 6), I put the findings of my doctoral research into a wider context. I integrate the outcomes of this thesis with the existing knowledge on the attachment of tree frogs and of current tree-frog-inspired adhesives to discuss the importance of the previously proposed mechanisms of tree frog attachment. Furthermore, I address the hypothesised convergent evolution of the digital pads of tree frogs in an attempt to illuminate the evolutionary history of the pads, and to identify pad components that may be 'optimised' for attachment. This section of the discussion is supported by a comparison of the structure and attachment performance of the digital pads of tree frogs to other bioadhesive systems. Finally, I discuss the biomimetic potential of tree frog attachment and suggest future directions in the development

of tree-frog-inspired adhesives based on the results of this thesis. I conclude with an outlook on future research on the attachment of frog pads, and address possible steps to deepen and expand the knowledge on tree frog attachment.





Any serious study is an orgy, a bacchanal of the supply of information. Of which one for the most part forgets again, as with every excess.

It depends on what gets stuck - but you never know what that will be. [...] Only when you have created a library, you can order it alphabetically.

W. Moers, 2011

CHAPTER 2

Tree frog attachment: Mechanisms, challenges, and perspectives

Abstract

Tree frogs have the remarkable ability to attach to smooth, rough, dry, and wet surfaces using their versatile toe pads. Tree frog attachment involves the secretion of mucus into the pad-substrate gap, requiring adaptations towards mucus drainage and pad lubrication. Here, we present an overview of tree frog attachment, with focus on (i) the morphology and material of the toe pad; (ii) the functional demands on the toe pad arising from ecology, lifestyle, and phylogenetics; (iii) experimental data of attachment performance such as adhesion and friction forces; and (iv) potential perspectives on future developments in the field. By revisiting reported data and observations, we discuss the involved mechanisms of attachment and propose new hypotheses for further research. Among others, we address the following questions: Do capillary and hydrodynamic forces explain the strong friction of the toe pads directly, or indirectly by promoting dry attachment mechanisms? If friction primarily relies on van der Waals (vdW) forces instead, how much do these forces contribute to adhesion in the wet environment tree frogs live in and what role does the mucus play? We show that both pad morphology and measured attachment performance suggest the coaction of several attachment mechanisms (e.g. capillary and hydrodynamic adhesion, mechanical interlocking, and vdW forces) with situation-dependent relative importance. Current analytical models of capillary and hydrodynamic adhesion, caused by the secreted mucus and by environmental liquids, do not capture

This chapter has been published as: LANGOWSKI, J.K.A., DODOU, D., KAMPERMAN, M. & VAN LEEUWEN, J.L. (2018a). Tree frog attachment: mechanisms, challenges, and perspectives. *Frontiers in Zoology* **15**, 1–21.

the contributions of these mechanisms in a comprehensive and accurate way. We argue that the soft pad material and a hierarchical surface pattern on the ventral pad surface enhance the effective contact area and facilitate gap-closure by macro- to nanoscopic drainage of interstitial liquids, which may give rise to a significant contribution of vdW interactions to tree frog attachment. Increasing the comprehension of the complex mechanism of tree frog attachment contributes to a better understanding of other biological attachment systems (e.g. in geckos and insects) and is expected to stimulate the development of a wide array of bioinspired adhesive applications.

Keywords: Toe pad; Attachment organ; Bioadhesion; Biotribology; Capillary adhesion; van der Waals; Drainage; Lubrication; Biomimetics; *Litoria caerulea*.

2.1 Introduction

Strong, reversible, and repeatable grip to diverse substrates is a basic requirement for climbing animals (Peattie, 2009). A wide range of attachment organs fulfilling this requirement has evolved in animals such as insects (Labonte & Federle, 2015b), reptiles (Gorb, 2008; Niewiarowski *et al.*, 2016), arachnids (Wolff & Gorb, 2016), and amphibians including tree (Hanna & Barnes, 1991) and torrent frogs (Endlein & Barnes, 2015). The research on torrent frogs is relatively new and limited to a few studies (Barnes *et al.*, 2002; Drotlef *et al.*, 2014; Endlein *et al.*, 2013; Iturri *et al.*, 2015; Ohler, 1995), and thus this review focusses on tree frogs.

With their toe pads, tree frogs attach to a wide range of substrates, from smooth glass to rough wood (Siedlecki, 1909) in both dry and wet environments (Endlein *et al.*, 2013). Tree frogs are a polyphyletic group (Duellman & Trueb, 1994; Faivovich *et al.*, 2005; Liem, 1970; Wells, 2007), but the basic morphology of their toe pads is consistent among frog families—a sign of convergent evolution (Barnes *et al.*, 2013; Green, 1979; Lee *et al.*, 2001; McAllister & Channing, 1983): the pads are soft (with an effective elastic modulus of ca. 20 kPa; e.g. Scholz *et al.*, 2009) and ventrally covered with a hierarchical, micro- to nanoscopic pattern of prismatic, epidermal cells separated by channels (Ernst, 1973a).

Several attachment mechanisms have been proposed for tree frogs' toe pads (e.g. Emerson & Diehl, 1980; Federle *et al.*, 2006; Hanna & Barnes, 1991). The prevailing hypothesis is that adhesion (i.e. the attachment force normal to the substrate surface) is induced by mucus that is present at the pad-substrate interface, leading to capillary and hydrodynamic forces (i.e. wet adhesion). Furthermore, intermolecular interactions (i.e. van der Waals [vdW] forces) and mechanical interlocking have been suggested to contribute to both adhesion and friction (i.e. the attachment force parallel to the substrate surface; Emerson & Diehl, 1980)¹.

¹'Holding' and 'attaching' synonymously describe combinations of adhesion and friction, whereas 'adhering' exclusively refers to adhesion.

Despite the substantial progress made in the understanding of tree frog attachment over the last centuries, several questions remain unanswered. For example, do capillary and hydrodynamic forces explain the strong friction of the toe pads directly, or indirectly by promoting dry attachment mechanisms? If friction primarily relies on vdW forces instead, how much do these forces contribute to adhesion in the wet environment tree frogs live in and what is the function of the mucus? Are there other attachment mechanisms active in the toe pads and how do these mechanisms interact? Several questions concerning the functional morphology of the attachment apparatus also remain open. Can the smooth soft toe pads of tree frogs conform closely to rough substrates to form a large area of dry contact and strong vdW forces, as described for the hairy attachment organs of geckos (Autumn *et al.*, 2000, 2002) and for the soft technical adhesives inspired thereof (Bartlett *et al.*, 2012a,b; Bartlett & Crosby, 2014)? Do the structures on (and in) the ventral epidermis support force generation and how are contact forces transmitted to other body parts? Do internal pad structures facilitate the spatial distribution of mechanical stresses or of energy?

We discuss these questions by revisiting evidence regarding the attachment performance of tree frogs or, when information is lacking, formulate new hypotheses for further research. First, we describe the morphology and material properties of the toe pads. Subsequently, a set of functional demands regarding adhesion and friction, which the toe pad presumably accommodates, is presented as well as the physical fundamentals of the mechanisms that have been proposed in previous research to explain tree frog attachment. Next, we discuss the observed attachment performance of tree frogs with respect to the stated questions, the functional demands, the morphological and material properties of the pad, and the physical fundamentals of attachment. Finally, we present conclusions of the reviewed knowledge available on tree frog attachment, and provide perspectives for potential future developments in the field.

2.2 Morphology and material properties of a toe pad

In this section, we describe the morphology of the limbs of tree frogs from the macroscopic anatomy (Fig. 2.1A₁) down to the nanoscopic features of the toe pad epidermis (Fig. 2.1D₂). To get insight in where and how contact forces are generated, we categorise the morphological elements based on their potential functionality (e.g. attachment control and force transmission). Furthermore, we discuss the material properties of the pad and the secreted mucus. For open questions on the pad morphology (and for possible approaches to answer these), we refer to the final section.

2.2.1 Functional morphology of limbs and toes

The tip of a tree frog's digit consists of the terminal phalanx, dermis, and epidermis (Fig. 2.1B₂; Ernst, 1973a,b; Hertwig & Sinsch, 1995). The dermis contains connective



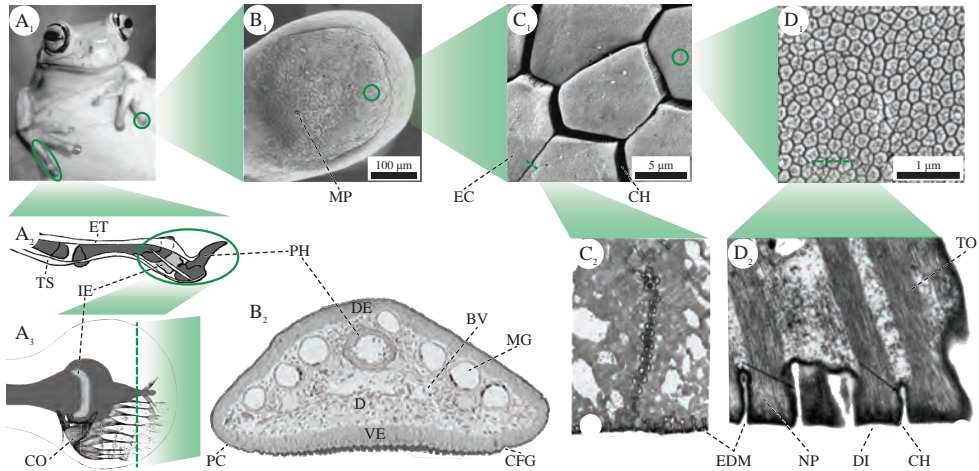


Figure 2.1 Morphology of a digit and toe pad of a hylid tree frog. (A) Macroscopic structures. (A₁) Forelimbs of *Litoria caerulea*. (A₂) Schematic lateral view of tendons, phalangi (dark grey), and the intercalary element (light grey) in a digit of *Scinax squalirostris*. (A₃) Schematic depiction of the collagen fibres in a pad of *Hyla dominicensis* in dorsal view. (B) Superficial and internal pad structures in *L. caerulea*. (B₁) SEM image of the ventral epidermis. (B₂) Transverse section through the toe of a juvenile frog. (C) Epidermal cells on the ventral surface. (C₁) SEM image of polygonal cells in *L. caerulea*. (C₂) TEM image of a tangential cross-section through the apical part of two adjacent cells in *Hyla cinerea*. (D) Fine structures of the apical surface of an epidermal cell. (D₁) High power SEM image of nanopillars and their central depressions ('dimples') in *L. caerulea*. (D₂) TEM image of a cross-section through a row of nanopillars in *H. cinerea* (black arrows: EDM). BV blood vessels, CFG circumferential groove, CH channel between two epidermal cells/nanopillars, CO collagen fibres, D dermis, DE dorsal epidermis, DI dimple, EC epidermal cell, EDM electron dense material, ET extensor brevis profundus tendon, IE intercalary element, MG mucus gland, MP mucus pore, NP nanopillar, PC pad curvature, PH (terminal) phalanx, TO tonofilaments, TS tendo superficialis, VE ventral epidermis. The illustrations are not to scale. A₁, B₁, C₁ and D₁ modified after Federle *et al.* (2006); A₂ modified after Manzano *et al.* (2007); A₃ modified after Noble & Jaekle (1928); B₂ modified after Barnes *et al.* (2011); C₂ and D₁ modified after Ernst (1973a). All figures printed with permission.

tissue, blood vessels, lymph space, mucus glands, as well as muscle and nerve fibres (Fig. 2.1B₂; Ernst, 1973a; Nakano & Saino, 2016; Siedlecki, 1910). The ventral epidermis constitutes the actual toe pad (Hertwig & Sinsch, 1995). The surface area A_p of single pads was reported by Linnenbach (1985; *Hyla cinerea*, 0.82–1.21 mm²), Ba-Omar *et al.* (2000; *Phyllomedusa trinitatis*, pad diameter d_p forelimb: 2.81 mm, d_p hindlimb: 2.47 mm), Mizuhira (2004; two Rhacophoridae, $A_p = 2.5 \text{ mm} \cdot 1.8 \text{ mm}$), Chakraborti *et al.* (2014; *Philautus annandalii*, $d_p = 1.2\text{--}1.5 \text{ mm}$), and Endlein *et al.* (2017; *Rhacophorus dennysi*, 2.1–4.7 mm²). The projected surface area A of all pads of an individual frog scales nearly isometrically with snout-vent-length ℓ_{SV} ($A \propto \ell_{SV}^{1.76\text{--}2.29}$; Barnes *et al.*, 2006; Smith *et al.*, 2006a,b) and with body mass m ($A \propto m^{0.68}$; Barnes, 1999).

2.2.1.1 Contact geometry

The distal portions of the toes are dilated (Emerson & Diehl, 1980; Noble & Jaeckle, 1928) and typically disc-shaped (Fig. 2.1B₁; Ba-Omar *et al.*, 2000). The unloaded ventral toe pad surface is convex (Green, 1981; Richards *et al.*, 1977), with a radius of curvature R of 0.72–1.57 mm in juveniles and 4.07–5.81 mm in adults of *Litoria caerulea* (Barnes *et al.*, 2011). Gu *et al.* (2016) suggested that the ball-on-flat arrangement of the curved pad on a flat substrate protects the pad from misalignment. Moreover, a curved pad might require less energy for active alignment of the pad with respect to the substrate. The ventral pad surface is divided into subunits forming a hierarchical surface pattern:

Macroscale In several species, grooves following the proximal-distal axis separate the pad surface, and a circumferential groove forms the lateroterminal pad boundary between proximal (squamous) and distal (columnar) ventral epidermis (e.g. Green, 1979; Hertwig & Sinsch, 1995; Lee *et al.*, 2001; Nokhbatolfighahai, 2013; Ohler, 1995; Siedlecki, 1910).

Microscale Prismatic cells on the ventral epidermis surface form a pattern of columnar pillars (Ernst, 1973a; Green, 1979; Hertwig & Sinsch, 1995). The apical parts of neighbouring surface cells are laterally separated by a channel network (Leydig, 1868; Welsch *et al.*, 1974; Fig. 2.1C₁). In *L. caerulea*, the superficial epidermal cells are skewed such that the apical cell surface is positioned more distally than the basal one (Nakano & Saino, 2016). The outline of the apical epidermal cell surface in *L. caerulea* and several other species is exclusively polygonal, ranging from pentagonal to octagonal (e.g. Barnes *et al.*, 2013; Dewitz, 1883; Scholz *et al.*, 2009). In *L. caerulea*, Barnes *et al.* (2013) found 65.4% hexagonal, 19.8% pentagonal, 14.2% heptagonal, and 0.6% octagonal, non-randomly distributed cells. Chen *et al.* (2015) reported a similar distribution with 55% of hexagonal cells, and an elongation of the cells along the proximal-distal pad-axis (aspect ratio = 1.46) in *Polypedates megacephalus*. The apical cell surfaces are curved convexly (Federle *et al.*, 2006; Leydig, 1868). In *H. cinerea*, the average edge length a_c of the apically separated cells is 10.2 μm (Ernst, 1973a), the cell height h_c is 6.5 μm , and the apical cell surface A_c is 64 μm^2 (Linnenbach, 1985). Similar values for A_c (63–172 μm^2) and cell diameter d_c (8–14.8 μm ; see Fig. 2.2B) were reported for a number of species (Ba-Omar *et al.*, 2000; Chakraborti *et al.*, 2012; Green, 1979, 1980; McAllister & Channing, 1983). Smith *et al.* (2006b) found a positive correlation between A_c and ℓ_{SV} ($r = 0.86$; $p = 0.01$; 1–2 frogs per species), which was observed neither by McAllister & Channing (1983; 1–2 frogs per species) nor by Green (1980; $r = 0.036$; 12–17 frogs per species). Further work is required to conclude on the scaling of cell dimensions with ℓ_{SV} . The cell density ρ_c (cells per mm^2 toe pad area) ranges between ca. 2450 and 15 700 mm^{-2} (Linnenbach, 1985; Rivero *et al.*, 1987; Smith *et al.*, 2006b).

The channels in between the superficial epidermal cells are 1–5 μm wide (Smith *et al.*,



2006b; Welsch *et al.*, 1974). In *P. megacephalus*, the channel alignment is anisotropic; the cumulative channel length is ca. 70% lower along the lateral pad axis than along the proximal-distal axis (Chen *et al.*, 2015). Mucus glands with large lumina are distributed in the dermis of the distal digital segment (Fig. 2.1B₂; Welsch *et al.*, 1974) and secrete mucus (Blackwall, 1845) via ducts and 7–8 μm wide pores into the epidermal channel network (Green & Carson, 1988). The spatial density and distribution pattern of the pores vary interspecifically (Ba-Omar *et al.*, 2000; Green, 1979; McAllister & Channing, 1983). A detailed analysis of the mucus gland morphology is unavailable.

Nanoscale Peg-like protrusions, called nanopillars (also plaques, pegs, or microvilli), cover the apical surface of the outermost epidermal cells (Siedlecki, 1910; Fig. 2.1D_{1,2}). Nanopillars are prismatic structures separated from each other by a nanoscopic channel network analogously to the microscopic channel network between the epidermal cells (Ernst, 1973a; Welsch *et al.*, 1974). For various species, nanopillar diameters (d_n) of 15–800 nm were reported (Barnes *et al.*, 2013; Ernst, 1973a; Green, 1979; Green & Simon, 1986; Mizuhira, 2004; Scholz *et al.*, 2009). In *L. caerulea*, the nanopillars have a (mostly) hexagonal outline with an aspect ratio of approximately 1 and a nanochannel width $w_n \ll d_n$ (Scholz *et al.*, 2009). Measurement of w_n by atomic force microscopy (AFM) presumably underestimates the channel width (and depth; Scholz *et al.*, 2009). AFM and transmission electron microscopy (TEM) measurements of the nanopillars (Ernst, 1973a; Federle *et al.*, 2006) and cryo-scanning electron microscopy (SEM; Barnes *et al.*, 2013) indicated a 7.7 ± 4.2 nm deep ‘dimple’ on the apical surface (Fig. 2.1D₂; Scholz *et al.*, 2009).

Geometrical model of the epidermis Based on the dimensions of the epidermal cells reported in literature, we built a geometrical model (Fig. 2.2) of the epidermis to predict the increase in surface area by the cellular structures and the effective contact surface (that we assume to be formed by the apical nanopillar surfaces not covered by dimples). For calculations of the parameter values, see Section 2.SI.2.1.

For an approximately circular pad with diameter $d_p = 3.6$ mm, we compute a projected ventral area $A_p \approx 10.2$ mm² covered with about $126 \cdot 10^3$ epidermal cells, which agrees with the cell densities reported for real animals (Linnenbach, 1985; Smith *et al.*, 2006b). Cells with a regular hexagonal outline ($d_c = 10$ μm , $h_c = 10$ μm , $w_c = 1$ μm) increase the wetted contact area (i.e. the projected ventral surface + surface of the channel walls) 4.7-fold compared to a smooth pad. Nanopillars ($d_n = 300$ nm, $h_n = 300$ nm, $w_n = 100$ nm according to Fig. 2.3 in (Barnes *et al.*, 2013), dimple diameter $\approx d_n - \Delta r = 240$ nm) cover the apical surface of every cell. The whole pad contains ca. $73 \cdot 10^6$ nanopillars. This corresponds with a nanopillar density of ca. $7.1 \cdot 10^6$ mm⁻², which is in the same order of magnitude as the setae densities reported in geckos (Arzt *et al.*, 2003). Together, the epidermal cells and nanopillars enlarge the wetted contact area 6.6-fold compared to a smooth pad. About 20% of A_p is formed by the intercellular channel network. Including the nanoscopic channel

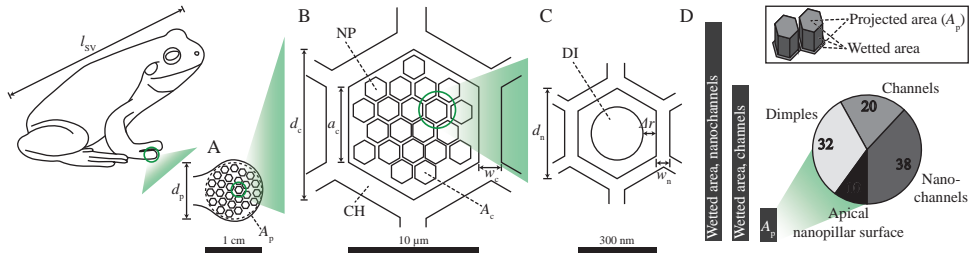


Figure 2.2 Geometrical model of the ventral toe pad epidermis in a tree frog with snout-vent-length ℓ_{SV} . (A) The approximately circular projected ventral pad area A_P (diameter d_P) is (B) covered by polygonal epidermal cells with diameter d_c , edge length a_c , channel width w_c , and apical surface area A_c . (C) Each cell accommodates polygonal nanopillars with diameter d_n , channel width w_n , and a distance Δr between dimple and nanopillar edge. (D) Enhancement (in %) of the wetted area by the micro- and nanochannels relative to A_P and composition of A_P (in %) assuming regular, hexagonal outlines of the epidermal cells and nanopillars. Inset: Definition of projected and wetted areas shown for a hexagonal pillar. CH channel, DI dimple, NP nanopillar.

network, this fraction rises to around 58%. Dimples occupy 32% of the pad. Finally, about 10% of A_P is not covered by channels or dimples.

2.2.1.2 Attachment control

Several morphological elements in the limbs and digits of tree frogs are likely to contribute to an active control of attachment. The forelimbs are adapted towards an arboreal lifestyle. Specifically, kinematic and electromyographic analyses in *L. caerulea* and *Phylllobates bicolor* revealed that variations in the concerted action of the forelimb musculature allow for a power grip (i.e. clamping an object between flexed digits and palm), a precision grip (i.e. pinching an object between digit tips), and active positioning of the hands during climbing on narrow substrates (Manzano *et al.*, 2008).

A single layer of smooth muscle cells is present in the wall of each mucus gland (Ernst, 1973b; Mizuhira, 2004). This muscle type accommodates large strains and might enhance the deformability of the glands, minimising unintentional mucus secretion during pad loading. A dermal nerve plexus probably innervates the glandular muscle cells and thus controls mucus squeeze-out (Welsch *et al.*, 1974). Several authors (Gadow, 1909; Schuberg, 1891; Siedlecki, 1910) reported smooth muscle fibres in tree frogs' toe pads, which, however, was not confirmed in later literature (Ernst, 1973b; Mizuhira, 2004).

The mucus ducts are surrounded by several layers of tightly interconnected cells (Ernst, 1973b), which support the ducts mechanically and presumably facilitate mucus squeeze-out. The dermal tissue between the terminal phalanx and the ventral epidermis is heavily vascularised (Fig. 2.1B₂; Noble & Jaekle, 1928), which might allow an active modification of pad curvature (Afferante *et al.*, 2016) and pad stiffness (Barnes *et al.*, 2011) by varying blood pressure.

2.2.1.3 Force transmission

The morphological basis of the transmission of attachment forces, generated at the pad-substrate interface, within the pad or to other body parts has not been studied extensively. An internal skeleton is the principle load bearing and transmitting structure in each limb (Fig. 2.1A_{2,3}). Many tree frog species have a cartilaginous intercalary element between the terminal and subterminal phalanx of each digit, which increases digit flexibility and facilitates axial rotations of the terminal phalanx (Fig. 2.1A_{2,3}; e.g. Hanna & Barnes, 1991; Manzano *et al.*, 2007; v. Wittich, 1854). In each digit, two tendons support the skeleton in load transmission: the dorsal *Tendo Superficialis* extends the digit, and a ventral tendon connected to the musculus extensor brevis profundus adducts the terminal phalanx (Fig. 2.1A₂; Hanna & Barnes, 1991; Manzano *et al.*, 2007).

Collagen fibres connect the terminal phalanx with the ventral basement membrane (Noble & Jaeckle, 1928; Schuberg, 1891; v. Wittich, 1854). The low lateral connectivity of the collagenous structures (Fig. 2.1A₃) suggests a low stiffness of the pad in dorso-ventral compression and lateral extension (Ernst, 1973b). The deformable lymph space (Nakano & Saino, 2016) and the blood-vessel network in the connective tissue also point towards low stiffness and viscoelastic properties of the pad.

The lateral membranes of adjacent epidermal surface cells are interconnected basally, which mechanically strengthens the epidermis (Fig. 2.1C₂; Ernst, 1973a; Mizuhira, 2004; Welsch *et al.*, 1974). Furthermore, tonofilament bundles—arranged parallel to the longitudinal axes of the superficial epidermal cells (Dewitz, 1883)—interconnect the cells through desmosomes (Ernst, 1973a,b), split up towards the ventral surface, and terminate at the apical ends of the nanopillars (Fig. 2.1D₂; Chakraborti *et al.*, 2014; Ernst, 1973a; Nakano & Saino, 2016; Welsch *et al.*, 1974). The ordered arrangement of the tonofilaments vanishes, as they extend into the deeper epidermal layers (Ernst, 1973a). We expect that tonofilaments, collagenous structures, and digital bones together facilitate the transmission of attachment forces from the pad-substrate interface to the rest of the body (e.g. for locomotion). The local expression of keratins forming the tonofilaments in the nanopillars (Vandebergh *et al.*, 2013) supports the relevance of the tonofilaments for force transmission. A thin layer of electron dense material covers the inner side of the plasma membrane of the apical cells (Fig. 2.1D₂; Ernst, 1973a; Welsch *et al.*, 1974).

2.2.2 Material properties

The high compliance of the toe pad in compression influences its attachment performance, for example by increasing the effective contact area on rough substrates. Compliance depends, among other properties, on the material-specific Young's modulus E , on the Poisson's ratio ν , and on geometry and spatial arrangement of load-bearing structures. Overall, the toe pads were reported to be very soft (v. Wittich, 1854), with an effective elastic modulus $E^* = E/(1 - \nu^2)$ of the whole epidermis

Table 2.1 Experimental findings on the effective elastic modulus E^* of tree frogs' toe pads.

Reference	Species	E^* [kPa]	d_i [μm]	r_i [μm]	Remarks
Barnes <i>et al.</i> (2013)	<i>L. caerulea</i>	33.5 ± 4.1	0.2	—	<i>Ex vivo</i> , AFM, Hertz theory
	<i>R. prominanus</i>	28.7 ± 10.5			
Scholz <i>et al.</i> (2009)	<i>L. caerulea</i>	14000	1.6	—	Pyramidal AFM tip
Barnes <i>et al.</i> (2011)	<i>L. caerulea</i>	4–25	200	—	Spherical MT, JKR-model
Kappl <i>et al.</i> (2016)	<i>L. caerulea</i>	54 ± 7	0.5	0.4	<i>Ex vivo</i> , Spherical AFM, Hertz theory
		40.7 ± 3.2		13.3	

d_i indentation depth, r_i indenter radius.
AFM atomic force microscopy, JKR Johnson-Kendall-Roberts, MT microtribometry.

reported to be lower than that of most biological materials (e.g. Vincent & Wegst, 2004). Repeated indentation experiments showed no plastic deformation of the pad (Scholz *et al.*, 2009). A small load-unload hysteresis in the force-displacement curve (Scholz *et al.*, 2009) and a decrease in the normal contact force during constant pad deformation (Barnes *et al.*, 2011) suggest viscoelasticity of the pad.

The effective elastic modulus of the toe pad varies by factors of up to 10^4 between studies (Table 2.1). Such variations might be explained by the structure of the cytoskeleton (Scholz *et al.*, 2009), which makes E^* strongly dependent on the location and direction of indentation, by the use of *in vivo* (e.g. Scholz *et al.*, 2009) versus *ex vivo* (e.g. Kappl *et al.*, 2016) samples, and by the use of different indenter shapes and contact mechanics models (e.g. Oliver-and-Pharr-theory in Scholz *et al.*, 2009; Johnson-Kendall-Roberts-/Hertz-model in other studies). Variations might also indicate a stiffness gradient (Barnes *et al.*, 2011) based on an increase of E^* with indentation depth d_i . The exact variation of E^* with d_i is unknown.

2.2.3 Mucus properties

The mucus forms a liquid bridge with a meniscus that fully surrounds the toe pad (Green, 1981) and has a wedge thickness of 5–10 μm (Barnes *et al.*, 2013). The meniscus height and curvature are unknown. The mucus viscosity μ in *L. caerulea* is about 1.43 mPa·s, measured with laser-tweezer micro-rheometry (Federle *et al.*, 2006). The mucus is often approximated as a Newtonian liquid (i.e. μ is strain-rate-independent), but non-Newtonian liquid properties are suggested by the presence of polysaccharides in filled mucus glands in *H. cinerea* (Ernst, 1973b). The static contact angle ϕ of mucus microdroplets on hydrophilic and hydrophobic substrates is low ($\phi \ll 10^\circ$), which indicates an adhesive capillary function of the mucus independent of the wetting properties of the substrate (Drotlef *et al.*, 2013).



2.3 Functional demands on a toe pad

Morphology and operation of an attachment organ are codetermined by the functional demands on the respective organ (Duellman & Trueb, 1994). In the tree frog, these demands arise, among others, from the environment, phylogeny, and lifestyle of the animals.

2.3.1 Directional contact forces

Directional contact forces allow tree frogs to climb into the higher ecological layers of forests and other vegetation (Crawford *et al.*, 2012). To stay attached to substrates with different inclination angles (e.g. overhanging leafs and vertical tree stems), tree frogs have to generate both strong adhesion and friction. The transmission of contact forces via skeletal elements suggests preferential directions of the contact force vector for whole limbs and single digits and thus anisotropic mechanisms of force generation. Gripping as a special case of force directionality is discussed elsewhere (Endlein *et al.*, 2017; Hill *et al.*, 2018; Manzano *et al.*, 2008; Tyler & Davies, 1993).

2.3.2 Substrates with diverse surface characteristics

Tree frogs encounter a variety of substrates such as plant leaves, tree bark, insect cuticle, and stones, with a wide range of random or structured roughness (Holdgate, 1955; Koch *et al.*, 2008; Vincent & Wegst, 2004), surface energy (i.e. the energy required to form a unit area of free surface of a given material; Labonte & Federle, 2015b), stiffness (Peattie, 2009), and wetting² level. Natural substrates can be wetted via rain (e.g. in tropical habitats) and the mucus secretion on amphibian skin (Stebbins & Cohen, 1995; Tracy *et al.*, 2011; Tyler & Davies, 1993). Environmental temperature, air humidity (e.g. Puthoff *et al.*, 2010), and (mechanical or chemical) surface pollution may also affect the attachment performance of tree frogs. The ability of tree frogs to clean their pads by repeated stepping was discussed by Crawford *et al.* (2012). Generating contact forces that are high enough to keep the animals attached to natural substrates with different properties is arguably a primary demand on the toe pads.

2.3.3 Static and dynamic attachment

Tree frogs use a combination of locomotory modes such as jumping, horizontal walking, and vertical climbing (Wells, 2007), for which reversible and repeatable attachment is crucial (Peattie, 2009). For dynamic conditions, attachment and deta-

²‘Wetting’: the presence of liquid on a substrate.

achment (and switching between the two states; Bullock *et al.*, 2008) should be fast and controlled (Bijma *et al.*, 2016), and contact forces need to be large enough to resist detachment from the substrate during sudden events such as the attack of a predator or the wind-induced shaking of a leaf (Drechsler, 2008). Additionally, toe pads enable static attachment, as observed in resting frogs (Siedlecki, 1909, 1910) or during copulation (Stebbins & Cohen, 1995).

2.3.4 Transmission of contact forces

We expect toe pads to transmit the generated forces internally and to other body parts. Force transmission within a morphological unit, for example the epidermis, has been suggested to distribute mechanical stresses at the pad-substrate interface, hence reducing the risk of unwanted detachment (Labonte & Federle, 2015b) or of damaging the epidermis (Duellman & Trueb, 1994). Force transmission between the epidermis and other body parts allows (directed) locomotion and requires a functional integration of the pads into the whole locomotory apparatus (Manzano *et al.*, 2008, 2007; see also Section 2.2.1.3), as observed in geckos (Autumn & Peattie, 2002).

2.4 Basic theory of potential attachment mechanisms in a toe pad

Various mechanisms of force generation (Emerson & Diehl, 1980), as well as lubrication (Federle *et al.*, 2006) and drainage of the secreted mucus (Persson, 2007) have been suggested to play a role in the attachment and detachment of tree frogs. Here, we introduce these mechanisms for the subsequent discussion of their possible contributions to attachment. For a list of the used symbols and for a discussion of suction as potential adhesion mechanism, we refer to Sections 2.SI.1.1 and 2.SI.3.4.

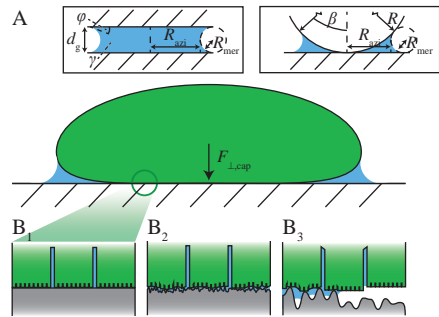
2.4.1 Force generation

2.4.1.1 Capillary forces

A liquid bridge in the gap between the toe pad and the substrate can be formed by the secretion of mucus, by capillary condensation of water vapour, or by external surface wetting (e.g. rain droplets). The meniscus of this bridge can cause capillary contact forces (Fig. 2.3A), arising from the surface tension γ of the liquid (Butt & Kappl, 2009). Capillary adhesion is attractive for a concave meniscus if seen from the gas phase (i.e. contact angle $\phi < 90^\circ$); for water, a circular, concave meniscus is present on a hydrophilic substrate up to a meniscus height $\kappa = (\gamma/g\rho)^{-0.5} \approx 2.7$ mm (g gravitational acceleration, ρ density).



Figure 2.3 Schematic representation of capillary adhesion between a toe pad (green) and a hydrophilic substrate caused by the formation of a mucus meniscus (blue). Left inset: Capillary adhesion between two flat, solid plates. Right inset: Capillary adhesion between a solid sphere and a flat, solid plate. (B) Hypothesised changes in wetting state with an increase in substrate roughness or pad-substrate gap width (Crawford *et al.*, 2016). d_g gap width, $F_{\perp,\text{cap}}$ capillary adhesion, R sphere radius, R_{mer} , R_{azi} meridional and azimuthal radius of meniscus curvature, β filling angle, γ mucus surface tension, ϕ contact angle. B modified after Crawford *et al.* (2016). Printed with permission.



A circular meniscus between two smooth, flat, rigid plates with equal contact angles (Fig. 2.3A, left inset) and with homogeneous surface energies is the first and most common model of capillary adhesion applied to tree frogs' toe pads (e.g. Emerson & Diehl, 1980). According to this model, the capillary adhesion $F_{\perp,\text{cap}}$ generated by a meniscus with azimuthal and meridional radii of curvature R_{azi} and R_{mer} , respectively, is (Labonte & Federle, 2015b):

$$F_{\perp,\text{cap}} = 2\pi R_{\text{azi}}\gamma \sin \phi + \pi R_{\text{azi}}^2\gamma \left(\frac{1}{R_{\text{mer}}} - \frac{1}{R_{\text{azi}}} \right) \quad (2.1)$$

$$R_{\text{mer}} = \frac{d_g}{2 \cos \phi}.$$

The first term represents the direct action of surface tension at the three-phase contact line (negligible at $R_{\text{azi}} \ll R_{\text{mer}}$), and the second term the effect of the Laplace pressure across the meniscus surface. In reality, the contact angle ϕ can differ strongly from the ideal case assumed in the described models, as a result of phenomena such as contact-line pinning, surface energy variations due to substrate roughness, or the entrapment of air between a rough substrate and a fluid meniscus (Fig. 2.3B; de Gennes *et al.*, 2004).

The capillary adhesion between a rigid sphere (radius R) and a flat plate may represent tree frog attachment more closely than the plate-plate contact. For equal contact angles and a filling angle β between the vertical and the three-phase contact line (Fig. 2.3A, right inset; Butt & Kappl, 2009), Equation 2.1 can be rewritten to model the sphere-plate contact:

$$F_{\perp,\text{cap}} = 2\pi R \sin \beta \gamma \sin (\phi + \beta) + \pi R^2 \sin^2 \beta \gamma \left(\frac{1}{R_{\text{mer}}} - \frac{1}{R_{\text{azi}}} \right) \quad (2.2)$$

$$R_{\text{mer}} = \frac{R(1 - \cos \beta)}{2c}$$

$$R_{\text{azi}} = R \sin \beta - R_{\text{mer}} [1 - \sin (\phi + \beta)]$$

$$c = \frac{\cos (\phi + \beta) + \cos \phi}{2}.$$

For $R \ll R_{\text{azi}} \ll R_{\text{mer}}$ and $\beta, \phi \approx 0$, Equation 2.2 simplifies to:

$$F_{\perp, \text{cap}} = 4\pi R\gamma. \quad (2.3)$$

The capillary adhesion between two deformable objects (one of them, for example, being a deformable sphere, which may represent a soft, round toe pad more closely than a rigid, flat plate) is stronger than between two rigid objects, because of an increased contact area in the former case (Butt *et al.*, 2010; Wexler *et al.*, 2014). For a discussion on the capillary adhesion of deformable objects and on capillary friction we refer to Sections 2.SI.3.2 and 2.SI.3.3, respectively.

2.4.1.2 Hydrodynamic forces

Mucus flow between toe pad and substrate during attachment and detachment generates hydrodynamic contact forces (Fig. 2.4). Hydrodynamic adhesion (also called Stefan or viscous adhesion) can be modelled assuming a flow between two flat, rigid plates with radius r_p fully immersed in a viscous liquid and initially separated by a distance d_g (Fig. 2.4A₂; Stefan, 1874). During separation of the plates, liquid flows from the surroundings into the widening gap. Hydrodynamic adhesion $F_{\perp, \text{hyd}}$ is the force required to overcome the viscous resistance against this flow (Reynolds, 1886; Stefan, 1874):

$$F_{\perp, \text{hyd}} = -\frac{\partial d_g}{\partial t} \frac{3}{2} \pi \mu \frac{r_p^4}{d_g^3}. \quad (2.4)$$

Whereas the attachment of two plates may represent the contact of a flattened pad with a substrate reasonably well, we expect that a sphere-plate contact describes the approach of a submerged, curved pad to the substrate better. Between a smooth sphere with radius R and a flat plate, $F_{\perp, \text{hyd}}$ is (Cox & Brenner, 1967):

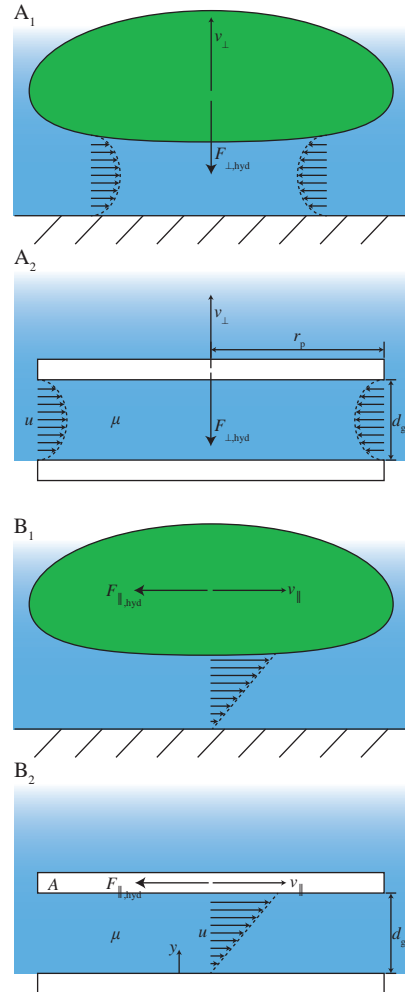
$$F_{\perp, \text{hyd}} = -\frac{\partial d_g}{\partial t} 6\pi\mu \frac{R^2}{d_g}. \quad (2.5)$$

Hydrodynamic forces act oppositely to the direction of surface movement and can hence also be repulsive. Hydrodynamic repulsion during the approach of deformable objects is lower, and adhesion during separation is higher than for rigid objects (Kaveh *et al.*, 2014).

Next to adhesion and repulsion, hydrodynamic effects can also cause hydrodynamic (viscous) friction. For the shear flow of liquid between a stationary plate (i.e. the substrate) and a plate sliding at a speed v_{\parallel} parallel to the stationary one (i.e. the toe



Figure 2.4 Hydrodynamic (A) adhesion and (B) friction (1) during the schematic interaction between a toe pad (green) and the substrate based on displacement-induced flow of mucus (blue) and (2) in a model of the contact of two flat and rigid (cylindrical) plates. A area, d_g gap width, $F_{\perp,\text{hyd}}$ hydrodynamic adhesion, $F_{\parallel,\text{hyd}}$ hydrodynamic friction, r_p plate radius, u flow speed, v_{\perp} detachment speed, v_{\parallel} sliding speed, y spatial coordinate normal to the substrate, μ viscosity.



pad; Fig. 2.4B₂), the hydrodynamic friction $F_{\parallel,\text{hyd}}$ is (Landau & Lifshitz, 1987):

$$\begin{aligned}
 F_{\parallel,\text{hyd}} &= \mu A \frac{\partial u}{\partial y} \\
 &= \mu A \frac{v_{\parallel}}{d_g}.
 \end{aligned}
 \tag{2.6}$$

Equation 2.6 is only valid for gaps large enough to allow free shear flow (with a linear velocity profile), and the concept of hydrodynamic friction should be applied with caution to tree frogs' toe pads. It is likely that liquid is drained out of the pad-substrate gap during sliding, in which case Equation 2.6 does not hold anymore, particularly with an increasing sliding distance. Alternatively, viscous-poroelastic

effects have been proposed to contribute to tree frog attachment (Tulchinsky & Gat, 2015).

2.4.1.3 Van der Waals forces

Van der Waals (vdW) interactions between single atoms or molecules of a toe pad and the substrate may cause adhesive and frictional contact forces (Fig. 2.5). VdW forces are known to be dominant in the attachment of geckos (e.g. Autumn & Peattie, 2002; Loskill *et al.*, 2013) and might also play a significant role in tree frogs (Emerson & Diehl, 1980; Federle *et al.*, 2006).

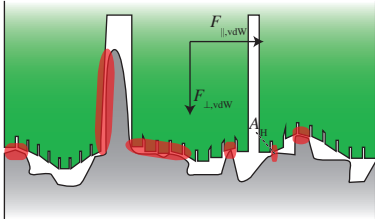


Figure 2.5 Schematic generation of van der Waals (vdW) forces ($F_{\perp,\text{vdW}}$, $F_{\parallel,\text{vdW}}$) between ventral toe pad epidermis (green) and substrate (grey) for a system-specific Hamaker constant A_H . VdW interactions occur in regions of close pad-substrate contact (red).

Between two flat plates with a contact area A separated by a distance d_g , the macroscopic vdW force $F_{\perp,\text{vdW}}$ is (Popov, 2010):

$$F_{\perp,\text{vdW}} = -A \frac{A_H}{6\pi} \frac{1}{d_g^3}, \quad (2.7)$$

where A_H is the system-specific Hamaker constant. A_H scales with the electron density of the interacting molecules and with temperature (Israelachvili, 2011).

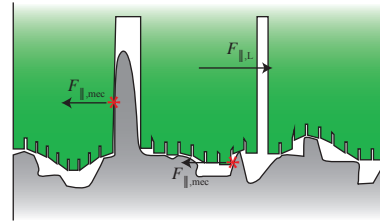
Friction arising from vdW interactions between two objects sliding along each other is termed dry (or Coulomb) friction. Dry friction $F_{\parallel,\text{vdW}}$ is proportional to the normal load $F_{\perp,\text{L}}$ (i.e. a body weight component $F_{\perp,\text{g}}$ and, if applicable, adhesion F_{\perp}) and the system-specific friction coefficient μ_{\parallel} (Israelachvili, 2011):

$$\begin{aligned} F_{\parallel,\text{vdW}} &= \mu_{\parallel} F_{\perp,\text{L}} \\ &= \mu_{\parallel} (F_{\perp,\text{g}} + F_{\perp}). \end{aligned} \quad (2.8)$$

2.4.1.4 Mechanical interlocking

Mechanical interlocking is the mutual intermeshing of (parts of) an attachment organ and substrate asperities (Gorb, 2008). In tree frogs, interlocking between the epidermal cells and the asperities of a rough substrate has been proposed to contribute to attachment (Fig. 2.6; Crawford *et al.*, 2016; Emerson & Diehl, 1980). Arguably, the attachment force generated by mechanical interlocking is proportional to the number of individual contact points.

Figure 2.6 Schematic mechanical interlocking between a superficial cell (left star) or a nano-pillar (right star) on the ventral toe pad epidermis (green) and asperities of a rough substrate (grey) at a shear load $F_{\parallel,L}$.



2.4.2 Liquid management

The mucus between toe pad and substrate not only introduces hydrodynamic or capillary forces, it may also lubricate the pad during sliding and hinder closure of the pad-substrate gap requiring drainage of surplus mucus. Here, we introduce the theories of lubrication and drainage with respect to their potential appearance in tree frog attachment.

2.4.2.1 Lubrication

Lubrication of an object sliding over a substrate with velocity v_{\parallel} changes the generated friction dramatically compared to dry friction (Fig. 2.7). The regime of lubrication of the pad-substrate-system depends on its Stribeck number $St = (\mu_{\parallel} v_{\parallel}) / (F_{\perp,L} A^{-1})$ (Pitenis *et al.*, 2014). At low St , dry pad-substrate contacts and dry friction dominate (boundary lubrication; Equation 2.8). At higher St (e.g. lower normal load $F_{\perp,L}$ per unit area), dry contacts between substrate asperities and the sliding toe pad become less frequent, and the load of the pad is carried both by dry contacts and enclosed volumes of mucus (mixed lubrication). At even higher St , the mucus carries most of the load, and the pad and substrate influence each other by deformation of substrate asperities through the mucus (elastohydrodynamic lubrication). At large St , loads are transmitted only via the mucus layer (hydrodynamic lubrication), and hydrodynamic friction occurs (Equation 2.6).

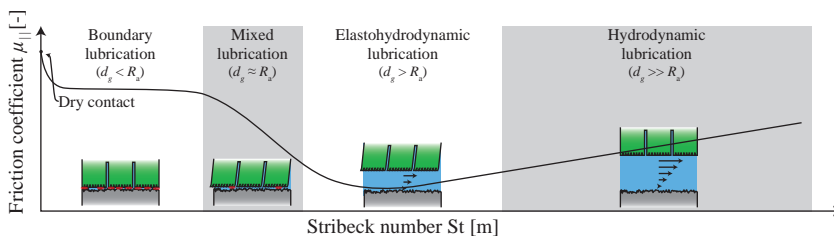


Figure 2.7 Stribeck diagram showing the proposed spectrum of lubrication modes and the resulting friction coefficients μ_{\parallel} in tree frogs' toe pads as a function of the Stribeck number St .

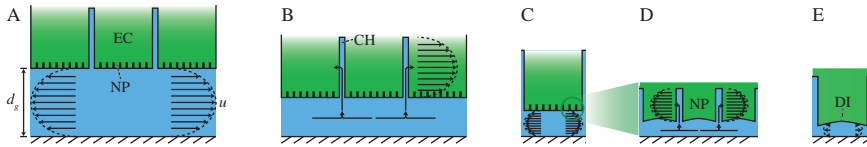


Figure 2.8 Hypothesised regimes of mucus drainage in a tree frog's toe pad. (A) Far field regime. (B) Intermediate field regime. (C) Near field regime. (D) Drainage through the nanochannel network and (E) the nanopillar-substrate gap. DI dimple, EC epidermal cell, NP nanopillar. d_g gap width, u flow speed. Modified after Gupta & Fréchet (2012). Printed with permission.

2.4.2.2 Drainage

In artificial adhesives (Dhong & Fréchet, 2015; Gupta & Fréchet, 2012), and possibly also in tree frogs, a channel network, which is separated by liquid from a substrate, leads to several drainage regimes depending on the gap width d_g . In the nomenclature of these regimes, we follow Gupta & Fréchet (2012). For $d_g \gg d_0$ ($= w_c(h_c/(w_c + d_c))^{1/3} \approx 1 \mu\text{m}$ in tree frogs; Dhong & Fréchet, 2015; Gupta & Fréchet, 2012), radial squeeze-out of liquid through the gap (far field regime; Fig. 2.8A) was confirmed experimentally in artificial surfaces covered with cylindrical pillars (Gupta & Fréchet, 2012). For $d_g \approx d_0$, liquid flows increasingly through the channels, which become the main source of hydrodynamic friction, down to a distance d_1 (intermediate field regime; Fig. 2.8B). For $d_g \ll d_0$, the viscous resistance against liquid flow between single pillars and substrate dominates (near field regime; Fig. 2.8C). Drainage in tree frogs through the nanopillar channels and single nanopillar-substrate gaps may be assessed analogously to the drainage through microscopic artificial surface structures (Fig. 2.8D,E; Persson, 2007). In torrent frogs, the epidermal channel system is elongated along the proximal-distal pad axis (Drotlef *et al.*, 2014; Ohler, 1995). This elongation may ease the drainage of water flowing around the toe pads, hence enabling the strong attachment of these animals on overflowed substrates (Barnes *et al.*, 2002; Drotlef *et al.*, 2014; Endlein *et al.*, 2013; Iturri *et al.*, 2015; Ohler, 1995).

2.5 Attachment performance of tree frogs

The adhesive and frictional performance of tree frogs have been studied for whole animals and single limbs or toe pads. Adhesion and friction of whole frogs have been typically measured using a platform that rotates around a horizontal axis (Tables 2.2 and 2.3, top; Fig. 2.SI.3), originally designed by Emerson & Diehl (1980) and refined by Hanna & Barnes (1991). Simple trigonometry allows a calculation of adhesion and friction based on the measured inclination angles at which the animals slide on (α_{\parallel}) and fall off (α_{\perp}) the platform (see Section 2.SI.3.1). For single limb/pad-measurements, various force transducers (Tables 2.2 and 2.3, bottom) have been used. Effects of substrate properties on attachment forces have been also measured and

behavioural traits related to attachment have been observed.

Here, we address findings on the attachment performance of tree frogs with respect to the questions stated in the introduction: Which mechanisms do contribute to tree frog attachment and how does the pad morphology support these mechanisms? We attempt to answer these questions by finding the best possible interpretation of the previous findings with regard to the pad properties, functional demands and, particularly, to the above described mechanisms, for example by comparison of measured contact forces with model predictions. Potential key questions and approaches for future developments in the field will be described in the final section.

2.5.1 Adhesion

2.5.1.1 Measured adhesion performance

Whole animals The adhesion measured for whole tree frogs ranges between 0.5 and 372 mN (Table 2.2, top) and scales above squared with snout-vent-length ℓ_{SV} ($F_{\perp} \propto \ell_{SV}^{2.19}$; Smith *et al.*, 2006b). Body mass m scales roughly volumetrically (i.e. isometrically) with ℓ_{SV} ($m \propto \ell_{SV}^3$), whereas the ventral pad area A scales approximately quadratically with ℓ_{SV} ($A \propto \ell_{SV}^2$; Smith *et al.*, 2006a). The resulting negative scaling of contact area per body mass with body size (Smith *et al.*, 2006a,b) leads to a decline in adhesive performance with body size (Barnes, 1999; Barnes *et al.*, 2006; Emerson & Diehl, 1980; Smith *et al.*, 2006a,b). Adhesion scales as $F_{\perp} \propto A^{1-1.19}$ (Barnes, 1999; Barnes *et al.*, 2006; Emerson & Diehl, 1980) and at a higher rate with ℓ_{SV} than A (Smith *et al.*, 2006a), which is favourable compared to the situation of isometric scaling. For a discussion of potential adaptations to the problem of isometric scaling, see Smith *et al.* (2006b).

Despite a variation of the measured adhesion by a factor of 10^4 , the tenacity (i.e. adhesive force per unit area) measured for whole tree frogs on smooth substrates varies relatively little, between 0.3 and 1.4 mN mm⁻² (Table 2.2, top). In these calculations, however, contact area was assumed to equal the total ventral area of all toe pads (e.g. Hanna & Barnes, 1991; Smith *et al.*, 2006a), whereas during the actual rotating platform experiments the frogs tend to change the number and size of pad contacts. Therefore, the maximum tenacity is presumably underestimated, and accordingly the goodness of fit of the interspecific tenacity scaling by Smith *et al.* (2006b) with body size ($r = 0.78$, $p = 0.04$) and epidermal cell size is low ($r = 0.81 - 0.92$, $p = 0.003 - 0.02$, min. 1 animal for A_p , min. 10 animals for F_{\perp}). Furthermore, a significant intraspecific correlation of σ_{\perp} with ℓ_{SV} is not found in all tree frog species (Smith *et al.*, 2006a).

Single limbs/pads Tenacities measured in single pads agree with whole animal tenacities (Table 2.2, bottom). Endlein *et al.* (2017) reported an effect of the detachment kinematics on tenacity: proximal pulling on the pads before detachment led to higher

Table 2.2 Measured adhesion performance of whole tree frogs (top) and of single limbs/toe pads (bottom; SP unless stated otherwise) on smooth dry substrates.

Reference	Species	Adhesion F_{\perp} [mN]	Tenacity σ_{\perp} [mN mm ⁻²]	Remarks
Emerson & Diehl (1980)	<i>H. cinerea</i>	39.24	1.4	Teflon
Hanna & Barnes (1991)	<i>O. septentrionalis</i>	75.5	1.2	PMMA
Barnes <i>et al.</i> (2006)	various hylids	2.0–372.0	0.4–1.3	PMMA
Smith <i>et al.</i> (2006a)	various hylids	4.3–180.2	0.4–0.7	PMMA
Smith <i>et al.</i> (2006b)	various hylids	0.5–200.0	0.30–1.08	PMMA
Crawford <i>et al.</i> (2012)	<i>L. caerulea</i>	255.3±73.7	—	Glass
v. Wittich (1854)	<i>H. arborea</i>	127.53	—	SL, Frontlimb, Metal SL
Hanna & Barnes (1991)	<i>O. septentrionalis</i>	5.9±2.1– 14.9±3.6	—	SL
Barnes <i>et al.</i> (2008)	<i>L. caerulea</i>	—	0.04–1.12	Varying load angle
Crawford <i>et al.</i> (2012)	<i>L. caerulea</i>	—	1.08±0.24	Glass
Endlein <i>et al.</i> (2012)	<i>L. caerulea</i>	13.9–34.0	—	SL
Endlein <i>et al.</i> (2013)	<i>R. pardalis</i>	—	1.5	PE
Crawford <i>et al.</i> (2016)	<i>L. caerulea</i>	—	1.74±1.90	Resin
		—	1.43±0.60	PDMS
Endlein <i>et al.</i> (2017)	<i>R. dennysi</i>	1.7–11.3	1.1–2.3	Varying detachment kinematics

PE polyethylene, PMMA polymethyl-methacrylate (acrylic glass), SL single limb measurement, SP single pad measurement.

tenacities compared to detachment in a dabbling movement. Similarly, Barnes *et al.* (2008) measured in *L. caerulea* a negative scaling of the tenacity with the pull off angle θ_L between substrate and pulling force from 1.12 mN mm⁻² at 53° to 0.04 mN mm⁻² at 170°, pointing towards peeling of the toe pads.

Local indentations In adult *L. caerulea*, Barnes *et al.* (2011) measured normal pull-off forces (i.e. adhesion) of 585–609 μ N using a spherical indenter with radius $r_i = 1.5$ mm at indentation depths $d_i \approx 50$ –350 μ m. Assuming a surface area $A = 2\pi d_i r_i$ for the spherical cap of the indenter in contact with the pad, we computed tenacities of 0.17–1.29 mN mm⁻², which overlaps with the values reported above. Similarly, Kappl *et al.* (2016) measured adhesion of 5 nN in dead *L. caerulea* using a spherical AFM-indenter ($r_i = 13.3$ μ m) at $d_i \approx 250$ –300 nm for submerged pads (i.e. no capillary force generation), from which we calculated tenacities of 0.12–0.24 mN mm⁻².

2.5.1.2 Adhesion mechanisms

Capillary adhesion Tree frog adhesion has been attributed primarily to wet adhesion considering that: (i) Mucus fills the pad-substrate gap and forms a capillary meniscus (Emerson & Diehl, 1980). (ii) Nachtigall (1974) measured for two glass



plates separated by distilled water a capillary tenacity of 7 mN mm^{-2} , which is in the same order of magnitude as tenacities measured for tree frogs. (iii) Tree frog adhesion scales linearly with A , as predicted by capillary adhesion based on Laplace pressure (Equation 2.1; Emerson & Diehl, 1980), assuming a size-invariant meridional meniscus curvature. (iv) On rough substrates, adding liquid improves the adhesive performance, proposedly by sustaining the meniscus.

To theoretically investigate the role of capillary adhesion, we calculated the capillary tenacity for various combinations of meniscus curvatures (i.e. meniscus height and pad diameter). Since the adhesion between a sphere and a plate (Equation 2.3) does not show the area-scaling measured in tree frogs (Barnes, 1999; Barnes *et al.*, 2006; Emerson & Diehl, 1980), we modelled the pad-substrate interaction as plate-plate contact (Equation 2.1). As shown in Fig. 2.9, a meridional radius of meniscus curvature R_{mer} similar in size to the micro- to nanoscopic height d_g of the mucus film (e.g. $5 \mu\text{m}$ estimated by Barnes *et al.*, 2006) would lead to capillary adhesion that is several orders of magnitude higher than the tenacities measured in tree frogs. In reality, the meniscus covers also the side of the pad (Barnes *et al.*, 2013) and therefore $R_{\text{mer}} \gg d_g/2$ (compare Fig. 2.3A, left inset). Thus, Equation 2.1 might well describe tree frog adhesion under the assumption of a realistic radius of meniscus curvature that is much larger than the narrow pad-substrate gap width. Based on Fig. 2.9, we predict $R_{\text{mer}} \approx 150 \mu\text{m}$. As discussed by Drechsler & Federle (2006), we would expect a minimisation of the radii of meniscus curvature (i.e. just enough mucus to fill the pad-substrate gap as found in artificial structured adhesives; Drotlef *et al.*, 2013) in pads adapted towards capillary adhesion.

Figure 2.9 Tenacity contours [mN mm^{-2}] computed for capillary adhesion at varying gap widths (i.e. twice the meridional radius of meniscus curvature) and azimuthal radii of meniscus curvature ($\approx 0.5d_p$), respectively, according to Equation 2.1. We assumed $\phi = 0^\circ$ and $\gamma = 71.97 \text{ mN m}^{-1}$. The green patch shows the combinations of R_{azi} and R_{mer} that lead to tenacities in the range of measured values (Barnes *et al.*, 2011).

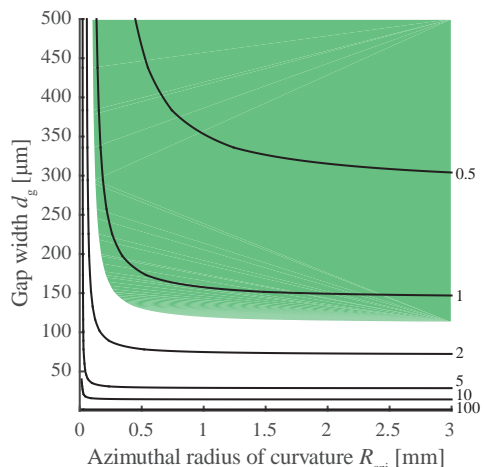


Fig. 2.9 further shows that, depending on pad size, both meniscus curvatures have to be considered in computing the capillary adhesion of tree frogs' toe pads. To our knowledge, models of the capillary adhesion of tree frogs, such as the ones discussed above or in previous works (e.g. Barnes, 2012; Emerson & Diehl, 1980; Endlein & Barnes, 2015; Hanna & Barnes, 1991), do not take into account variations in the

contact angle (and hence of meniscus curvature) related to wetting phenomena such as contact-line pinning or substrate roughness (de Gennes *et al.*, 2004).

The linear scaling of adhesion with contact area (Smith *et al.*, 2006a) is not only explained by capillary adhesion. For example, such scaling might also originate from suction, mechanical interlocking, or vdW forces, assuming a uniform load-distribution over the contact area. In contrast to capillary effects, the latter two mechanisms might directly explain the friction of tree frogs' toe pads.

With respect to morphology, the micro- to nanoscopic channel system has been suggested to support capillary adhesion by quickly spreading the mucus over the pad surface for a rapid formation of the liquid bridge (Barnes *et al.*, 2002; Persson, 2007). In addition, the channels may facilitate the capillary condensation of water vapour into the pad-substrate gap, reducing the need to actively secrete mucus. However, the distance at which a capillary bridge forms between substrate and an artificial adhesive covered with a channel network is reduced, presumably because liquid is redistributed from the liquid bridge into the channels (Drotlef *et al.*, 2013). Accordingly, channels could also counteract quick generation of capillary adhesion, particularly if there is only little liquid present in the pad-substrate gap.

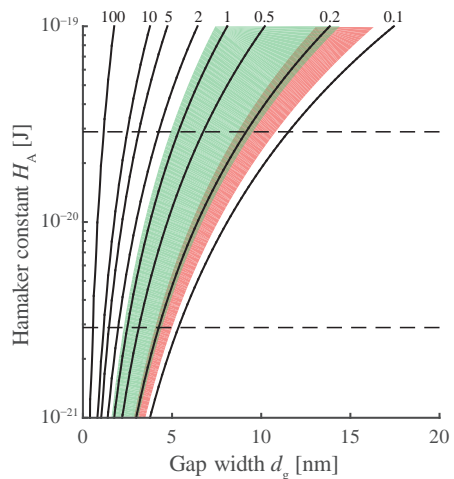
Hydrodynamic adhesion Hydrodynamic models predict an above-area scaling of adhesion with ℓ_{SV} , which disagrees with the area-scaling measured in tree frogs. Therefore, viscosity-based forces are not believed to play an important role in tree frog adhesion (Emerson & Diehl, 1980; Hanna & Barnes, 1991). Due to its inherent rate-dependency, hydrodynamic adhesion might prevent rapid detachment (Smith *et al.*, 2006a), which would inhibit, for example, jumping. Other adhesive mechanisms such as capillary adhesion or vdW forces do not show such an inherent rate-dependency (Parsegian, 2006). Furthermore, hydrodynamic adhesion requires continuous pad movements, rendering this mechanism ineffective against continuous forces such as gravity. For a deformable pad, gap closure (and hence the formation of potential dry contacts or of low gap widths for strong hydrodynamic adhesion) presumably is even slower compared to a rigid one (Kaveh *et al.*, 2014). In other words, hydrodynamic adhesion seems more of a hindrance for the animal (i.e. attachment and detachment are retarded and adaptations towards control of hydrodynamic forces may be needed), rather than a primary mechanism of adhesion.

The empirical and modelling evidence of hydrodynamic adhesion in the soft and patterned toe pads of tree frogs is limited. Current analytical models assume the contact of rigid objects. With decreasing stiffness, fluid-structure interactions increasingly affect hydrodynamic adhesion (Kaveh *et al.*, 2014), and contact forces resulting from viscoelastic substrate deformations can even exceed the hydrodynamic forces (Leroy & Charlaix, 2011). Moreover, current models assume smooth surfaces. Modified hydrodynamic boundary conditions are needed to model flow over structured surfaces (Pilkington *et al.*, 2016). Further work is required to examine if current analytical models of hydrodynamic adhesion can represent tree frog attachment accurately.



Van der Waals forces Previously, large gap widths and a decrease of A_H as a result of the liquid present in the pad-substrate gap were stated to prevent any significant contribution of vdW forces in tree frog attachment (Emerson & Diehl, 1980). To examine the possibility of vdW forces in tree frogs, we calculated the vdW-tenacity using Equation 2.7 for various combinations of pad-substrate gap width d_g and Hamaker constant A_H for a range of values expected for tree frogs' toe pads (Fig. 2.10; max. $A_H \approx 10^{-19}$ J in dry conditions (Israelachvili, 2011); min. $A_H \geq 0.7k_bT = 2.9 \cdot 10^{-21}$ J for water between two similar materials at temperature $T = 26^\circ$ and Boltzmann constant $k_b = 1.4 \cdot 10^{-23}$ J K $^{-1}$). Even in a conservative prediction using $A_H = 2.9 \cdot 10^{-21}$ J and an effective contact area of 10% of A , this model yields vdW tenacities equal to or higher than 1 mN mm $^{-2}$ at $d_g \leq 2.5$ nm on a smooth substrate. For a 10-fold higher Hamaker constant, which is in the range of values reported for two dissimilar organic objects interacting across water (Israelachvili, 2011; Parsegian, 2006), vdW forces are equal to or higher than the adhesion measured in tree frogs at $d_g \leq 6.7$ nm. Using interference reflection microscopy, Federle *et al.* (2006) measured $d_g \leq 5$ nm for more than 40% (and $d_g \leq 10$ nm for more than 55%) of the analysed epidermal cells. This sensitivity analysis suggests that tree frogs are potentially able to conform close enough to the substrate to generate significant vdW forces despite liquid in the pad-substrate gap and a reduced Hamaker constant.

Figure 2.10 Tenacity contours [mN mm $^{-2}$] computed for van der Waals (vdW) interactions at various Hamaker constants and gap widths according to Equation 2.7. We assumed that 10% of the contact area contributes to vdW force generation. Dashed lines: Theoretical minimum Hamaker constant for water separating two similar materials at 26 °C (bottom) and a 10-fold higher Hamaker constant (top). Coloured patches show the combinations of A_H and d_g leading to tenacities in the range of measured values (Barnes *et al.*, 2011, green; Kappl *et al.*, 2016, red).



Morphological observations also support the action of vdW forces in toe pads. The accumulation of electron dense material in the outermost layer of the nanopillars (Fig. 2.1D $_2$) could increase vdW interactions (Parsegian, 2006), analogously to the effects of varying thicknesses of the substrate backing material on the vdW forces reported for geckos (Loskill *et al.*, 2013).

Summarizing, the contribution of vdW forces to adhesion cannot be excluded in tree frogs (although more experimental evaluation is needed). Quantifications of the Hamaker constant, the pad-substrate gap width, and the attachment performance on substrates with different surface energies or with chemically different backing layers

(as performed for geckos by Loskill *et al.*, 2013) are required for a detailed assessment of the contribution of vdW forces to tree frog attachment.

Drainage Most mechanisms described in this review predict an increase in adhesion (and friction) with decreasing pad-substrate gap width. Liquid in the pad-substrate gap impedes a close conformation of the pad, and adaptations towards liquid drainage might be at play. The different drainage regimes could help explain the function of the micro- to nanoscopic channel network in between the ventral epidermal cells and nanopillars. These channels might effectively enlarge the gap width (Persson, 2007), and reduce hydrodynamic repulsion (Equations 2.4 and 2.5). Thus, drainage would alleviate a reduction of the gap width and reduce the duration of contact formation (and separation). The grip to the substrate would be closer and faster, as demonstrated for artificial surface structures (Chen *et al.*, 2015; Dhong & Fréchet, 2015; Drotlef *et al.*, 2013; Gupta & Fréchet, 2012). As described above, the flow through the channel network is dominated by viscous effects (Dhong & Fréchet, 2015; Gupta & Fréchet, 2012).

2.5.2 Friction

2.5.2.1 Measured friction performance

Table 2.3 summarizes the friction F_{\parallel} and shear stress σ_{\parallel} measured for whole tree frogs and single limbs/toe pads. Static friction exceeds adhesion in terms of force (Barnes *et al.*, 2002) and stress (Crawford *et al.*, 2016; Endlein *et al.*, 2017). The static friction coefficient μ_{\parallel} of a pad ranges between 0.77 and 1.98 in various species tested on PMMA (Barnes *et al.*, 2006, 2002). For single toe pads, Chen *et al.* (2015) measured that friction during sliding along the longitudinal pad axis exceeds the friction of lateral sliding by ca. 20%. Kappl *et al.* (2016) reported a contradictory trend of 29–71% higher friction coefficients for lateral sliding of single epidermal cells. Friction scales with ℓ_{SV} just below cubed ($F_{\parallel} \propto \ell_{SV}^{2.76-2.78}$; Barnes *et al.*, 2006, 2002), indicating an approximately linear scaling with body mass. Federle *et al.* (2006) measured a static shear stress of 1.12 mN mm^{-2} two minutes after the end of sliding, which was explained by boundary lubrication (i.e. dry friction).

Friction dynamics are hardly studied in tree frogs. Single pad friction scales positively with sliding velocity in *Osteopilus septentrionalis* (Hanna & Barnes, 1991). In *L. caerulea*, a (median) dynamic shear stress of 2.1 mN mm^{-2} was reported (Federle *et al.*, 2006). Dynamic peak friction values of up to 1270 mN , equivalent to 14.4 times the body weight, were reported for single pads of *Trachycephalus resinifictrix* (Bijma *et al.*, 2016). We expect that the high frictional performance reported in recent studies (Bijma *et al.*, 2016; Chen *et al.*, 2015; Crawford *et al.*, 2016; Endlein *et al.*, 2017) can be explained by a scaling of friction with normal load and shear velocity.



Table 2.3 Measured friction performance of whole tree frogs (top) and of single limbs/toe pads (bottom); SP unless stated otherwise). For explanation of abbreviations see Table 2.2.

Reference	Species	Friction F_{\parallel} [mN]	Shear stress σ_{\parallel} [mN mm ⁻²]	$F_{\perp,L}$ [mN]	v_{\parallel} [µm s ⁻¹]	Remarks
Barnes <i>et al.</i> (2006)	various hylds	5.5–585.7	—	—	—	PMMA
Crawford <i>et al.</i> (2012)	<i>L. caerulea</i>	285.4±94.5	—	—	—	Glass
Green (1981)	<i>H. versicolor</i>	357.1	—	—	—	Pulling experiment, Frontlimbs
Hanna & Barnes (1991)	<i>O. septentrionalis</i>	24.9±6.6–55.4±6.3	—	—	—	SL
Federle <i>et al.</i> (2006)	<i>L. caerulea</i>	3.0–130.3	—	2.5	10–2500	Glass
Endlein <i>et al.</i> (2012)	<i>L. caerulea</i>	1.6–10.4	1.08–2.01	0.1	500	SL
Endlein <i>et al.</i> (2013)	<i>R. pardalis</i>	—	—	—	—	Glass
Chen <i>et al.</i> (2015)	<i>P. megacephalus</i>	17.52	—	1.5	300	Glass
Bijina <i>et al.</i> (2016)	<i>T. resinifictrix</i>	110–1270	—	—	—	Jumping kinematics, Wood; SL
Crawford <i>et al.</i> (2016)	<i>L. caerulea</i>	—	7.8±12.9	2	1000	Resin
Zhang <i>et al.</i> (2016)	<i>P. megacephalus</i>	14.5–122.7	5.9±2.6	—	—	PDMS
Endlein <i>et al.</i> (2017)	<i>R. demysti</i>	25.1–51.2	9.6	2	600	Repeated sliding Varying detachment kinematics

$F_{\perp,L}$ normal load, v_{\parallel} sliding speed.



2.5.2.2 Friction mechanisms

Mechanical interlocking Interlocking of epidermal cells or nanopillars with substrate asperities might contribute to friction (and adhesion) of tree frogs (Green, 1981). Interlocking might explain the enhanced attachment forces measured on substrates covered with artificial pillars similar in size to the epidermal cells (and channels; Crawford *et al.*, 2016). An enhanced contact area for dry or hydrodynamic friction might be an alternative explanation of this observation.

Overall, interlocking, as described for stiffer attachment organs such as claws (Bullock & Federle, 2011; Dai *et al.*, 2002), is debatable for the delicate epidermal cells of tree frogs. The use of substrates with a well-defined topography (e.g. structured or random roughness as in Crawford *et al.*, 2016) is crucial in future investigations.

Lubrication: from dry to hydrodynamic friction The measured mass- (and therefore load-) scaling of friction (Barnes *et al.*, 2006), the observation of static friction, and nanoscopic pad-substrate gap widths (Federle *et al.*, 2006) indicate the presence of dry friction. However, the measurement of a lower static than dynamic friction (Federle *et al.*, 2006) conflicts with dry friction and suggests the action of additional friction mechanisms.

For example, the presence of mucus and the positive scaling of friction with sliding velocity point towards hydrodynamic friction (or possibly rubber friction; Barnes *et al.*, 2002; Popov, 2010). Physiological adaptations towards enhanced hydrodynamic friction could target the mucus viscosity, velocity gradients, and contact area: the wetted contact area, which is considerably larger than the projected area, and high velocity gradients because of the nanoscopic pad-substrate distances may enhance hydrodynamic friction, despite a low mucus viscosity.

Overall, we expect that tree frogs experience the whole lubrication spectrum from dry to hydrodynamic friction, with boundary lubrication as preferred regime of lubrication, because it provides static friction, which is load-dependent and hence controllable.

Lubrication might also explain the large amount of glands secreting mucus into the pad-substrate gap. Compared to geckos (Autumn & Peattie, 2002), the surface of tree frogs' toe pads is keratinised only little and is accordingly very soft. While this facilitates the uptake of water and oxygen through the skin (Wu *et al.*, 2017) and enhances the substrate conformability, we also expect the soft pads to be more susceptible to abrasive wear (Popov, 2010). A thin layer of mucus (i.e. a few layers of mucus molecules) might act as lubricant to avoid excessive damage of the pad epidermis while maintaining a sufficiently high pad friction.

Friction anisotropy Lubrication could also cause the anisotropic friction of polygonal surface structures observed in toe pads (Chen *et al.*, 2015), with a higher friction in the longitudinal direction than in the lateral direction, and in artificial surfaces (Iturri



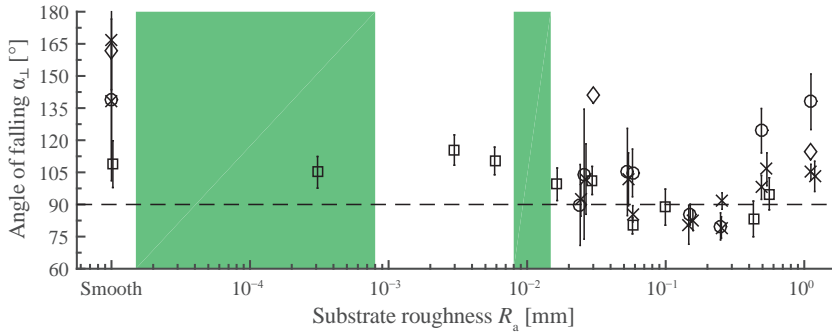


Figure 2.11 Variation of the falling angle α_{\perp} with substrate roughness R_a on an inclined, dry substrate (circles from Fig. 5 by Barnes, 1999, *Hyla microcephala*; crosses from Fig. 8A by Barnes *et al.*, 2002, *Colostethus trinitatis*; diamonds from Fig. 3B by Endlein *et al.*, 2013, *Rhacophorus pardalis*; squares from Fig. 1B by Crawford *et al.*, 2016, *Litoria caerulea*). Green areas denote the diameter range of nanopillars (left) and epidermal cells (right) reported in the main text. Dashed line: Falling angles below 90° show the lack of adhesive abilities. Most roughness values mentioned in the references are approximations and do not originate from measurements.

et al., 2015), where the friction of a regular pattern of regular hexagonal pillars is 60° -symmetric: friction anisotropy might arise from direction-dependent liquid flow in the channel network because of anisotropic channel alignment (Chen *et al.*, 2015), or from the anisotropic geometry and bending stiffness of the surface structures (Iturri *et al.*, 2015). Furthermore, we propose that the anisotropic channel alignment could lead to anisotropic sliding velocities and a direction-dependent transition to another lubrication regime (and friction coefficient). In tree frogs, high friction along the proximal-distal pad axis seems most important, as suggested by yawing motions of the toe pads in jumping frogs before landing (Bijma *et al.*, 2016), which agrees with anisotropic friction predicted by the theories of anisotropic flow.

2.5.3 Effects of variations in substrate properties on attachment

2.5.3.1 Measured effects

Roughness In Fig. 2.11, we provide an overview of tree frog adhesion as a function of the (arithmetic) average roughness R_a of the substrate. For $R_a < 6 \mu\text{m}$, the tenacity was reported to increase compared to a smooth surface (Crawford *et al.*, 2016). Crawford *et al.* (2016) also measured a higher tenacity on a substrate with structured roughness (i.e. $3 \mu\text{m}$ high and $2 \mu\text{m}$ wide pillars with variable spacing) than on a smooth substrate. With increasing pillar spacing, the tenacity returns to the values measured for smooth substrates at a spacing $\geq 10 \mu\text{m}$. Tree frogs tend to adhere worse to rough substrates (Barnes, 1999), for example wood or coarse sandpaper, which was also observed for smooth substrates contaminated with glass beads with a diameter of $50 \mu\text{m}$ (Crawford *et al.*, 2012). At $R_a \geq 0.5 \text{ mm}$, adhesion increases again.

Effects of R_a on friction have been hardly studied. Compared to various other sub-

strates, in ten species the highest friction coefficients were found on wood (Barnes *et al.*, 2002). Similar to adhesion, higher shear stresses were measured on substrates with $R_a = 3\text{--}6\ \mu\text{m}$ than on smoother substrates (Crawford *et al.*, 2016). For microscopic glass beads (diameter $< 3\ \mu\text{m}$), Crawford *et al.* (2016) observed interlocking of the beads in the intercellular epidermal channels.

Wetting Tree frogs cannot attach to a fully wetted, smooth substrate (Brehm, 1892; Emerson & Diehl, 1980; Siedlecki, 1909; v. Wittich, 1854). Endlein *et al.* (2013) described a reduction of σ_{\perp} from ca. $1.5\ \text{mN mm}^{-2}$ to ca. $0.1\ \text{mN mm}^{-2}$ when wetting the pad with $10\ \mu\text{L}$ of water, which is equivalent to a $2.3\ \text{mm}$ thick liquid film assuming an average pad surface of $4.3\ \text{mm}^2$. On rough substrates, on the other hand, light wetting (i.e. rates of $0.8\text{--}1.9\ \text{mL s}^{-1}$ of water flowing over the test substrate or spraying water on the substrate) increases adhesion compared to dry conditions (Barnes, 1999; Barnes *et al.*, 2002; Crawford *et al.*, 2016; Endlein *et al.*, 2013). Crawford *et al.* (2016) reported the ability of *L. caerulea* to fill gaps—created by $50\text{--}75\ \mu\text{m}$ large glass beads contaminating the substrate—with mucus. For even larger beads, air bubbles formed in the pad-substrate gap.

‘Full’ wetting weakens friction on smooth and rough substrates (Endlein *et al.*, 2013). In repeated friction measurements on individual toe pads (10 consecutive steps), Zhang *et al.* (2016) measured an increase of friction with step number (from $14.5\ \text{mN}$ to $122.7\ \text{mN}$), presumably because of a reduction of the liquid volume between pad and substrate. Similar to adhesion, friction on a rough substrate ($58.5\ \mu\text{m}$) increases by light wetting (Crawford *et al.*, 2016).

Surface energy/tension The only study investigating the influence of substrate surface energy on adhesion reported a difference of the mean falling angle by 9° in frogs sitting on glass versus teflon (Emerson & Diehl, 1980). A reduction in surface tension of the intervening liquid by wetting a substrate with water mixed with a detergent led to a complete loss of friction (Green, 1981).

2.5.3.2 Functional interpretation of measured effects

Capillary adhesion The reduced adhesion of tree frogs on dry, rough substrates has been attributed to the formation of bubbles within substrate cavities (Fig. 2.3B₃), reducing the contact area available for capillary adhesion (Barnes, 1999). However, meniscus cavitation around glass beads in the pad-substrate gap occurs only for bead diameters $> 50\ \mu\text{m}$ (Crawford *et al.*, 2016), leaving the reduced adhesion at lower roughnesses unexplained by reduced capillary forces. In addition, capillary adhesion is unlikely to explain the increased adhesion on rough substrates for $R_a \leq 6\ \mu\text{m}$ (Crawford *et al.*, 2016), unless the low contact angle is further reduced because of roughness. These observations point towards the action of other adhesion mechanisms that are affected by microscopic roughness levels.



The loss of adhesion on a fully wetted substrate may result from a complete destruction of the meniscus and of capillary force generation (Emerson & Diehl, 1980). Alternatively, strong wetting could widen the pad-substrate gap, weakening all potentially involved mechanisms.

The enhanced adhesion on rough substrates by light wetting has been explained by ‘filling’ of substrate cavities and by the preservation of the liquid bridge (i.e. capillary adhesion; Barnes, 1999). However, stronger capillary adhesion may also lead to a reduction of the pad-substrate gap width or an enlargement of the area of dry contact, hence indirectly enhancing other mechanisms of force generation, which are likely to be weakened at the tested roughness levels of ca. 30–60 μm (Crawford *et al.*, 2016; Endlein *et al.*, 2013).

‘Dry’ adhesion mechanisms The enhanced adhesion on substrates with asperities $\lesssim 6 \mu\text{m}$ may be explained by mechanical interlocking (Crawford *et al.*, 2016). One could also attribute this finding to an enhanced contact area and vdW forces. The seemingly continuous decrease of α_{\perp} shown in Fig. 2.11 for $R_a = 2\text{--}60 \mu\text{m}$ suggests a continuous reduction of the effective ‘dry’ contact area and vdW forces with increasing roughness (in contrast to an expected drop of capillary adhesion because of meniscus cavitation at a critical roughness). Also, the weakened adhesion on rough (i.e. a reduced effective contact area) as well as wetted smooth substrates (i.e. a wider pad-substrate gap and a reduced Hamaker constant) and the scaling of tenacity with the number of beads contaminating the pad-substrate gap (i.e. a reduced effective contact area) reported by Crawford *et al.* (2012) are consistent with vdW forces. The enhanced adhesion on very rough substrates ($R_a \geq 0.2 \text{ mm}$) might be created by the whole toe pad interlocking with macroscopic substrate projections.

Friction mechanisms Similar to adhesion, the increase of friction on microrough compared to smooth substrates may originate from mechanical interlocking (Crawford *et al.*, 2016). Alternatively, an increase in effective contact area and vdW forces could explain this finding. The negative correlation between friction and the mucus volume present in the pad-substrate gap suggested by the findings of Endlein *et al.* (2013) and Zhang *et al.* (2016) may originate from the inverse scaling of hydrodynamic friction with mucus film thickness. Alternatively, more (and stronger) dry contacts could explain this observation.

2.5.4 Behavioural adaptations and attachment control

Studying the use of a pad (and of other body parts) during locomotion provides insight into the dynamic mechanisms of force generation and attachment control in tree frogs. For example, the digits in the forelimbs perform a proximal pulling movement during attachment in normal walking (Hanna & Barnes, 1991; Schuberg, 1891). Such movements increase the attachment force (Endlein *et al.*, 2017), possibly because of

an increased contact area, enhanced mucus spread, a more uniform load distribution, or pad cleaning (Crawford *et al.*, 2012).

On an increasingly tilted substrate, *L. caerulea* begins to splay the initially adducted limbs until all appendages are maximally extended (Endlein *et al.*, 2013, 2012). Limb splaying reduces the angle θ_L between substrate and pulling force, which is aligned approximately with the limb, and thus increases the force at which the pad peels off (see Section 2.SI.3.5); sliding of the limbs and an increase of θ_L because of gravity result in the need to continuously reposition the fore- and hindlimbs, which explains the ‘dance-like’ movements of tree frogs on overhanging substrates (Endlein *et al.*, 2013).

During attachment, tree frogs rely not only on their pads but also on portions of belly and thighs to create contact forces (Hanna & Barnes, 1991). At a slope of 90° , belly and thigh form 73% of the total contact area (Endlein *et al.*, 2013). However, on an overhanging substrate the contact area is largely formed by the toe pads (Endlein *et al.*, 2013). Torrent frogs show a different behaviour, with an increasing contribution of belly and thighs to the contact area with an increase of the substrate inclination from 90° to 180° (Endlein *et al.*, 2013), highlighting the importance of considering animal behaviour while studying the attachment performance of whole animals.

The toe pads detach from the substrate during normal walking in a peeling motion from posterior to anterior (Hanna & Barnes, 1991). Detachment is probably controlled by the tendons and muscles (Hanna & Barnes, 1991), and peeling occurs passively when the pad is pulled from the substrate. On a vertical substrate, tree frogs that are rotated around the sagittal body axis realign their bodies towards the vertical axis, presumably to avoid passive peeling (Barnes *et al.*, 2006; Hanna & Barnes, 1991).

2.6 Conclusions and perspectives

Studies on morphology, material, and attachment forces of the toe pads of tree frogs have contributed considerably to the understanding of the attachment of these animals. We offer a systematic review of these studies, facilitating an in-depth discussion of the mechanisms involved in the generation, transmission, and control of attachment forces in the toe pads. Research which integrates contributions from experimental and computational biomechanics, physics, biochemistry, morphology, ecology, phylogenetics, and biomimetics is required to further deepen our understanding of tree frog attachment. Simultaneously, the discussion on tree frog attachment should be extended beyond isolated theories and pad features. An overarching model is needed, which integrates the functional demands on the toe pads, the pad morphology, and the various mechanisms contributing to time-dependent adhesion and friction. Here, the formulation and testing of a systematic series of hypotheses may help to identify the mechanisms to be considered. Moreover, we emphasise the role of friction in tree frog attachment. Recent works (e.g. Endlein *et al.*, 2012, 2017; Federle *et al.*, 2006;



Kappl *et al.*, 2016) have highlighted the importance of friction in tree frog attachment and future studies on toe pad friction may advance the understanding of the functioning of tree frog toe pads. Due to the diversity of the involved phenomena, achieving an understanding of tree frog attachment arguably is even more complicated than for the attachment in geckos. Below, we outline possible contributions from various disciplines which may improve our understanding of tree frog attachment.

We argue that the pad-substrate contact area has been overestimated in previous research (Bijma *et al.*, 2016; Crawford *et al.*, 2016), pointing towards an underestimation of the adhesive and frictional performance of tree frogs. In addition, tenacity and shear stress of so-called subarticular/digital tubercles—more proximal regions of digital epidermis covered with surface structures similar to those on the pads—were measured to be on average 3.2–8.8 times higher compared to the pads (Endlein *et al.*, 2017). The difference in attachment performance between the toe pads and tubercles is not yet explained.

It is likely that tree frogs rely on several attachment mechanisms, and that the relative importance of these mechanisms varies with the circumstances (Emerson & Diehl, 1980), because tree frogs have to interact with a wide diversity of natural surfaces, requiring static and dynamic, adhesive and frictional, reversible, and repeatable force generation. In addition, tree frog species vary greatly in size (with ranges of snout-vent-length and body mass covering up to two orders of magnitude; Smith *et al.*, 2006b). Next to variations of substrate properties, the attachment apparatus of tree frogs has to deal with this scaling.

A liquid bridge in the pad-substrate gap most likely enables capillary adhesion. Current analytical plate-plate models overpredict the generated capillary adhesion by several orders of magnitude, sphere-plate models do not predict an area-scaling of adhesion, and experimental findings (e.g. pad-substrate gap widths ≤ 5 nm and increased adhesion on microrough compared to smooth substrates) indicate the involvement of other adhesion mechanisms. To directly evaluate the applicability of current models of capillary forces in tree frog attachment, we propose the simultaneous measurement of the capillary pressure within the meniscus and of meniscus parameters such as height (i.e. curvature), diameter, and contact angle.

Hydrodynamic adhesion is hard to predict by analytical models. This mechanism seems more of a hindrance for the animal (e.g. slower attachment and detachment), rather than a primary mechanism of adhesion. We suggest a combination of the visualisation of the mucus flow under a real pad (e.g. via micro-particle-image-velocimetry), the development of a computational fluid dynamics model including fluid-solid interactions, and measurements on artificial hierarchically structured surfaces to further investigate the mucus flow dynamics and the resulting hydrodynamic forces in tree frogs.

A sensitivity analysis shows that even in a conservative computation van der Waals (vdW) forces could contribute to tree frog adhesion. Measurement of the attachment performance on substrates with similar surface energies but different subsurface ener-

gies, as done for geckos (Loskill *et al.*, 2013), may help to conclude on the possibility of vdW forces contributing to tree frog attachment.

Mechanical interlocking and suction cannot be ruled out as additional adhesion mechanisms. Variation of the environmental pressure should directly affect the hypothetical suction of tree frog toe pads. In line with previous experiments (Emerson & Diehl, 1980; Schuberg, 1891), we suggest single pad force measurements in a pressure chamber to test whether suction is present.

A simultaneous measurement of the three-dimensional contact force exerted by a single pad over a whole step cycle, contact area, and pad deformation is still missing. Such an observation is crucial for enhancing the understanding of the fundamentals of tree frog attachment. In such an experiment, control—or at least reporting—of experimental parameters such as normal load, sliding speed, contact area, or gap width is crucial, as presented in recent studies (e.g. Crawford, 2016; Endlein *et al.*, 2017). This also includes a characterisation of the used test substrates and of environmental conditions (e.g. temperature and air humidity). Also, the amount of mucus in the pad-substrate gap should get controlled, for example by bringing the pad in contact with a glass slide under defined conditions (as shown for insects; Bullock *et al.*, 2008; Dirks & Federle, 2011). Comprehensive control and reporting of the experimental conditions may facilitate future meta-analyses on the attachment performance of tree frogs.

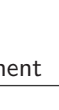
With respect to the effects of the variation of substrate properties on tree frog attachment, only roughness has been tested extensively. In geckos, the effects of variations in surface and subsurface energy as well as stiffness of the substrate have been analysed experimentally (Klittich *et al.*, 2017; Loskill *et al.*, 2013). Analogously, we suggest systematic variations of substrate properties (e.g. roughness and surface energy), properties of the wetting liquid (e.g. surface tension and viscosity), and simultaneous measurements of adhesion, friction, and contact area of single pads in combination with variations of preload, sliding speed, and detachment speed, to determine the full range of the attachment performance of tree frogs. In particular, a parametric friction study with control of normal load, sliding speed, and gap width would help to establish the dependence of friction on the Stribeck number (i.e. the Stribeck curve). Such a study could give a better understanding of the involved tribological mechanisms (e.g. the role of the mucus in friction) and might allow for conclusions on liquid and material properties (Pitenis *et al.*, 2014) of the pad by comparison to Stribeck curves of known systems.

In contrast to geckos, tree frogs secrete mucus, which presumably fulfils various functions: (i) epidermal water and oxygen uptake, (ii) capillary and hydrodynamic force generation, (iii) avoidance of pad stiffening and a reduced conformability, and (iv) lubrication and hence reduction of abrasive wear. Studying the mucus properties is central to elucidating tree frog attachment.

Considering the effects of variations of roughness and wetting on tree frog attachment, we propose an interplay of vdW and capillary forces depending of substrate roughness:



On low-roughness substrates ($R_a \leq 10\text{--}20\ \mu\text{m}$), vdW forces could be dominant and any liquid between pad and substrate would weaken this adhesion component. On rougher substrates, a liquid filled pad-substrate gap may support capillary adhesion, which then could (partially) compensate for the expected reduction of vdW forces. Based on this hypothetical interplay, we predict a trade-off in force generation based on capillarity and vdW interactions: Liquid filling the pad-substrate gap enhances capillary forces, but too much liquid reduces the Hamaker constant and vdW interactions.

2  Morphology and material composition of the toe pad suggest a high conformability to the substrate (i.e. reduced pad-substrate gap width and enhanced effective contact area) and consequently the importance of dry contacts: The hierarchical surface pattern on the ventral pad surface presumably reduces the effective bending stiffness of the surface and increases the wetted area of the pad. The intercellular channel network, the convex pad curvature, and macroscopic grooves on the ventral epidermis may facilitate viscosity-dominated drainage of interstitial liquids and gap-closure in the central part of the pad, and inertia-dominated drainage in the grooves and in the peripheral contact region, unaffected by the presence of epidermal surface structures (similar to, for example, car tires; Persson, 2007). Furthermore, the pads are very soft, enabling the conformation to a rough substrate. Barnes *et al.* (2011) reported a negative spatial stiffness gradient from the pad surface towards deeper tissues. Analysing the shape of this gradient may help to understand the conformability and distribution of mechanical stresses within the pad epidermis. Considering the load transmitting elements such as tonofilaments, we expect a higher tensile stiffness than the compressive stiffnesses reported in Table 2.1. The effects of such a variable elastic modulus or of potential non-Hookean material properties (e.g. strain stiffening) on force generation are unknown.

The trajectories of the epidermal tonofilaments presumably facilitate force transmission through the epidermis, but how are forces transmitted from there to the phalanx and to other body parts? We suggest a detailed morphological analysis (employing histology, immunohistochemistry, and micro-computer-tomography) of tree frogs' toe pads, with focus on force-transmitting structures, such as cytoskeletal elements, connective tissue, and muscular tissue. Such an analysis may show (i) where exactly contact forces are generated, (ii) which types of loading are dominant in the pads, and (iii) whether shear stiffening, as observed in geckos (Bartlett *et al.*, 2012b; Gilman *et al.*, 2015), is common in both dry and wet adhesives. We expect that force transmission within the epidermis limits local stress concentrations, enhancing adhesion (Labonte & Federle, 2015b).

Little is known about active components and attachment control in the toe pads. Can tree frogs actively modify the geometry of the epidermal channels to control, for example, hydrodynamic force generation? Do the pads facilitate energy recovery during take offs from compliant substrates (Astley *et al.*, 2015)? The muscular complex in the limbs of tree frogs suggests that tree frogs can control alignment of the pads and parameters such as normal and shear loading forces and speeds, thus regulating

attachment force generation.

Next to capillary friction and suction (see Sections 2.SI.3.3 and 2.SI.3.4), there may be other attachment mechanisms that have not yet been identified or have been only hypothesised. For example, Bijma *et al.* (2016) explained the high friction of toe pads wrapped around curved substrates by capstan friction (i.e. the increased holding force of a rope wrapped around a winch). Friction of a soft pad could also partially arise from pad deformations due to surface tension at the three-phase contact line. During pad sliding, a movement of the contact line might induce dynamic pad deformations leading to energy dissipation in the potentially viscoelastic pad (Karpitschka *et al.*, 2015). Furthermore, viscoelasticity of the soft pads may affect friction independently of the presence of a meniscus (Labonte & Federle, 2015a): In so-called rubber friction, substrate roughness causes dynamic deformations of the toe pad. Thus, during sliding, energy is continuously dissipated in the material, which can be seen as friction resisting sliding (Barnes *et al.*, 2002; Popov, 2010).

The toe pads of tree frogs can serve as a model system for the design of biomimetic adhesives, inspiring novel versatile attachment solutions. A deeper understanding of the attachment mechanisms and functional advantages of the hierarchically structured ventral pad surface (i.e. epidermal cells and nanopillars) could further advance the design of biomimetic adhesives. In this light, we propose a comparative examination of intraspecific differences in habitat, attachment performance, and morphology of the whole pad as well as the epidermal surface structures, as done in geckos (Elstrott & Irschick, 2004; Irschick *et al.*, 1996). One could expect, for example, fore-hindlimb differences in morphology and attachment performance because of different functions (hindlimbs serve in jumping Emerson, 1978; forelimbs serve as shock absorbers Nauwelaerts & Aerts, 2006). Furthermore, adhesion was reported to correlate with cell size (Smith *et al.*, 2006b). Although not fully substantiated, the examination of such a correlation may lead to new insights in the role of the different attachment mechanisms in tree frogs. Are cell geometry, size of the intercellular channels, or the stiffness of a cell (or a combination of these features) causal factors affecting attachment? What is the optimal geometry of the polygonal surface structures? The hierarchical surface structures on the ventral toe pad epidermis, the scaling of attachment performance with cell size, and the potential presence of vdW forces in tree frog attachment may also hint towards the working of contact splitting (i.e. the increase of attachment force resulting from subdivision of the contact area), which has been discussed for various biological and technical attachment systems (Arzt *et al.*, 2003; Jagota & Hui, 2011; Kamperman *et al.*, 2010; Labonte *et al.*, 2015; Labonte & Federle, 2015b). Further work is required to elucidate the importance of contact splitting in tree frogs. We expect that the design of biomimetic adhesives will benefit significantly from addressing these issues.



2.SI Supporting information

2.SI.1 Symbols and abbreviations

2.SI.1.1 List of symbols

Table 2.SI.1 List of Roman (top) and Greek (bottom) symbols in alphabetical order.

Symbol	SI Unit	Description
A	m^2	Ventral surface area of all toe pads / Contact area
a_c	m	Edge length of the hexagonal, apical surface of epidermal cell
A_c	m^2	Apical surface area of an epidermal cell
$A_{c,c}$	m^2	Projected area of an epidermal cell and the surrounding channel
$A_{c,w}$	m^2	Wetted area of an epidermal cell and the surrounding channel
A_H	$\text{J} = \text{kg m}^2 \text{s}^{-2}$	Hamaker constant
$A_{n,\text{eff}}$	m^2	Apical surface area of a nanopillar uncovered by a dimple
A_{eff}	m^2	Apical surface area of all nanopillars uncovered by a dimple, i.e. potential contact area for vdW interactions
A_p	m^2	Ventral surface area of a single toe pad (i.e. apparent contact area)
b	m	Tape width
d_c	m	Approximate diameter of the hexagonal, apical surface an epidermal cell
d_g	m	Width of gap between substrate and an object (e.g. toe pad or synthetic adhesive)
d_i	m	Indentation depth
d_n	m	Approximate diameter of a nanopillar
d_p	m	Diameter of the contact area of a single toe pad
d_0, d_1	m	Critical gap widths in drainage flow
$E_{f,m,c}$	$\text{Pa} = \text{kg m}^{-1} \text{s}^{-2}$	Young's modulus [of the fibre (f) and matrix (m) fraction of a composite material (c)]
E_s	$\text{Pa} = \text{kg m}^{-1} \text{s}^{-2}$	Effective elastic modulus of a system of two contacting objects
E^*	$\text{Pa} = \text{kg m}^{-1} \text{s}^{-2}$	Effective elastic modulus
F_L	$\text{N} = \text{kg m s}^{-2}$	Load
F_m	$\text{N} = \text{kg m s}^{-2}$	Body weight
F_{\perp}	$\text{N} = \text{kg m s}^{-2}$	(Maximum) adhesion, generated by capillary effects ($_{\text{cap}}$), hydrodynamic effects ($_{\text{hyd}}$), vdW interactions ($_{\text{vdW}}$), mechanical interlocking ($_{\text{mec}}$), or suction ($_{\text{suc}}$)
$F_{\perp,g}$	$\text{N} = \text{kg m s}^{-2}$	Body weight component normal to surface
$F_{\perp,L}$	$\text{N} = \text{kg m s}^{-2}$	Normal load
F_{\parallel}	$\text{N} = \text{kg m s}^{-2}$	(Maximum) friction, generated by capillary effects ($_{\text{cap}}$), hydrodynamic effects ($_{\text{hyd}}$), vdW interactions ($_{\text{vdW}}$), mechanical interlocking ($_{\text{mec}}$), or suction ($_{\text{suc}}$)
$F_{\parallel,g}$	$\text{N} = \text{kg m s}^{-2}$	Body weight component parallel to surface
$F_{\parallel,L}$	$\text{N} = \text{kg m s}^{-2}$	Shear load
g	m s^{-2}	Gravitational acceleration
h	m	Film thickness
h_c	m	Height of a freestanding hexagonal cell
h_m	m	Height of artificial surface structure
h_n	m	Height of a nanopillar
k_b	$\text{JK}^{-1} = \text{kg m}^2 \text{s}^{-2}$	Boltzmann constant

— continues on the next page —

— continued from the previous page —

Symbol	SI Unit	Description
$k_1, k_2, k...$	var.	Constants used in curve fits
ℓ_{SV}	m	Snout-vent-length
m	kg	Body mass
n_c	-	Number of cells per toe pad
$n_{n,c}$	-	Number of nanopillars per cell
$n_{n,p}$	-	Number of nanopillars per toe pad
p	-	Probability value
P_{in}	Pa = $\text{kg m}^{-1} \text{s}^{-2}$	Suction pressure
P_{env}	Pa = $\text{kg m}^{-1} \text{s}^{-2}$	Environmental pressure
r	-	Coefficient of determination
r_i	m	Indenter tip radius
r_n	m	Dimple radius
R	m	Radius of curvature of a toe pad or sphere
R_a	m	Arithmetic average roughness
R_{azi}	m	Azimuthal radius of meniscus curvature
R_{mer}	m	Meridional radius of meniscus curvature
r_p	m	Radius of cylindrical plate
St	-	Stribeck number
\tilde{R}_s	m	Radius of curvature of a system of two contacting objects
St	-	Stribeck number
t	s	Time
T	K	Temperature
u	m s^{-1}	Flow speed
v_{\perp}	m s^{-1}	Normal detachment speed
v_{\parallel}	m s^{-1}	Sliding speed
V_f	-	Volume fraction of the fibres of a composite material
w_c	m	Width of a channel between two epidermal cells
w_n	m	Width of a channel between two nanopillars
W_{\perp}	$\text{J m}^{-2} = \text{kg s}^{-2}$	Work of adhesion
α_c	$^{\circ}$	Internal angle of a hexagonal epidermal cell
α_{\perp}	$^{\circ}$	Falling angle in rotation table experiments
α_{\parallel}	$^{\circ}$	Sliding angle in rotation table experiments
β	$^{\circ}$	Meniscus filling angle
Δc	m	Peeling distance
ΔP	Pa = $\text{kg m}^{-1} \text{s}^{-2}$	Suction pressure difference
Δr	m	Distance between dimple perimeter and midpoint of an edge of a nanopillar
$\Delta\gamma$	$\text{N m}^{-1} = \text{kg s}^{-2}$	Fracture energy
γ	$\text{N m}^{-1} = \text{kg s}^{-2}$	Surface tension
κ	m	Maximum meniscus height for capillary condensation
η	-	Drainage efficiency factor
θ_L	-	Angle between load and surface
μ	Pa s = $\text{kg m}^{-1} \text{s}^{-1}$	Dynamic viscosity
μ_{\parallel}	-	Friction coefficient
ν	-	Poisson's ratio
ρ	kg m^{-3}	Fluid density
ρ_c	m^{-2}	Density of epidermal cells per toe pad area
ρ_{ch}	m m^{-2}	Length of channels between epidermal cells per toe pad area
σ_{\perp}	Pa = $\text{kg m}^{-1} \text{s}^{-2}$	Tenacity
σ_{\parallel}	Pa = $\text{kg m}^{-1} \text{s}^{-2}$	Shear stress
$\sigma_{\perp, \max}$	Pa = $\text{kg m}^{-1} \text{s}^{-2}$	Maximal tenacity

— continues on the next page —

— continued from the previous page —

Symbol	SI Unit	Description
$\phi_{1,2,l,t}$	$^{\circ}$	Contact angle between gas-solid (1) and gas-liquid interface (2) at leading (l) and trailing edge (t), respectively

2.SI.1.2 List of abbreviations

Table 2.SI.2 List of abbreviations in alphabetical order.

Abbreviation	Description
AFM	Atomic force microscopy
CI	Confidence interval
JKR	Johnson-Kendall-Roberts
MT	Microtribometry
PDMS	Polydimethylsiloxane
PE	Polyethylene
PMMA	Polymethyl-methacrylate
PVS	Polyvinylsiloxane
SE	Standard error
SEM	Scanning electron microscopy
SL	Single limb measurement
SP	Single pad measurement
TEM	Transmission electron microscopy
vdW	van der Waals

2.SI.2 Morphological and material properties of a toe pad

2.SI.2.1 Geometrical model of the surface of the ventral toe pad epidermis

The symbols b , c , d , e , l , β_c , and r_n are not listed in the table of symbols for the sake of clarity. A circular toe pad with a diameter d_p has a ventral surface area A_p of:

$$A_p \approx \pi \left(\frac{d_p}{2} \right)^2 \quad (2.SI.1)$$

Assuming an equilateral hexagonal outline, the projected apical surface area A_c of a single cell is (Fig. 2.SI.1A):

$$A_c = 2 b c + 2 b a_c \quad (2.SI.2a)$$

$$\alpha_c = 2 \arccos \left(\frac{c}{a_c} \right) \quad (2.SI.2b)$$

$$b = a_c \sin \left(\frac{\alpha_c}{2} \right) \quad (2.SI.2c)$$

$$c = a_c \cos \left(\frac{\alpha_c}{2} \right) \quad (2.SI.2d)$$

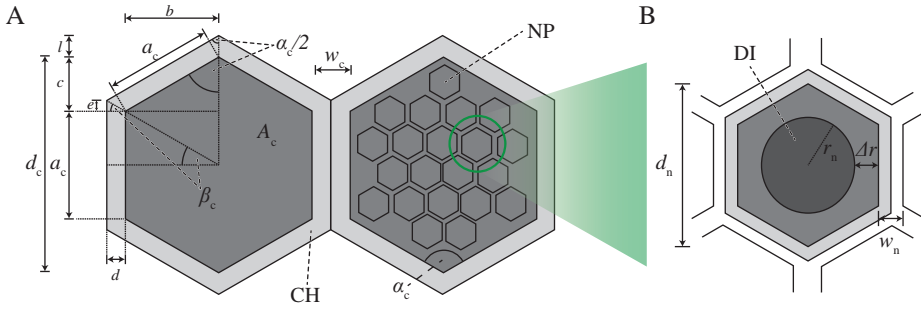


Figure 2.SI.1 Geometrical parameters of our model of the ventral surface of a tree frog's toe pad. (A) Calculation of the projected surface area of a single epidermal cell (A_c , dark) and the surrounding channel (light). (B) Calculation of the projected surface area of a single nanopillar (medium), the surrounding channel (light) and the dimple (dark). d_c cell diameter, a_c cell edge length, w_c channel width, α_c opening angle, A_c apical surface area, d_n nanopillar diameter, w_n nanopillar channel width, Δr distance between dimple and nanopillar edge. CH channel, DI dimple, NP nanopillar.

The projected area covered by a cell and the surrounding channel $A_{c,c}$ is:

$$A_{c,c} = 2(b+d)(c+l-e) + 2(b+d)(a_c+2e) \quad (2.SI.3a)$$

$$\beta_c = \arctan \left(\frac{a_c}{b} \right) \quad (2.SI.3b)$$

$$d = \frac{w_c}{2} \quad (2.SI.3c)$$

$$e = d \tan(\beta_c) \quad (2.SI.3d)$$

$$l = \frac{d}{\sin(\alpha_c)} \quad (2.SI.3e)$$

This gives ca. n_c cells per toe pad:

$$n_c \approx \frac{A_p}{A_{c,c}} \quad (2.SI.4)$$

The wetted area $A_{c,w}$, neglecting the nanopillars, of a single cell is:

$$A_{c,w} = A_{c,c} + 6 a_c h_c \quad (2.SI.5)$$

where h_c is the height of the free-standing cell. Equations 2.SI.2a, 2.SI.3a and 2.SI.5 can be used analogously to calculate the different areas of a single nanopillar (assuming an equilateral hexagonal outline; Fig.2.SI.1B), which gives $n_{n,c}$ nanopillars per cell and in total $n_{n,p}$ nanopillars per pad:

$$n_{n,c} = \frac{A_c}{A_{n,c}} \quad (2.SI.6)$$

$$n_{n,p} = n_c n_{n,c} \quad (2.SI.7)$$

We exclude the dimples on the apical nanopillar surfaces from the effective apical contact area of the whole toe pad in close contact to the substrate. Assuming a circular dimple on a nanopillar with a regular, hexagonal outline with a minimal distance Δr between dimple perimeter and nanopillar edge centroid, the effective apical area is:

$$A_{n,\text{eff.}} = A_n - \pi r_n^2 \quad (2.SI.8a)$$

$$r_n = \frac{a_n \sqrt{3}}{2} - \Delta r \quad (2.SI.8b)$$

The total ventral pad area effective for vdW force generation is:

$$A_{\text{eff.}} = A_{n,\text{eff.}} n_{n,p} \quad (2.SI.9)$$

2.SI.2.2 Fibre-matrix analogy of a toe pad

Scholz *et al.* (2009) proposed an analogy of the tree frog's toe pad epithelium with a fibre-reinforced material. Assuming the layer of nanopillars to be a simple, unidirectional fibre-matrix-composite, the effective elastic modulus of the composite E_c is (Kitchener & Vincent, 1987):

$$E_c = E_f V_f + E_m (1 - V_f) \quad (2.SI.10)$$

The indices mark the elastic modulus E and the volume fraction V of the fibres (_f) and the matrix (_m). With this relation, we can compute the expected volume fraction of fibres for a given composite's effective elastic modulus. We assume a composite stiffness of 14 MPa, as found for the keratinised layer, and further a matrix stiffness of 20 kPa, as found for the whole pad (e.g. Barnes *et al.*, 2011), which presumably is dominated by the underlying matrix (Table 2.1). With $E^* = 4$ GPa for keratinous tonofilaments (e.g. Vincent & Wegst, 2004), Equation 2.SI.10 results in a fibre volume fraction of 0.2%. As shown in Fig. 2.1D₂, the apical ends of the epithelial cells are densely packed with tonofilaments and 0.2% underpredicts the fibre content.

The hypothesised asymmetric stiffness of the tonofilaments with a higher stiffness in tension than in compression most likely explains this deviation. In compression, the fibre stiffness E_f arguably will be arguably lower, for which Equation 2.SI.10 predicts a higher fibre ratio V_f with E_f .

2.SI.2.3 Scaling of tenacity with snout-vent-length

Previously, the relation between tenacity σ_{\perp} and snout-vent-length ℓ_{SV} has been modelled linearly (e.g. Smith *et al.*, 2006a). A linear model is not able to predict local optima or asymptotic limit values in the σ_{\perp} - ℓ_{SV} -relationship, thus possibly neglecting physical limitations (e.g. a maximum possible tenacity for a given attachment mechanism). As shown in Fig. 2.SI.2, linear scaling of σ_{\perp} with snout-vent-length ℓ_{SV} results in $\sigma_{\perp} = k_1 + k_2\ell_{SV}$ [where $k_1 = 0.45 \pm 0.09 \text{ mN mm}^{-2}$, $k_2 = 0.006 \pm 0.001 \text{ mN mm}^{-3}$, mean \pm 95% confidence-interval (CI), Standard error (SE) = 0.23 mN mm^{-2}] using total least squares regression. We quantified CI with a Monte Carlo approach (1000 iterations). One could argue that a relation converging to a limit value, for example an exponential growth decay model ($\sigma_{\perp} = \sigma_{\perp, \max} [1 - e^{-k_1(\ell_{SV} - k_2)}$]), represents the tenacity scaling of tree frogs more closely than a linear one, which predicts unrealistically large adhesive tenacities in frogs larger than 10 cm. In the exponential growth decay model, k_1 and k_2 are fitting constants and $\sigma_{\perp, \max}$ is the maximum tenacity. By fitting this function to the maximum tenacities measured in tree frogs, we can compute a maximum adhesive tenacity $\sigma_{\perp, \max} = 0.88 \pm 0.07 \text{ mN mm}^{-2}$ (standard error SE = 0.21 mN mm^{-2} ; Fig. 2.SI.2).

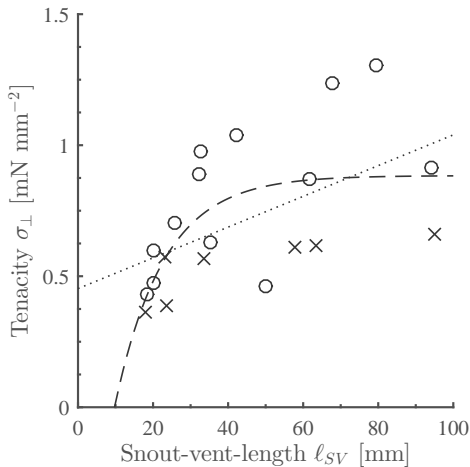


Figure 2.SI.2 Measured maximum pad tenacity σ_{\perp} in various hylids (circles: redrawn from Fig. 3D by Barnes *et al.*, 2006; crosses: redrawn from Fig. 1D by Smith *et al.*, 2006b). The scaling of σ_{\perp} with snout-vent-length ℓ_{SV} is modelled linearly (dotted) and as exponential growth decay (dashed).

2.SI.3 Attachment performance of tree frogs

2.SI.3.1 The rotation platform experiment

For a frog sliding/falling on/from a platform that rotates around a horizontal axis, adhesion F_{\perp} , friction F_{\parallel} and friction coefficient μ_{\parallel} calculate as follows from the angles of falling (α_{\perp}) and slipping (α_{\parallel} ; Fig. 2.SI.3):

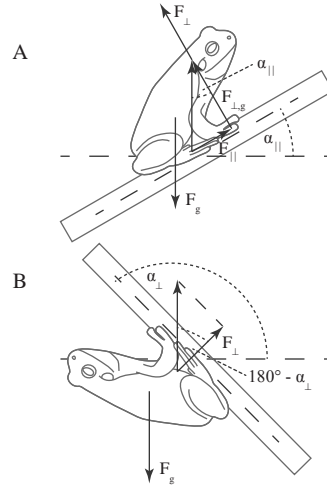
$$F_{\parallel} = m g \sin(\alpha_{\parallel}) \quad 0^{\circ} < \alpha_{\parallel} < 90^{\circ} \quad (2.SI.11a)$$

$$F_{\perp} = m g \cos(180 - \alpha_{\perp}) = -m g \cos(\alpha_{\perp}) \quad 90^{\circ} < \alpha_{\perp} < 180^{\circ} \quad (2.SI.11b)$$

$$\mu_{\parallel} = \frac{F_{\parallel}}{m g \cos(\alpha_{\parallel}) + F_{\perp}} = \frac{\sin(\alpha_{\parallel})}{\cos(\alpha_{\parallel}) - \cos(\alpha_{\perp})} \quad (2.SI.11c)$$

Here, m is the body mass and g is the gravitational acceleration.

Figure 2.SI.3 Function principle of the rotation table experiment. A frog is placed on a platform that rotates (around a horizontal axis) into an overhanging position and the angles of initial slipping (A, α_{\parallel}) and falling (B, α_{\perp}) of the animal are recorded. Based on vector decomposition and measurement of body mass, the maximum adhesion (F_{\perp}) and friction (F_{\parallel}) as well as the coefficient of static friction (μ_{\parallel}) are computed.



2.SI.3.2 Capillary adhesion of deformable objects

Butt *et al.* (2010) extended Equation 2.1 to model the capillary adhesion between a deformable, smooth sphere with radius R and a plate with contact angles ϕ_1 (sphere-liquid) and ϕ_2 (plate-liquid; Fig. 2.SI.4), which they proposed to represent the capillary adhesion of a soft, curved toe pad more closely than a plate-plate contact (Fig. 2.3A). A deformable sphere experiences stronger adhesion than a rigid one of the same dimensions, because of the larger contact area of the former. Assuming $R \gg R_{\text{azi}} \gg R_{\text{mer}}$, a large indentation depth compared to R_{mer} , very hydrophilic materials ($\phi_1 = \phi_2 \approx 0$), an effective elastic modulus of the system (i.e. pad-substrate) $E_s^* = E_1^* + E_2^*$, and an effective radius of the system $R_s = R_1 R_2 / (R_1 + R_2)$, capillary

adhesion can be calculated as (Butt *et al.*, 2010):

$$F_{\perp} = 4 \pi \gamma R_s + \left(\frac{\pi \gamma}{2 R_{\text{mer}}} \right)^3 \frac{2 R_s^2}{3 E_s^{*2}} \quad (2.\text{SI.12})$$

In the deduction of this model, indentation depths being much larger than the meniscus height are assumed, which may lead to unrealistic results in the case of tree frog attachment: the expected meniscus height (see main text and Fig. 2.9) is in the order of indentation depths reported for real animals (e.g. Barnes *et al.*, 2011) and the meniscus shape might be affected by the indentation.

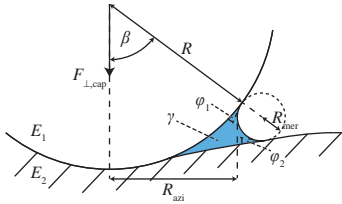


Figure 2.SI.4 Model of capillary adhesion between a sphere and a deformable flat plate ($R_2 = \infty$). d_g gap width, $F_{\perp,\text{cap}}$ capillary adhesion, $R = R_1$ radius of sphere, R_{mer} , R_{azi} meridional and azimuthal radius of meniscus curvature, γ mucus surface tension, ϕ_1 , ϕ_2 sphere-liquid and substrate-liquid contact angle.

2.SI.3.3 Capillary friction

Next to adhesion, capillary effects can also generate friction. Assuming a shear load acting on a pad with width b , the substrate-liquid contact angle shifts asymmetrically at leading (ϕ_l) and trailing edge (ϕ_t). The resulting capillary friction $F_{\parallel,\text{cap}}$ is (Federle *et al.*, 2006):

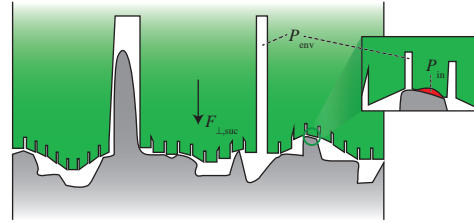
$$F_{\parallel} = 2 b \gamma (\cos \phi_t - \cos \phi_l) \ll 4 b \gamma \quad (2.\text{SI.13})$$

Equation 2.SI.13 predicts a maximum shear stress of around 0.14 mN mm^{-2} , which is below the stresses measured for toe pads (Federle *et al.*, 2006). Also, capillary friction does not explain the scaling of friction with sliding speed and normal load. If present at all, capillary friction only plays a minor role in tree frog attachment.

2.SI.3.4 Suction

Suction has been suggested early to explain tree frog attachment (Mohnik, 1879). In particular, the volume enclosed between the dimples found on the apical nanopillar surface (Barnes *et al.*, 2013; Ernst, 1973a; Federle *et al.*, 2006; Scholz *et al.*, 2009) and the substrate might give rise to suction (Barnes *et al.*, 2013; Fig. 2.SI.5). Importantly, the dimensions of the dimples could be distorted because of deeper AFM indentations in the centre than at the edges of the nanopillars due to a spatial variation in stiffness. In TEM measurements, shrinkage could distort the dimple shape.

Figure 2.SI.5 Schematic representation of the suction between ventral toe pad epidermis (green) and substrate (grey). Suction forces $F_{\perp, \text{suc}}$ might arise at a normal load $F_{\perp, \text{L}}$ from a difference between environmental pressure P_{env} and the pressure P_{in} in the volumes enclosed between the ‘dimples’ on the apical surfaces of the nanopillars and the substrate (inset; red).



By enlarging the enclosed volume, the pressure P_{in} in the enclosed region decreases relative to the environmental pressure P_{env} . A pressure difference ΔP acting across the dimple surface A results in adhesion (Fig. 2.SI.5, inset; Ditsche & Summers, 2014; Emerson & Diehl, 1980; Gorb, 2008):

$$F_{\perp} = (P_{\text{env}} - P_{\text{in}}) A = \Delta P A \quad (2.\text{SI}.14)$$

Typically, biological suckers are flexible, have a concave shape and a smooth rim for more effective sealing (e.g. by vdW interactions), and rely on muscles to change the size of the enclosed volume (Gorb, 2008). In tree frogs, the secreted mucus might improve the sealing of the enclosed volume (Leydig, 1868) and the maximally achievable pressure difference of 1 bar ($= 100 \text{ mN mm}^{-2}$) would be sufficient to explain the measured adhesion of these animals. However, Emerson & Diehl (1980) found that the attachment of *Smilisca phaeota* to a vertical glass plate is not affected by a change of the environmental pressure P_{env} of ca. 30 mN mm^{-2} (i.e. 0.32 bar). Schuberg (1891) also described that *Hyla arborea* is able to climb in a partial vacuum. Further studies with experimental control of the environmental pressure are required to conclude on the role of suction in tree frogs. Because of the surface-normal orientation of suction forces, we do not expect a direct contribution of suction to the friction of the pads.

2.SI.3.5 Kendall peeling model

At the onset of peeling of a thin, linearly elastic film (width b , thickness h , elastic modulus E , fracture energy per unit area $\Delta\gamma$) at a load F_{L} under an angle θ_{L} to the substrate over a distance Δc (Fig. 2.SI.6), elastic energy (i.e. stretching of the film), potential energy (i.e. pulling of the film), and fracture energy (i.e. energy required to fracture a unit interfacial area) are in balance. The balance of fracture, potential and elastic energy yields (Kendall, 1975):

$$-\Delta\gamma b \Delta c + F_{\text{L}} (1 - \cos \theta_{\text{L}}) \Delta c + \frac{F_{\text{L}}^2 \Delta c}{2 b h E} = 0 \quad (2.\text{SI}.15)$$

Rewriting Equation 2.SI.15, one can compute the normal (adhesive) peeling force component:

$$F_{L,\perp} = \sin \theta b t E \left(\cos \theta - 1 + \sqrt{1 - 2 \cos \theta + \cos^2 \theta + 2 \frac{\Delta \gamma}{t E}} \right) \quad (2.SI.16)$$

The frictional component is calculated analogously by replacing $\sin \theta$ with $\cos \theta$.

The fracture energy $\Delta \gamma$ depends on peeling speed (Kendall, 1975) as well as adhesion (Pesika *et al.*, 2006). Measurement of F_{\perp} at $\theta_L = 90^\circ$ allows an approximation of $\Delta \gamma$ with Equation 2.SI.16 for an inextensible film, because then $\Delta \gamma = F_{\perp}/b$. Based on data by Barnes *et al.* (2008), we obtain $\Delta \gamma = [0.65 \text{ mN mm}^{-2} \pi (1.5 \text{ mm})^2] / [\pi (1.5 \text{ mm})^2]^{-0.5} = 1.74 \text{ N m}^{-1}$ for an assumed pad diameter $d_p = 3 \text{ mm}$ [average pad width $b \approx (\pi d_p^2)^{-0.5}$].

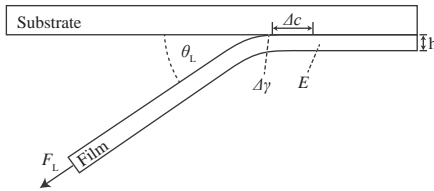


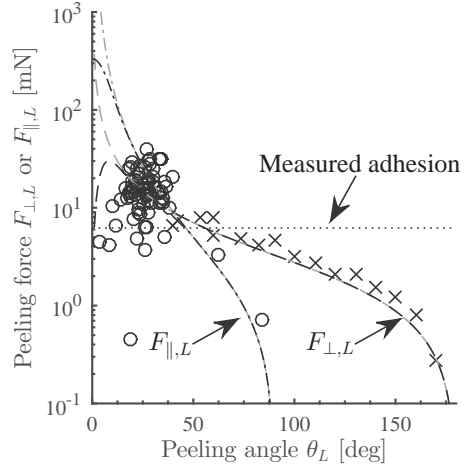
Figure 2.SI.6 Kendall peeling of a thin film (Kendall, 1975). E elastic modulus, h film thickness, F_L Load, Δc peeling distance, θ_L peeling angle.

Further, we estimate $\Delta \gamma$ by fitting Equation 2.SI.16 ($E = 15 \text{ kPa}$, $h = 0.5 \text{ mm}$) to peel off forces measured by Barnes *et al.* (2008) and Endlein *et al.* (2012; Fig. 2.SI.7). The fitted curve represents measured data well ($SE = 0.01 \text{ mN}$) and results in $\Delta \gamma = 1.24 \text{ N m}^{-1}$. The peel forces for an inextensible and an elastic film deviate from each other by more than 5% at $\theta_L < 16^\circ$, as to be expected (Kendall, 1975). The finite peel off force components predicted by elastic theory at load angles approaching zero are more realistic than the continuously increasing forces in inextensible peeling (Endlein *et al.*, 2012). At $\theta_L < 40^\circ$, no force data with controlled peeling angle are available as reference. The complex material properties (e.g. anisotropic or viscoelastic stiffness) of toe pads might prohibit the application of Kendall peeling theory at such low angles.

2.SI.3.6 Johnson-Kendall-Roberts model

Johnson, Kendall & Roberts (1971) extended the Hertz model (Kendall, 2004) and implemented the effect of adhesion on the contact between two spherical objects. In the JKR-model, the work of adhesion W_{\perp} , a system-specific quantity describing the energy per unit area required to irreversibly separate two objects (Johnson *et al.*, 1971), of a sphere with radius R relates to the maximal adhesion F_{\perp} (i.e. pull off

Figure 2.SI.7 Peeling force components of single toe pads of *Litoria caerulea* [$E = 15 \text{ kPa}$, $d_p = 3 \text{ mm}$, $h = 0.5 \text{ mm}$, $A_p = \pi (d_p/2)^2$, $b = A_p^{-0.5}$; crosses: redrawn from Fig. 1B by Barnes *et al.* (2008); circles: recomputed from Fig. 6 by Endlein *et al.* (2012)] for uncontrolled peeling angles. Non-linear total least squares regression of the surface-normal (dashed) peeling force component of an elastic film (dark) to the data by Barnes *et al.* (2008) gives $\Delta\gamma = 1.24 \pm 0.003 \text{ N m}^{-1}$ (95% CI, SE = 0.01 N m^{-1}). Parallel peeling forces (dashed-dotted) and the peel off force of a stiff film (light) are shown for comparison. Adhesion deduced from rotation table measurements (dotted) serves as reference (Fig. 2.SI.3).



force) as:

$$W_{\perp} = -\frac{2}{3} \frac{F_{\perp}}{\pi R} \quad (2.SI.17)$$

Using this model, Barnes *et al.* (2011) measured $W_{\perp} \approx 0.02\text{--}0.11 \text{ N m}^{-1}$. Further, they reported a positive scaling of W_{\perp} with indentation depth and a negative scaling with pad size.

However, the JKR model is only valid for elastic objects and for small indentations compared to the sphere size (Popov, 2010). In contrast, tree frogs' toe pads are potentially viscoelastic and presumably experience large deformations during contact. Further work is required to examine to what extent the JKR-model captures the contact mechanics of tree frogs' toe pads accurately.



*Thus, the adhesive toe not only carries the whole
body weight of the now hanging animal, it also
has to overcome the whole force of the jump.*

v. Wittich, 1854

CHAPTER 3

Force-transmitting structures in the digital pads of the tree frog *Hyla cinerea*: a functional interpretation

Abstract

The morphology of the digital pads of tree frogs is adapted towards attachment, allowing these animals to attach to various substrates and to explore their arboreal habitat. Previous descriptions and functional interpretations of the pad morphology mostly focussed on the surface of the ventral epidermis and little is known about the internal pad morphology and its functional relevance in attachment. In this study, we combine histology and synchrotron micro-computer-tomography to obtain a comprehensive 3-D morphological characterisation of the digital pads—in particular of the internal structures involved in the transmission of attachment forces from the ventral pad surface towards the phalanges—of the tree frog *Hyla cinerea*. A collagenous septum runs from the distal tip of the distal phalanx to the ventral cutis and compartmentalises the subcutaneous pad volume into a distal lymph space and a proximal space, which contains mucus glands opening via long ducts to the ventral pad surface. A collagen layer connects the ventral basement membrane via interphalangeal ligaments with the middle phalanx. The collagen fibres forming this layer curve around the transverse pad axis and form laterally separated ridges below the gland space. The topological optimisation of a shear-loaded pad model using finite element analysis (FEA) shows that the curved collagen fibres are oriented along the trajectories of

This chapter has been published as: LANGOWSKI, J.K.A., SCHIPPER, H., BLIJ, A., VAN DEN BERG, F.T., GUSSEKLOO, S.W.S. & VAN LEEUWEN, J.L. (2018b). Force-transmitting structures in the digital pads of the tree frog *Hyla cinerea*: a functional interpretation. *Journal of Anatomy* **233**, 478–495.

the maximum principal stresses and the optimisation also results in ridge-formation, suggesting that the collagen layer is adapted towards a high stiffness during shear loading. We also show that the collagen layer is strong, with an estimated tensile strength of 2.0–6.5 N. Together with longitudinally skewed tonofibrils in the superficial epidermis, these features support our hypothesis that the digital pads of tree frogs are primarily adapted towards the generation and transmission of friction rather than adhesion forces. Moreover, we generate—based on a simplified FEA model and predictions from analytical models—the hypothesis that dorsodistal pulling on the collagen septum facilitates proximal peeling of the pad and that the septum is an adaptation towards detachment rather than attachment. Lastly, by using immunohistochemistry, we (re-)discovered bundles of smooth muscle fibres in the digital pads of tree frogs. We hypothesise that these fibres allow the control of (i) contact stresses at the pad-substrate interface and peeling, (ii) mucus secretion, (ii) shock-absorbing properties of the pad, and (iv) the macroscopic contact geometry of the ventral pad surface. Further work is needed to conclude on the role of the muscular structures in tree frog attachment. Overall, our study contributes to the functional understanding of tree frog attachment, hence offering novel perspectives on the ecology, phylogeny, and evolution of anurans, as well as the design of tree-frog-inspired adhesives for technological applications.

Keywords: Attachment organ; Bioadhesion; Collagen; Connective tissue; Fibre-matrix-composite; Material stiffness; Shear load; Smooth muscle.

3.1 Introduction

Tree frogs possess adhesive digital pads that enable these animals to climb vertical substrates, hence allowing the exploration of arboreal habitats, the evasion of ground-borne predators, and the disclosure of otherwise unreachable food sources. Studying the morphology and functioning of these organs helps to unravel the ecology (Emerson, 1991; Green & Simon, 1986), evolution (Moen *et al.*, 2013; Sustaita *et al.*, 2013), and phylogeny (Green, 1979, 1980; Hertwig & Sinsch, 1995; McAllister & Channing, 1983) of tree frogs, as well as to design bioinspired adhesives (Drotlef *et al.*, 2013; Iturri *et al.*, 2015; Murarash *et al.*, 2011; Tsipenyuk & Varenberg, 2014; Xue *et al.*, 2017; Zhang *et al.*, 2016).

The digital pads are macroscopically smooth, soft (Scholz *et al.*, 2009), and proposedly adhere by wet adhesion (Emerson & Diehl, 1980; Hanna & Barnes, 1991; Nachtigall, 1974; Schuberg, 1891; Siedlecki, 1909; v. Wittich, 1854): tree frogs secrete a watery mucus into the gap between pad and substrate (Blackwall, 1845; Federle *et al.*, 2006), which may cause surface-tension-dependent capillary forces and viscosity-dependent hydrodynamic forces (Barnes, 2012; Endlein & Barnes, 2015). The surface of the adhesive epidermis on the ventral (throughout this paper, we use ‘ventral’ to describe the palmar/plantar side of the digits; Fig. 3.1) side of the distal digital segment (for the digital segments and the phalanges, we use ‘distal’ and ‘middle’ to describe the

ultimate/terminal and penultimate/subterminal ones, respectively; Fig. 3.1A) consists of prismatic cells separated by channels and covered with nanoscopic cellular protrusions, so called ‘nanopillars’ (Scholz *et al.*, 2009), forming a hierarchical micro-to nanoscopic surface pattern (Ernst, 1973a). This epidermal morphology presumably evolved convergently in multiple tree frog clades (Barnes *et al.*, 2013; Green, 1979; Lee *et al.*, 2001; McAllister & Channing, 1983) and could facilitate—in addition to wet adhesion—attachment mechanisms such as mechanical interlocking (Emerson & Diehl, 1980), suction (Mohnike, 1879), and van der Waals (vdW) interactions (Emerson & Diehl, 1980; Federle *et al.*, 2006).

Previously, the discussion on the generation of adhesion and friction (i.e. the attachment force normal and parallel to the substrate surface, respectively) in tree frogs strongly focused on the superficial epidermis (Ernst, 1973a; Hanna & Barnes, 1991). The morphology and attachment-related functions of dermal and subcutaneous structures of the digital tip, such as the transmission of adhesion and friction forces from the epidermis to the skeleton and hence to the rest of the body, remained largely unstudied. Here, we define the digital tip as the distal phalanx and all subdermal, dermal, and epidermal tissues (Ernst, 1973a,b; Hertwig & Sinsch, 1995) surrounding it. Dermal and subdermal structures include connective—mainly collagenous—tissue, muscle fibres, blood vessels, a lymph space, and mucus glands (Fig. 3.1A; Ernst, 1973a; Nakano & Saino, 2016; Siedlecki, 1910). To our knowledge, the adhesive epidermis is mechanically linked to the distal phalanx and the rest of the body by connective tissue only. Various authors described different collagenous structures such as loose connective tissue forming the basement membrane and the dermal stratum spongiosum (Leydig, 1868; Nakano & Saino, 2016; Noble & Jaeckle, 1928; Schuberg, 1891; Siedlecki, 1910), collagen fibres traversing the distal lymph space (Dewitz, 1883; Leydig, 1868; v. Wittich, 1854), and laterally separated bundles of collagenous fibres running along the ventral pad surface (Noble & Jaeckle, 1928). However, others termed the fibres in the lymph space (Schuberg, 1891) and the ventral bundles (Siedlecki, 1910) muscular instead of collagenous structures, whereas more recently the presence of muscular structures was negated completely (except for smooth muscle cells surrounding the mucus glands; Ernst, 1973b; Mizuhira, 2004). Furthermore, the 3-D arrangement of connective (and muscular) tissues, lymph space, and skeleton (and accordingly the potential of these structures for force transmission) is largely unknown.

In the light of a recent report of a load of up to 14.4 times the body weight withstood by a single digital pad during landing in *Trachycephalus resinifictrix* (Bijma *et al.*, 2016), we address in this paper the morphology and function, in particular in the transmission of attachment forces, of dermal and subcutaneous structures in the digital pads of the tree frog *Hyla cinerea*. As tree frogs arguably encounter mostly vertical substrates while climbing up and down in their arboreal habitat, we expect that the pads are primarily adapted towards the transmission of friction forces (i.e. shear loads). We employ a combination of histology, immunohistochemistry, and synchrotron micro-computer-tomography (μ -CT) to obtain a 3-D characterisation of the pad morphology. Furthermore, we numerically predict the stiffness-optimised topo-

logy of the collagenous tissue in the ventral pad region during shear loading, and we estimate, by measuring cross-sectional areas, the tensile strength of the structures involved in force transmission. In combination, these approaches enable us to address the following questions:

- How are force-transmitting structures such as connective tissue, lymph space, and skeletal elements distributed within the digital tip (and relative to each other)? Which pathways of transmission of adhesive and frictional forces do these structures accommodate?
- How do the pad and adjacent structures transmit shear loads equivalent to several times the body weight?
- Are there muscular structures involved in force transmission? If so, what function(s) could these structures fulfil?

3.2 Materials and methods

3.2.1 Experimental animals

For morphological analyses, we used three adult *Hyla cinerea*, that died of unknown causes (*post mortem* snout-vent-length 40–46 mm, body mass 6.2–8.2 g, age \leq 1 year). We collected the distal limbs at most 5:30 h after death by disarticulation of the elbow and knee joints. Until further use, the right forelimb (F) and the left hindlimb (H; Fig. 3.1B) of each individual were fixed and decalcified for 2–12 weeks in Bouin's liquid [37% formaldehyde, saturated picric acid and acetic acid (Merck, USA) with a ratio of 5:15:1] and subsequently stored in 70% ethanol, which was renewed multiple times. All following steps were executed at room temperature, unless mentioned otherwise.

3.2.2 Histology

Before histological staining, the two most distal segments of digits F_I, F_{II}, and F_{III} of the forelimb and of digits H_I and H_{II} of the hindlimb (Fig. 3.1B) were cut through the central part of the middle phalanx. For easy handling and correct alignment of the samples with respect to the desired cutting planes, they were preembedded in small blocks of agarose gel [1% low-melting agarose (Sigma-Aldrich, USA) in demineralised water] before dehydrating and embedding the agarose blocks in paraffin (KP Paraclean I, VWR International B.V., The Netherlands; see Section 3.SI.4). The embedded samples were cut into 5 μ m thick sections using a microtome (Microm 305S, Microm GmbH, Germany) and placed on egg-glycerin coated object slides (Menzel, Germany). Digit F_I was cut parallel to the ventral pad surface (i.e. horizontal sections), F_{II} parallel to the median digital plane (i.e. sagittal sections), and F_{III} perpendicularly

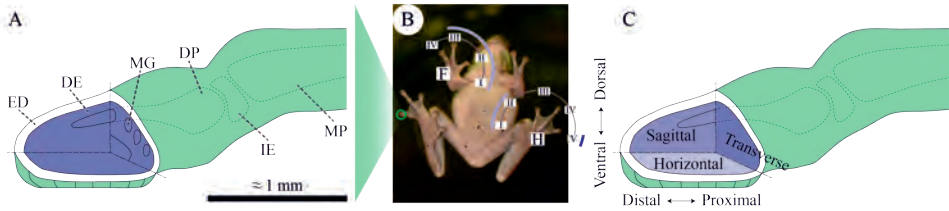


Figure 3.1 (A) Basic morphological terminology of the digital tip and the distal interphalangeal joint of the tree frog *Hyla cinerea*. The blue region depicts the largely uncharacterised dermal and subdermal space including connective, muscular, vascular and other tissues. (B) Nomenclature and usage of the digits I–IV in the right forelimb (F) and I–V in the left hindlimb (H) [light blue arcs (F_{I–III}, H_{I–II}): histology/immunohistochemistry, dark blue arc (H_V): μ -CT]. (C) Definition terms of anatomical location and of the cutting and viewing planes. DE dermis, DP distal phalanx, ED epidermis, IE intercalary element, MG mucus gland, MP middle phalanx.

to the longitudinal digital axis (i.e. transverse sections; Fig. 3.1C). Digits H_I and H_{II} were cut sagittally and transversally, respectively.

The samples on every 2nd object slide in sequence (transverse and horizontal sections) and on the slides holding the left half of the digits (sagittal sections), respectively, were stained using Crossmon's light green trichrome including Mayer's haematoxylin and Alcian blue (see Section 3.SI.4). Images of the stained sections were obtained using a digital microscope camera (DFC450c, Leica, Germany) mounted on an upright microscope (DM6b, Leica) with a HC PL APO 40 \times /0.85 objective controlled with the Leica Application Suite X (Version 2.0). High-resolution images of the whole sections were obtained by merging tile-scanned images. Post-processing (cropping, rotating, scaling, white balancing, and arranging) of the images was done in Photoshop CC (Version 2017.1.1, Adobe Systems Incorporated, USA) and in Illustrator CS6 (Version 16.0.3, Adobe). Geometrical parameters of interest were measured with ImageJ (Version 1.51f, National Institutes of Health, USA).

3.2.3 Immunohistochemistry

To revise the presence of muscular tissues within the digital tip, we stained the remaining slides of frogs 1 and 2 using an actin-antibody (A5228, Merck), which is specific for smooth-muscle- α -actin (Skalli *et al.*, 1986). Before immunohistochemical staining (see Section 3.SI.5), the sections were deparaffinised towards demineralised water, endogenous peroxidase was removed with a solution of 0.3% H₂O₂ (Merck) in buffer, and aspecific antibody-binding was blocked by the application of 10% goat serum (Vector Laboratories, USA) in combination with 1% acetylated bovine serum albumin (BSA-c, Aurion, The Netherlands). The primary α -actin-antibody was applied over night at 4 $^{\circ}$ C (dilution 1:400), followed by a secondary goat-anti-mouse/horseradish-peroxidase-antibody (Agilent, Canada) for 45 min (dilution 1:100). Structures containing smooth-muscle- α -actin were stained brown using 3,3'-diaminobenzidine (7–10 min; Sigma) as substrate. Finally, we applied Mayer's

haematoxylin as described above as counterstain, and dehydrated and sealed the sections with DPX mounting medium (VWR, USA). Imaging and post-processing of the images were done as described above.

3.2.4 Synchrotron micro-computer-tomography

The digit used for μ -CT (Frog 3, H_V ; Fig. 3.1B) was dissected, fixed, and stored as described for histology. The digit was transferred into phosphotungstic acid (PTA; 0.3% PTA in 70% ethanol; according to Metscher, 2009) contrast stain to enhance the contrast of the soft tissues of interest. The PTA-stain was refreshed several times over the course of 9 days to ensure penetration of the whole sample. Before scanning, the sample was washed in 70% ethanol and dehydrated stepwise (45 min 80% ethanol, 30 min 90% ethanol, 20 min 96% ethanol, 2 · 15min 100% ethanol). 100% ethanol was used as scanning medium.

The μ -CT-scan of the digit was acquired at the Tomographic Microscopy and Coherent Radiology beamline (TOMCAT, X02DA) of the Swiss Light Source facility at the Paul Scherrer Institute, Switzerland, using a monochromatic 14-keV-beam with almost parallel geometry and a LuAG:Ce-scintillator. A high-quality optical microscope (Optique Peter, France) with an UPLAPO10 \times -objective (Olympus, Japan; numerical aperture 0.4) was used in combination with a pco.edge 5.5 camera (PCO AG, Germany; exposure time 100 ms, 2560 · 2160 pixels, pixel size 6.5 · 6.5 μm^2), resulting in an effective pixel size of 0.65 · 0.65 μm^2 and a field of view of 1.7 · 1.4 mm^2 . We mounted a pipette tip containing the sample within the scanning liquid on a rotation platform (ABRT150, Aerotech Inc., USA) and rotated the sample around its approximate longitudinal axis, which was aligned perpendicularly to the beam. The scan angle was varied from 0° to 180° in 0.1° steps. The scans were reconstructed using propagation-based phase contrast imaging as described by Paganin *et al.* (2002). Because the sample was larger than the field of view, it was scanned in two batches along the proximal-distal digit-axis (2160 images per batch) with an overlap of 262 images (i.e. 170 μm). The batches were merged and overlapping images were removed.

Filtering of the reconstructed transverse sections and segmentation of the structures of interest were done in Seg3D (Version 2.4.0, NIH, USA). To reduce the efforts of computation and manual segmentation, every 8th transverse section was imported and the scanned volume was cropped closely around the sample; this resulted in 1759 · 1754 · 410 voxels—each with a size of 0.65 · 0.65 · 5.2 μm^3 —in transversal, dorso-ventral and proximal-distal direction, respectively. We used grey-value thresholding on median filtered sections to mask most of the background voxels, which were then removed from the original sections, and automatic histogram equalisation to enhance the contrast of the internal digital structures (see Section 3.SI.3). The phalanges, intercalary element, tendons, ligaments, ventral collagen, smooth muscle fibres, and mucus glands were segmented section-wise by masking the according structures manually using the ‘polyline’ and ‘paintbrush’ tools. To distinguish the different tissues, we considered density differences (e.g. muscle fibres appeared brighter than collage-

nous fibres), differences in fibre orientation (to distinguish individual collagen bands), and knowledge on the digital morphology from the histological sections and from literature. The outlines of most structures were clearly distinguishable. However, the segmentation of fine structures (e.g. the side arms of the ligaments, the ventral collagen ridges, and the mucus ducts within the ventral epidermis) and of connections between collagenous and other tissues (i.e. entheses and apophyses) was less accurate due to the absence of distinct visual features.

3.2.5 Topological optimisation of a shear-loaded pad model

To provide a functional explanation for the distribution of collagenous tissue found in the digital pad, we performed a topological optimisation of a shear-loaded pad model via finite element analysis (FEA). This is the optimisation of the distribution of material within a design space for a set of boundary conditions and optimisation goals (Suresh, 2013). We created a simplified, non-optimised geometrical model of the ventral cutis with the approximate dimensions of a real pad (0.45 mm high, 1 mm wide, 1.5 mm long, Fig. 3.10A) in Solidworks (Version 2015 SP5.0 Education Edition, Dassault Systèmes, USA). Proximally, material was recessed to model the neighbouring proximal epiphysis of the distal phalanx. We implemented three longitudinal rows of each 5 vertical holes ($\varnothing = 0.1$ mm, hole spacing = 0.14 mm, row spacing = 0.25 mm) to represent mucus ducts piercing the connective tissue. In contrast to the effective elastic modulus of the pad epidermis (Barnes *et al.*, 2013, 2011; Kappl *et al.*, 2016; Scholz *et al.*, 2009), the elastic modulus E , yield strength σ , and Poisson's ratio ν of deeper lying structures to our knowledge are unknown. We verified the independency of the qualitative optimisation results from variations in elastic modulus, and applied $E = \sigma = 20$ MPa and $\nu = 0.33$, which is within the range of values reported for collagenous tissues (Biewener, 2008).

Using Paretoworks (Version 2017.04, SciArt, USA), we created a mesh of ca. 250000 elements (edge length ≈ 13 μm). Displacement and removal of the ventral model surface were prohibited and a normal tensile load of 3.815 mN ($=7 \text{ g} \cdot 9.81 \text{ m s}^{-2} / 18$, equivalent to an uniform distribution of the approximate body weight over all 18 digits) was applied on the most proximal model surface (red area in Fig. 3.10A₁) to simulate a shear load as experienced by an animal attaching to a vertical surface with its head facing upwards. Using the geometrical lateral symmetry to reduce computational efforts, the initial model volume was reduced by 60% in 2.5%-steps (see Section 3.SI.7) while maintaining maximum stiffness. We exported the optimised geometry as .stl-file ('very fine' resolution) and reimported it using Power Surfacing (Version 4.1.0008, IntegrityWare, USA) into Solidworks for postprocessing. The surface of the optimised geometry was remeshed with the 'quad wrap' function (polygon size = 2.2% of the length of the whole geometry); small mesh inaccuracies were corrected manually. The resulting surface mesh was transformed into a 'medium'-quality volume mesh. Using the in-house FEA-solver of Solidworks, we remeshed the non-optimised and optimised model (with 365000 and 187000 elements, respectively; edge length ≈ 20 μm) and computed von Mises stresses to identify regions of low mechanical loading, as well as

maximum principal stresses to visualise the trajectories of force transmission through the pad model. The same material properties and loading were used as described above.

3.3 Results

The general bauplan of the digital tip of *Hyla cinerea* does not vary in between digits, limbs, and individuals (see Section 3.SI.6) and is described below. Epidermal tissue encloses the digital tip (Figs. 3.2–3.4,3.5A). Collagenous tissue and blood vessels form the dermis. The dorsal dermis contains numerous mucus glands, which are not found in the ventral dermis. The nearly hemispherical proximal epiphysis of the distal phalanx (referred to as the base of the distal phalanx) fills the ventroproximal part of the subdermal pad space. Distally, the distal phalanx tapers into a curved diaphysis protruding approximately halfway into the digital tip, with an upward pointing angle of ca. 30–40°. A collagenous septum runs from the distal tip of the distal phalanx towards the ventral cutis and compartmentalises the subdermal space: lymph fills a substantial portion the space distal to the septum (referred to as lymph space; Nakano & Saino, 2016; Noble & Jaekle, 1928) and a dense cluster of glands occupies the space proximal to the septum (referred to as gland space). Mucus ducts connecting the glands to the ventral pad surface and numerous bundles of smooth muscle fibres traverse the lymph space. Ventrally, a layer of collagen fibres runs longitudinally through the digital pad (referred to as ventral collagen layer). As mentioned before, we will focus on the structures relevant to force transmission, both within the distal interphalangeal joint region and in the digital tip.

3.3.1 Phalanges and the distal interphalangeal joint

A biconcave intercalary element, which is wider than thick, is found between the distal and middle phalanx (Fig. 3.3D). The articulating surface of the intercalary element with the distal phalanx is concave and counterfits the base of the distal phalanx, whereas the articulating surface with the middle phalanx is almost horizontal and flat.

The distal interphalangeal joint is bridged by a dorsal tendon attached to the Mm. *Extensores breves* (Burton, 1998), and by the ventral *Tendo Superficialis* attached to the flexor muscles (Manzano *et al.*, 2007; Fig. 3.5B_{II,III}). The extensor tendon consists of two strands connected via a thin collagenous sheath, which together span the distal epiphysis of the middle phalanx (referred to as the head of the middle phalanx), and connect dorsally to the distal phalanx, just distally of the base of the distal phalanx. The *Tendo Superficialis* runs ventral of the middle phalanx and splits below the intercalary element into two strands. These strands flatten out below the base of the distal phalanx, follow its curved ventral surface, and connect distoventrally

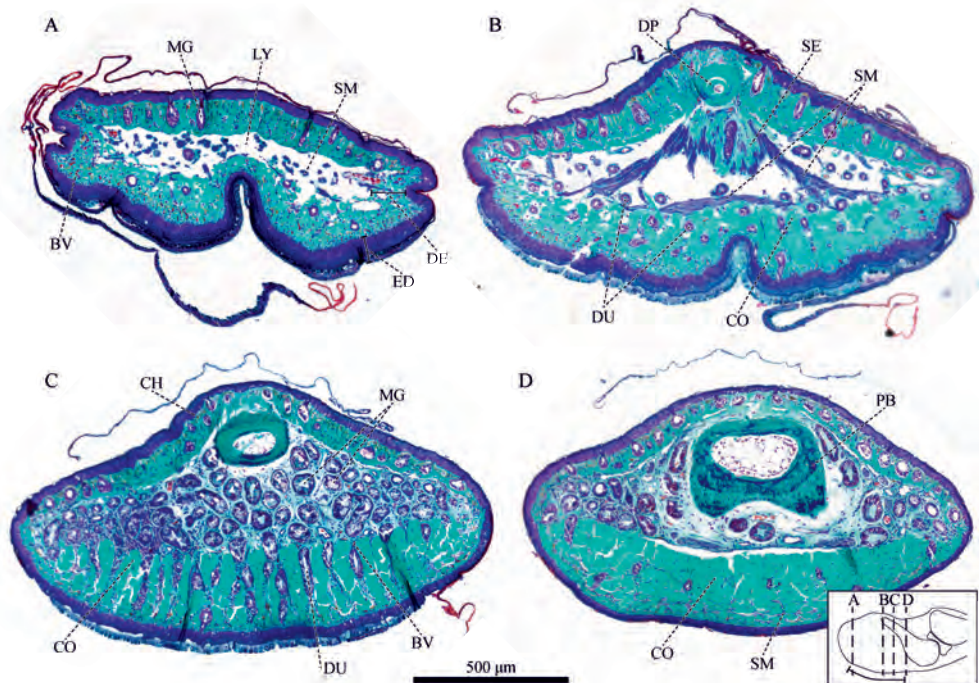


Figure 3.2 Series of transverse sections of a digital pad of *Hyla cinerea* (Frog 3, digit F_{III}) from distal to proximal stained with Crossmon's light green trichrome including Mayer's haematoxylin and Alcian blue [see inset for the approximate locations and the extent of the adhesive ventral epidermis (curved solid line)] through (A) the lymph space, (B) the approximate septum plane, (C) the gland space, and (D) the distal end of the base of the distal phalanx. BV blood vessel, CH chromatophore, CO collagen tissue, DE dermis, DP distal phalanx, DU mucus duct, ED epidermis, LY lymph space, MG mucus gland, PB base of the distal phalanx, SE septum, SM smooth muscle.

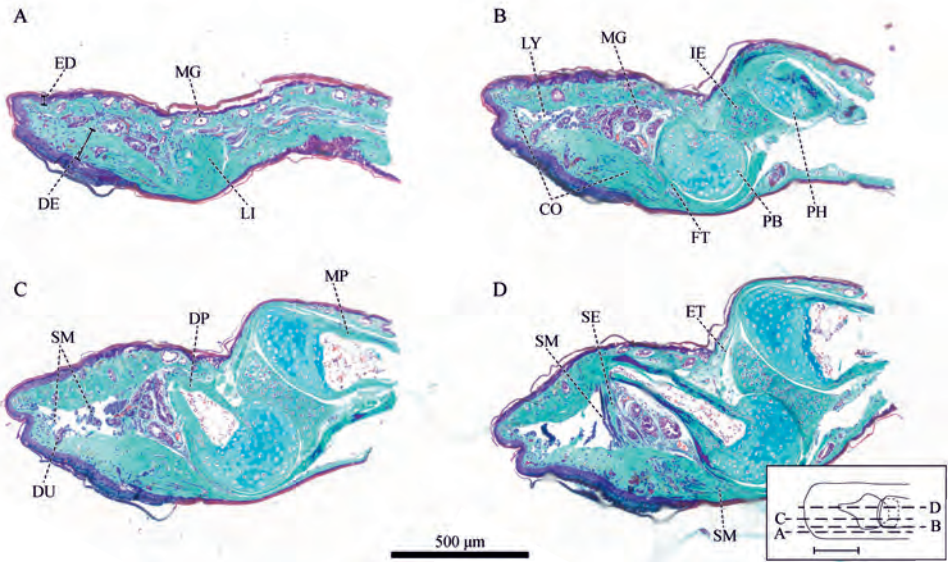


Figure 3.3 Series of sagittal sections of a digital pad of *Hyla cinerea* (Frog 3, digit H_I) from lateral to mid-sagittal stained as in Fig. 3.2 [see inset for the approximate locations and the extent of the adhesive ventral epidermis (solid line)] (A) close to the lateral epidermis, (B) through the lateral part of the base of the distal phalanx, (C) through the lateral part of the diaphysis of the distal phalanx, and (D) in an approximately mid-sagittal plane. Abbreviations as in Fig. 3.2 with the following additions: ET tendon of the extensor muscle, FT tendon of the flexor muscle, IE intercalary element, LI ligament, MP middle phalanx, PH head of the middle phalanx.

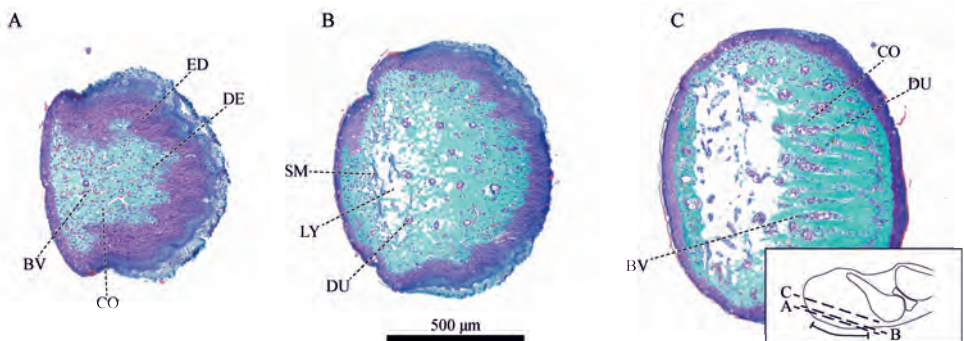


Figure 3.4 Series of horizontal sections of a digital pad of *Hyla cinerea* (Frog 3, digit F_I) from ventral to dorsal stained as in Fig. 3.2 [see inset for the approximate locations and extent of the adhesive ventral epidermis (curved solid line)] through (A) the apical dermis (stratum spongiosum), (B) the ventral part of the ventral collagen layer, and (C) the dorsal part of the ventral collagen layer. Abbreviations as in Figs. 3.2–3.3.

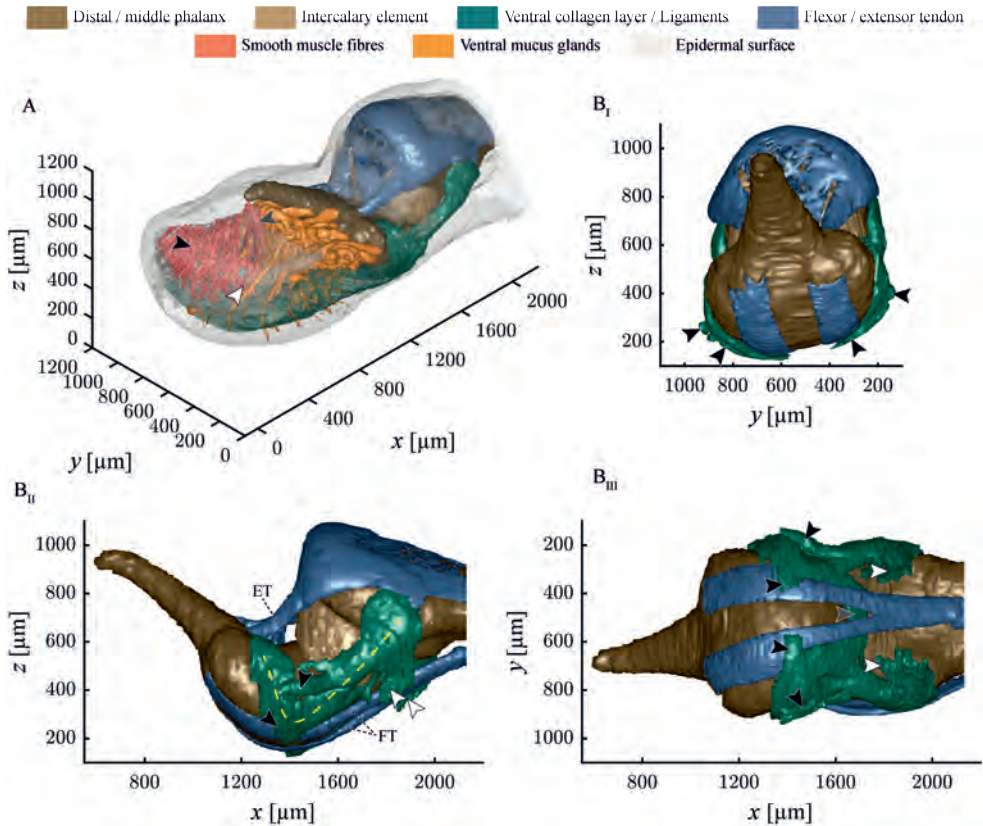


Figure 3.5 3-D visualisation of the structures of force transmission in a digital pad of *Hyla cinerea* (Frog 3, digit H_V). (A) 3-D view of the whole digital tip and internal structures. Only half of the approximately bi-laterally symmetric smooth muscle fibres (black arrowhead: thin muscle fibre bundle, grey arrow-head: thick muscle fibre bundle, white arrowhead: distal-cross-lateral muscle fibre) are shown. (B_I) Frontal, (B_{II}) lateral, and (B_{III}) ventral view of the joint region: The collateral ligaments (yellow dashed line) give rise to several side arms, which connect to the ventral cutis in the middle digital segment (white arrowheads) and the ventral collagen layer (black arrowheads). The two collateral ligaments are connected via a medial strand that also connects to the intercalary element (grey arrowhead). Abbreviations as in Figs. 3.2–3.4. x longitudinal spatial coordinate, y lateral spatial coordinate, z vertical spatial coordinate.

to its base. Whereas the *Tendo Superficialis* inserts nearly parallel to the surface of the base of the distal phalanx, the extensor tendon attaches at an angle of ca. 45°.

Two collagenous ligaments (referred to as collateral ligaments) strengthen the distal interphalangeal joint ventrolaterally (Fig. 3.5B_{II,III}). Each collateral ligament attaches laterally to the head of the middle phalanx, traverses past the intercalary element towards the ventrolateral side of the base of the distal phalanx, and from there towards the dorsolateral side of the base of the distal phalanx. From proximal to distal, various side arms branch off from the collateral ligaments (Fig. 3.5B_{II,III}): (i) several side arms run towards the ventral cutis of the middle digital segment, (ii) below the intercalary element, the two main arms connect dorsally of the flexor tendon with each other via a medial running side arm, which also connects to the intercalary element, and (iii) below the base of the distal phalanx some branches run towards the ventral collagen layer. Low contrasts between neighbouring collagen strands impede the exact identification of the trajectories and attachment points of the collateral ligaments and the ventral collagen layer.

3.3.2 Internal structures of the digital tip

3.3.2.1 Ventral epidermis

The ventral epidermis is thicker than the dorsal one (Fig. 3.6A), stratified, and consists of up to 6 cell layers (Fig. 3.6B), numbered I to VI from basal to apical (Ernst, 1973a). Whereas the cells in layers I (i.e. the germinal layer) and II are shaped and arranged irregularly, the cells in layers III to VI are columnar. The cells of layers V and VI (i.e. the superficial layer) differ morphologically and arguably also functionally from the deeper cell layers: The cell bodies are skewed such that the apical cell surface is positioned distally to the basal one. Reddish staining indicates the presence of fibrous structures that connect broadly to the apical cell surface and merge into a thin bundle running towards the proximal-basal cell surface. These structures are known to be tonofibrils (Ernst, 1973a; Nakano & Saino, 2016). The basal part of layer VI contains less tonofibrils than in layer V, presumably due to physiological changes impending ecdysis (Ernst, 1973a).

3.3.2.2 Collagenous structures

The digital tip of *H. cinerea* includes several networks of collagen fibres with approximately isotropic fibre arrangements. The reticular collagen of the basement membrane (Fig. 3.6B) connects to the dermal stratum spongiosum (Fig. 3.3). Fine collagen fibres without a clear preferential orientation traverse the interglandular space. At the borders of the gland space, these fibres connect with the surrounding dermal connective tissue (Fig. 3.7B).

The pad also contains collagenous structures with distinctly anisotropic fibre arrangements. The thin septum, which compartmentalises the subdermal volume into the

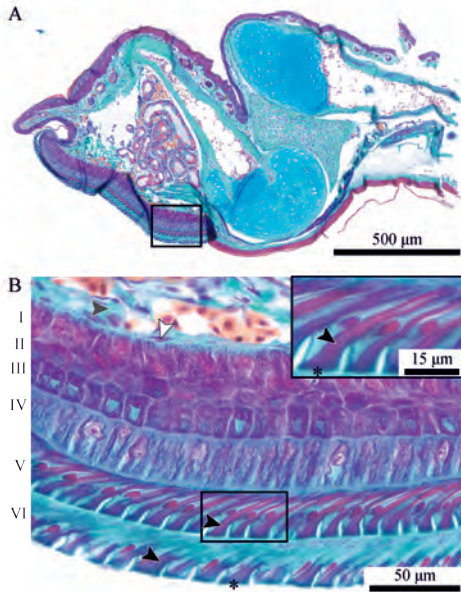


Figure 3.6 Approximately mid-sagittal section through a digital pad of *Hyla cinerea* (Frog 2, digit H_I) stained with Crossmon's light green trichrome including Mayer's haematoxylin and Alcian blue. (B) Magnified view of the ventral epidermis (see box in A) containing tonofibrils (reddish; black arrowheads), reticular cells (white arrowhead), and reticular connective tissue (grey arrowhead). Layer numbering after Ernst (1973a).

gland and lymph space (Fig. 3.7C), is fan-shaped and consists of collagen fibres extending radially from the distal tip of the distal phalanx towards the ventral cutis. Collagen fibres connecting the dorsal and ventral cutis form the lateral fractions of the septum. The plane, in which the septum fibres run, is rotated by ca. 15–25° about the transverse pad-axis, such that the dorsal tip of the septum is located distally from its ventral attachment.

The ventral collagen layer is the most prominent collagenous structure in the digital pads of *H. cinerea* (Fig. 3.8). This layer fills the space between ventral epidermis, gland space, and ventral surface of the base of the distal phalanx, converges below this base, and connects to the side arms of the collateral ligaments, as described above. Whereas the collagen layer is only ca. 10–20 µm thick below the base of the distal phalanx, it reaches a thickness of up to 290 µm below the gland space. Distally of the septum, the layer thickness decreases towards the distal pad end (down to ca. 60–120 µm). At the location of minimum thickness below the base of the distal phalanx, the ventral collagen layer has a transversal cross-sectional area in the order of 20 000–65 000 µm² (measured for digits F_{III}, H_{II}, and H_V of Frog 3).

The ventral collagen layer consists of regular collagen fibres oriented along the distal-proximal digit-axis. As seen in sagittal sections (Fig. 3.8C), the fibre trajectories are curved around the transverse pad-axis. The fibres are arranged in vertically separated bundles (Figs. 3.2D, 3.8A) and connect approximately perpendicular with the ventral basement membrane. The distal extension of the collagen fibres increases from ventral to dorsal.

Below the gland space, the ventral collagen layer is laterally separated into around 15–20 longitudinal ridges divided by troughs (Figs. 3.2B,C, 3.8A,B). These ridges are

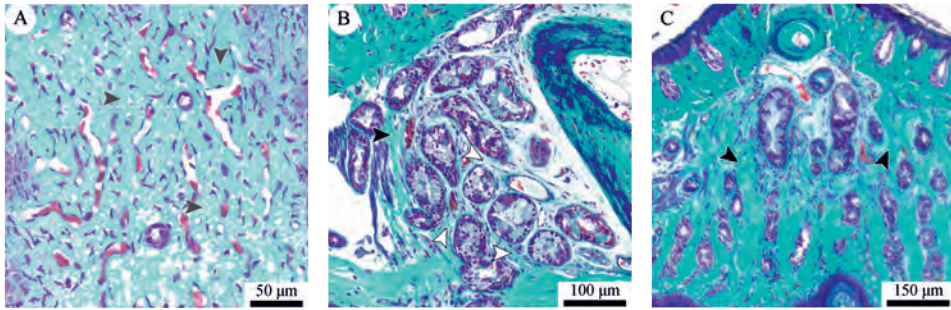


Figure 3.7 Collagen networks in a digital pad of *Hyla cinerea*. (A) Loose network of collagen fibres (light turquoise; grey arrowheads) in the ventral stratum spongiosum; horizontal section (Frog 3, digit F_I). (B) Loose collagen network in the gland space (white arrowheads) and collagenous septum (black arrowheads); sagittal section (Frog 3, digit F_{II}). (C) Septum (black arrowheads) separating the gland and lymph space; transverse section (Frog 3, digit F_{III}). Transverse and sagittal sections are oriented upright; in sagittal and horizontal sections, the distal digit side is on the left and at the top, respectively.

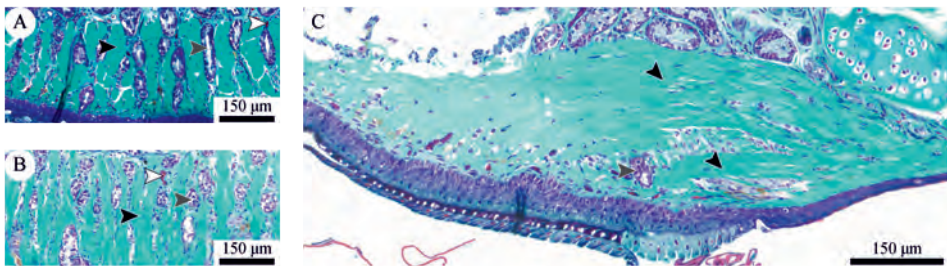


Figure 3.8 Ventral collagen layer and ridges (light turquoise; black arrowheads) in a digital pad of *Hyla cinerea* in (A) transverse (Frog 3, digit F_{III}), (B) horizontal (Frog 3, digit F_I), and (C) sagittal (Frog 3, digit F_{II}) section. The ridges consist of collagen fibres curved around the lateral pad axis. The troughs between the ridges are filled with mucus ducts (grey arrowheads) and blood vessels (white arrowheads). Section orientations as in Fig. 3.7.

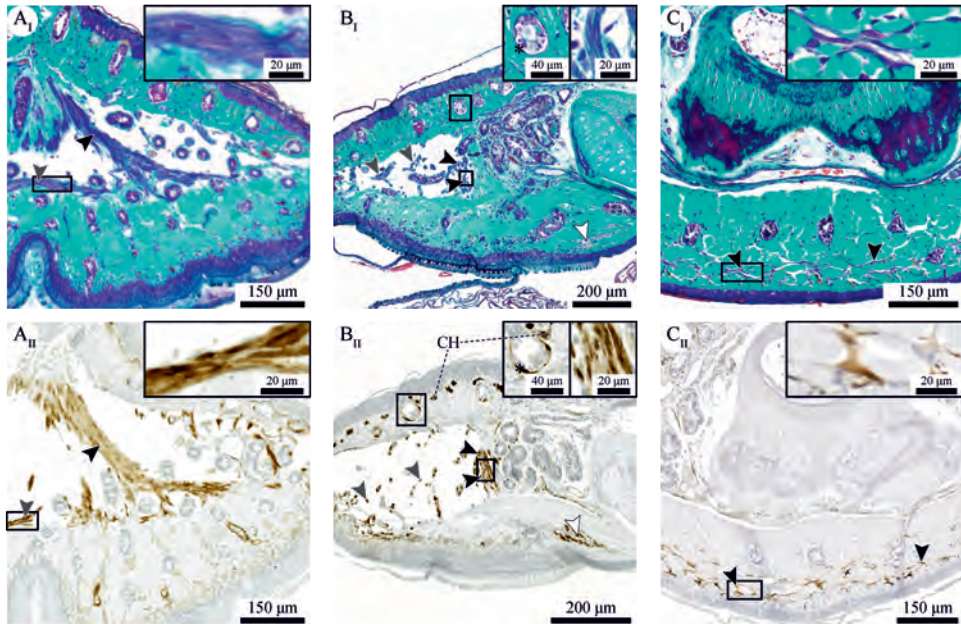


Figure 3.9 (I) Histochemically (purple-dark blue) and (II) immunohistochemically (brown) stained smooth muscle fibres in a digital pad of *Hyla cinerea*. (A) Two thick muscle fibre bundles (black arrowheads in A and B) run from the distal tip of the distal phalanx towards the ventral epidermis, and distal-cross-lateral muscle fibres traverse the lymph space above the ventral dermis (grey arrowhead in A); transverse section (A_I: frog 3, digit F_{III}, A_{II}: frog 1, digit F_{III}). (B) Thin muscle fibre bundles (grey arrowheads in B) traverse the lymph space ventrodorsally; sagittal section (B_I: frog 3, digit F_{II}, B_{II}: frog 1, digit H_I). Smooth muscle fibres also surround the mucus glands (stars). (C) A fine network of proximal-cross-lateral muscle fibres runs laterally through the ventral collagen layer below the widening base of the distal phalanx (black arrowhead in C and white arrowhead in B); transverse section (C_I: frog 3, digit F_{III}, C_{II}: frog 1, digit F_{III}). Section orientations as in Fig. 3.7. CH chromatophore.

not present in the proximal, expanding part of the collagen layer, and they gradually flatten and vanish towards the distal end of the digital pad. The troughs contain mucus ducts and blood vessels running from the gland space towards the ventral pad surface.

3.3.2.3 Muscular structures

The combination of histology, immunohistochemistry, and μ -CT reveals the presence of muscular structures in the digital pads of *H. cinerea* (Figs. 3.5A,3.9). Generally, these structures appear as (bundles of) long cellular fibres with diameters $\leq 5 \mu\text{m}$ containing elongated nuclei. Based on the positive immunohistochemical staining and the absence of striations, we identify the fibres as smooth muscle fibres.

Most muscle fibres are located in the distal lymph space. Two distinct bundles of muscle fibres (referred to as thick muscle fibre bundles) extend from the distal tip

of the distal phalanx ventrolaterally towards the ventral cutis (Fig. 3.9A,B). More distally, numerous finer muscle fibre bundles (referred to as thin muscle fibre bundles) traverse the lymph space in between dorsal and ventral dermis (Figs. 3.5A,3.9B). These bundles are occasionally interconnected within the lymph space and are, in general, rotated about the transverse pad-axis such that their dorsal attachment is located more proximally than their ventral attachment. The total horizontal cross-sectional area of all (thin and thick) muscle fibre bundles traversing the lymph space dorsoventrally ranges approximately from $7000\ \mu\text{m}^2$ to $14\,000\ \mu\text{m}^2$ (measured for digits F_I and H_V of Frog 3 and digit F_I of Frog 1). Additionally, several bundles of smooth muscle fibres run cross-laterally through the lymph space close to the ventral dermis (referred to as distal-cross-lateral muscle fibre bundles; Fig. 3.9A). These bundles appear mostly in the proximal half of the lymph space and connect to the dorsoventrally oriented fibres.

Another fine network of smooth muscle fibres is present in the proximal, widening part of the ventral collagen layer below the base of the distal phalanx. These fibres (referred to as proximal-cross-lateral muscle fibre bundles) run cross-laterally through the apical third to half of the collagen layer between the longitudinal bundles of collagen fibres. The position of this muscle fibre network along the longitudinal pad-axis coincides with the proximal begin of the pillar pattern on the ventral epidermis (Fig. 3.8C).

3.3.3 Topologically optimised pad model under shear load

The finite element analysis of a non-optimised, shear-loaded model of the ventral collagen layer in the digital pad of *H. cinerea* shows higher von Mises stresses between the longitudinal rows of holes piercing the model than in between the holes within a row (Fig. 3.10A_{II}). Overall, von Mises stresses decrease from proximal to distal. The maximum principal stress trajectories are curved around the transverse model axis and run from the most proximal model surface towards the ventral surface (Fig. 3.10A_{III}). The distal extension of the stress trajectories increases from ventral to dorsal.

Topological optimisation leads to distal flattening of the model and to the ‘carving out’ of longitudinal, curved ridges between the rows of holes. The ridges are separated by troughs running in line with the rows of holes (Fig. 3.10B_I). Von Mises stresses are lower in the material separating the holes within a row than in between the rows (Fig. 3.10B_{II}). The maximum principal stress trajectories follow the curved shape of the ridges (Fig. 3.10B_{III}).

3.4 Discussion

The dermal and subcutaneous structures in the digital pads of tree frogs have received little attention in previous research. To our knowledge, the latest reported efforts to analyse the internal morphology of the pads were made 90 years ago (Noble & Jaeckle,

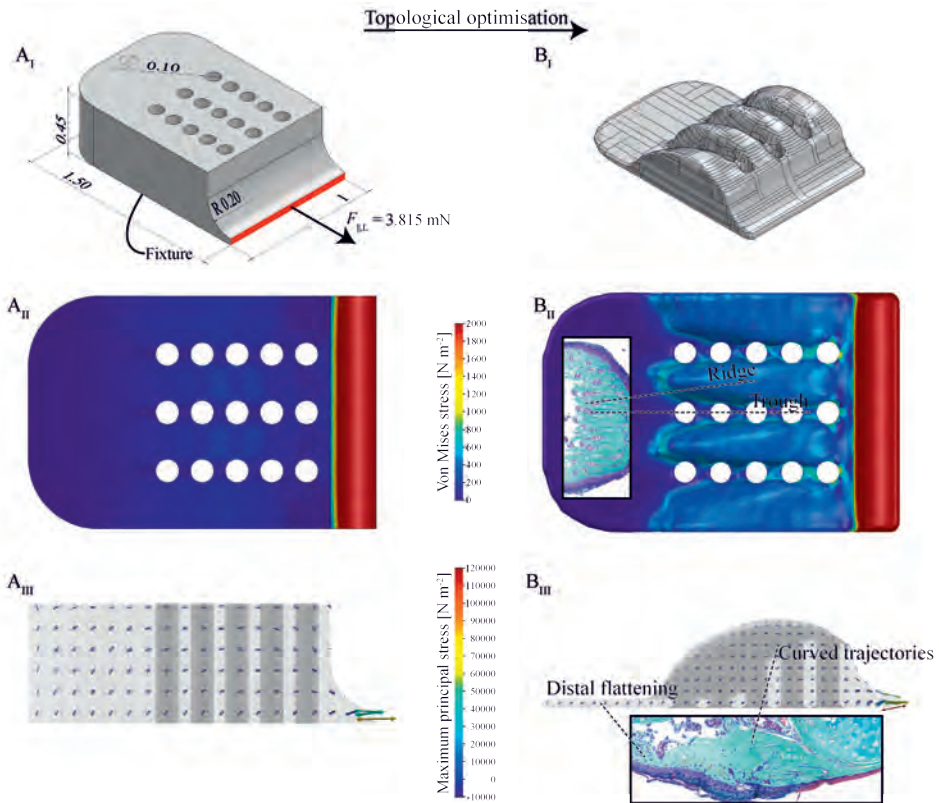


Figure 3.10 Topological optimisation of a shear-loaded pad model. (A) Non-optimised, ventrally fixed model (Young's modulus $E = 20$ MPa, Poisson's ratio $\nu = 0.33$) with the approximate shape and size of the ventral collagen layer in a digital pad under a shear load $F_{\parallel,L}$ acting on the proximal surface (red). (B) Topological optimisation leads to the formation of longitudinal ridges, to distal flattening, and to curved stress trajectories, similar to the ridges and the distribution as well as orientation of the collagen fibres, respectively, in the ventral collagen layer in the digital pads of *Hyla cinerea* (see insets). (I) Geometrical models in dorsoproximal view. The non-optimised model is dimensioned in mm. (II) Von Mises stresses (dorsal view) indicating regions of low mechanical loading. (III) Vector plot of the maximum principal stresses (lateral view) showing the trajectories of force transmission.

1928) while later studies focussed on bony and cartilaginous structures (Kamermans & Vences, 2009; Manzano *et al.*, 2007; Paukstis & Brown, 1991) and the superficial epidermis (Barnes *et al.*, 2013; Chakraborti *et al.*, 2012, 2014; Drotlef *et al.*, 2015; Ernst, 1973a; Green, 1979; Green & Simon, 1986; Hertwig & Sinsch, 1995; Mizuhira, 2004; Nakano & Saino, 2016; Nokhbatolfighahai, 2013; Scholz *et al.*, 2009). Overall, we find a number of tissues that were until now undescribed or have been characterised only partially. As we discuss below, some of these tissues clearly are involved in attachment, particularly offering pathways for the transmission of adhesive and frictional attachment forces. Although adhesion and friction are interdependent and some of the structures (e.g. the ventral epidermis) obviously are loaded during normal and shear loading, this may not be the case for all structures (e.g. the collateral ligaments). Moreover, some structures seem primarily involved in either normal (e.g. the septum) or shear loading (e.g. the ventral collagen layer). Therefore, we separately discuss the transmission of shear loads from the ventral epidermis via the ventral collagen layer to the collateral ligaments (Fig. 3.11A_I), the transmission of normal loads through the septum (Fig. 3.11B), and potential functions of the smooth muscle fibres in the digital pads of tree frogs (Fig. 3.11C).

3.4.1 Transmission of shear loads

During contact formation, mechanical loads are initially taken up by the ventral epidermis. Overall, the epidermal morphology found in this study agrees with the extensive description for the same species by Ernst (1973a). The presence of skewed cells in the second most apical layer of epidermal cells in *H. cinerea* (this study), *Litoria caerulea* (Nakano & Saino, 2016), and *Staurois parvus* (Drotlef *et al.*, 2015) contradicts cell skewing to be a mere age effect, as suggested previously (Ernst, 1973a; Schuberg, 1891). We hypothesise that the longitudinally skewed tonofibrils increase the stiffness of the apical epidermis during the transmission of shear loads deeper into the digital pad, possibly increasing friction by the distribution of mechanical stresses over a larger volume of pad material (Xue *et al.*, 2017) and maintaining the structural integrity of the epidermal surface. The dense ‘sponge-like’ network of tonofibrils within the apical regions of the superficial cells may locally increase the mechanical resilience of the epidermis surface (Drotlef *et al.*, 2015; Nakano & Saino, 2016). Moreover, the skewed tonofibrils may help to increase the pad-substrate contact area and adhesion during proximal pulling of the pad (Drotlef *et al.*, 2015), thus explaining the anisotropic friction measured in tree frogs (Chen *et al.*, 2015; Hanna & Barnes, 1991). Anisotropic friction has also been reported for smooth insect pads containing cuticle fibrils (Bullock *et al.*, 2008; Dirks *et al.*, 2012) as well as the skewed fibrous attachment systems of geckos (Autumn *et al.*, 2006) and technical adhesives (Murphy *et al.*, 2007; Xue *et al.*, 2014). Further work is needed to illuminate the function of the skewed tonofibrils in tree frog attachment.

The basal epidermal layers are in earlier stages of ecdysis than the apical ones and do not show the longitudinally skewed tonofibrils, as observed previously (Ernst, 1973a). We hypothesise that the basal epidermis forms a layer with (nearly) isotropic material

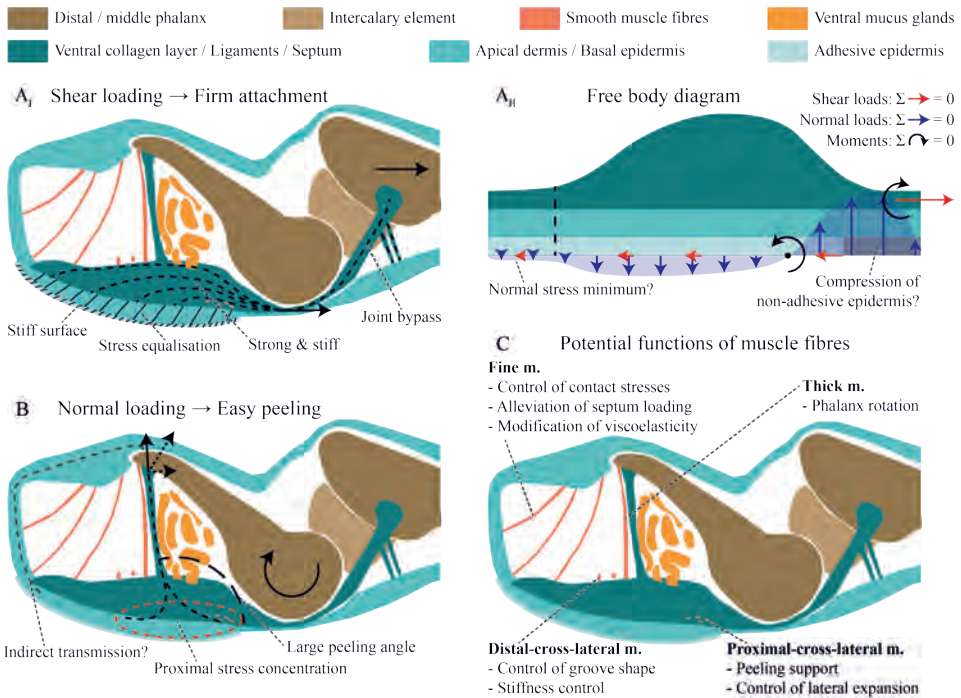


Figure 3.11 Schematic representation of a digital pad of *Hyla cinerea* in the midsagittal plane. (A_I) Proposed mechanism of shear load transmission during proximal pulling on the middle phalanx. (A_{II}) Equilibrium of the external forces and moments (free body diagram) acting on the shear-loaded ventral cutis and collagen layer with a hypothetical distribution of shear and normal loads acting on the ventral pad surface during steady attachment. In reality, shear loads will be orders of magnitude higher than normal loads. (B) Hypothesised mechanism of normal load transmission and the induction of peeling during extension of the distal phalanx. (C) Proposed functions of the smooth muscle fibres (m.).

properties, together with the approximately randomly oriented collagen fibres in the basement membrane and in the stratum spongiosum, which agree with general descriptions of these tissues in amphibians (Haslam *et al.*, 2014; Toledo & Jared, 1993). A direct fibrous connection between the epidermal surface and the skeleton concurs with the risk of local overloading of the fibres or of the contact interface, causing local material failure or peeling, respectively. We hypothesise that the (nearly) isotropic layer serves in the horizontal distribution and equalisation of mechanical stresses taken up from the superficial epidermis, hence reducing the risk of local peeling or material damage (Fig. 3.11A_I). Furthermore, deformations during loading arguably are higher in the softer basal epidermal layers than in the stiffer apical ones. Accordingly, the basal epidermis may contribute to viscoelastic shock absorption, as suggested for the strongly vascularised ventral stratum spongiosum (Barnes *et al.*, 2011). Further work, for example immunohistochemistry and transmission electron microscopy, is required to analyse the molecular and structural basis of anchoring of the ventral collagen layer in the basement membrane.

The ventral collagen layer arguably takes up mechanical loads from the more ventral tissues. The high level of structural ordering and the strong connectivity with more ventral structures suggest that the collagen layer is the dermal stratum compactum (Haslam *et al.*, 2014; Toledo & Jared, 1993). The laterally separated ridges in the ventral collagen layer in *H. cinerea* have been also reported for various other species (Noble & Jaeckle, 1928). Both the toe pad and the numerical model show a flat and relatively unperforated region distally of the (artificial) mucus ducts, laterally separated ridges in the duct region, and curved trajectories of the collagen fibres and the maximum principal stresses, respectively (Fig. 3.10B). These similarities between the morphology of the ventral collagen layer and the morphology predicted from the numerical pad model support our hypothesis that the collagen layer is adapted towards a high stiffness during proximal shear loading of the ventral pad surface. Material in the dorsodistal pad region contributes only little to the stiffness and hence is not required. Mucus glands, which are present in normal amphibian skin (Haslam *et al.*, 2014), would weaken the collagen layer mechanically. We argue that the ‘outsourcing’ of the glands is a consequence of the need for a high stiffness/strength of the collagen layer. In turn, the ridges result from the need for ducts connecting the glands with the ventral pad surface. It is unavoidable that also the ducts locally weaken the collagen layer. The serial duct arrangement arguably agrees with the lowest possible loss of material in the transverse plane and accordingly with the highest possible stiffness for a given transverse cross-sectional area. The material between the ducts within a row experiences relatively low mechanical stresses (Fig. 3.10A_{II},B_{II}), contributes only little to the stiffness, and therefore is recessed in the numerical model. The structural ‘pre-alignment’ of the unloaded collagen layer and epidermis suggests the importance of rapid mechanical functioning of these structures at the event of (shear-)loading. Comparing the morphology of the whole digital pad for different load cases such as shear and (compressive and tensile) normal loading, as done for the superficial epidermis (Nakano & Saino, 2016), may help to quantify the amount of deformation of the various internal pad structures and to illuminate the attachment-related functions of these structures.

The presence of ridges in the collagen layer is also practically relevant for future studies: the ridges presumably give the pad anisotropic material properties, with a lower stiffness in the transverse direction than along the longitudinal pad axis. Accordingly, the pad deformation during (de-)hydration, for example by vacuumisation in electron microscopy, may be anisotropic, which should be considered in the quantification of geometrical parameters of the superficial epidermal cells. In microindentation-studies, variations of pad parameters such as stiffness and work of adhesion (Barnes *et al.*, 2011) may be partially related to the location of the indentation with respect to the ridges.

Proximally, the ventral collagen layer connects via the collateral ligaments with the middle phalanx, as described by Noble & Jaeckle (1928). We propose that these ligaments represent a bypass in force transmission around the distal joint complex: a shear load acting on the ventral collagen layer is transmitted via the ligaments directly to the middle phalanx and further. Hence, force transmission is achieved

quickly and without the need of stabilising the distal phalanx by muscle activity. The ligament side arms connecting to the ventral cutis of the middle digital segment, which were observed also in *Osteopilus septentrionalis* (Noble & Jaeckle, 1928), may provide additional proximal ‘anchor points’ for the collateral ligaments, hence supporting the ligaments in load transmission.

Overall, the structures connecting the ventral pad surface with the middle phalanx are presumably adapted towards a high stiffness and strength as well as the equalisation of local stresses during shear loading (Fig. 3.11A_I). For example, we estimate that the ventral collagen layer can withstand a tensile load of 2.0–6.5 N before material failure, based on the measured transverse cross-sectional area and assuming a tensile strength of 100 MPa (Biewener, 2008). This is well above the maximum load of 1.27 N measured for single digital pads of *T. resinificatrix* (Bijma *et al.*, 2016). Considering peak shear stresses of up to 70 kPa (*Rhacophorus dennysi*; Endlein *et al.*, 2017) and 140 kPa (*L. caerulea*; Crawford *et al.*, 2016) withstood by the epidermal surface, and the high tensile strength of the collagen layer, we argue that the digital pads are adapted primarily towards the generation and transmission of frictional rather than adhesive forces. This agrees with the functional demands on the pad arising from the locomotion and habitat of tree frogs. During jumping and landing, terrestrial frogs regularly experience ground reaction forces in the range of 1–5 N (Nauwelaerts & Aerts, 2006). Frictional pad loading might be even higher and a high pad strength even more important when a tree frog falls in its arboreal habitat and has to hold to a leaf or twig (Bijma *et al.*, 2016) to avoid death. Next to frictional forces, it is unavoidable that adhesive forces also act on the ventral pad surface during shear loading (Fig. 3.11A_{II}): A proximal shear load acts not within the contact interface, but more dorsally, on the load-transmitting structures, hence creating a moment acting on the ventral pad surface. The generation of (compressive and tensile) normal attachment forces at the pad surface is unavoidable to counteract this moment during steady attachment (Fig. 3.11A_{II}). The spatial distribution of the normal mechanical stresses is still unclear, but they are arguably lower in magnitude than the occurring shear stresses.

Importantly, tree frogs have been observed to pull their digital pads proximally over the substrate after contact formation (Hanna & Barnes, 1991; Schuberg, 1891); this movement may also occur when pulling proximally on the flexor tendon (Schuberg, 1891). Endlein *et al.* (2017) measured increased adhesion and friction as a consequence of such pulling movements. In geckos and gecko-inspired adhesives (Bartlett *et al.*, 2012b), a similar correlation between attachment force and shear loading has been assigned to a scaling of the attachment force with the effective stiffness of the according adhesive systems. Although the physics of the scaling of attachment force with material stiffness are still under debate (Mojdehi *et al.*, 2017), the presence of a stiff load-transmitting structure connecting the adhesive surface with the skeleton both in the ‘dry’ digital pads of geckos (Russell, 1986) and the ‘wet’ pads of tree frogs suggests functional relevance of these internal structures in attachment. In general, an adhesive should be soft to facilitate the conformation to the substrate and the enlargement of the contact area (Bartlett *et al.*, 2012b). During adhesive loading,

however, a stiff material arguably promotes the rapid formation of a mechanical link between contact surface and substrate. Furthermore, a stiff material may facilitate the spatial distribution of contact stresses and hence could impede detachment. The digital pads of tree frogs (Fig. 3.11A_I) that are soft in normal loading (Barnes *et al.*, 2013, 2011; Kappl *et al.*, 2016) and stiff in shear loading (as suggested in this study) might make use of these effects. As discussed above, the basal epidermal cell layers form a nearly isotropic (and potentially soft) link in the transmission of shear loads, which may help to reduce peak loads. The epidermis is, however, quite thin. Also, the basal epidermal cells are interdigitated and connected via desmosomes with the basal dermal structures as well as with the more distal epidermal cells (Ernst, 1973a). Hence, the basal epidermis presumably does not have a strong adverse effect on the shear stiffening discussed here. Simultaneous measurements of the elastic modulus, compliance, and attachment force as well as a quantification of the spatial contact stress distribution at the pad-substrate interface are needed to analyse the shear stiffening of the digital pads of tree frogs.

3.4.2 Transmission of normal loads: the septum as an adaptation towards peeling?

As in shear loading, the normal adhesive loads acting on the ventral pad surface must be transmitted through the cutaneous and subcutaneous structures to the internal skeleton. As discussed above, the ventral cutis seems to be adapted primarily towards the transmission of shear rather than normal loads: The naturally skewed trajectories of the tonofibrils in the superficial epidermal cells negate potential adhesion-enhancing effects found in tree-frog-inspired adhesives including normally oriented fibres (Xue *et al.*, 2017).

Load transmission from the ventral cutis to the distal phalanx could be achieved by the collagenous septum separating the distal lymph space and the proximal gland space, and by the (thick and thin) smooth muscle fibre bundles traversing the lymph space dorsoventrally (Fig. 3.11B). To our knowledge, the septum has not been described previously although Schuberg (1891) mentioned the thick muscle fibre bundles that reinforce the septum distally. Clearly, the septum functions as a separating wall between gland and lymph space. However, it is unclear if the septum mainly serves for clustering the glands or for creating a ‘free’ lymph space. The septum has a horizontal cross-sectional area of ca. 6500–7500 μm^2 (measured for digits F_{III} of Frog 1 and H_V of Frog 3), which corresponds with a maximum tensile load before material failure of 0.65–0.75 N, assuming the same tensile strength as for the ventral collagen layer. In total, the dorsoventral muscle fibre bundles can only bear a drastically lower load of 2.8–5.6 mN (assuming a tensile strength of 0.2–0.4 MPa of skeletal muscle; Biewener, 2008), which suggests that these muscle fibre bundles—if involved at all—only have a supportive role in normal force transmission. In total, the muscle-collagen-complex should be well able to withstand the fraction of the approximate body weight acting on a single digit (i.e. 3.815 mN). However, (i) the tensile strength and the cross-sectional area mentioned above may have been overestimated for the relatively loose collagenous

septum and (ii) it is unclear, how loads are distributed between the stronger septum and the weaker muscle fibre bundles.

The muscle-septum-complex connects with the ventral cutis along a cross-lateral line that results from the intersection of the horizontal dermal plane and the septum plane. This locally confined conjunction of septum and cutis implies a local concentration of mechanical stresses during dorsodistal pulling on the septum as a result of extension or translation of the distal phalanx, which increases the probability of peeling at the proximal pad surface (Fig. 3.11B). In fact, a simplified FEA model shows (i) the highest normal contact stress at the proximal edge of the ventral contact surface of a pad model when loading the septum dorsodistally, and (ii) a higher averaged normal contact stress when loading the pad model via the septum compared to loading via the proximal end surface of the pad model (Fig. 3.11B; see Section 3.SI.8). Moreover, dorsodistal pulling on the septum coincides with a large peeling angle ($> 90^\circ$) relative to the substrate, reducing the pulling force needed for peeling according to peeling theory (Kendall, 1975). The induction of peeling by pulling proximally (via the collateral ligaments) on the ventral collagen layer, as suggested by Hanna & Barnes (1991), requires either a higher pulling force than for pulling on the septum, or an increase of the peeling angle by forward-rotation of the whole digit. Overall, these observations support the hypothesis that the septum represents an adaptation towards (rapid and efficient) detachment rather than for attachment (Fig. 3.11B). Peeling-induction via the septum may be especially important for the detachment of tree frogs in their typical resting position, when the limbs are positioned closely below the body (own observations but also Endlein *et al.*, 2012; Siedlecki, 1909) and large-scale limb movements may be hindered, in escape manoeuvres, when fast detachment is decisive, or during locomotion, when detachment should be as energy-efficient as possible. The hypothesised role of the septum in detachment could be tested, for example, by comparing the pull-off forces of an unmodified digital pad and a pad with disjointed septum; if peeling occurs via septum peeling, the original pad should detach more easily than the manipulated one.

Alternatively, normal force transmission might be achieved indirectly via the dorsal and lateral cutis. In *Hyla arborea* and *Rhacophorus reinwardtii*, the distal phalanx is known to bulge out the dorsal cutis (Schuberg, 1891; Siedlecki, 1910), which is also seen in the segmented digital tip of *H. cinerea* (Fig. 3.5A). In indirect force transmission, contact stresses would be automatically concentrated at the edge of the contact surface, making peeling more likely. If present at all, indirect force transmission is less favourable than a direct one.

3.4.3 Attachment-related functions of the smooth musculature

We find several muscular structures in the digital pads of *H. cinerea*, that are not mentioned in the current literature (Ernst, 1973b; Mizuhira, 2004). The primary locomotory musculature is located more proximally (Manzano *et al.*, 2008) and the muscle fibres in the digital tip most likely facilitate fine modulations of the digital tip

(Fig. 3.11C).

The two thick bundles of smooth muscle fibres mentioned above observed also in *H. arborea* (Schuberg, 1891) connect the distal tip of the distal phalanx with the ventral cutis. Schuberg (1891) argues that the muscle fibre bundles support the flexion of the distal phalanx and hence the exertion of pressure on the gland space and the secretion of mucus. The large moment arm created by the attachment of these muscle fibre bundles at the distal end of the distal phalanx with respect to the distal joint supports a function in phalanx flexion.

The thin bundles of smooth muscle fibres traversing the lymph space dorsoventrally have been described previously for *H. arborea* as connective tissue (Dewitz, 1883; Leydig, 1868; v. Wittich, 1854), although their muscular nature was later confirmed (Schuberg, 1891). The μ -CT-data show that these thin muscle fibre bundles do not connect to the distal tip of the distal phalanx, as stated previously, but to the dorsal dermis. Therefore, they presumably do not fulfil the same function as the thick muscle fibre bundles. Instead, the concerted activation and contraction of the thin fibres might enable the spatial control of contact stresses at the pad-substrate interface, thus promoting or avoiding peeling. Moreover, contraction of the thin muscle fibre bundles might alleviate the mechanical stresses in the two thick muscle fibre bundles and the septum, hence avoiding peeling via septum-loading as discussed above. Additionally, contraction of the fibres in the lymph space might allow for the active modification of the stiffness and hence the contact area (Afferante *et al.*, 2016), or of the viscoelasticity of the lymph space, which could act as macroscopic shock absorber with muscle-modulated dampening properties.

Distal-cross-lateral muscle fibres have also been found in other hylids by Schuberg (1891) and Gadow (1909), who suggested that these fibres control the shape of the longitudinal macroscopic grooves (Lee *et al.*, 2001; Nokhbatolfoghahai, 2013; Ohler, 1995) observed in the ventral pad surface.

The—to our knowledge previously undescribed—proximal-cross-lateral muscle fibres described in Section 3.3.2.3 might aid in controlling the lateral expansion of the ventral collagen layer during normal loading and hence the secretion of mucus. Alternatively, contraction of these fibres might increase contact stresses at the proximal edge of the contact surface. As discussed above, the pad starts peeling off proximally during regular walking (Hanna & Barnes, 1991) and local contact stress enhancement might ease this peeling motion.

Further research is needed to conclude on the function(s) of the smooth muscle fibres. Observing geometrical changes in the digital pad during local *in vivo in situ* electrostimulation of muscular or neural structures may help to elucidate the mechanical function of the contraction of specific muscle fibre groups. As a first step towards such an experiment, we suggest studying the innervation of the muscular structures in the digital tip (e.g. Is the nervous system sympathetic or parasympathetic? Are the neural and muscular structures arranged in motor units?). Clarifying the function(s) of the muscle fibres is not only relevant from a biomechanical viewpoint; understand-

ding the insertion of the muscle fibres at the distal phalanx may also generate new impulses in the phylogenetic classification of tree frogs based on the phalangeal morphology (Kamermans & Vences, 2009). The presence of muscular structures also has practical consequences: The (hemi-)spherical shape assumed in current contact mechanics models applied to tree frog attachment (e.g. the Johnson-Kendall-Roberts-model; Johnson *et al.*, 1971) may be an oversimplification of the digital pads of tree frogs, as these animals are potentially able to actively modulate the pad geometry as well as the distribution of contact stresses at the contact interface. In addition to common artifacts such as swelling/shrinkage of the samples, measurements on anaesthetised or euthanised animals may come with morphological artifacts due to the relaxed state of the muscles, that do not occur during *in vivo* measurements.

3.5 Conclusions

- The 3-D morphological analysis of the digital pads of the tree frog *Hyla cinerea* reveals a general bauplan, which comprises, among others, a ventral collagen layer, collateral ligaments, a septum compartmentalising the subcutaneous volume into a distal lymph space and a proximal gland space, and muscular structures.
- The ventral collagen layer consists of longitudinally oriented collagen fibres and forms, together with collateral ligaments, a mechanical link between the ventral pad surface and the middle phalanx during shear loading. Similarities in the morphology of the ventral collagen layer and a numerically optimised model suggest that the collagen layer is primarily adapted towards the transmission of shear loads. We estimate that the collagen layer can withstand a shear load of up to 6.5 N.
- The septum forms a mechanical link between the ventral cutis and the distal tip of the distal phalanx. Further work is required to test our hypothesis that dorsodistal pulling of the septum facilitates proximal peeling of the pad.
- The digital pads of *H. cinerea* (and of other species) contain smooth muscular structures besides the myoepithelial cells around the mucus glands. Numerous thin muscle fibre bundles and two thick muscle fibre bundles traverse the lymph space dorsoventrally. Furthermore, several muscle fibre bundles run cross-laterally through the lymph space as well as through the proximal-apical part of the ventral collagen layer. Further work is needed to conclude on the attachment-related function(s) of these muscular structures.
- Overall, this study adds to the knowledge on the digital pads of tree frogs, hence offering novel perspectives on the ecology, phylogeny, and evolution of anurans, as well as contributing to the functional understanding of tree frog attachment: We expect that the digital pads of tree frogs will provide inspiration for the design of biomimetic adhesives beyond geometrical modifications of the contact surface.



3.SI Supporting information

3.SI.1 Symbols and abbreviations

Table 3.SI.1 List of Roman (top) and Greek (bottom) symbols in alphabetical order.

Symbol	SI Unit	Description
E	$\text{Pa} = \text{kg m}^{-1} \text{s}^{-2}$	Young's modulus
$F_{\parallel, \perp}$	$\text{N} = \text{kg m s}^{-2}$	Shear load
x	m	Longitudinal spatial coordinate
y	m	Lateral spatial coordinate
z	m	Vertical spatial coordinate
ν	-	Poisson's ratio
σ	$\text{Pa} = \text{kg m}^{-1} \text{s}^{-2}$	Yield strength
$\bar{\sigma}_{\perp}$	$\text{Pa} = \text{kg m}^{-1} \text{s}^{-2}$	Mean normal contact stress

3.SI.1.1 List of abbreviations

Table 3.SI.2 List of abbreviations of morphological (top) and other (bottom) terms in alphabetical order.

Abbreviation	Description
BV	Blood vessel
CH	Chromatophore
CO	Collagen tissue
DE	Dermis
DP	Distal phalanx
DU	Mucus duct
ED	Epidermis
ET	Tendon of the extensor muscle
F	Forelimb
FT	Tendon of the flexor muscle
H	Hindlimb
IE	Intercalary element
LI	Ligament
LY	Lymph space
m. / mm.	Muscle / muscles
MG	Mucus gland
MP	Middle phalanx
SE	Septum
SM	Smooth muscle
PB	Base of the distal phalanx
PH	Head of the middle phalanx
ca.	circa
FEA	Finite Element Analysis
μ -CT	Synchrotron micro-computer-tomography
PTA	Phosphotungstic acid
stl	SurfaceTessellationLanguage

3.SI.2 Housing conditions

The animals were housed in $0.6 \cdot 0.6 \cdot 1.2 \text{ m}^3$ (width · length · height) large terraria, with six frogs per terrarium, at the CARUS research facility at WUR. The terraria were enriched with plants (*Ficus spec.*) and a scaffold of polypropylen-pipes. The temperature was kept at 24–26 °C with heating mats and the relative air humidity was kept at 45–85% with a semi-automatised sprinkler system using demineralised water (Bitter Watertreatment, The Netherlands). The frogs were kept at a 12 h : 12 h dark-light-cycle and fed 2–3 times per week with 3–5 live crickets enriched with vitamin/mineral powder (Dendrocare, AmVirep, Netherlands) per individual; water was supplied *ad libitum*. The room air was filtered for pathogens using an air purifier (WINIX U300, Winix, USA). The frogs were monitored daily for feeding state and abnormal behaviour.

3.SI.3 μ -CT image analysis

1. Median filter
 - (a) Radius = 1
2. Grey-value thresholding
 - (a) Filter band: 32772–35779
3. Grey-value thresholding
 - (a) Equalisation = 1
 - (b) Number of bins = 100
 - (c) Number of ignored bins = 10

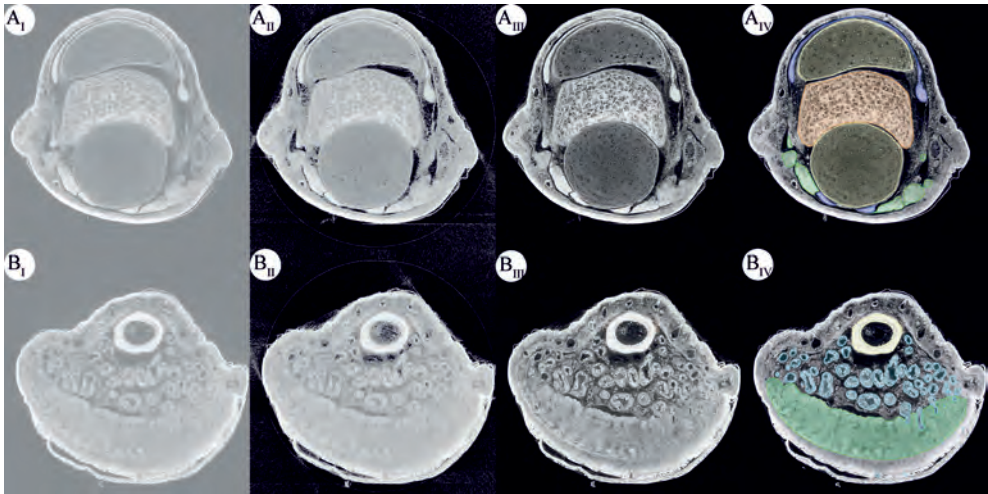


Figure 3.SI.1 The steps of image processing for transverse sections through a digital pad of *Hyla cinerea* (A) in the joint region and (B) through the digital gland space. (I) Original image, (II) background removal by grey-value-thresholding, (III) histogram equalisation, and (IV) segmentation (yellow: distal and middle phalanx, orange: intercalary element, light blue: ventral mucus glands, dark blue: tendons of the flexor and extensor muscles, green: ligaments and ventral collagen layer).

3.SI.4 Histochemical protocols

3.SI.4.1 Embedding protocol

- 1) Fixation and storage (see main text)
 - 2) Rehydration
 - a. Transfer of sample to 35% ethanol
 - b. Distilled water
 - c. Short submerging of sample in lukewarm 1% agarose gel
- 2 min

- 3) Agarose embedding
 - a. Orientation of sample in lukewarm 1% agarose gel using a SZ-4 stereo microscope (Olympus, Japan)
 - b. Hardening of agarose on a cold glass plate
 - c. Cutting of agarose block according to desired cutting plane
- 4) Tissue-processing
 - a. Dehydration
 - i. 70% ethanol overnight
 - ii. 80% ethanol 1 h
 - iii. 90% ethanol 45 min
 - iv. 96% ethanol 30 min
 - v. 100% ethanol 20 min
 - vi. 100% ethanol 20 min
 - b. Cleaning
 - i. Xylene bath 3 · 1 h
- 5) Paraffin embedding
 - a. Paraffin (KP Paraclean) 1 h
 - b. Vacuum oven 3 · 15 min

3.SI.4.2 Staining solutions

Acetic acid (3%)

Acetic acid, glacial	3 mL
Distilled water	97 mL

Alcian blue (pH 2.5)

Acetic acid, glacial	3 mL
Distilled water	97 mL
Alcian Blue GS	1 g

Mayer's Haematoxylin

Haematoxylin	1 g
Distilled water	1000 mL
Sodium iodate	0.2 g
Potassium Alum	50 g
Chloral hydrate	50 g
Citric acid	1 g

Fuchsin/Orange G

Acid fuchsin	1.3 g
Orange G	1 g
Acetic acid, glacial	5 mL
Distilled water	500 mL
Thymol	0.33 g

Phosphomolybdic acid (5%)

Phosphomolybdic acid	25 g
Distilled water	500 mL



Light green (1%)

Light green SF	10 g
Acetic acid, glacial	10 mL
Distilled water	1000 mL

3.SI.4.3 Staining protocol

1)	Deparaffinisation and rehydration to distilled water	
2)	Acetic acid (3%)	3 min
3)	Alcian blue (pH 2.5)	30 min
4)	Rinsing in Acetic acid (3%)	20–30 s
5)	Rinsing in distilled water	2 · 2 min
6)	Mayer's Haematoxylin	7 min
7)	Rinsing in running tap water	10 min
8)	Fuchsin/Orange G	1 dip
9)	Rinsing in distilled water	2 min
10)	Phosphomolybdic acid (5%)	4 min
11)	Rinsing in distilled water	2 min
12)	Solution Light green (1%)	10 min
13)	Rinsing in distilled water	2 · 1 min
14)	Washing in 100% ethanol	4 · 2 min
15)	Clearing with Xylene	3 · 2 min
16)	Mounting with DPX	

3.SI.5 Immunohistochemical protocols

3.SI.5.1 Staining solutions

Peroxidase removal and blocker

TBS-triton

Sodium chloride	8.8 g
Tris(hydroxymethyl)aminomethane (TRIS)	6.06 g
Triton 10%	2.5 mL
Hydrochloric acid (HCl)	until pH = 7.4 is reached
Distilled water	fill up to 1000 mL

TBS-triton / H₂O₂

TBS-triton	222.75 mL
H ₂ O ₂ 30%	2.25 mL

Blocker - goat serum 10% / BSA 1%

TBS-triton	3200 µL
Goat serum	400 µL
BSA-c 10%	400 µL

Goat serum 2%

TBS-triton	8820 µL
Goat serum	180 µL

Peroxidase removal and blocker

1st antibody -

anti- α -smooth-muscle-actin (1:400)

Goat serum 2%	3990 μ L
anti- α -smooth-muscle-actin	10 μ L

2nd antibody - goat-anti-mouse/HRP (1:100)

Goat serum 2%	3960 μ L
GaM/HRP	40 μ L

DAB-stain

TRIS-HCl

TRIS	6.06 g
HCl	until pH = 7.6 is reached
Distilled water	fill up to 1000 mL

3,3'-diaminobenzidine(DAB)-stain

TRIS-HCl	4500 μ L
DAB stock (5 mg mL ⁻¹)	500 μ L
H ₂ O ₂ 30%	5 μ L

3.SI.5.2 Staining protocol

1)	Deparaffinisation and rehydration to distilled water	
2)	TBS-triton / H ₂ O ₂	20 min
3)	Washing in TBS-triton	2 · 5 min
4)	Blocking with Blocker - goat serum 10% / BSA 1% in TBS-triton	30 min
5)	Incubation in 1st antibody - anti- α -smooth-muscle-actin (1:400)	overnight at 4 °C
6)	Washing in TBS-triton	3 · 5 min
7)	Incubation in 2nd antibody - goat-anti-mouse/HRP (1:100)	45 min
8)	Washing in TBS-triton	2 · 5 min
9)	Washing in TRIS-HCl	2 · 5 min
10)	Staining with 3,3'-diaminobenzidine(DAB)-stain	8 min
11)	Rinsing in running tap water	10 min
12)	Mayer's haematoxylin staining	1 min
13)	Rinsing in running tap water	10 min
14)	Dehydration (70% to 100% ethanol)	
15)	Clearing with Xylene	3 · 2 min
16)	Mounting with DPX	



3.SI.6 Interdigital, interlimbal, interindividual, and intermethodological comparisons of the internal pad morphology

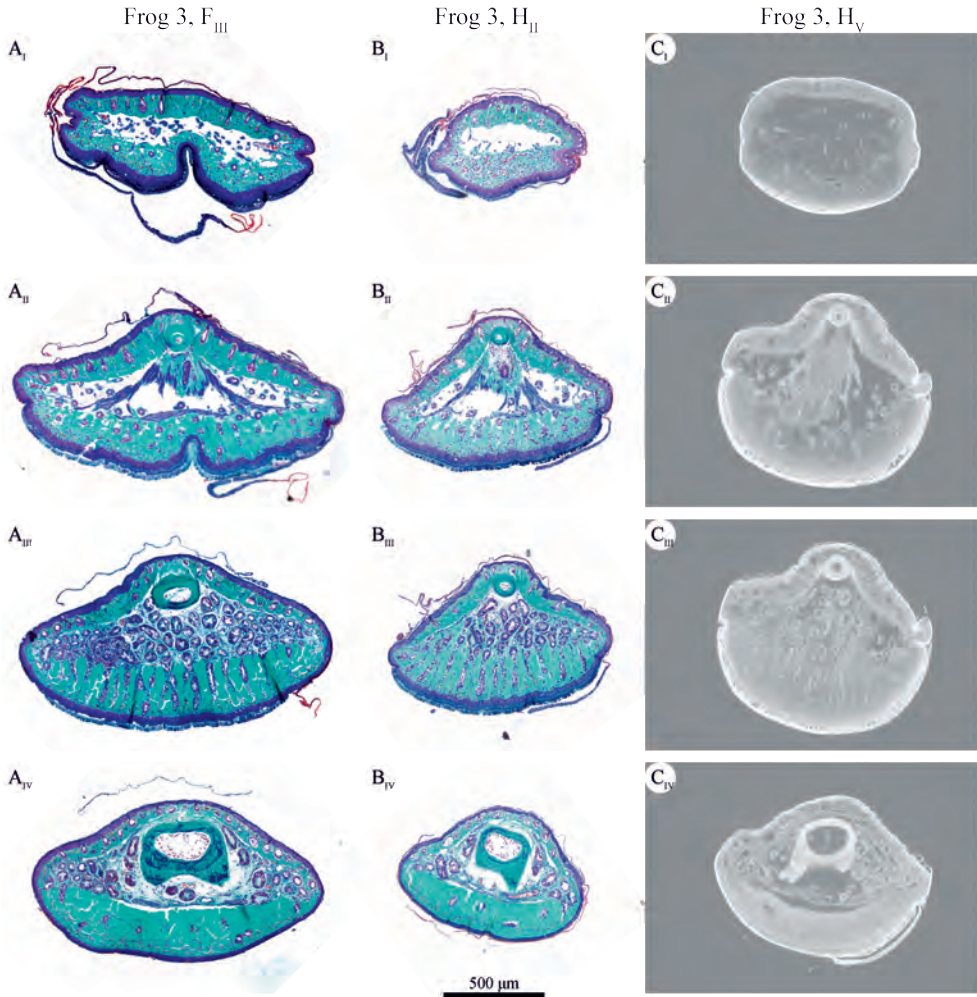


Figure 3.SI.2 Series of transverse sections through digital pads of the (A) fore- and (B,C) hindlimbs of *Hyla cinerea* obtained by (A,B) histology and by (C) μ -CT, from distal to proximal. The histological sections were stained with Crossmon's light green trichrome including haematoxylin and Alcian blue.

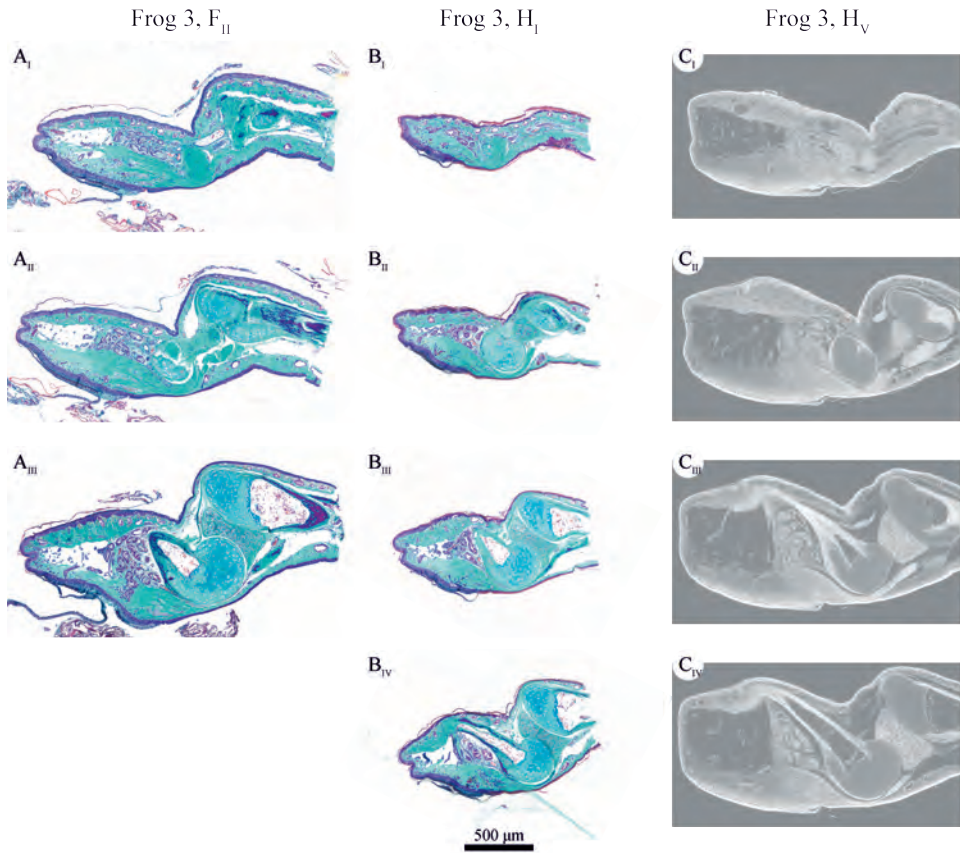


Figure 3.SI.3 Series of sagittal sections through digital pads of the (A) fore- and (B,C) hindlimbs of *Hyla cinerea* obtained by (A,B) histology and by (C) μ -CT, from lateral to mid-sagittal. The histological sections were stained with Crossmon's light green trichrome including haematoxylin and Alcian blue.

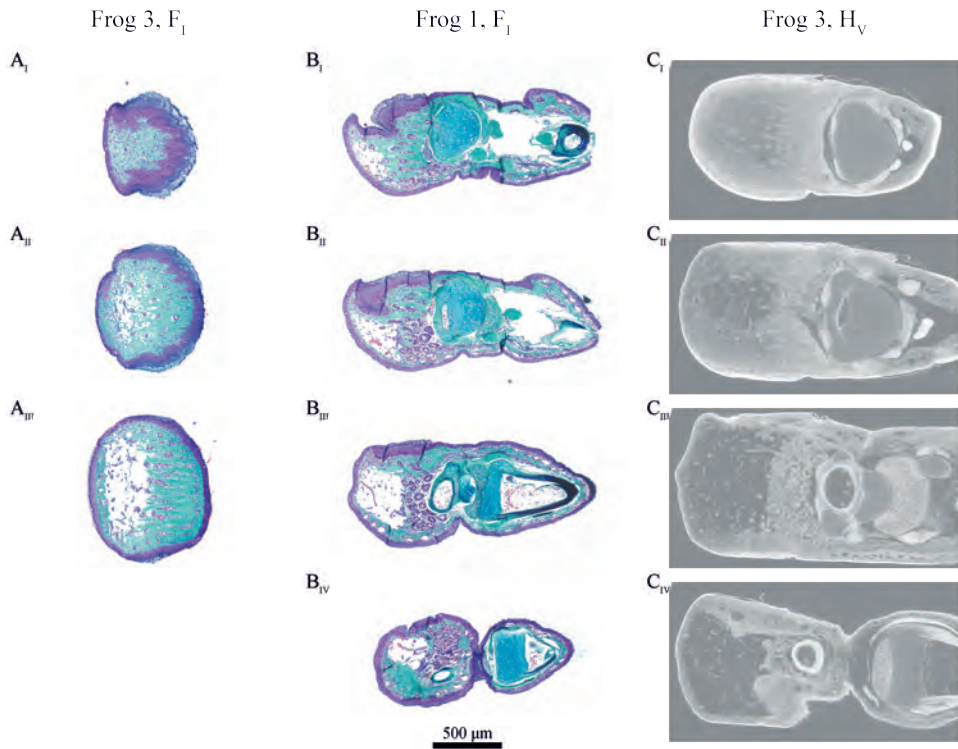


Figure 3.SI.4 Series of horizontal sections through digital pads of the (A) fore- and (B,C) hindlimbs of *Hyla cinerea* obtained by (A,B) histology and by (C) μ -CT, from ventral to dorsal. The histological sections were stained with Crossmon's light green trichrome including haematoxylin and Alcian blue.

3.SI.7 Intermediate topologically optimised geometries

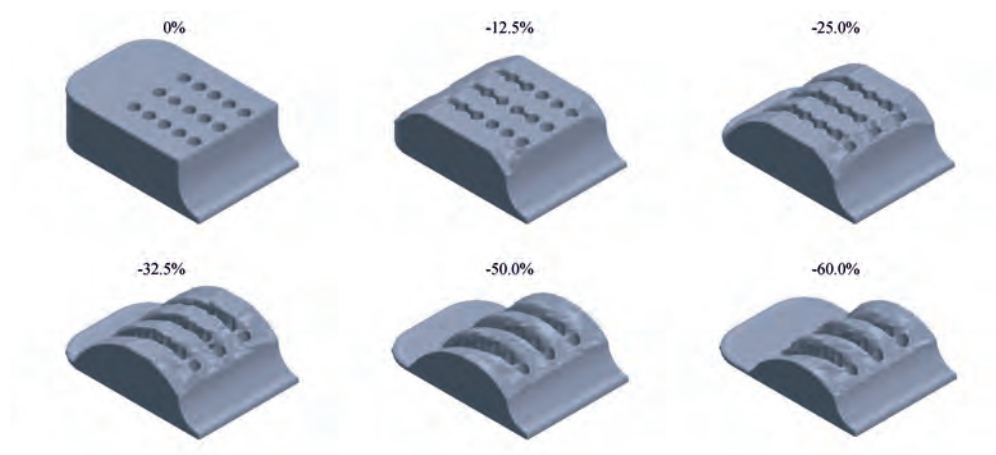


Figure 3.SI.5 Intermediate geometries resulting from the topological optimisation for increasing volume reduction.

3.SI.8 Modelling of the normal contact stresses during peeling

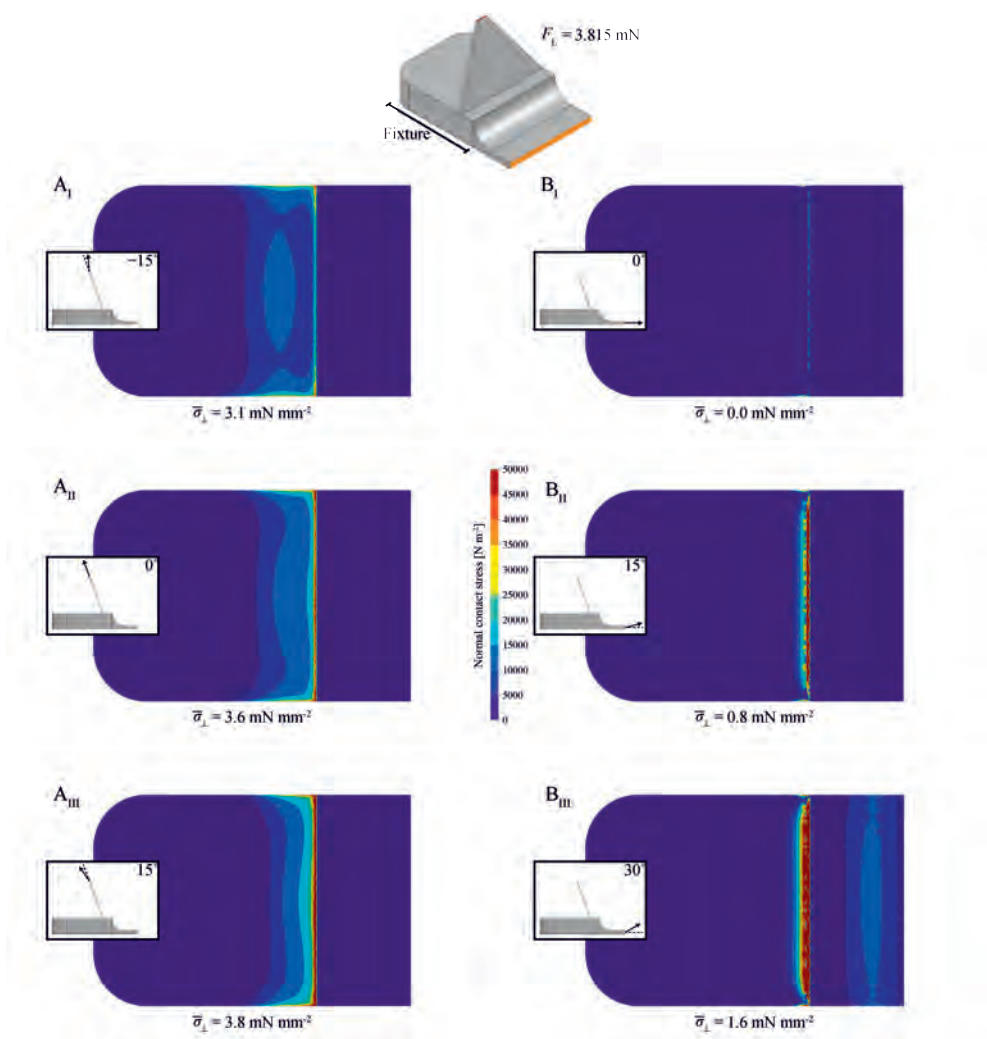


Figure 3.SI.6 Normal contact stresses in a simplified finite element model (element size = 15 μm) as prediction of the peeling stresses in the digital pads of tree frogs during (A) dorsodistal loading of the septum and (B) proximal loading of the ventral collagen layer. Displacement of the ventral model surface is prohibited as indicated by the black solid line; the proximal model section is not fixed. A load of 3.815 mN is applied on the dorsal surface of the septum (red surface in top model) and on the proximal surface of the ventral collagen layer (orange surface in top model), respectively, at three different angles with respect to the according surface normal. The surface plots show the spatial distribution and the average value of the normal contact stresses at the ventral model surface.

3.SI.9 Structures of force transmission in 3-D

Video 2.SI.1 The digital tip and internal structures of *Hyla cinerea* (Frog 3, digit H_V) in dorsolateral view rotated by 360° around the dorsal-ventral pad axis. Colour coding of the structures as in Fig. 3.5. Available in the published online version of this chapter.

Video 2.SI.2 The digital tip and internal structures of *Hyla cinerea* (Frog 3, digit H_V) in ventrolateral view rotated by 360° around the dorsal-ventral pad axis. Colour coding of the structures as in Fig. 3.5. Available in the published online version of this chapter.





[...] tree-frogs [...] are enabled to move on the perpendicular sides of polished objects by the agency of adhesive matter [...].

J. Blackwall, 1845

CHAPTER 4

Comparative and functional analysis of the digital mucus glands and secretions of tree frogs

Abstract

Background: Mucus and mucus glands are important features of the amphibian cutis. In tree frogs, the mucus glands and their secretions are crucial components of the adhesive digital pads of these animals. Despite a variety of hypothesised functions of these components in tree frog attachment, the functional morphology of the digital mucus glands and the chemistry of the digital mucus are barely known. Here, we use an interdisciplinary comparative approach to analyse these components, and discuss their roles in tree frog attachment.

Results: Using synchrotron micro-computer-tomography, we discovered in the arboreal *Hyla cinerea* that the ventral digital mucus glands differ in their morphology from regular anuran mucus glands and form a subdermal gland cluster. We show the presence of this gland cluster also in several other—not exclusively arboreal—anuran families. Using cryo-histochemistry as well as infrared and sum frequency generation spectroscopy on the mucus of two arboreal (*H. cinerea* and *Osteopilus septentrionalis*) and of two terrestrial, non-climbing frog species (*Pyxicephalus adspersus* and *Ceratophrys cranwelli*), we find neutral and acidic polysaccharides, and indications

This chapter has been accepted in revised form for publication as: LANGOWSKI, J.K.A., SINGLA, S., NYARKO, A., SCHIPPER, H., VAN DEN BERG, F.T., KAUR, S., ASTLEY, H.C., GUSSEKLOO, S.W.S., DHINOJWALA, A. & VAN LEEUWEN, J.L. (2019). Comparative and functional analysis of the digital mucus glands and secretions of tree frogs. *Frontiers in Zoology*.

for proteinaceous and lipid-like mucus components. The mucus chemistry varies only little between dorsal and ventral digital mucus in *H. cinerea*, ventral digital and abdominal mucus in *H. cinerea* and *O. septentrionalis*, and between the ventral abdominal mucus of all four studied species.

Conclusions: These results shed new light on the role of mucus glands and their secretions in tree frog attachment. The presence of a digital mucus gland cluster in various anuran families, as well as the absence of differences in the mucus chemistry between arboreal and non-arboreal frog species indicate an adaptation towards generic functional requirements rather than attachment-related requirements. Overall, this study contributes to the understanding of the role of glands and their secretions in tree frog attachment and in bioadhesion in general, as well as the evolution of anurans.

Keywords: *Hyla cinerea*; Macrogland; Mucosubstance; Lubrication; Wet adhesion; Cryo-histochemistry; Infrared spectroscopy; Sum frequency generation spectroscopy; Synchrotron micro-computer-tomography.

4.1 Background

Climbing is an important aspect of terrestrial locomotion, as it allows animals to avoid ground-dwelling predators and to access elevated habitats, but poses significant challenges (Cartmill, 1985), especially on wet and slippery surfaces. For successful climbing, many species from various clades have developed a wide range of attachment structures (Gorb, 2008). Studying the various bioadhesive solutions found in nature helps not only to unravel the evolution of the according species (Hertwig & Sinsch, 1995; Moen *et al.*, 2013), but also contributes to the understanding of the fundamental physics and chemistry of attachment, hence providing inspiration for the design of technical adhesives (von Byern & Grunwald, 2010).

Traditionally, biological adhesives have been categorised into ‘dry’ (e.g. the ‘hairy’ digital pads of geckos covered with numerous setae; Autumn *et al.*, 2002; Niewiarowski *et al.*, 2016) and ‘wet’ systems (e.g. the adhesive pads of various arachnids, insects, and amphibians such as tree frogs; Dirks & Federle, 2011; Wolff & Gorb, 2016). Wet adhesives are characterised by the presence of a liquid layer in between the adhesive organ and the substrate, which arguably increases the complexity of the attachment system compared to dry adhesives (Dirks, 2014; Dirks & Federle, 2011; Ditsche & Summers, 2014).

Tree frogs, with a snout-vent-length (ℓ_{SV}) of up to 13.5 cm and a body mass (m) up to 160 g, are among the largest terrestrial organisms having wet attachment organs (Endlein *et al.*, 2017; Tyler, 1968), and therefore an interesting group to study the attachment mechanisms in. Generally, amphibians have a moist skin (Toledo & Jared, 1995) that contains mucus, granular (also serous, poisonous, or venomous), mixed (also seromucous), and lipid glands, which secrete various muco- and other substances (Brizzi *et al.*, 2001; Clarke, 1997; Mills & Prum, 1984; Toledo & Jared, 1995);

see Section 4.SI.2 for the associated mucus nomenclature. The epidermal mucus is involved in various functions including thermoregulation, cutaneous gas exchange, reproduction, and defense against predators and pathogens (Clarke, 1997; Haslam *et al.*, 2014; Toledo & Jared, 1993, 1995).

The mucus on the adhesive digital pads has been suggested to (i) enable wet adhesion (i.e. capillary and hydrodynamic adhesion; Emerson & Diehl, 1980; Nachtigall, 1974), (ii) lubricate the skin (Federle *et al.*, 2006) and hence to avoid abrasive wear (Clarke, 1997; Langowski *et al.*, 2018a), (iii) avoid stiffening, the loss of conformability, and the resulting decrease in attachment performance on rough substrates, and (iv) allow the control of the relative contribution of capillary and van der Waals (vdW) forces to attachment by active changes in the mucus chemistry (Li *et al.*, 2018b).

Considering this wide range of potential functions of the mucus in tree frog attachment, surprisingly little is known on the chemical nature of the secreted mucus and on the morphology of the glands that produce it. The glands appear to be clustered in the basal-proximal dermis (Gaupp, 1904; v. Wittich, 1854). Since these early descriptions, the clustered ventral digital glands received to our knowledge little attention. Individual glands are tubuloalveolar with a single-layered cuboidal epithelium (Leydig, 1868; Noble & Jaeckle, 1928), covered by a layer of smooth muscle cells (Ernst, 1973b; Langowski *et al.*, 2018b; Schuberg, 1891). Their ducts open via pores on the ventral pad surface (Dewitz, 1883; v. Wittich, 1854). Although the glands have been described as mucus glands (Ernst, 1973b; Nakano & Saino, 2016; Noble & Jaeckle, 1928; Nokhbatolfoghahai, 2013; Welsch *et al.*, 1974), we are not aware of a detailed histochemical characterisation of their secretory content. Also, the exact gland morphology, the gland volumina (i.e. the available amount of mucus), and the distribution of the pores over the ventral epidermal surface (i.e. the spatial distribution of mucus on the pad surface) are unknown.

Here, we present a quantitative analysis of the mucus glands and their secretory products in the digital pads of tree frogs. We focus on *Hyla cinerea* (American green tree frog), one of the most frequently studied tree frog species (Emerson & Diehl, 1980; Ernst, 1973a,b; Linnenbach, 1985; Noble & Jaeckle, 1928). By combining synchrotron micro-computer-tomography (μ -CT) and cryo-histochemistry, we study the functional morphology of the dorsal and ventral glands in the digital pads in 3D. Furthermore, we analyse the digital mucus prior to secretion within the glands by cryo-histochemistry as well as after secretion by attenuated total reflectance-infrared spectroscopy (ATR-IR) and interface-sensitive sum frequency generation spectroscopy (SFG), aiming for a characterisation of the chemical composition of the mucus and of its interaction properties at the pad-substrate interface. With these techniques, we compare (i) the mucus from the ventral and the dorsal pad surface in *H. cinerea*, (ii) from the ventral pad surface and the ventral abdomen in the arboreal species *H. cinerea* and *Osteopilus septentrionalis* (Cuban tree frog), and (iii) the abdominal mucus of arboreal (*H. cinerea*, *O. septentrionalis*) and non-arboreal (*Ceratophrys cranwelli*, Pacman frog; *Pyxicephalus adspersus*; African bullfrog) frog species (Table 4.SI.3). Based on these analyses, we address the following questions:



- Do the ventral mucus glands and their secretions differ from the dorsal mucus and mucus glands in the digital pads? Does the ventral digital mucus differ from ventral abdominal mucus? And does the abdominal mucus differ between arboreal and non-arboreal frog species? Positive findings on these questions would support a functional specialisation of mucus and glands in tree frogs towards attachment.
- Can the ventral mucus glands produce enough mucus to fill the pad-substrate gap, which is imperative for wet adhesion, or do tree frogs rely on additional liquid sources?
- How are the ventral digital mucus gland pores distributed across the pad surface?

4.2 Results

4.2.1 Mucus gland morphology

The digital pads of *H. cinerea* contain several types of glands in different regions of the pad (Fig. 4.1). Dorsally, the dermal stratum spongiosum contains numerous ($n = 158$ for the left half of the dorsal digital cutis) ‘regular’ mucus glands that are evenly distributed across the whole dorsal dermis of the terminal digital segment, with a nearest-neighbour-distance (NND) of $57.3 \pm 10.2 \mu\text{m}$ (throughout the manuscript we report mean \pm standard deviation unless mentioned otherwise) and a density (ρ_d) of 191.3 gland openings per mm^2 . The dorsal glands have an approximately spherical body with a diameter (d_d) of $45.0 \pm 5.5 \mu\text{m}$ (assuming spherical gland volumes; Fig. 4.1) and a volume (V_{dg}) of $0.050 \pm 0.019 \text{ nL}$ (Fig. 4.SI.1), summing up to a total dorsal gland volume (V_d) of ca. 15.8 nL per pad. The dorsal gland volume per pad surface area (ρ_{dV}) is 9.5 nL mm^{-2} . The gland bodies connect to the dorsal pad surface via short straight ducts, which run approximately perpendicularly to the epidermal surface. Only a few granular glands are present in the dorsal dermis (identified according to Mills & Prum, 1984).

Ventrally, almost no glands are found in the stratum spongiosum. Only at the proximal, distal, and lateral edges of the adhesive pad, a few glands ($n = 12$) are present in the dermal stratum compactum (Fig. 4.1). The majority of mucus glands ($n = 49$) secreting to the ventral pad surface is located in the subdermal space delimited by the ventral (and ventrolateral) surface of the terminal phalanx, dorsal and ventral cutaneous collagen, and a collagenous dorsoventral septum running from the distal tip of the terminal phalanx to the ventral cutis (for a detailed description of these structures see Langowski *et al.*, 2018a). We refer to the combined gland bodies inside this space as ‘gland cluster’.

These ventral mucus glands are clearly tubular, with a mean length (ℓ) of $769.2 \pm 251.2 \mu\text{m}$. Their alveolar bodies are elongated—with the longitudinal gland

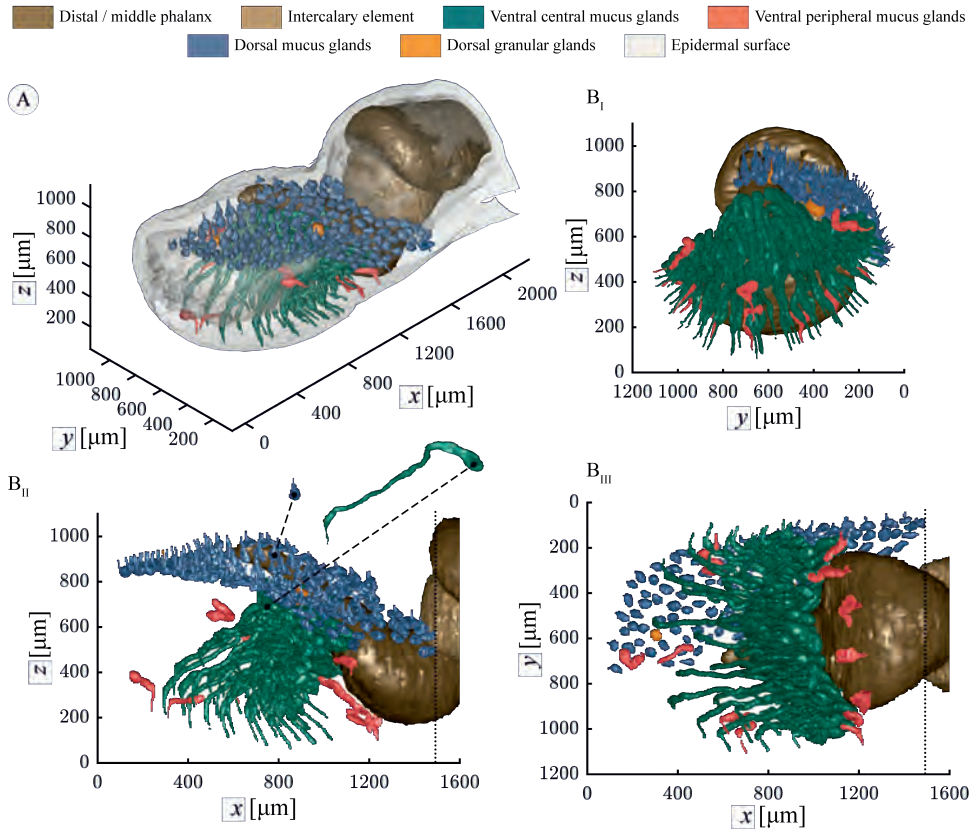


Figure 4.1 Mucus glands in a digital pad of *Hyla cinerea*. (A) 3D view of the whole digital tip. Only the left half of the approximately bi-laterally symmetric dorsal mucus glands is shown. (B_I) Frontal, (B_{II}) lateral, and (B_{III}) ventral view of the glands. The dotted lines indicate the proximal border of gland segmentation. x , y , z : longitudinal, lateral, and vertical spatial coordinates.

axis running from proximal-ventral towards distal-dorsal—and strongly convoluted. Each gland connects via a thin ($d \approx 30 \mu\text{m}$) duct to the ventral pad surface. Beginning from the gland body, most ducts turn towards the ventral epidermis just proximally of the dorsoventral septum (Fig. 4.1B_I). After piercing the septum, the ducts traverse the internal pad space at an angle of about 45° with respect to the horizontal plane towards the ventral surface. Upon entering the ventral pad epidermis, the ducts take another sharp turn, such that they run approximately normally towards the pad surface. A single gland has a volume (V_{vg}) of $0.78 \pm 0.28 \text{ nL}$, which is significantly higher than that of the dorsal ones (Two-sample t-test, $t = 18.24$, $p < 0.001$; Fig. 4.SI.1). The total ventral gland volume (V_{v}) sums up to 38.0 nL . The ventral gland pores have a NND of $120.8 \pm 27.1 \mu\text{m}$, and a gland density (ρ_{v}) of 52.7 pores per mm^2 pad surface area. This corresponds with a gland volume density (ρ_{vV}) of 40.8 nL mm^{-2} .

The dorsal pore NND, an inverse proxy of the pore density, decreases along the lateral pad axis towards the sagittal pad plane ($t[155] = 5.16$, $p < 0.001$), whereas such a

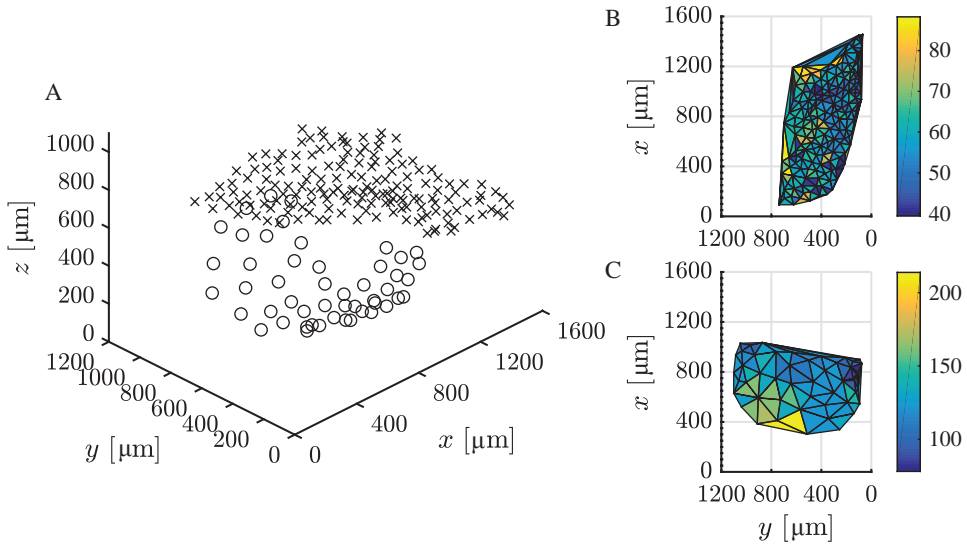


Figure 4.2 Spatial distribution of the digital mucus gland pores in *Hyla cinerea*. (A) 3D view of the dorsal (crosses; only the left half of the dorsal mucus pores is shown) and ventral (circles) pores on the digital pad cutis. (B) Spatial variation of the dorsal and (C) ventral mucus pore density, approximated by the nearest-neighbour-distance NND [colour-coded in μm], across the pad surface in dorsal view.

trend was not observed for the longitudinal pad axis ($t[155] = 1.82$, $p = 0.07$, Fig. 4.2). For the ventral glands, NND significantly increases along the lateral ($t[46] = 6.30$, $p < 0.001$) and decreases along the longitudinal ($t[46] = -9.55$, $p < 0.001$) pad axis. The change in NND, and hence in pore density, is stronger along the longitudinal ($0.11 \mu\text{m} \mu\text{m}^{-1}$) than along the lateral pad axis ($0.04 \mu\text{m} \mu\text{m}^{-1}$), with an increasing pore density towards the proximal end of the digital pad.

Immunohistochemical staining reveals that both dorsal and ventral glands are ensheathed by myoepithelial cells (Fig. 4.SI.3), visible as brown fibres containing elongated, relatively thick nuclei. The myoepithelial cells of the dorsal glands appear thicker and are more intensively stained than those of the ventral glands.

4.2.2 Mucus gland cryo-histochemistry

Crossmon trichrome staining in combination with Mayer's haematoxylin and Alcian blue (CRO; Fig. 4.3, Table 4.SI.4) reveals that the walls of the dorsal and ventral digital mucus glands consist of single layers of columnar mucocytes. The nuclei are located basally in the mucocytes. The apical cell portions are filled with cytoplasm and flocculent content. Locally, mucosubstance is observed within single mucocytes. The gland lumina are largely empty, but occasional turquoise staining of flocculent content (by Alcian blue) confirms the presence of mucosubstances. Staining intensity

is particularly high for the material in the ventral mucus ducts, suggesting local concentrations of mucus.

Periodic acid-Schiff staining (PAS; Fig. 4.3) results in violet staining of the mucosubstance described above. Similar observations are made for PAS staining following diastase treatment (PAS-D), hence excluding glycogen as sole source of positive PAS staining. The staining intensity of the mucosubstance is pH-dependent for Alcian blue: Whereas at pH = 1 (AB-1; Fig. 4.3) no or only faint blue staining is observed, at pH = 2.5 (AB-2.5) the mucosubstance in the lumen and in the mucocytes stains clearly turquoise.

All four protein stains resulted in negative or equivocal staining. Ninhydrin-Schiff staining (NIN; Fig. 4.3) generally is very faint for the mucus glands and their content, if compared for example to the ventral collagen layer or epidermal tissues. Also for Coomassie blue (COO; Fig. 4.3), the mucocytes and their secretory products stain only weakly compared to the ventral collagen and epidermal tissue. However, COO clearly accentuates the outlines of the glands. In contrast to NIN and COO, mercuric bromophenol blue (BRO; Fig. 4.3) causes strong, seemingly unselective staining of epidermal, dermal, and glandular tissues (greenish-blueish staining at pH = 3.8, BRO-3.8; blue staining at pH = 4.6, BRO-4.6). The flocculent mucosubstance stained by PAS and AB is not stained by BRO.

Finally, lipids were observed using Oil Red O (OIO; Fig. 4.3) only in the medullary cavity of the terminal phalanx and in a thin layer basally of the dorsal epidermis that coincides with the distribution of cutaneous melanophores.

4.2.3 Mucus chemistry

4.2.3.1 Bulk chemistry

ATR-IR spectroscopy allows the investigation of small amounts of mucus residues adsorbed to a silicon crystal due to a multiple bounce geometry. With a typical probe depth of ~ 250 nm, the signatures observed in the obtained ATR-IR-spectra reflect the bulk composition of the mucus.

The ATR-IR spectrum collected for the ventral digital mucus in *H. cinerea* shows amide I (~ 1640 cm^{-1}), amide II (~ 1540 cm^{-1}), and N-H stretch (~ 3280 cm^{-1}) peaks (Hopkins *et al.*, 1991; Omoike *et al.*, 2004) as well as a shoulder peak (~ 3060 cm^{-1}) assigned to aromatic C-H stretch vibrations, which indicate a proteinaceous component of the mucus (Fig. 4.4A). Further, the presence of aliphatic C-H stretch peaks (symmetric and asymmetric methylene and methyl stretches) in the hydrocarbon region (2800 – 3000 cm^{-1}), along with a shoulder around 3500 cm^{-1} assigned to OH vibrations, indicates carbohydrates, consistent with our histochemistry results. A similar spectral profile is observed for the ventral abdominal mucus. However, the relative composition of the proteinaceous mucus components could vary between the two as

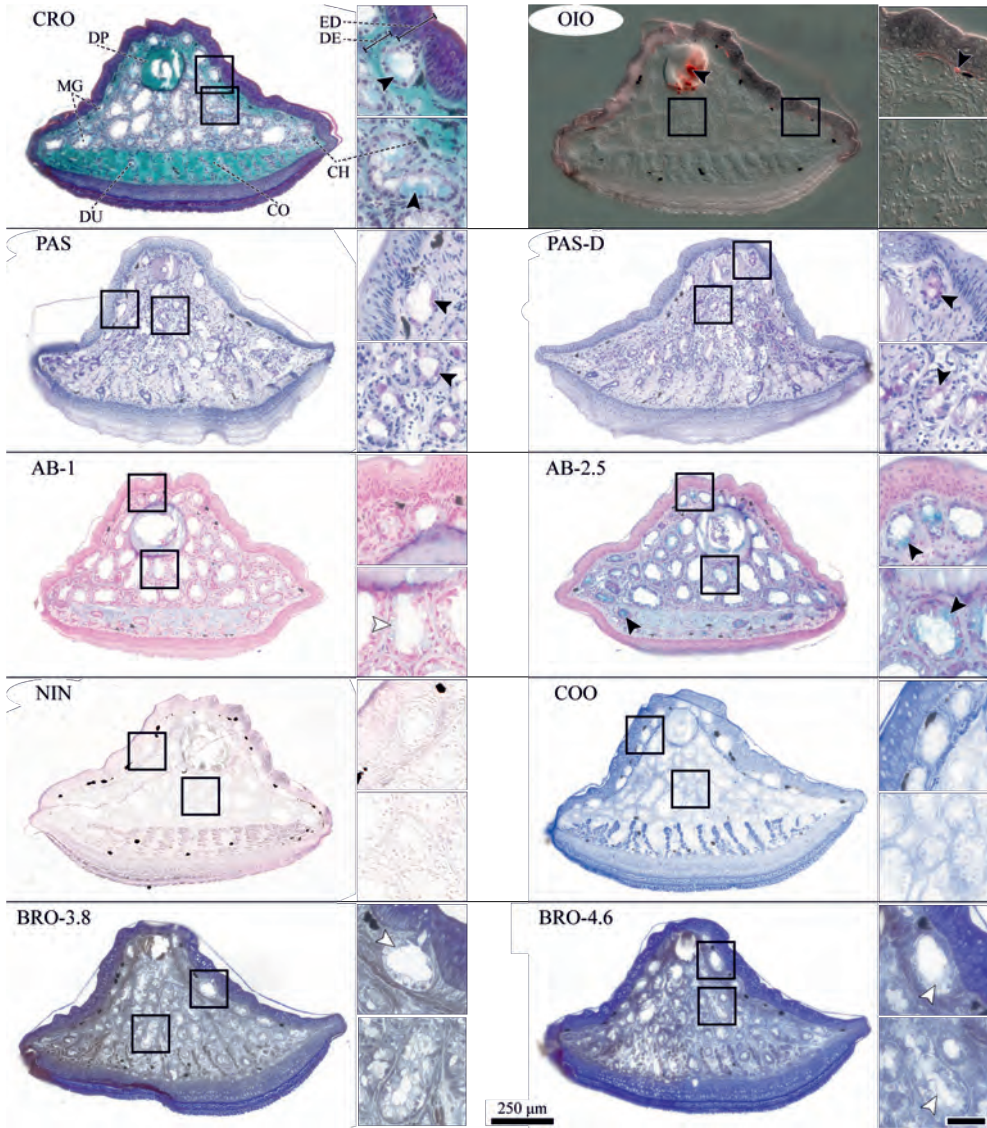


Figure 4.3 Brightfield micrographs of cryo-histochemically stained mucus glands in the digital pads of *Hyla cinerea*. Per staining, an overview of a whole representative transverse section through the gland space is shown. Insets: magnified views of a dorsal (top) and a ventral (bottom) mucus gland; black arrowheads: positive staining, white arrowheads: equivocal staining, Scale bar = 25 μ m; CRO Crossmons's light green trichrome including Mayer's haematoxylin and Alcian blue, OIO Oil Red O, PAS Periodic acid-Schiff, PAS-D Periodic acid-Schiff-Diastase, AB Alcian blue (pH = 1, pH = 2.5), NIN Ninhydrin-Schiff, COO Coomassie blue, BRO Mercuric bromophenol blue (pH = 3.8, pH = 4.6). CH Chromatophore, CO Collagen, DE Dermis, DP Digital phalanx, DU Mucus gland duct, ED Epidermis, MG mucus glands. OIO- and NIN-stained sections were imaged using differential interference contrast.

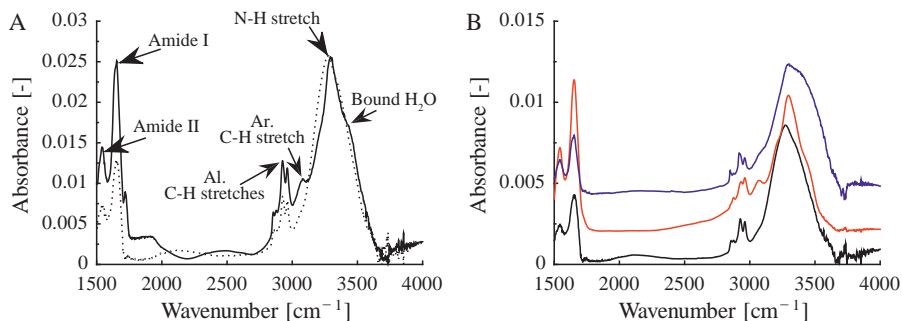


Figure 4.4 ATR-IR spectra of frog mucus. (A) Comparison of ventral digital (solid line) and abdominal (dotted line; absorbance scaled by $\times 3$) mucus in *Hyla cinerea*. Vibrational peaks attributed to amide, N-H stretch, aromatic C-H stretch and aliphatic C-H stretches were obtained. (B) Comparison of abdominal mucus spectra of the arboreal frog species *H. cinerea* (black) and *Osteopilus septentrionalis* (red; absorbance scaled by $\times 0.1$) as well as the terrestrial species *Ptychocheilus adspersus* (blue; absorbance scaled by $\times 0.5$). The spectra are offset along the ordinate axis in steps of 0.002 for clarity.

seen in the stronger N-H peak relative to hydrocarbon peak for the digital mucus compared to abdominal mucus.

To evaluate the similarity in chemistry between digital and abdominal mucus, we compared the peak area ratios of the amide I and amide II peaks of the ventral digital (1.52 ± 0.40 , $n = 4$) and abdominal (0.99 ± 0.03 , $n = 2$) mucus in *H. cinerea*, as this ratio is sensitive to the protein structure (Omoike *et al.*, 2004). However, no significant differences are found between the digital and abdominal median peak area ratios of the amide I and amide II peaks in *H. cinerea* (Wilcoxon rank sum test, ranksum = 7, $p = 0.20$) and *O. septentrionalis* (ranksum = 18, $p = 0.13$, Fig. 4.SI.4), confirming a similarity in the chemical nature of the digital and abdominal mucus in both tree frog species.

Finally, comparison of the ATR-IR spectra of the ventral abdominal mucus across the arboreal frog species *H. cinerea* and *O. septentrionalis* as well as the terrestrial species *P. adspersus* suggests that the mucus chemistry is similar in all tested species (Figs. 4.4B, 4.SI.4).

4.2.3.2 Surface chemistry

Residues of (digital or abdominal) mucus on a sapphire substrate were investigated using SFG spectroscopy. Contrasting to ATR-IR, SFG has a probe depth of only a few nanometers, making it a highly surface-sensitive tool for monitoring interfacially ordered molecular groups.

In the hydrocarbon region ($2750\text{--}3100\text{ cm}^{-1}$), we observed methyl symmetric (2875 cm^{-1}), methyl Fermi (2940 cm^{-1}), and methyl asymmetric (2955 cm^{-1}) vibrations in the PPP polarization spectrum for the digital mucus of *H. cinerea* (Fig. 4.5;

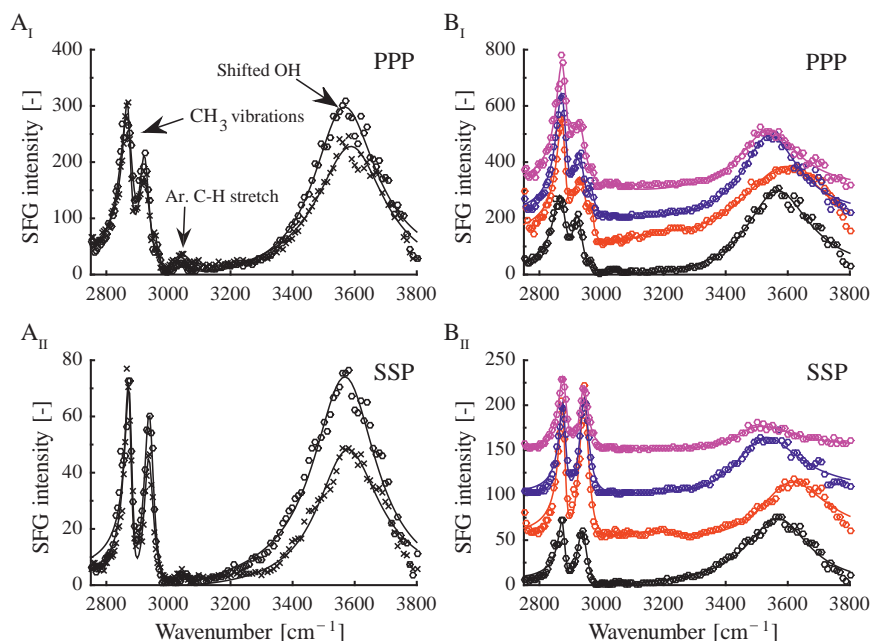


Figure 4.5 SFG spectra of frog mucus. (A) Comparison of ventral digital (crosses) and abdominal (circles) mucus in *Hyla cinerea* in (I) PPP and (II) SSP polarisations. CH₃ vibrations include methyl symmetric, methyl Fermi, and methyl asymmetric vibrations. (B) Comparison of the ventral abdominal mucuses of the arboreal frog species *H. cinerea* (black) and *Osteopilus septentrionalis* (red) as well as the terrestrial species *Pyrricephalus adspersus* (blue) and *Ceratophrys cranwelli* (magenta) in (I) PPP and (II) SSP polarisations. The solid lines represent the fitting curves using the Lorentzian equation (Equation 4.2). The spectra are offset along the ordinate axis in steps of 100 (PPP) and 50 (SSP) for clarity.

Wang *et al.*, 2002). Similar results were obtained for SSP polarization, where only methyl symmetric and methyl Fermi vibrations were observed (Fig. 4.5). The presence of predominantly methyl vibrations at the interface in both PPP and SSP polarization may be associated to the presence of a well-ordered monolayer formed by long chain fatty acids or lipids present in the mucus (Hsu *et al.*, 2011; Zhu & Dhinojwala, 2015). Additionally, a small peak at $\sim 3050\text{ cm}^{-1}$ assigned to the C-H stretch of aromatic amino acids groups (Fowler *et al.*, 2018; Kim & Somorjai, 2003; Wang *et al.*, 2002) indicates hydrophobic amino acid residues. The hydroxyl region ($3100\text{--}3800\text{ cm}^{-1}$) shows a broad peak around $\sim 3550\text{ cm}^{-1}$ in both PPP and SSP polarizations. This peak is caused by strong polar (typically acid-base) interactions between molecules present in the ventral digital mucus and sapphire surface hydroxyls, causing the shift of a typically sharp peak at $\sim 3710\text{ cm}^{-1}$ (assigned to the O-H stretch vibrations of the sapphire free surface hydroxyl groups; Kurian *et al.*, 2010) towards lower wavenumbers.

Similar to the ventral digital mucus, the SFG spectra for abdominal mucus show peaks in the hydrocarbon region and the hydroxyl region associated with lipid-like mucus

constituents and polar interactions of the mucus (Fig. 4.5A). The interaction strength of the abdominal mucus was compared to that of the digital mucus using the average peak shift of the sapphire surface hydroxyl peak. The average sapphire hydroxyl peak shifts for abdominal and digital mucus were $117 \pm 14 \text{ cm}^{-1}$ ($n = 2$) and $94 \pm 23 \text{ cm}^{-1}$ ($n = 3$) in PPP polarization, and $116 \pm 2 \text{ cm}^{-1}$ ($n = 2$) and $109 \pm 6 \text{ cm}^{-1}$ ($n = 3$) in SSP polarization, respectively (Fig. 4.SI.5). However, no significant differences were observed between the mucus from two different body locations (ranksum = 7, $p = 0.40$ for PPP; ranksum = 6.5, $p = 0.40$ for SSP), highlighting the conservation of the mucus surface chemistry across different body parts. In *O. septentrionalis*, also no significant differences were observed between the digital and abdominal mucus (ranksum = 14.5, $p = 0.20$ for PPP; ranksum = 15, $p = 0.10$ for SSP; Fig. 4.SI.5).

Further comparisons were made across the abdominal mucus collected from the four different frog species (Fig. 4.5B). The spectral signatures (methyl vibrations with a shifted sapphire hydroxyl peak) observed for *O. septentrionalis*, *C. cranwelli*, and *P. adspersus* are similar to *H. cinerea*, indicating no or only little changes of the mucus surface chemistry in the evolution of anurans.

4.3 Discussion

This study offers a comparative analysis of the mucus glands and their secretory products in the digital pads of tree frogs, in order to evaluate the function(s) of gland morphology and mucus chemistry related to the attachment of these animals. We will first discuss the morphology of the digital mucus glands in tree frogs, before addressing the chemistry of the secreted mucus.

4.3.1 Mucus gland morphology

In all anurans, mucus glands cover large fractions of the body surface and seem to be the most uniform gland type (Brizzi *et al.*, 2002). Surprisingly, the mucus glands and their secretory products have received relatively little attention in previous research. Our 3D analysis of the mucus glands of anurans—and of the digital glands of tree frogs in particular—shows that the digital glands vary in shape and size, allowing the distinction of dorsal and ventral glands based on features other than gland location.

The morphology of the dorsal glands agrees with general descriptions for amphibian mucus glands (Brizzi *et al.*, 2001; Ferraro *et al.*, 2011; Goniakowska-Witalińska & Kubiczek, 1998; Haslam *et al.*, 2014; Mills & Prum, 1984; Toledo & Jared, 1995). The diameter of the dorsal digital glands measured in our study falls in the range of values reported for mucus glands in the dorsal skin of other anurans (Table 4.1). The dorsal pore density of ca. 190 mm^{-2} lies at the high end of the range of previously measured values for various anuran families ($32\text{--}128 \text{ mm}^{-2}$, Blaylock *et al.*, 1976; 60 mm^{-2} , Engelmann, 1872; $30\text{--}50 \text{ mm}^{-2}$, Skoglund & Sjöberg, 1977; $8\text{--}190 \text{ mm}^{-2}$,



Table 4.1 Comparison of mucus gland diameters in neobatrachians.

Family	Diameter [μm]	Reference
Hylidae	45.0 \pm 5.5	This study
	34.8–47.9	Barbeau & Lillywhite (2005)
	42.0–94.9	Goniakowska-Witalińska & Kubiczek (1998)
Leptodactylidae	24.0–76.8	Ferraro <i>et al.</i> (2011)
Ranidae	41.6–52.2	Barbeau & Lillywhite (2005)
	47.0–95.0	Le Quang Trong (1971)
Rhacophoridae	46.2–63.0	Lillywhite <i>et al.</i> (1997)

Czopek, 1965; 55–253 mm⁻², Le Quang Trong, 1971). Ecomorphological studies are needed to investigate if variations in gland density relate to the habitat, with higher gland densities in species living in arid areas (Le Quang Trong, 1971).

To our knowledge, the volume of the mucus glands has not been measured directly before. Compared to earlier estimates (0.1 nL, Blaylock *et al.*, 1976; 1 nL, Seldin & Hoshiko, 1966), we measured lower volumes for the dorsal glands (0.05 nL), despite including the mucus duct in the volume. The volumes measured in this study may be underestimated due to potential shrinkage of the analysed pad during sample preparation. The discrepancy between the gland volumes and densities measured here and the ones reported in literature may be explained by our 3D-analysis, which allows the identification and accurate quantification of all glands in a given sample. We conclude that the dorsal digital mucus glands of *H. cinerea* have a similar geometry as the mucus glands of other body parts and species, except for the distinct ventral digital glands discussed below.

4.3.2 Digital mucus gland clusters in anurans

The morphology of the ventral digital mucus glands deviates strongly from the general morphology of the ‘regular’ anuran mucus glands found in the dorsal dermis: The glands are clustered in the proximal part of the subdermal pad cavity rather than distributed across the stratum spongiosum, the gland bodies are elongated instead of spherelike, and the ventral glands are significantly larger than the dorsal ones (Figs. 4.5,4.SI.1). This difference in size between dorsal and ventral digital glands in *H. cinerea* was also observed, but not quantified, previously (Ernst, 1973b). The elongated shape and the subdermal clustering of the ventral glands were both previously described in *H. cinerea* (Ernst, 1973a), *H. arborea* (Dewitz, 1883; Leydig, 1868; Noble & Jaeckle, 1928; Schuberg, 1891; v. Wittich, 1854), and *Rana temporaria* (Gaupp, 1904), although not always together in a given species. The ventral digital mucus glands may represent a ‘modified form’ of the dorsal ones (Dewitz, 1883).

Although not explicitly described in the according references, screening the available literature reveals the presence of digital mucus gland clustering in numerous anuran groups other than *Hyla* (Table 4.SI.6). This shows that a cluster of digital mucus

glands is not unique to *H. cinerea* or hylid tree frogs, but is present in at least 10 neobatrachian families, although sometimes described as rows instead of clusters (Noble & Jaeckle, 1928; Siedlecki, 1910).

Locally clustered amphibian glands are also termed macroglands (Brizzi *et al.*, 2001). In amphibians, several granular macroglands have been described, which generally are involved in defence, reproduction, and communication (Brizzi *et al.*, 2002; Toledo & Jared, 1995). We identified an anuran mucus macrogland—namely the subdermal cluster of digital mucus glands—in the digital pads of tree frogs and other neobatrachian families. As for the already known granular macroglands (Antoniazzi *et al.*, 2013; Brizzi *et al.*, 2001, 2002; Toledo & Jared, 1995), the ‘strategic’ positioning of the digital gland cluster suggests a specific functionality. However, the digital macrogland is not only present in arboreal species, but also in terrestrial ones (Noble & Jaeckle, 1928).

4.3.3 Functional morphology of the digital gland cluster

The presence of the ventral mucus gland cluster also in not purely arboreal species (e.g. *Acris gryllus* or *Rana temporaria*; Table 4.SI.6) supports the hypothesis that the morphology of the cluster is determined by generic functional requirements arising from ‘ground contact’ (addressed below) and possibly by specific requirements for climbing and attachment.

Repeated substrate-contact during locomotion leads to a loss of mucus from the ventral pad surface to the environment. This loss presumably is enhanced by the high wettability of the mucus, as indicated by the lipid-like substances found in our study, which potentially act as surfactants, and by measured contact angles $< 10^\circ$ (Drotlef *et al.*, 2013). Compared to the dorsal pad side, we showed for the tree frog *H. cinerea* an approximately 2.4 higher total gland volume at the ventral side. Mucus loss is compensated by enhancing the volume of individual glands rather than by increasing the gland number. Enlarging or multiplying ‘regular’ glands may reduce the mechanical strength of the ventral cutis, which is an important mechanical link between the adhesive pad surface and the internal skeleton (Langowski *et al.*, 2018b). Thus, the location of the ventral glands in the internal pad space enables a volume increase and a 4.3 times higher volume per pad surface area, compared to the dorsal pad surface, helping to avoid desiccation of the ventral pad surface. After secretion, mucus may be stored in the hierarchical network of micro- to nanoscopic channels formed between the ventral epidermal surface cells (Persson, 2007). Such mucus storage may be especially important to reduce the metabolic costs of mucus production as frogs cannot suck mucus back into the ducts (Engelmann, 1872).

A sufficient mucus volume is also important for attachment. Capillary adhesion relies on the formation of a liquid bridge between digital pad and substrate, and the question remains if tree frogs possess enough mucus to form this bridge themselves, or if an accumulation of environmental water is necessary (Green & Carson, 1988). The minimal volume of the liquid bridge can be approximated with a geometrical



model of the pad-substrate gap (Langowski *et al.*, 2018a). For a circular ventral pad surface of 1.1 mm^2 (measured in this study) and a median pad-substrate gap width of 6 nm (Federle *et al.*, 2006), the model predicts a volume of the liquid bridge of 2.3 nL . For the axisymmetric volume of the free meniscus, we estimate a volume of the same order of magnitude. With a total ventral gland volume of around 38 nL , tree frogs seem to be well able to create capillary adhesion using only secreted mucus.

The volume enhancement by larger and longer, but fewer ventral glands may be explained by hydrodynamic considerations. The mucus flow through the glandular ducts during secretion can be approximated as steady pipe flow, described by the Hagen-Poiseuille equation:

$$\Phi = \frac{2\pi d^4 \Delta p}{\mu L}, \quad (4.1)$$

where Φ is the volumetric flow rate (i.e. volume flux) generated by a pressure difference Δp driving a liquid with a dynamic viscosity μ through a circular pipe with length L and diameter d . While moving the glands into the inner pad space inevitably increases L and reduces the volume flux, the enlargement of the ventral glands (and hence of d) has an opposite, stronger, effect. The same mucus flux as in the dorsal glands may be obtained in the ca. 20-fold longer ventral glands with a duct diameter that is approximately doubled.

Further potential adaptations to counteract a reduction in volume flux with increasing duct length include changes to the mucus chemistry (i.e. the viscosity μ) or to the pressure drop between glandular lumen and pad surface (see Equation 4.1). For *L. caerulea*, a mucus viscosity of 1.43 mPa s has been measured (Federle *et al.*, 2006), which is similar to the viscosity of water at room temperature and arguably almost as low as possible in an animal, potentially resulting in a low work needed for secretion. Additionally, capillary action in the micro- to nanoscopic channels on the pad surface could increase Δp (Persson, 2007), hence supporting mucus secretion through the ventral ducts.

The glandular secretion mechanism plays a major role in generating the pressure difference driving mucus flow. Generally, amphibian mucus glands secrete their content by sympathetic autonomic innervation of the myoepithelial cells—sometimes also referred to as smooth muscle fibres (Bovbjerg, 1963; Wanninger *et al.*, 2018)—surrounding the glands (Holmgren & Olsson, 2011), leading to continuous (Brizzi *et al.*, 2002) and synchronous (Lillywhite, 1971; Lillywhite & Licht, 1975) mucus secretion. In the closed pad-substrate gap, continuous secretion is not needed, and may even contribute to the loss of mucus. Moreover, the long ventral gland ducts cause a higher viscous resistance against secretion. Accordingly, it may be expected that the secretory mechanism differs between the ventral and dorsal glands. Contraction of the glandular muscle fibres previously was assumed to be the primary driver of digital mucus secretion (Ernst, 1973a). However, our study does not show a stronger myoepithelial support of the ventral glands (i.e. an increased number or thickness of the myoepithelial cells covering the ventral glands compared to the dorsal ones; Fig. 4.SI.3), disagreeing

with the hypothesis of the glandular muscle fibres driving secretion. An analysis of the arrangement of the myoepithelial structures surrounding the ventral digital mucus glands—as performed for the salamander *Tylototriton verrucosus* (Wanninger *et al.*, 2018)—may illuminate their biomechanical relevance.

A secretory mechanism independent of myoepithelial action may be found in the internal clustering of the ventral glands below the distal phalanx. Flexion of the distal phalanx by contraction of the flexor muscles (Manzano *et al.*, 2007) would help to build up pressure within the glands, effectively enhancing Δp . Such secretion by compressive action of the distal phalanx might also be faster than measured for regular mucus glands (Skoglund & Sjöberg, 1977; Tyler *et al.*, 1992), enabling a faster control of the amount of mucus at the pad-substrate interface. Moreover, the location of the glands in the internal pad space helps to circumvent unintentional mucus secretion by mechanical loading of the ventral pad cutis during locomotion.

Finally, a generic, non-adhesive function of the ventral digital glands (and their secretions) is also indicated by the spatial distribution of the mucus pores. We showed that the pores are distributed across the whole ventral pad surface, in contrast to earlier observations of the ducts only ending in the cuticular groove around the digital pad (Leydig, 1868).

However, the density of the pores, inversely approximated by their nearest-neighbour-distance, increases by 40% from the distal to the proximal side of the pad surface (Fig. 4.2). This suggests more mucus being present proximally than distally, which is also shown by the quadratic increase in cumulative gland volume from distal to proximal (Fig. 4.SI.2). This concentration of mucus pores near the proximal pad edge quantitatively supports the hypothesised function of amphibian mucus as lubricant (Barrett, 1971; Toledo & Jared, 1993). During attachment, tree frogs regularly pull the digital pads towards the body, resulting in proximally directed sliding (Hanna & Barnes, 1991; Schuberg, 1891) across the mucus secreted by the proximal mucus glands, which presumably distributes the mucus over the ventral pad surface.

Strategic gland positioning is also observed in the dorsal mucus glands, which are less dense above the distal phalanx than next to it. As described for *H. cinerea* (Langowski *et al.*, 2018b), *H. arborea* (Schuberg, 1891), and *Rhacophorus reinwardtii* (Siedlecki, 1910), the distal phalanx can bulge out the dorsal cutis during locomotion. Such movements arguably result in deformations of the dorsal cutis and the glands therein, potentially causing unfavourable mucus loss. The reduced gland density above the distal phalanx helps to reduce or even avoid such mucus loss.

4.3.4 Mucus chemistry

We used histochemical and spectroscopic methods in our chemical analysis of the digital mucus in tree frogs, which is needed to understand its role in attachment (Els & Henneberg, 1990).



4.3.4.1 The chemical composition of tree frog mucus

Overall, neither the histochemical nor the spectroscopic (IR and SFG) analyses reveal major variations in the types of molecules (i.e. mucosubstances, proteins, and lipids) and in the spectroscopic characteristics of these molecules present in frog mucus as a function of location on the body (ventral digital, dorsal digital, or ventral abdominal) or lifestyle (arboreal or terrestrial). Whereas variations on an intramolecular level, such as the presence of specific functional groups, may have not been picked up by histochemistry, spectroscopic analyses do not produce evidence for such variations.

The histochemical examination of the digital mucus of *H. cinerea* reveals carbohydrate components such as neutral polysaccharides, glycoproteins, and -lipids (indicated by Periodic acid-Schiff), as well as acidic (i.e. carboxylated) but no sulfated mucopolysaccharides (indicated by Alcian blue). These results agree with the majority of histochemical analyses of anuran mucus glands (Table 4.SI.5), including the digital glands of hylids (Barnes *et al.*, 2011; Ernst, 1973b). Acid mucopolysaccharides have been indicated in *H. cinerea* also by positive staining with toluidine blue (Ernst, 1973b). The flocculent nature of the mucosubstances has been described previously (Fontana *et al.*, 2006; Mills & Prum, 1984), confirming that the mucus was not washed out prior to or during the staining.

All protein-specific stainings generated negative results. Mercuric bromophenol blue has been used repeatedly as ‘general protein stain’ (Antoniazzi *et al.*, 2013; Dapson, 1969; Table 4.SI.5), but its specificity is not fully resolved (Hornatowska, 2005; Kanwar, 1960). The weaker staining by BRO of the glands compared to other tissues can be interpreted as a negative result (Antoniazzi *et al.*, 2013). Arguably, a single protein staining would not be conclusive, but—as pointed out by Thomas *et al.* (1993)—the combination of negative results from three different tests is evidence for the absence of proteins in the digital mucus of tree frogs (or concentrations too low to be detected by histochemistry). Negative staining of non-digital anuran mucus glands with Ninhydrin-Schiff, Coomassie blue, and Bromophenol blue was also found in other studies using various fixation treatments (Table 4.SI.5). In contrast, the signatures observed in the ATR-IR spectra indicate a protein-like constituent of both digital and abdominal mucus. The proteins could be present by themselves (in small quantities) or as part of the histochemically identified glycoproteins. Also in the SFG spectra of both digital and abdominal mucus, the strongly ordered methyl peaks (in both PPP and SSP polarizations) may be explained by the presence of molecules containing hydrophobic amino acids with their side chain methyl groups ordered at the air interface. The absence of a N-H peak (typically at 3300 cm^{-1} ; Chen *et al.*, 2005) could be due to a disordered protein backbone. Interestingly, indications of methyl and methylene groups as found in the amino acid side chains in mucosubstances were also observed in the SFG spectrum of the tongue mucus of *Ceratophrys spec.* (Fowler *et al.*, 2018). A future analysis of IR spectra below 1500 cm^{-1} and of SFG spectra in the amide I/II region would allow a direct comparison between the two spectroscopic methods and hence an investigation of the proteinaceous components of tree frog

mucus (e.g. the confirmation of glycoproteins), which was not possible here due to technical limitations of our setups.

We did not detect lipids or lipoproteins in the mucus using Oil Red O (OIO) staining. Importantly, we found lipids inside the medullary cavity and in a thin subepidermal layer, which has both been observed previously (Amey & Grigg, 1995; Tanaka, 1976), confirming proper functioning of our OIO protocol. In contrast to histochemistry, the strongly ordered methyl peaks in the SFG spectra for the digital and abdominal mucus could reflect the presence of a well-ordered self-assembled monolayer formed by long chain fatty-acid-like molecules (or lipids). These opposed findings may be due to low concentrations of lipids present in the mucus along with a difference in sensitivity between the used histochemical and spectroscopic techniques. Literature reports on lipids in frog mucus are inconclusive. The absence of lipids has been confirmed by various stains for other hylids (Barbeau & Lillywhite, 2005; Centeno *et al.*, 2015; Goniakowska-Witalińska & Kubiczek, 1998), bufonids (Regueira *et al.*, 2016), and pipids (Thomas *et al.*, 1993; Table 4.SI.5). Using other chemoanalytical methods, however, several authors reported lipids in frog mucus (Centeno *et al.*, 2015; Crawford, 2016; Dewitz, 1883; Schuberg, 1891). Many of these lipids are commonly found in plants (Centeno *et al.*, 2015), possibly hinting towards sample contamination. In our study, the similarity of the ATR-IR and SFG spectra between the tested arboreal (kept without plants) and terrestrial (kept with plants) species suggests that such contamination did not occur. In conclusion, the presence of lipids in digital tree frog mucus is still uncertain.

Variations in staining intensity of the digital glands may be explained by a number of factors. Intraglandular staining variation has been described in *H. cinerea* (Ernst, 1973b) and *Rana fuscigula* (Els & Henneberg, 1990), with individual mucocytes reacting differently to PAS and AB staining. Such differences may be explained by different biosynthetic stages of single mucocytes (Els & Henneberg, 1990; Ferraro *et al.*, 2011; Mills & Prum, 1984). Overall, tree frog mucus has to be considered a heterogeneous substance that originates from mucocytes and glands of varying biosynthetic stages (Els & Henneberg, 1990; Ferraro *et al.*, 2011), epidermal transudate secretion (Campbell *et al.*, 1967; Haslam *et al.*, 2014), and environmental liquids (Haslam *et al.*, 2014). The good agreement of our findings on samples of *H. cinerea* that were not fixed directly after the death of the animals with literature results on immediately fixed samples (Table 4.SI.5) suggests that *post mortem* changes in mucus chemistry were insignificant.

Overall, our results indicate that the mucus chemistry has been largely conserved in frogs. This suggests that the digital mucus of tree frogs (a) fulfills generic functions of amphibian mucus, and (b) possibly got incorporated into the attachment apparatus without extensive modifications of its chemistry. Detailed analyses of the mucus molecules using mass-spectrometry, of the concentration of these molecules, and of the physical mucus properties affected by the presence of these molecules (e.g. viscosity and surface tension) are required to advance the understanding of the functionality of frog mucus and the mucus of tree frogs in particular.

4.3.4.2 Functional chemistry of digital tree frog mucus

The chemical similarity of the dorsal and ventral digital mucus in tree frogs suggests that the mucus at the contact interface fulfills the same functions as regular amphibian mucus. These functions comprise, most importantly, cutaneous respiration, homeostasis, water regulation, defence, and lubrication (Brizzi *et al.*, 2001; Clarke, 1997; Haslam *et al.*, 2014; Probst *et al.*, 1992; Toledo & Jared, 1993).

Proteoglycans such as the mucopolysaccharides detected here by PAS- and AB-staining are affine to water (Barrett, 1971), enabling the formation of a mucus layer lubricating the skin (Barrett, 1971; Toledo & Jared, 1993). The resulting reduced skin friction makes it more difficult for predators to grip the frog (Toledo & Jared, 1993), and reduces abrasive wear and damage of the soft skin (Clarke, 1997), as indicated by the proximal concentration of mucus on the ventral pad surface found in our study. Similarly, in the burrowing caecilian *Siphonops annulatus* mucus glands are concentrated anteriorly (Jared *et al.*, 2018). In the digital pads of tree frogs, however, a reduced friction would be detrimental as the push-off force parallel to the substrate—for example during jumping—would be lowered, too. Here, the epidermal micropatterns found on the pad surface may help to drain excess liquid, hence increasing friction (Gupta & Fréchet, 2012; Langowski *et al.*, 2018a; Persson, 2007).

The presence of large molecules, such as the polysaccharides and glycoproteins detected here, suggests an increased viscosity of the mucus compared to pure water (Barrett, 1971; Toledo & Jared, 1993), which affects the generation of hydrodynamic adhesive forces. These forces scale with the concentration of mucosubstances in water (Hanna & Barnes, 1991), assuming a constant distance between pad and substrate. Although not believed to play an important role in tree frog attachment (Langowski *et al.*, 2018a), a quantification of the mucus viscosity is required for an investigation of its role in the generation of hydrodynamic attachment forces. Dilution of the mucus by environmental water (e.g. rain), and non-Newtonian liquid behaviour due to the presence of mucosubstances—potentially as a function of concentration of these substances—should be considered in such analyses. Frogs may modulate the concentration of mucosubstances to control the relative contribution of hydrodynamic and capillary adhesion (as shown in a technical system; Barnes *et al.*, 2006), depending on the circumstances.

The mucus chemistry also plays a role in the proposed capillary adhesion of tree frogs. Generally, capillary adhesive forces scale with the surface tension of the liquid forming the meniscus, and with the area covered by the liquid bridge (Butt & Kappl, 2009). Our ATR-IR and SFG results indicate the presence of amphiphilic lipid-like molecules. Similar to surfactants, such molecules help in reducing the effective surface tension and enhance the wetting of a liquid. The presence of surfactants in tree frog mucus is also indicated by the low contact angles of tree frog mucus measured on hydrophilic and hydrophobic substrates (Drotlef *et al.*, 2013). Similar to the balance between spreading and viscous resistance observed in spider glue (Amarpuri *et al.*, 2015), a trade-off between contact area enhancement and surface tension reduction as

a function of surfactant concentration may be present. In a technical adhesive system (Li *et al.*, 2018b), the concentration of surfactants in a capillary bridge determines the stability of the bridge, and as a result the amount of adhesive forces. Analogously, tree frogs could control their attachment strength by varying the concentration of lipids in the mucus. The loss of van der Waals forces (vdW) due to a too high surfactant concentration (Li *et al.*, 2018b) may also explain the complete failure in attachment of tree frogs when adding soap or detergent into the pad-substrate gap (Green, 1981).

The evolution of anurans may have led to a mucus composition that exploits the aforementioned trade-offs while minimising the metabolic costs of the production of the required mucus components. To further explore these trade-offs, dynamic measurements of the mucus composition and of the generated attachment forces are required. Several other effects may be considered in future research. The ability of the mucopolysaccharides detected in our study to bind water may allow for the formation of large mucopolysaccharide-water-complexes. If present in the intercellular channels on the ventral pad epidermis, such complexes may help to avoid clustering of the epidermal cells, hence supporting the geometrical integrity of the epidermal surface pattern for attachment. Also, the glycoproteins detected by PAS may act as adhesive binding agents, as indicated by the hydroxyl peak shift in the SFG spectra and observed in the aggregate glue of orb web spiders (Singla *et al.*, 2018) and in numerous other bioadhesive systems (Hennebert *et al.*, 2018). A layer of glycoproteins adhering to the substrate or the pad epidermis may help to remove water from the pad-substrate gap, thus reducing the gap width and enabling dry contact for the generation of vdW forces. A more elaborate analysis of the protein content of tree frog mucus, as outlined by Hennebert *et al.* (2018), may help to understand the role of these molecules in attachment. The interaction of glycoproteins with other compounds should be studied, as such interactions affect the functioning of glycoproteins in attachment (Sahni *et al.*, 2014; Singla *et al.*, 2018).

4.4 Conclusions

Despite a variety of functions related to physiological processes and to attachment, anuran mucus glands and their secretions have received relatively little attention. To our knowledge, we present here the first 3D, quantitative assessment of anuran mucus glands in the adhesive digital pads of the tree frog *H. cinerea*. We show that the ventral digital mucus glands form a digital gland cluster, or macrogland, with a 2.4-fold larger volume of available mucus compared to the ‘regular’ dorsal glands, which presumably helps to compensate mucus loss while reducing unintentional mucus secretion and structural weakening of the adhesive epidermis. The gland cluster is also present in non-climbing frog families and hence may represent a previously unrecognised adaptation of amphibians to a terrestrial lifestyle. Using histochemical and spectroscopic methods, we found indications of carbohydrates, proteinaceous, and lipid-like substances in frog mucus, and show that frog mucus varies only little



between different body locations (digital vs. abdominal) and as a function of lifestyle (arboreal vs. terrestrial). This result indicates a conservation of the cutaneous mucus chemistry in the evolution of anurans. Our functional and comparative analysis of the digital macrogland morphology and mucus chemistry contributes to a better understanding of the bioadhesion of these animals, and of anuran evolution. As the ventral digital mucus and cutis are the primary barrier against environmental pathogens, further studies on these components may also help to understand the current global decrease in amphibian populations due to the fungus *Batrachochytrium dendrobatidis* (Fisher *et al.*, 2009). Finally, highlighting analogies between the glandular systems of tree frogs and of other attachment systems in nature (e.g. in insects), and placing these analogies in a functional context, will advance the general understanding of bioadhesion and may stimulate novel trends in the design of bioinspired adhesives.

4.5 Methods

4.5.1 Experimental animals

For histochemical and morphological analyses, we used three adult *Hyla cinerea* that died of unknown causes (*post mortem* snout-vent-length $\ell_{SV} = 40\text{--}46$ mm, body mass $m = 6.2\text{--}8.2$ g, age ≤ 1 year). For a description of the housing conditions, see Langowski *et al.* (2018b). We collected the distal limbs before 5:30 h after death by disarticulation of the elbow and knee joints. Until further use, the right hindlimb of each individual was quick-frozen in liquid nitrogen and subsequently stored at -80°C . All following steps were executed at -20°C , unless mentioned otherwise. For $\mu\text{-CT}$, we chemically fixated and stored one digit of the left hindlimb as described elsewhere (Langowski *et al.*, 2018b).

For comparative spectroscopic analyses of the mucus chemistry, two adult *H. cinerea* ($\ell_{SV} = 40\text{--}44$ mm, $m = 2.1\text{--}4.2$ g) and four adult *O. septentrionalis* ($\ell_{SV} = 69\text{--}85$ mm, $m = 14.7\text{--}28.1$ g) were acquired from commercial vendors and housed individually in plastic containers with water *ad libitum* and biweekly feedings of gut-loaded cockroaches. Three juvenile individuals each of *C. cranwelli* ($\ell_{SV} = 32\text{--}45$ mm, $m = 4.7\text{--}9.7$ g) and *P. adspersus* ($\ell_{SV} = 32\text{--}37$ mm, $m = 2.1\text{--}3.9$ g) were acquired as part of an unrelated study and mucus samples were taken before euthanasia; both species are terrestrial ambush predators.

4.5.2 3D reconstruction of the digital gland morphology

We analysed the morphology of the digital glands in *H. cinerea* in 3D using $\mu\text{-CT}$. The digit used for $\mu\text{-CT}$ was contrast-stained, scanned, and segmented as described by Langowski *et al.* (2018b). We segmented all glands opening to the ventral pad surface

(termed ventral glands) and—to reduce the efforts of manual segmentation—the left half of the glands opening to the dorsal pad surface (termed dorsal glands).

We quantified the morphology of the individual glands using a custom-made MATLAB routine (Version R2016b, The Mathworks, USA). Voxel size was set to $1.3 \cdot 1.3 \cdot 1.3 \mu\text{m}^3$ (original $\mu\text{-CT}$ voxel size: $0.65 \cdot 0.65 \cdot 0.65 \mu\text{m}^3$) to reduce the computational effort. Individual volumes of dorsal and ventral glands were computed by summing up the segmented voxels. Using MATLAB, the dorsal (V_{dg}) and ventral (V_{vg}) gland volumes were tested for normal distribution using an one-sample Kolmogorov-Smirnov test, and for a difference of the means of the two groups using a two-sample t-test. We used for all statistical analyses a significance level $\alpha = 5\%$. Further, each ventral gland was skeletonised using an accurate fast marching algorithm to extract the length of the gland centerline l . The distal end of the centerline was used as the spatial coordinate of the mucus pore. The location of the dorsal pores was set as the most dorsal segmented voxel of each gland. Pore density was approximated by the nearest-neighbour-distance (NND) between the pores. To test for spatial patterns in the distribution of the mucus pores, we performed with MATLAB a multiple linear regression of NND as a function of the lateral and longitudinal pore coordinates (x and y), using t-tests to identify significant deviations of the fitted slopes from 0. The dorsal and ventral pad surface area was determined by Delaunay triangulation of the respective pore vertices, and by taking the sum of the resulting triangular areas.

4.5.3 General chemistry of glandular mucus

We applied various cryo-histochemical stains to investigate which classes of molecules are present in tree frog mucus. The staining of the mucus still present in the glands helps to reduce contamination with, for example, environmental substances, mucus from other body parts, or non-mucus related molecules such as cuticular proteins or lipids. Before histological staining, the two most distal segments of digits of the hindlimb of *H. cinerea* were cut from the frozen limb through the central part of the middle phalanx. The frozen samples were mounted on specimen discs using KP-CryoCompound (Klinipath, The Netherlands), cut perpendicularly to the longitudinal digital axis (i.e. transverse) into $7 \mu\text{m}$ thick sections ($10 \mu\text{m}$ for Ninhydrin-Schiff staining) using a CM3050S cryostat (Leica Microsystems B.V, The Netherlands), and placed on object slides (Menzel, Germany).

As general overview stain, we applied Crossmon's light green trichrome stain (CRO) in combination with Mayer's haematoxylin and Alcian blue as described by Langowski *et al.* (2018b). We used Periodic acid-Schiff stain (PAS) according to Romeis (Mulisch & Welsch, 2010; Romeis, 1968) to detect neutral polysaccharides, mucopolysaccharides, glycoproteins, and -lipids containing 1,2-glycols (or their amino- and alkylamino-derivatives; Kiernan, 2015). A diastase treatment prior to PAS-staining (PAS-D) was applied to exclude the presence of glycogen (Mulisch & Welsch, 2010; Romeis, 1968). To detect acid mucopolysaccharides such as sialin and uronic acids

and some glycoproteins, we used Alcian blue (Mulisch & Welsch, 2010); to distinguish between highly acidic (i.e. sulfated) and acidic (i.e. carboxylated) mucopolysaccharides, Alcian blue was applied at pH = 1 (AB-1) and at pH = 2.5 (AB-2.5), respectively (Lev & Spicer, 1964; Luna, 1968; Mulisch & Welsch, 2010). As general protein stains (Brizzi *et al.*, 2002; Dapson, 1969; Prates *et al.*, 2012; Thomas *et al.*, 1993), we used Ninhydrin-Schiff (NIN), which stains α -amino-acids by binding with their free NH₂ groups (Bancroft & Stevens, 1996; Bottom *et al.*, 1978; Rappay, 1963), Coomassie blue R250 (COO, Kiernan, 2015), which stains proteins by a combination of hydrophobic interactions and heteropolar bonding with basic amino acids (Congdon *et al.*, 1993; Georgiou *et al.*, 2008; Kiernan, 2015), and Mercuric bromophenol blue (Hornatowska, 2005), which has been reported to react with acidic, sulphhydryl, and aromatic protein residues (Subramoniam, 1982). The pH-sensitive bromophenol blue was used at pH = 3.8 (BRO-3.8) and at pH = 4.6 (BRO-4.6). Hydrophobic lipids (and lipoproteins; Guigui & Beaudoin, 2007) were stained with Oil Red O (OIO; Lillie & Ashburn, 1943). By using cryo-samples and lyophobic solvents, we reduced the risk of washing out of lipid-like mucosubstances (Barrett, 1971; Els & Henneberg, 1990). Finally, Bouin-fixated sections of digits from the left hindlimb and the right forelimb were stained immunohistochemically as by Langowski *et al.* (2018b) to test for differences in the amount of smooth muscle α -actin—present in muscular and myoepithelial structures—in between dorsal and ventral mucus glands. For detailed staining protocols, we refer to Section 4.SI.3.2.

Images of the stained sections were obtained using a digital microscope camera (DFC450c, Leica, Germany) mounted on an upright microscope (DM6b, Leica) with a HC PL APO 40 \times /0.85 objective controlled with the Leica Application Suite X (Version 2.0). High-resolution images of whole sections were obtained by merging tile-scanned images. For relatively faint stains (NIN and OIO), differential interference contrast was used to show the internal pad structures. Post-processing (cropping, rotating, scaling, white balancing, and arranging) of the images was done in Photoshop CC (Version 2017.1.1, Adobe Systems, USA) and in Illustrator CS6 (Version 16.0.3, Adobe).

4.5.4 Bulk chemistry of secreted mucus

Infrared spectra were acquired using an iS50 Fourier Transform Infrared spectroscopy (IR) system equipped with a mercury-cadmium-tellurium (MCT) detector (Thermofisher, USA). A horizontal attenuated total internal reflection accessory (PIKE Technologies, USA) was used to collect multibounce (10 bounces) attenuated total reflection infrared spectra (ATR-IR) from a pristine silicon crystal. The crystal surface was cleaned by soaking in hot Piranha solution (7:3 H₂SO₄ and H₂O₂) for 1 h followed by sonication in ultrapure water (Millipore filtration system, 18.2 M Ω -cm with pH = 6–7) for 1 h. Prior to cleaning, a 5 wt.% solution of hydrofluoric acid in deionized water was used to remove the native silicon oxide (SiO₂) layer. A spectrum from the pristine crystal was used as background for the ATR-IR measurements. To obtain a spectrum, we averaged 100 interferograms with a 4 cm⁻¹ step scan. ATR-IR

spectra of the frog mucus were obtained by gently rubbing a clean Si crystal on the according part of the frog's body (i.e. digital pad or abdomen) to deposit the ventral mucus on the crystal. Prior to mucus collection, the respective body part was rinsed with tap water, followed by rinsing with ultrapure water, and gently dried with a kimwipe to avoid potential contamination of the mucus from other body portions or the environment. The mucus deposit on the Si crystal surface was dried overnight in vacuum to ensure the evaporation of bound water. ATR-IR scans were then collected as described above. Calculation and analysis of peak areas were done with Igor Pro (Vers. 6.37, Wavemetrics, USA) with the Multipeak fitting analysis package (Vers. 2, Wavemetrics). At least 3 repeats from different individuals were done per species for both the digital and abdominal mucus for *H. cinerea* (2 individuals) and *O. septentrionalis* (3 individuals). One repeat was done for *P. adspersus* (1 individual), as the animal was euthanized for another experiment shortly after mucus sampling. Comparisons were made between the digital and abdominal mucus spectra for both *H. cinerea* and *O. septentrionalis*. A Wilcoxon rank sum test was performed in MATLAB to detect significant differences in the medians of the amide I/II ratios between the two species. Further comparisons were made between the IR spectra of the abdominal mucus from the three studied frog species.

4.5.5 Surface chemistry of secreted mucus

SFG spectra were collected using a ps Spectra Physics laser system, details of which are provided elsewhere (Anim-Danso *et al.*, 2013; Hsu *et al.*, 2011). Briefly, it involves the overlap of a fixed 800 nm visible laser beam with a tunable infrared beam (2000–3800 cm^{-1}). SFG being an interface-sensitive technique, provides information about molecular stretching vibrations at the interface, where there is a breakdown in inversion symmetry. Equilateral sapphire prisms (15 cm·15 cm·15 cm·10 cm, c-axis $\pm 2^\circ$ parallel to the prism face, Meller Optics Inc.) were used as substrates for the experiment. The sapphire prisms were first baked for 2 h at 760 °C followed by sonication with a series of different organic solvents (toluene, chloroform, acetone, and ethanol) for 45 min each. The sapphire prisms were then sonicated with ultrapure water (18.2 M Ω ·cm) for about 1 h, blow dried with N₂, and finally plasma sterilized (Harrick Plasma, PDC-32G) for 5 min to remove remaining hydrocarbon residues. The stainless-steel sample holder was cleaned using the same method as used for the sapphire prisms with exception of the baking step. Blank scans were collected for the clean sapphire prisms using a total internal reflection geometry to ensure a clean sapphire surface and to locate the position of the sapphire free hydroxyl peak. After cleaning the frog's body surface as described for ATIR-IR, ventral mucus was deposited by rubbing the digital pad or abdomen on the sapphire surface. At least 3 repeats (from different individuals) were done for both the digital and abdominal mucus for *H. cinerea* (2 individuals) and *O. septentrionalis* (3 individuals). One and two repeats were done for *P. adspersus* (1 individual) and *C. cranwelli* (2 individuals), respectively. The SFG spectra were collected using PPP (P-polarized SFG, P-polarized visible, P-polarized infrared) and SSP (S-polarized SFG, S-polarized vi-



sible, P-polarized infrared) polarizations, where S and P relate to the direction of the electric field with respect to the incident plane. We used the Lorentzian equation to fit the measured SFG spectra:

$$I_{\text{SFG}} \propto \left| \chi_{\text{NR}} + \sum \frac{A_q}{\omega_{\text{IR}} - \omega_q + i\Gamma_q} \right|^2, \quad (4.2)$$

where χ_{NR} describes the non-resonant contribution that does not change with scanning wavenumber ω_{IR} . A_q , Γ_q , and ω_q are the amplitude strength, damping constant, and resonant frequency of the q th vibrational resonance, respectively.

4.SI Supporting information

4.SI.1 Symbols and abbreviations

4.SI.1.1 List of symbols

Table 4.SI.1 List of Roman (top) and Greek (bottom) symbols in alphabetical order. a.u. arbitrary unit.

Symbol	Unit	Description
A_q	a.u.	Amplitude strength of the q th vibrational resonance
d	m	Ventral duct diameter / Pipe diameter
d_d, d_v	m	Dorsal and ventral gland diameter
l	m	Ventral gland length / length of the gland centerline
L	m	Pipe length
ℓ_{SV}	m	Snout-vent-length
m	kg	Body mass
n	-	Number of glands/data points
NND	m	Nearest-neighbour-distance
p	-	p-value
t	-	t-statistic
V_{dg}, V_{vg}	L	Dorsal and ventral gland volume
V_d, V_v	L	Total dorsal and ventral gland volume
α	-	Significance level
Γ_q	cm^{-1}	Damping constant of the q th vibrational resonance
Δp	-	Pressure difference
μ	$\text{kg m}^{-1} \text{s}^{-1}$	Dynamic fluid viscosity
ρ_d, ρ_v	m^{-2}	Dorsal and ventral gland density
ρ_{dV}, ρ_{vV}	L m^{-2}	Dorsal and ventral gland volume density
χ_{NR}	a.u.	Non-resonant susceptibility
Φ	$\text{m}^3 \text{s}^{-1}$	Volumetric flow rate, volume flux
ω_{IR}	cm^{-1}	Scanning wavenumber
ω_q	cm^{-1}	Resonant frequency of the q th vibrational resonance



4.SI.1.2 List of abbreviations

Table 4.SI.2 List of abbreviations.

Abbreviation	Description
AB	Alcian blue
AICc	Akaike information criterion for low sample sizes
ATR-IR	Attenuated total reflectance-infrared spectroscopy
BRO	Mercuric bromophenol blue
CH	Chromatophore
CO	Collagen
COO	Coomassie blue
CRO	Crossmon's trichrome stain in combination with Mayer's haematoxylin and Alcian blue
DE	Dermis
DP	Digital phalanx
DU	Mucus gland duct
ED	Epidermis
MG	Mucus gland
μ -CT	Synchrotron micro-computer-tomography
NIN	Ninhydrin-Schiff staining
OIO	Oil red O
PAS	Periodic acid-Schiff staining
PAS-D	Periodic acid-Schiff staining with subsequent diastase treatment
PPP	P-polarized SFG, P-polarized visible, P-polarized infrared
SFG	Sum frequency generation spectroscopy
SMA	Smooth muscle α -actin-antibody
SSP	S-polarized SFG, S-polarized visible, P-polarized infrared
vdW	Van der Waals
WUR	Wageningen University & Research

4.SI.2 Nomenclature of mucosubstances

Throughout the manuscript, we follow in the description of the various secretory products of amphibian mucus glands largely the nomenclature proposed by Kiernan (2015):

- **Mucus** The entire secretory product.
- **Mucosubstance** Polymeric sugar-protein-complexes.
- **Polysaccharides** (also: carbohydrates) Pure oligo- or polysaccharides (e.g. glycogen).
- **Proteoglycans** (also: heteroglycans) Heavily glycosilated proteins with long (hetero-)polysaccharide side-chains (e.g. mucopolysaccharides and acid mucopolysaccharides).
- **Mucopolysaccharides** (also: glycosaminoglycans, heteropolyaminosaccharides, or polyanionic glycoproteins) Proteoglycan side chains of polymeric disac-

charides (e.g. Sialoglycans). Acid mucopolysaccharides are also termed glycosaminoglucuronoglycans.

- **Glycoproteins** (also: mucins, i.e. glycoproteins with high sugar content) Proteins bearing covalently bound oligosaccharide chains (2 – 12 monosaccharide units).

4.SI.3 Materials

4.SI.3.1 Schematics of comparative approach

Table 4.SI.3 Comparative investigation of the ventral (ven.) and dorsal (dor.) mucus glands and secretions in arboreal (A, 'tree frogs') and terrestrial (T) frogs.

Technique	Comparison	Species
Synchrotron μ -CT	ven. vs. dor. digital glands	<i>Hyla cinerea</i> (A)
Cryo-histochemistry	ven. vs. dor. digital glands/mucus	<i>H. cinerea</i> (A)
ATR-IR & SFG	ven. digital vs. ven. abdominal mucus	<i>H. cinerea</i> (A), <i>Osteopilus septentrionalis</i> (A)
	ven. abdominal mucuses	<i>H. cinerea</i> (A), <i>O. septentrionalis</i> (A), <i>Ceratophrys cranwelli</i> (T), <i>Pyxicephalus adspersus</i> (T)

4.SI.3.2 Histochemistry procedures

Prior to all histochemical stainings, the cryo-sections were allowed to warm up to room temperature before fixing with 4% formalin.

Crossmon-Alcian blue (CRO) The Crossmon-Alcian blue stain was performed as described by Romeis (1968):

Solutions:

Acetic acid (3%)

Acetic acid, glacial	Merck, Germany	3 mL
Distilled water		97 mL

Alcian blue (pH 2.5)

Acetic acid, glacial		3 mL
Distilled water		97 mL
Alcian Blue GS	Fluka AG, Buchs SG, Switzerland	1 g

Mayer's Haematoxylin

Haematoxylin	VWR, The Netherlands	1 g
Distilled water		1000 mL
Sodium iodate	Merck, Germany	0.2 g
Potassium Alum	Merck, Germany	50 g
Chloral hydrate	VWR, The Netherlands	50 g
Citric acid	Sigma, USA	1 g
Filtrate before use		

Fuchsin/Orange G

Acid fuchsin	Merck, Germany	1.3 g
Orange G	Merck, Germany	1 g
Acetic acid, glacial		5 mL
Distilled water		500 mL
Thymol	Merck, Germany	0.33 g

Phosphotungstic acid (5%)

Phosphotungstic acid	Merck, Germany	25 g
Distilled water		500 mL

Light green (1%)

Light green SF	Chroma-Gesellschaft Schmid GmbH & Co, Germany	10 g
Acetic acid, glacial		10 mL
Distilled water		1000 mL

Protocol:

1)	Fixation with formalin	10 min
2)	Rinsing in distilled water	2 · 1 min
3)	Acetic acid (3%)	3 min
4)	Alcian blue (pH 2.5)	30 min
5)	Rinsing in acetic acid (3%)	20 s
6)	Rinsing in distilled water	2 · 2 min
7)	Mayer's Haematoxylin	7 min
8)	Rinsing in running tap water	10 min
9)	Fuchsin/Orange G	15 s
10)	Rinsing in distilled water	2 min
11)	Phosphotungstic acid (5%)	2 min
12)	Rinsing in distilled water	2 min
13)	Light green (1%)	2 min
14)	Rinsing in distilled water	2 · 1 min
15)	Dehydration (100% ethanol)	4 · 2 min
16)	Clearing with Xylene	3 · 2 min
17)	Mounting with DPX	

VWR, The Netherlands
BDH Laboratory Supplies, UK

Periodic acid-Schiff (PAS, PAS-D) The Periodic acid-Schiff stain was performed as described by Romeis (Mulisch & Welsch, 2010; Romeis, 1968):

Solutions:

Periodic acid (0.5%)		
Periodic acid	Merck, Germany	2.5 g
Distilled water		500 mL
K₂S₂O₅ (10%)		
K ₂ S ₂ O ₅	Merck, Germany	50 g
Distilled water		500 mL
HCl (1N)		
HCl (37%)	Merck, Germany	50 mL
Distilled water		500 mL
SO₂-water		
K ₂ S ₂ O ₅ (10%)		10 mL
HCl (1N)		10 mL
Distilled water		180 mL

Protocol:

1)	Fixation with formalin	10 min
2)	Rinsing in distilled water	2 · 1 min
3)	PAS: Distilled water / PAS-D: Saliva (diluted 1:2 with demineralised water at 37 °C)	60 min



4)	Rinsing in distilled water	3 · 1 min
5)	Periodic acid 0.5%	10 min
6)	Rinsing in distilled water	3 min
7)	Schiff's reagent	20 min
8)	Freshly made SO ₂ -water	3 · 2 min
9)	Rinsing in running tap water	5 min
10)	Rinsing in distilled water	2 min
11)	Counterstain with Mayer's Hematoxylin	3 min
12)	Rinse in running tap water	10 min
13)	Dehydration (96% to 100% ethanol)	
14)	Clearing with Xylene	3 · 2 min
15)	Mounting with Depex	

Alcian blue (pH 1.0, pH 2.5; AB) The Alcian blue stain was performed as described by Mulisch & Welsch (2010):

Solutions:

Alcian Blue pH 2.5

<u>Acetic acid 3%</u>	
Distilled water	194 mL
Acetic acid, glacial	6 mL
<u>Alcian Blue pH 2.5</u>	
Alcian Blue GS	2.0 g
Acetic acid (3%)	200 mL

Alcian Blue pH 1.0

<u>0.1 N HCl</u>	
1 N HCl	20 mL
Distilled water	180 mL
<u>Alcian Blue pH 1.0</u>	
Alcian Blue GS	2.0 g
0.1 N HCl	200 mL

Kernechtrot

<u>Aluminium sulphate 5%</u>		
Aluminium sulphate Al ₂ (SO ₄) ₃ · 18 H ₂ O	Merck, Germany	19.34 g
Distilled water		200 mL
<u>Kernechtrot</u>		
Kernechtrot	Chroma-Gesellschaft, Germany	0.2 g
Aluminium sulphate 5%		200 mL

Protocol:

1)	Fixation with formalin	10 min
2)	Rinsing in distilled water	2 · 1 min
3)	HCl 0.1N (for AB pH 1.0) / Acetic acid 3% (for AB pH 2.5)	5 min
4)	Alcian Blue (pH 1.0 or pH 2.5)	30 min

5)	Rinsing in running tap water	10 min
6)	Rinsing in distilled water	2 · 2 min
7)	Kernechtrot	5 min
8)	Rinsing in running tap water	2 min
9)	Rinsing in distilled water	2 · 2 min
10)	Dehydration (96% to 100% ethanol)	
11)	Cleaning with Xylene	3 · 2 min
12)	Mounting with Depex	

Coomassie Blue R250 (COO) The Coomassie blue stain was performed as described by Kiernan (2015):

Solutions:

Acetic ethanol

Acetic acid, glacial		100 mL
Ethanol 100%	Fisher Scientific, UK	300 mL

Staining solution

Coomassie blue R250	Bio-Rad, USA	40 mg
Acetic ethanol		200 mL

Staining solution diluted 1:3

Staining solution		25 mL
Acetic ethanol		75 mL

Protocol:

1)	Fixation with formalin	10 min
2)	Rinsing in distilled water	2 · 1 min
3)	Ethanol 100%	10 min
4)	Diluted staining solution	15 min
5)	Acetic ethanol	5 min
6)	Dehydration (96% to 100% ethanol)	
7)	Cleaning with Xylene	3 · 2 min
8)	Mounting with DPX	

Mercuric bromophenol blue (BRO) The Mercuric bromophenol blue stain was performed as described by Hornatowska (2005):

Solutions:

Staining solution

Mercuric chloride	Merck, Germany	10 g
Bromophenol blue	Fluka, Switzerland	100 mg
Distilled water		100 mL



Adjust pH of staining solution (pH 3.8 and pH 4.6) with HCl/NaOH.
NaOH

Merck, Germany

Protocol:

- | | | |
|----|--------------------------------|-----------|
| 1) | Fixation with formalin | 10 min |
| 2) | Hydration (Distilled water) | 2 · 1 min |
| 3) | Staining solution | 15 min |
| 4) | Acetic acid (0.5%) | 2 min |
| 5) | Rinsing in distilled water | 1 min |
| 6) | Dehydration (Tertiary butanol) | 1 min |
| 7) | Dehydration (Tertiary butanol) | 2 min |
| 8) | Clearing with Xylene | 1 min |
| 9) | Mounting with Depex | |

4 *Ninhydrin-Schiff (NIN)* The Ninhydrin-Schiff stain was performed as described by Bancroft & Stevens (1996):

Solutions:

Ninhydrin solution (0.5%)

Ninhydrin
Ethanol 100%

Merck, Germany

0.5 g
100 mL

Protocol:

- | | | |
|-----|--|-----------|
| 1) | Fixation with formalin | 10 min |
| 2) | Rinsing in distilled water | 2 · 1 min |
| 3) | Ethanol 70% | 10 min |
| 4) | Ninhydrin solution (37 °C), freshly made | Overnight |
| 5) | Rinsing in running tap water | 3 min |
| 6) | Schiff's reagent | 75 min |
| 7) | Rinsing in running tap water | 3 min |
| 8) | Dehydration (70% to 100% ethanol) | |
| 9) | Clearing with Xylene | 3 · 2 min |
| 10) | Mounting with Depex | |

Oil Red O (OIO) The Oil Red O stain was performed as described by Lillie & Ashburn (1943):

Solutions:

Oil Red O

Stock

Oil Red O
Isopropanol

Chroma-Gesellschaft
Merck, Germany

0.5 g
100 mL

Working solution

30 mL stock + 20 mL distilled water

Allow to stand for 10 min

Filtrate and cover immediately

Protocol:

- | | | | |
|----|--|-----------|----------------|
| 1) | Fixation with formalin | 10 min | |
| 2) | Rinsing in running tap water | 2 min | |
| 3) | Isopropanol 60% | 10 s | |
| 4) | Oil Red O, working solution,
freshly made | 10 min | |
| 5) | Isopropanol 60% | 1 dip | |
| 6) | Rinsing in distilled water | 4 · 1 min | |
| 7) | Mounting with glycerol | | Merck, Germany |

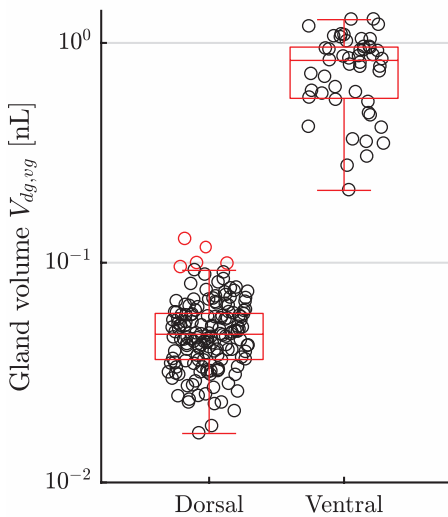
4.SI.4 Results**4.SI.4.1 Comparison of dorsal and ventral digital gland volumes**

Figure 4.SI.1 Individual digital mucus gland volumes in *Hyla cinerea*. Boxes indicate median, and 25th and 75th percentiles of the measured volumes of the dorsal (V_{dg} , $n = 158$) and ventral (V_{vg} , $n = 49$) digital glands. Values that are located more than 1.5 times the interquartile range above or below the boxes are shown as outliers (red circles).



4.SI.4.2 Distribution of the cumulative ventral gland volume along the longitudinal pad axis

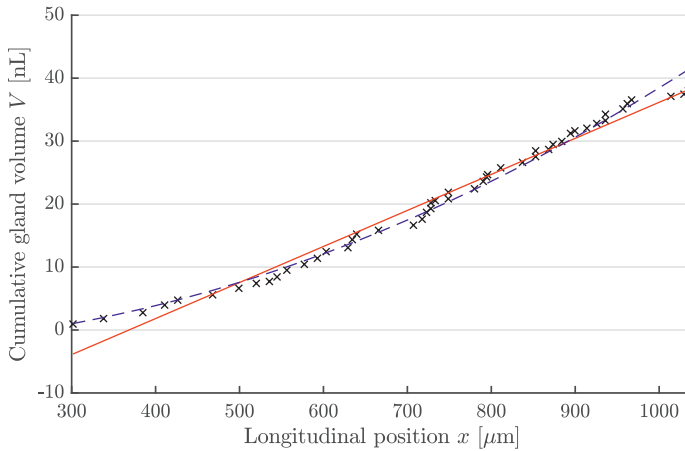
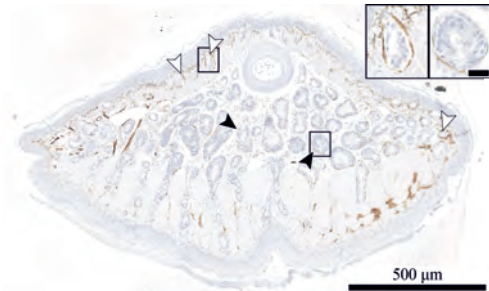


Figure 4.SI.2 Mucus distribution on the ventral pad surface. Cumulative ventral gland volume (i.e. the summarised volume of all glands distal to a given position along the longitudinal pad axis) as a function of longitudinal position x (low x : distal, high x : proximal). For an uniform gland pore distribution, a linear curve would be expected. A quadratic model ($V = -2.7 \text{ nL} + 4.1 \cdot 10^{-5} \text{ nL } \mu\text{m}^{-2} x^2$; Akaike information criterion for low sample sizes $\text{AICc} = -527.9$; blue dashed curve) fits the data better than a linear one ($V = -21.1 \text{ nL} + 5.7 \cdot 10^{-2} \text{ nL } \mu\text{m}^{-1} x$; $\text{AICc} = -498.4$; red continuous curve). The quadratic trend suggests an increased mucus volume present on the proximal half of the ventral pad surface.

4.SI.4.3 Myoepithelial cells of dorsal and ventral digital mucus glands

Figure 4.SI.3 Glandular myoepithelial cells in *Hyla cinerea*. Transverse section of the digital pad showing the immunohistochemically stained myoepithelial cells (brown) surrounding the dorsal (white arrowheads) and ventral (black arrowheads) mucus glands. Insets: Dorsal (left) glands appear to have a more strongly developed myoepithelial sheath than ventral ones (right); scale bar = 25 μm .



4.SI.4.4 Summary of histochemistry results

[See next page.]

Table 4.SI.4 Cryo- and immunohistochemical staining results of the dorsal and ventral mucus glands in the digital pads of *Hyla cinerea*.

	Dorsal			Ventral		
	Stain	Mucocytes	Lumen	Mucocytes	Lumen	
Overview						
Mucosubstances	CRO	+	+	+	+	+
	PAS	+	+	+	+	+
	PAS-D	+	+	+	+	+
	AB-1	-/0	-/0	-/0	-/0	-/0
	AB-2.5	+	+	+	+	+
	NIN	-	-	-	-	-
Proteins	BRO-3.8	0	0	0	0	0
	BRO-4.6	0	0	0	0	0
	COO	-	-	-	-	-
Lipids	OIO	-	-	-	-	-
Muscular structures	SMA	+	N/A	+	N/A	N/A

Staining results: + Staining, - No staining, 0 Equivocal staining.

Staining method: CRO Crossmon's light green trichrome including Mayer's haematoxylin and Alcian blue, PAS Periodic acid-Schiff, PAS-D Periodic acid-Schiff-Diastase, AB Alcian blue (pH = 1, pH = 2.5), NIN Ninhydrin-Schiff, BRO Mercuric bromophenol blue (pH = 3.8, pH = 4.6), COO Coomassie blue, OIO Oil red O, SMA Smooth muscle α -actin-antibody.

4.SI.4.5 Comparison of IR and SFG results

Interspecific comparison of IR spectra

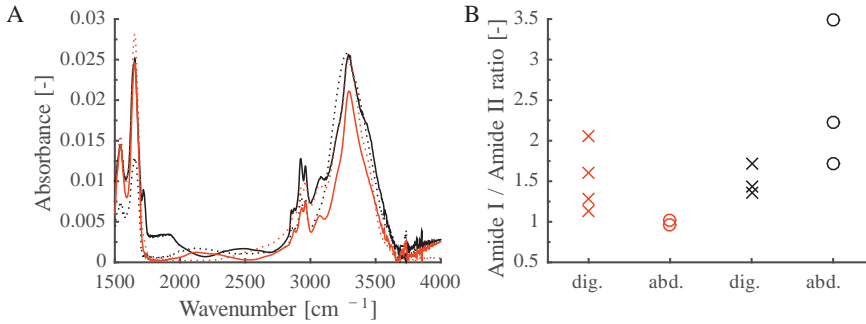


Figure 4.SI.4 Interspecific comparison of frog mucus IR spectra. (A) Comparison of ventral digital (solid line) and abdominal (dotted line) mucus in *Hyla cinerea* (black; abdominal spectrum scaled by ×3) and *Osteopilus septentrionalis* (red; digital spectrum scaled by ×0.8; abdominal spectrum scaled by ×0.3). (B) Comparison of amide I/amide II peak area ratios of mucus obtained from the digits (dig., crosses) and the abdomen (abd., circles) of *H. cinerea* (red) and *O. septentrionalis* (black). No significant differences were found in the peak area ratios between digital and abdominal mucus for both *H. cinerea* and *O. septentrionalis*. The statistical results are discussed in the main text.

Interspecific comparison of hydroxyl peak shifts in SFG spectra

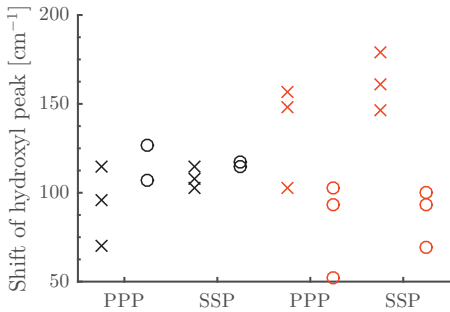


Figure 4.SI.5 Interspecific comparison of frog mucus SFG spectra. Comparison of hydroxyl peak shifts of mucus obtained from the digits (crosses) and the abdomen (circles) of *H. cinerea* (red) and *O. septentrionalis* (black) analysed with SFG in PPP and SSP polarisation. No significant differences were found in hydroxyl peak shifts between digital and abdominal mucus for both *H. cinerea* and *O. septentrionalis* in both polarisations. The statistical results are discussed in the main text.

4.SI.5 Discussion

4.SI.5.1 Histochemistry reports of anuran mucus in literature

[See next page.]

Table 4.SI.5 Histochemical staining results for the mucus glands of neobatrachians (top) and other anurans (bottom).

Family	Species	Mucosubstances	Proteins	Lipids	Reference
Bufoiidae	<i>Rhinella arenarum</i>	PAS-HE +, AB-2.5 +, HE/SAF +	COO -	SURIII -	Regueira <i>et al.</i> (2016)
Dendrobatidae	<i>Ameerega picta</i>	-	BRO -	-	Prates <i>et al.</i> (2012)
Hyliidae	<i>Bokermannohyla alvarengai</i>	PAS +, AB +	BRO 0	SUBB -	Centeno <i>et al.</i> (2015)
	<i>Hyla cinerea</i>	PAS +	-	-	Ernst (1973b)
	<i>H. arborea</i>	-	-	-	Gonlakowska-Wrhalinska & Kubicek (1998)
	various <i>Hyla</i>	PAS +, AB-1 -, AB-2.5 +	-	Nile blue -, Potassium dichromate and osmium tetroxide -	Barbeau & Lillywhite (2005)
	<i>Litoria caerulea</i>	PAS +	-	OIO -, SUBB - (secretion +)	Barnes <i>et al.</i> (2011); Wardburg <i>et al.</i> (2000)
Leiuperidae	various <i>Pleurodema</i> , <i>Sommuncaria</i>	PAS-HE +, AB-2.5 +	NIN -	-	Ferraro <i>et al.</i> (2011)
Leptodactylidae	<i>sommuncurensis</i>	-	BRO -	-	Prates <i>et al.</i> (2012)
	<i>Leptodactylus lineatus</i>	PAS-AB-2.5 +, PAS +, AB-2.5 +	NIN -, Performic acid-AB +	SUBB -, Copper Phthalocyanin -	Thomas <i>et al.</i> (1993)
Pipidae	<i>Xenopus laevis</i>	AB-2.5 +	-	-	Antoniazzi <i>et al.</i> (2013)
Phyllomedusidae	<i>Phyllomedusa distincta</i>	PAS-AB-2.5 +	BRO -	OIO -, SUBB - (secretion +)	Barbeau & Lillywhite (2005)
	<i>P. hypochondriacalis</i>	PAS +, AB-1 -, AB-2.5 +	-	-	Le Quang Trong (1971)
	various	PAS +, AB-0.2 +	-	-	Dapson (1969)
	<i>Phrynobatrachus</i>	-	-	-	Barbeau & Lillywhite (2005)
	<i>Rana pipiens</i>	PAS +, AB-0.4 +, AB-2.8 +	BRO -	-	Elis & Herneberg (1990)
	<i>R. utricularia</i>	PAS +, AB-1 -, AB-2.5 +	-	OIO -, SUBB - (secretion +)	Brizzi <i>et al.</i> (2002)
	<i>R. fuscigulara</i>	PAS +, PAS-AB +	NIN +	-	Ferraro <i>et al.</i> (2011)
	various <i>Rana</i>	PAS +, AB-2.5 +	-	-	Barbeau & Lillywhite (2005)
	<i>Polypedutes muculatus</i>	PAS +, PAS-D +, PAS (acetylated) -, PAS-AB +, AB-2.5 -/+	-	SUBB +, Br-SUBB +, SUIII -, Nile blue sulphate +	Barbeau & Lillywhite (2005)
Rhacophoridae					
Amphiumidae	<i>Amphiuma tridactylum</i>	PAS-AB-2.5 +, AB-2.5 +	BRO 0	-	Pereira <i>et al.</i> (2018)
Plethodontidae	<i>Ensatina eschscholtzii</i>	PAS +, AB-2.5 -	-	-	Fontana <i>et al.</i> (2006)
Salamandridae	<i>Typhlotriton verrucosus</i>	PAS +, AB-2.5 +	COO -	-	Wanninger <i>et al.</i> (2018)
Siphonopidae	<i>Siphonops annulatus</i>	PAS +, AB-2.5 +	BRO -	SUBB +	Javed <i>et al.</i> (2018)

Staining result: - Negative, 0 Equivocal, + Positive. Staining method: PAS Periodic acid-Schiff, AB-X Alcian blue (-pH), TOB Toluidine blue, SUBB Sudan black B, SUX Sudan I to IV, SURIII Sudan red III, OIO Oil red O, HE-EO Hematoxylin-eosin.



4.SI.5.2 Anuran gland cluster reports in literature

Table 4.SI.6 Depictions and mentions of digital mucus gland clustering in neobatrachians.

Family	Species	Reference
Centrolenidae	<i>Centrolenella parabambae</i>	Noble & Jaeckle (1928)
Dendrobatidae	<i>Dendrobates tinctorius</i>	Noble & Jaeckle (1928)
	<i>Phyllobates latinus</i>	Noble & Jaeckle (1928)
Hemiphractidae	<i>Acris gryllus</i>	Noble & Jaeckle (1928)
	<i>Gastrotheca christiani</i>	Manzano <i>et al.</i> (2007)
	<i>G. marsupiata</i>	Hertwig & Sinsch (1995)
Hylidae	<i>Hyla cinerea</i>	This study
	<i>Hypsiboas riojanus</i>	Manzano <i>et al.</i> (2017)
	<i>Litoria caerulea</i>	Personal observation, Nakano & Saino (2016)
	<i>Phyllomedusa sawagii</i>	Manzano <i>et al.</i> (2007)
	<i>P. trinitatis</i>	Ba-Omar <i>et al.</i> (2000)
	<i>Scinax fuscovarius</i>	Fabrezi <i>et al.</i> (2017)
Hylodidae	<i>Elosia bufonia</i>	Noble & Jaeckle (1928)
Hyperoliidae	<i>Leptopelis karissimbenses</i>	Drewes (1984)
Mantellidae	<i>Guibemantis timidus</i>	Manzano <i>et al.</i> (2007)
Phrynobatrachidae	<i>Phrynobatrachus dendrobates</i>	Noble & Jaeckle (1928)
Ranidae	<i>Rana temporalis</i>	Gaupp (1904)
Rhacophoridae	<i>Philautus annandalii</i>	Chakraborti <i>et al.</i> (2012)
	<i>Polypedates reinwardtii</i>	Siedlecki (1910)





Since each cell protrudes slightly with its free end, thus forming innumerable fine protuberances over the entire pad, they can interlock with the unevenness of even the seemingly smoothest surface, by pressing on it.

F. Leydig, 1868

CHAPTER 5

Estimating the maximum attachment performance of tree frogs on rough substrates

Abstract

Tree frogs can attach to smooth and rough substrates using their adhesive toe pads. We present the results of an experimental investigation of tree frog attachment to rough substrates, and of the role of mechanical interlocking between superficial toe pad structures and substrate asperities in the tree frog species *Litoria caerulea* and *Hyla cinerea*. Using a rotation platform setup, we quantified the adhesive and frictional attachment performance of whole frogs clinging to smooth, micro-, and macrorough substrates. The transparent substrates enabled quantification of the instantaneous contact area during detachment by using frustrated total internal reflection. A linear mixed-effects model shows that the adhesive performance of the pads does not differ significantly with roughness (for nominal roughness levels of 0–15 μm) in both species. This indicates that mechanical interlocking does not contribute to the attachment of whole animals. Our results show that the adhesion performance of tree frogs is higher than reported previously, emphasising the biomimetic potential of tree frog attachment. Overall, our findings contribute to a better understanding of the complex interplay of attachment mechanisms in the toe pads of tree frogs, which may promote future designs of tree-frog-inspired adhesives.

Keywords: Bioadhesion; Biomimetics; Bioinspired adhesive; *Litoria caerulea*; *Hyla cinerea*; Surface roughness; Mechanical interlocking.

This chapter has been published as: LANGOWSKI, J.K.A., RUMMENIE, A., PIETERS, R.P., KOVALEV, A., GORB, S.N. & VAN LEEUWEN, J.L. (2019). Estimating the maximum attachment performance of tree frogs on rough substrates. *Bioinspiration & Biomimetics* **14**, 2, p. 025001.

5.1 Introduction

Strong, reversible, and repeatable attachment to a variety of substrates with different geometrical, mechanical, and chemical properties is a basic requirement both for climbing animals and for next-generation technological adhesives (Peattie, 2009). This overlap in functional demands has led to a considerable transfer of knowledge between the fields of biological and technical adhesion (e.g. von Byern & Grunwald, 2010; Creton & Gorb, 2007; Favi *et al.*, 2014; Gebeshuber, 2007; Lepora *et al.*, 2013; Smith, 2016), and to the design of a large number of biomimetic and bioinspired adhesives (Bogue, 2008; Favi *et al.*, 2014; Flammang & Santos, 2015; Li *et al.*, 2013).

Geckos and tree frogs are the most prominent vertebrate models for the design of biomimetic adhesives (Barnes, 2007a; Chen *et al.*, 2015; Drotlef *et al.*, 2013; Jagota & Hui, 2011; Kamperman *et al.*, 2010). The toes of geckos are ‘hairy’ structures covered by numerous microscopic setae ending in nanoscopic spatulae and can conform to minute asperities of the substrate, hence facilitating the generation of ‘dry’ intermolecular van der Waals (vdW) forces between toe and substrate (Autumn *et al.*, 2000, 2002; Filippov & Gorb, 2015; Huber *et al.*, 2005). The ventral epidermis on the toe pads of tree frogs is relatively smooth compared to that of the gecko, but it also forms a surface pattern consisting of microscopic prismatic cells that are covered with nanoscopic cellular protrusions (‘nanopillars’) and separated by channels (Ernst, 1973a; Scholz *et al.*, 2009). In contrast to geckos, tree frogs rely on a wet environment, and their permeable skin is inherently moist (Haslam *et al.*, 2014; Stebbins & Cohen, 1995; Wells, 2007). Accordingly, their toe pads stand out as a model system for attachment in wet conditions. The toe pads have been proposed to give rise to ‘wet adhesion’ (Emerson & Diehl, 1980; Hanna & Barnes, 1991; Nachtigall, 1974; Schuberg, 1891; Siedlecki, 1909; v. Wittich, 1854), which comprises capillary and hydrodynamic attachment forces (Barnes, 2012; Endlein & Barnes, 2015; e.g. Stefan adhesion). VdW forces (Emerson & Diehl, 1980; Federle *et al.*, 2006) and mechanical interlocking (Crawford *et al.*, 2016; Emerson & Diehl, 1980; Green, 1981; Komnick & Stockem, 1969) have also been discussed to contribute to the adhesion (i.e. the attachment force normal to the substrate surface) and friction (i.e. the attachment force parallel to the substrate surface) of tree frogs.

Studying the fundamental mechanisms of tree frog attachment contributes not only to the understanding of the ecology (Emerson, 1991; Green & Simon, 1986) and evolution (Moen *et al.*, 2013; Sustaita *et al.*, 2013) of these animals, but also promotes the technical development of biomimetic adhesives for operation in a wet environment, for example in surgery (Barnes *et al.*, 2011) or robotics (Barnes *et al.*, 2008). Measuring adhesion, friction, and the respective contact-area-normalised contact stresses as a function of substrate properties such as free surface energy, stiffness, or roughness is a common approach to elucidate the fundamental mechanisms of an attachment apparatus (Barnes *et al.*, 2002; Bullock & Federle, 2011; Klittich *et al.*, 2017; Stark *et al.*, 2013). For example, insect claws can only interlock mechanically with substrate asperities above a critical roughness (Dai *et al.*, 2002; Ditsche-Kuru *et al.*, 2012).

Analogously, mechanical interlocking of the superficial structures on a tree frogs' toe pad with substrate asperities should be—if present at all—maximal when the nominal roughness R of the substrate (defined, unless mentioned otherwise, as the characteristic size of the substrate asperities) is similar or larger in size than the pad surface structures (i.e. ≈ 300 nm for the nanopillars (Scholz *et al.*, 2009) and ≈ 10 μm for the epidermal cells Ernst, 1973a). The attachment forces generated by the other proposed attachment mechanisms might also be critically attenuated with increasing substrate roughness, for example by reducing the effective contact area (Vakis *et al.*, 2018) or by meniscus cavitation (Barnes, 1999; Crawford *et al.*, 2016).

Traditionally, the attachment performance of a whole tree frog is quantified by measuring the angles at which a frog begins to slide on (sliding angle α_{\parallel}) and finally falls off (falling angle α_{\perp}) from a substrate rotating around a horizontal axis (referred to as 'rotation platform'; Barnes, 1999; Barnes *et al.*, 2006; Emerson & Diehl, 1980). These angles are proxies for the whole-animal (static) friction and adhesion, respectively. Previous work shows slight variations of falling and sliding angle with increasing roughness up to ca. 15 μm (Barnes, 1999; Barnes *et al.*, 2002; Crawford *et al.*, 2016; Endlein *et al.*, 2013). At higher roughness levels, adhesive (Barnes, 1999; Crawford *et al.*, 2016) as well as frictional (Crawford *et al.*, 2016) performance decline. For computation of the contact-area-normalised whole-animal adhesion (i.e. tenacity), previous studies exclusively used the maximum total contact area of all toe pads and neglected inertial loads acting on the pads. Measurements of the whole-animal attachment performance on nano- to microrough substrates under control of substrate surface energy, and under consideration of the instantaneous contact area (i.e. the actual contact area just before falling) and of dynamic loads are largely missing, which may have led to an underestimation of the attachment performance of tree frogs.

Here, we present a study of the whole-animal attachment performance of tree frogs as a function of substrate roughness on smooth (i.e. a nominal roughness $R = 0$ μm), micro- ($R = 0.1$ μm , 0.5 μm , 6 μm , and 15 μm), and macrorough ($R = 200$ μm) substrates in the species *Litoria caerulea* and *Hyla cinerea*, which are among the most intensively studied tree frog species (Barnes *et al.*, 2008, 2011; Emerson & Diehl, 1980; Ernst, 1973a,b; Federle *et al.*, 2006; Green, 1981; Linnenbach, 1985; Scholz *et al.*, 2009). Most previous studies included smooth and macrorough substrates, distinguishing these roughness levels as reference cases. Using a custom-built rotation platform, which allows the dynamic measurement of the instantaneous contact area, we aim to (i) characterise the whole-animal attachment performance on rough substrates, (ii) test whether mechanical interlocking contributes to the adhesion of the toe pads, and (iii) provide an estimate for the maximum adhesion performance of tree frogs' toe pads. As tree frogs frequently encounter substrates with diverse properties (Koch *et al.*, 2008), we expect that adhesion and friction are insensitive towards a large range of substrate roughness levels. If mechanical interlocking is present as proposed previously, we expect an increase in attachment performance with increasing roughness. In particular, the attachment performance should increase stepwise when the substrate roughness gets larger than the nanopillars (i.e. switching from 0.1 nm

to $0.5\ \mu\text{m}$) or the epidermal cells (i.e. switching from $6\ \mu\text{m}$ to $15\ \mu\text{m}$). A stepwise decrease in attachment performance may be expected at an even higher roughness (i.e. $200\ \mu\text{m}$), when the substrate asperities become too large to allow interlocking with the micro- to nanoscopic pad surface structures. As the animal-substrate contact area in friction measurements is dominated by the belly (Brehm, 1892; Endlein *et al.*, 2013; Gadow, 1909; Schuberg, 1891; Siedlecki, 1909), we can only analyse the whole-animal performance with respect to friction.

5.2 Materials and methods

5.2.1 Experimental animals

Experiments were performed with adult individuals of *Litoria caerulea* (number $n = 6$, body mass $m = 46.8 \pm 13.4\ \text{g}$, snout-vent-length $\ell_{\text{SV}} = 79.2 \pm 5.6\ \text{mm}$; unless mentioned otherwise, we report mean \pm standard deviation throughout this study) and *Hyla cinerea* ($n = 6$, $m = 8.7 \pm 1.7\ \text{g}$, $\ell_{\text{SV}} = 48.7 \pm 1.6\ \text{mm}$). The animals were housed, separated by species, in $0.6 \cdot 0.6 \cdot 1.2\ \text{m}^3$ (width \cdot length \cdot height) large terraria, with six frogs per terrarium, at the CARUS research facility at WUR. The terraria were enriched with plants (*Ficus spec.*) and scaffolds of polypropylene-pipes. Temperature and relative air humidity were kept at $24\text{--}26\ ^\circ\text{C}$ and $45\text{--}85\%$, using heating mats and a semi-automatised sprinkler system spraying demineralised water (Bitter Watertreatment, The Netherlands), respectively. The frogs were kept at a 12 h : 12 h dark-light-cycle and fed 2–3 times per week with 3–5 live crickets enriched with vitamin/mineral powder (Dendrocare, AmVirep, The Netherlands) per individual; water was supplied *ad libitum*. The room air was filtered for pathogens with an air purifier (WINIX U300, Winix, USA). The frogs were monitored daily for their wellbeing.

5.2.2 Test substrates

Transparent, stiff substrates with a defined roughness and a surface area of $290 \cdot 210\ \text{mm}^2$ were produced in a two-stage-casting-process (similar to Gorb, 2007; Koch *et al.*, 2008). To create substrates with nominal roughness levels of $0\ \mu\text{m}$ (smooth), $0.1\ \mu\text{m}$, $0.5\ \mu\text{m}$, $6\ \mu\text{m}$, $15\ \mu\text{m}$, and $200\ \mu\text{m}$ (macrorough), a thin sheet of plexiglas, diamond lapping film (661X, 3M, USA), or conventional sandpaper (grit size 80, KWB, Germany) with the according particle size was glued into an aluminium mould (Fig. 5.1A). Polydimethylsiloxane (PDMS; Sylgard 184, Dow Corning, USA) was prepared at a base:curing-agent ratio of 10:1, degassed in a vacuum-oven, and filled into the mould to create a negative of the rough surface (Fig. 5.1B). Before casting, the mould was slightly tilted to avoid bubble formation. After curing, the PDMS-negative was removed (Fig. 5.1C) and filled with vacuum-degassed epoxy resin prepared at a base:curing-agent ratio of 1:0.9 (Crystal Clear 200, Smooth-On, USA; Shore hardness

Table 5.1 Conventional roughness parameters R_a (arithmetic average roughness) and RMS (root mean squared roughness) of the used substrates in μm (mean \pm standard deviation, $n = 10$). For the smooth to $15\ \mu\text{m}$ substrates, roughness was measured by white light interferometry, for the macrorough substrate with profilometry ($120\times$ magnification).

	Mag.	Smooth	0.1 μm	0.5 μm	6 μm	15 μm	Macrorough
R_a	5 \times	.024 \pm .007	.438 \pm .022	.476 \pm .017	.405 \pm .025	.441 \pm .046	88.214 \pm 11.893
	50 \times	.005 \pm .002	.425 \pm .023	.474 \pm .032	.410 \pm .072	.484 \pm .122	
RMS	5 \times	.053 \pm .014	.591 \pm .030	.628 \pm .055	.684 \pm .029	.965 \pm .076	N/A
	50 \times	.006 \pm .002	.534 \pm .028	.579 \pm .034	.667 \pm .096	.961 \pm .141	

Mag. Magnification.

= 80 D, Elastic modulus ≈ 400 MPa; Fig. 5.1D), which resulted in a positive cast of the rough surface (Fig. 5.1E).

Surface roughness was characterised and spatial homogeneity of the surface profiles of the test substrates was ensured using a VR-3100 3D measuring macroscope (Keyence, Japan) and a New View 6000 white light interferometer (Zygo, USA). Conventional roughness parameters of the substrates are shown in Table 5.1, a more elaborate roughness analysis can be found in Section 5.SI.2.1. With an OCAH 200 contact angle measuring system (DataPhysics Instruments, Germany) and the sessile drop method, we computed for the hydrophilic substrate material (water contact angle $71.92 \pm 2.07^\circ$, $n = 5$) a free surface energy γ of $39.2\ \text{mJ m}^{-2}$ (dispersive component $\gamma_d = 30\ \text{mJ m}^{-2}$, polar component $\gamma_p = 9.2\ \text{mJ m}^{-2}$) with the Owens, Wendt, Rabel, and Kaelble (OWRK) method (Kaelble, 1970; Owens & Wendt, 1969; Rabel, 1971; see Section 5.SI.2.2).

5.2.3 Experimental setup and protocol

A custom-built rotation platform was used to quantify the whole-animal attachment performance of the studied frog species (Fig. 5.2A). The test substrates were rotated around a horizontal axis at an angular speed of ca. 3.6°s^{-1} , driven by a RS Pro brushed DC geared motor (RS Components, The Netherlands) via a pulley-timing-belt-system (27-T5; Madler, Germany). A custom-programmed Arduino (Arduino Uno revision 3, Arduino) read out the platform angle from an angle sensor (981 HE

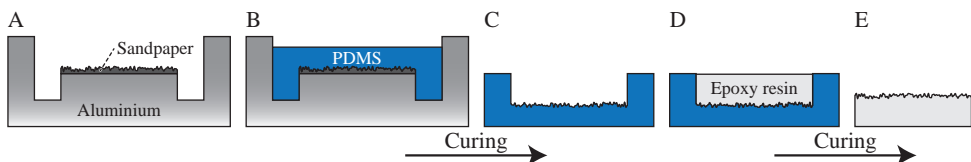


Figure 5.1 Generation of the transparent and stiff test substrates with defined roughness. (A) Roughness template (e.g. sandpaper) glued with double-sided tape into an aluminium mould. (B) Polydimethylsiloxane (PDMS) cast into the aluminium mould. (C) Cured negative PDMS-cast of the rough surface. (D) Epoxy resin cast into the PDMS-mould. (E) Cured positive epoxy-cast of the rough surface.

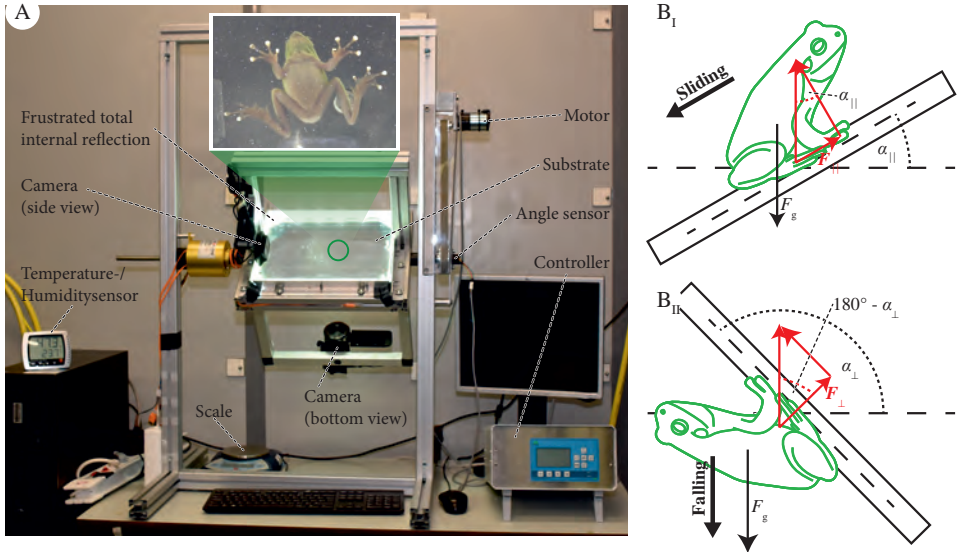


Figure 5.2 (A) Rotation platform setup (inset: example of the recorded bottom view of a frog clinging to the rotating substrate). (B) Free body diagrams of a frog at the onset of (B_I) sliding and (B_{II}) falling. α_{\perp} falling angle, α_{\parallel} sliding angle, F_g body weight, F_{\perp} adhesion, F_{\parallel} friction.

special, Vishay Spectrol, USA; linearity $\pm 0.5\%$).

Four LED-strips (LS-OO06-STWH-SD111; Intelligent LED Solutions, UK) were mounted at the sides of the transparent substrate such that the emitted light was reflected internally. This allowed us to visualise the instantaneous pad-substrate contact area by frustrated total internal reflection (FTIR; Hill *et al.*, 2018), which utilises the frustration of the internal reflection at locations of animal-substrate contact, causing local light scattering (inset in Fig. 5.2A). The contact area was recorded ventrally with a HC-VX980 camcorder rotating with the substrate (Panasonic, Japan; $3840 \cdot 2160$ pixels, effective pixel size $\approx 90 \cdot 90 \mu\text{m}^2$) at 30 frames per second, resulting in an angular step size of 0.12° per frame. The video recordings and angle measurements were synchronised using a sound signal (duration < 5 ms) at regular time intervals ($\Delta t \approx 2.14$ s). The animals were filmed laterally with a C930e webcam (Logitech, Switzerland; $1920 \cdot 1080$ pixels, 30 frames per second) to inspect general body positing and movements.

Prior to each trial, the animals were rinsed carefully with demineralised water to remove contaminations that could influence attachment performance, and subsequently put on a smooth polymer sheet to standardise the amount of liquid covering the ventral body surface. Six individuals each of *L. caerulea* and *H. cinerea* were tested for the six substrates with different roughness levels in a randomised order. To compensate for the variation in the measurements due to behavioural variation in the animals, we repeated each individual-roughness-combination 10 times (i.e. a trial), leading to a total of 720 trials (60 per species and roughness level). In each trial, individual

animals were placed head upwards on the substrate and rotated from a horizontal (0°) into a vertical (90°) and finally an overhanging position ($> 90^\circ$). Belly-substrate contact was impaired by gently prodding the animals with a soft object. Trials were excluded when the frogs jumped off the substrate, moved outside the substrate area with specified roughness, or made extensive contact with body parts other than the toe pads before falling (in adhesion measurements), leading to 133 and 72 trials of *L. caerulea*, and 106 and 70 trials of *H. cinerea* for further analysis of their adhesion and friction performance, respectively. These trials include cases with only a few toes in contact.

5.2.4 Data analysis and statistics

Data analysis was performed with a custom-made MATLAB routine (Version R2015a, The Mathworks, USA). From the videos, the angles at which the frogs started sliding (α_{\parallel}) and lost contact to the substrate (α_{\perp}) with all four limbs were identified. For the determination of the instantaneous contact area A just before falling, we measured the contact area of all toes in contact at the last recorded moment before detachment, at which the number of toes in contact was constant and the contact area of individual toes was not yet decreasing (i.e. static contact; see also Fig. 5.SI.2). The instantaneous contact area was quantified with ImageJ (Version 1.51g, National Institutes of Health, USA). This was not possible for the macrorough substrate because of too strong scattering of the totally internally reflected light.

For each frog individual, the snout-vent-length ℓ_{SV} was recorded by a calibrated dorsal photograph made with a Nikon 5500 camera using a Nikon AF-NIKKOR 24 mm f/2.8 D lens ($6000 \cdot 4000$ pixels, effective pixel size $47 \cdot 47 \mu\text{m}^2$); immediately after each trial, body mass m , environmental temperature T , and relative air humidity H were recorded using an OHAUS Scout Pro balance (Parsippany, USA; resolution: 0.01 g) and a testo 608-H1 hygrometer (Testo Ltd, UK; resolution: 0.1°C , 0.1%), respectively.

From the sliding and falling angle (α_{\parallel} and α_{\perp}), body mass m , and instantaneous contact area A , we computed adhesion F_{\perp} , static friction F_{\parallel} , and the adhesive contact stress (i.e. tenacity σ_{\perp}) as follows (Fig. 5.2B; Barnes, 2006):

$$F_{\perp} = m g \cos(180 - \alpha_{\perp}) = -m g \cos(\alpha_{\perp}) \quad 90^\circ < \alpha_{\perp} < 180^\circ \quad (5.1a)$$

$$F_{\parallel} = m g \sin(\alpha_{\parallel}) \quad 0^\circ < \alpha_{\parallel} < 90^\circ \quad (5.1b)$$

$$\sigma_{\perp} = \frac{F_{\perp}}{A} \quad (5.1c)$$

In these equations, we assume an equal distribution of load over all limbs and toes, and neglect inertial effects. The potential effects of substrate roughness on the attachment performance of tree frogs were analysed by fitting the falling angle α_{\perp} and sliding angle α_{\parallel} as a function of substrate, species, and body mass in a linear mixed-effect model in MATLAB (significance level $\alpha = 0.05$). Based on the Akaike information criterion

adjusted for small sample sizes (AICc; Burnham & Anderson, 2002), snout-vent-length, temperature, and relative humidity were excluded as fixed effects. Individual identity was fitted as random intercept to correct for interindividual variation that is not accounted by the fixed effects. Measurement date was fitted as additional random intercept to correct for variation between measurement days. Moreover, the interaction between individual identity and substrate, as well as between individual identity and repetition number were fitted as random intercepts to correct for pseudo-replication and to quantify the variation of an individual within a given substrate and repetition number, respectively. For the model diagnostics see Section 5.SI.4.

5.3 Results

Tree frogs are able to generate adhesion and friction on substrates with different roughness levels. Over the course of measurements, temperature and relative air humidity were 23.3–26.3 °C and 39.8–69.0%, respectively. During single trials, the animals regularly moved across the rotating platform, requiring prodding with the hands of the experimenter to keep the frogs on the platform (Fig. 5.3). Typical changes in body posture were observed, with frogs taking a splayed body posture with increasing substrate inclination, as discussed in detail elsewhere (Endlein *et al.*, 2013, 2012). Over the course of one trial, large changes in the number of contact points and in the size of the instantaneous contact area were observed, ranging from—in addition to the toes—full belly contact to the contact of only a few toes of two limbs (Fig. 5.3).

Interestingly, we observed several instances where frogs clinging to the substrate at an angle of approximately 120–130° were able to remain attached although temporarily the forelimbs completely detached from the substrate and the animals swung back-and-forwards (Fig. 5.4).

In the following sections, we describe the adhesion performance of the toe pads and the friction performance of whole animals for the studied frog species.

5.3.1 Adhesion performance

For *L. caerulea*, the falling angle α_{\perp} ranges from $93.0 \pm 13.4^{\circ}$ (macrorough substrate) to $129.1 \pm 11.2^{\circ}$ (0.1 μm substrate; Fig. 5.5). The falling angles on the 0.1 μm , 0.5 μm ($118.1 \pm 24.4^{\circ}$), 6 μm ($128.2 \pm 12.6^{\circ}$), and the 15 μm substrate ($128.8 \pm 14.7^{\circ}$) do not differ significantly from α_{\perp} on the smooth substrate ($119.4 \pm 18.2^{\circ}$), whereas falling angles on the macrorough substrate are significantly lower by $36.1 \pm 4.9^{\circ}$ than on the smooth substrate (estimate \pm 95% confidence interval [CI]; see Table 5.2 for the linear mixed-effect model statistics). The falling angle scales negatively with body mass m (slope = $-0.34 \pm 0.28^{\circ} \text{g}^{-1}$, estimate \pm 95% CI; $t = -2.337$, DF = 231, $p = 0.020$).

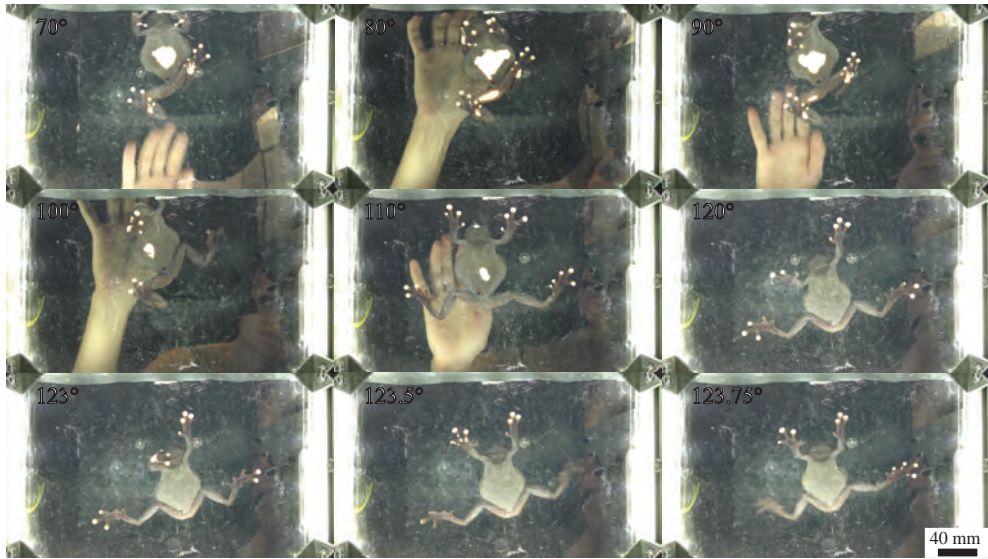


Figure 5.3 Rotation platform trial for an individual of *L. caerulea* on a smooth substrate. At platform angles $\leq 100^\circ$, the belly contributes to the overall contact area. Just before detachment (angles $\leq 123^\circ$), quick limb movements are visible, which result in time and space dependent variations of the ensemble of pad-substrate contact areas.

The adhesion F_\perp of *L. caerulea* ranges between 192.8 ± 85.7 mN and 282.1 ± 88.5 mN for roughness levels between smooth and $15 \mu\text{m}$. On the macrorough substrate, F_\perp drops by 81% to 50.2 ± 63.5 mN, if compared to the smooth substrate; adhesion on the macrorough substrate is significantly different from the other roughness levels according to one-way ANOVA with Bonferroni correction ($F[5,100] = 29.98$, $p < 0.001$). The adhesive tenacity σ_\perp ranges from 2.1 ± 0.8 mN mm $^{-2}$ (smooth substrate) to 2.8 ± 0.9 mN mm $^{-2}$ ($15 \mu\text{m}$ substrate). The tenacity measures are not significantly different, as determined by one-way ANOVA with Bonferroni correction ($F[4,88] = 1.46$, $p = 0.220$). Tenacity could not be quantified for the macrorough substrate because of too strong scattering of the internally reflected light. Peak tenacities of

Table 5.2 Fixed-effects coefficient estimates of the linear mixed-effects model for the falling angles of tree frogs on substrates with different roughnesses (in degree). *SE* standard error, *DF* degrees of freedom, *t* t-statistic, *p* p-value.

	Estimate	SE	DF	<i>t</i>	<i>p</i>
Intercept ^a	142.73	7.26	231	19.665	<0.001
<i>Hyla cinerea</i>	-11.60	6.07	231	-1.912	0.057
0.1 μm	0.60	2.36	231	0.254	0.799
0.5 μm	-1.78	2.69	231	0.287	0.774
6 μm	0.71	2.48	231	0.419	0.676
15 μm	1.02	2.42	231	-0.661	0.510
Macrorough	-36.12	2.47	231	-14.619	<.001
Body mass	-0.34	0.14	231	-2.337	0.020

^a *Litoria caerulea* on the smooth substrate.

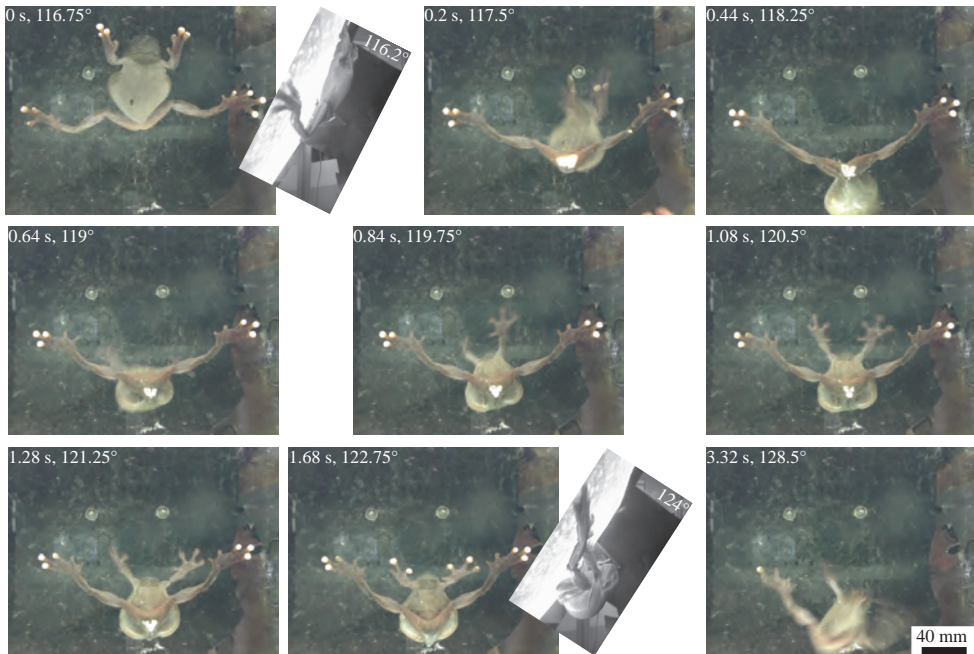


Figure 5.4 Attachment dynamics of *L. caerulea* clinging to a rotating, overhanging, smooth substrate. After detachment of the forelimbs, the body swings backwards by more than 90°. During the swinging phase, inertial loads are likely to act on the attachment interface in addition to the static body weight. Insets show the body posture in lateral view. To improve clarity, the images were filtered by outlier-removal (ImageJ).

8.8 mN mm⁻² were measured.

Similar trends were observed for the adhesion performance of *H. cinerea*, and the linear mixed-effects model does not show significant differences between the two species ($t = -1.912$, $DF = 231$, $p = 0.057$). Falling angles range from $126.9 \pm 8.2^\circ$ to $130.1 \pm 9.2^\circ$ for roughness levels between smooth and $15 \mu\text{m}$, and the falling angle decreases significantly on the macrorough substrate, if compared to the other roughness levels. Compared to *L. caerulea*, *H. cinerea* generates much lower adhesion of 46.9 ± 15.1 mN to 54.5 ± 16.0 mN for roughness levels between smooth and $15 \mu\text{m}$. On the macrorough substrate, *H. cinerea* barely adheres ($F_{\perp} = 2.0 \pm 14.2$ mN). The tenacity varies between 1.5 ± 0.7 mN mm⁻² and 2.8 ± 1.1 mN mm⁻² on the five less rough substrates, mostly without significant differences; only on the $0.1 \mu\text{m}$ ($p = 0.003$) and the $15 \mu\text{m}$ ($p = 0.003$) substrate, the frogs generated significantly higher tenacities compared to the smooth substrate, as found in a multiple comparison using Bonferroni correction.

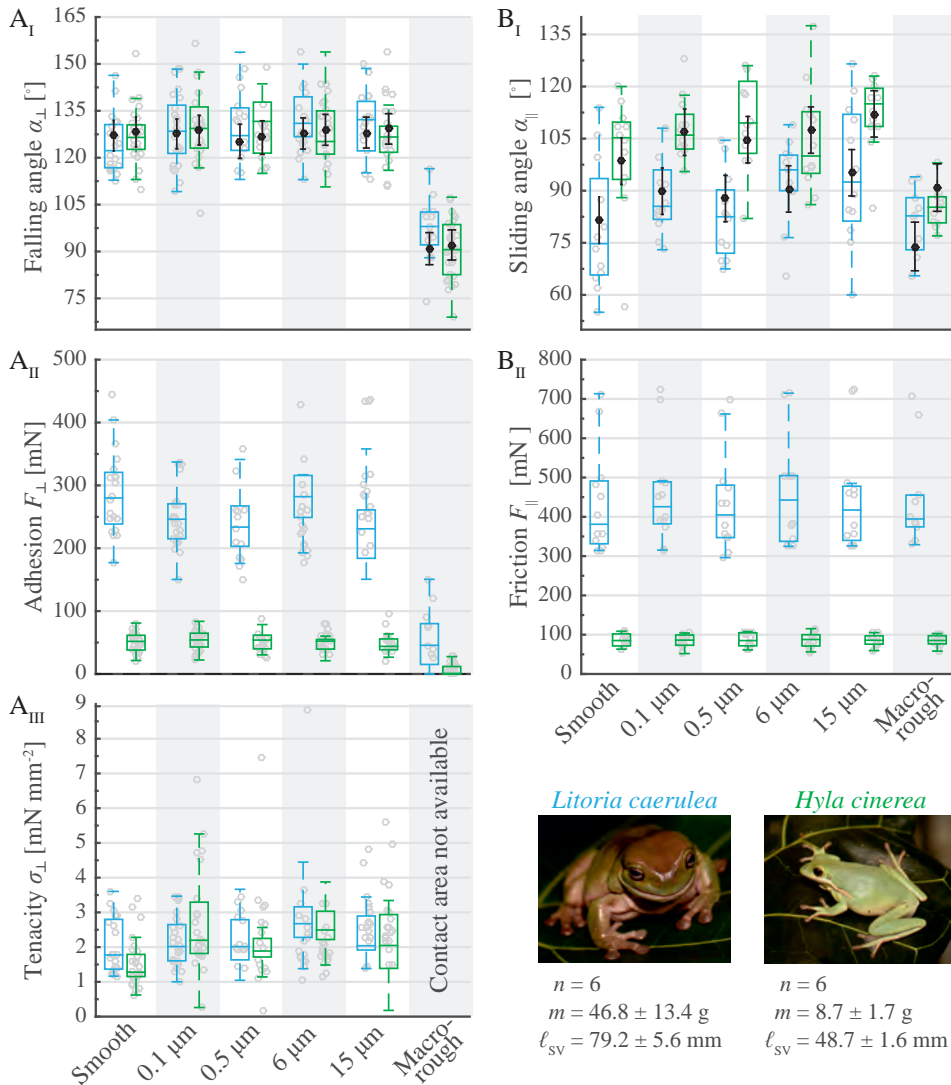


Figure 5.5 (A_I) Falling angle α_{\perp} , (A_{II}) adhesion F_{\perp} , and (A_{III}) tenacity σ_{\perp} , as well as (B_I) sliding angle α_{\parallel} and (B_{II}) (static) friction F_{\parallel} as a function of (nominal) substrate roughness R for *Litoria caerulea* (blue) and *Hyla cinerea* (green). For sliding angles $\alpha_{\parallel} > 90^{\circ}$, the friction F_{\parallel} was computed with $\alpha_{\parallel} = 90^{\circ}$. Boxes indicate median, and 25th and 75th percentiles of the measured values. Values that are located more than 1.5 times the interquartile range above or below the boxes are shown as outliers. For the falling and sliding angle, black dots and whiskers denote the mean values and the 95% confidence intervals predicted from the linear mixed-effects models. Strong scattering of the internally reflected light prevented the measurement of the contact area and thus of the tenacity on the macro-rough substrate.

Table 5.3 Fixed-effects coefficient estimates of the linear mixed-effects model for the sliding angles of tree frogs on substrates with different roughnesses (in degree). Symbols as in Table 5.2.

	Estimate	SE	DF	t	p
Intercept ^a	87.94	7.75	134	11.352	<0.001
<i>Hyla cinerea</i>	11.73	6.33	134	1.855	0.066
0.1 μm	8.35	4.21	134	1.984	0.049
0.5 μm	6.22	4.21	134	1.478	0.142
6 μm	8.98	4.21	134	2.135	0.035
15 μm	13.64	4.21	134	3.242	0.002
Macrorough	-7.58	4.31	134	-1.760	0.081
Body mass	-0.14	0.15	134	-0.923	0.358

^a *Litoria caerulea* on the smooth substrate.

5.3.2 Friction performance

The sliding angle α_{\parallel} of *L. caerulea* ranges between $79.4 \pm 18.6^{\circ}$ (smooth) and $81.1 \pm 9.5^{\circ}$ (macrorough). Compared to the smooth substrate, α_{\parallel} is significantly higher by 8.4 – 13.6° (estimates) on the $0.1 \mu\text{m}$, the $6 \mu\text{m}$, and the $15 \mu\text{m}$ substrate (Table 5.3). For the macrorough substrate, lower sliding angles were measured than on the smooth substrate (difference = $-7.6 \pm 8.5^{\circ}$, estimate $\pm 95\%$ CI), but this difference is just not statistically significant ($p = 0.081$). In contrast to the falling angle, the scaling of sliding angle with body mass m is not significant (slope = $-0.14 \pm 0.29^{\circ} \text{g}^{-1}$; $t = -0.923$, $DF = 134$, $p = 0.358$).

The maximum friction force F_{\parallel} generated by *L. caerulea* ranges between $435.4 \pm 135.3 \text{ mN}$ (smooth) and $458.0 \pm 131.6 \text{ mN}$ ($0.1 \mu\text{m}$). Differences between the roughness levels are not significant, as determined by one-way ANOVA with Bonferroni correction ($F[5,64] = 0.08$, $p = 0.995$).

H. cinerea shows sliding angles α_{\parallel} between $85.2 \pm 5.6^{\circ}$ (macrorough) and $112.3 \pm 10.5^{\circ}$ ($15 \mu\text{m}$). The sliding angle was not significantly different between *L. caerulea* and *H. cinerea* ($t = 1.855$, $DF = 134$, $p = 0.066$). The friction F_{\parallel} of *H. cinerea* ranges between $83.4 \pm 18.4 \text{ mN}$ ($0.1 \mu\text{m}$) and $86.3 \pm 18.5 \text{ mN}$ ($0.5 \mu\text{m}$). An one-way ANOVA with Bonferroni correction does not show significant differences in the friction generated on the different substrates ($F[5,66] = 0.05$, $p = 0.998$).

5.4 Discussion

5.4.1 Effects of substrate roughness on attachment performance

Fig. 5.6 provides an overview of the effect of substrate roughness variations on the adhesive performance of *L. caerulea* and *H. cinerea* studied here as well as of various tree frog species studied in previous research (Barnes, 1999; Barnes *et al.*, 2002; Crawford *et al.*, 2016; Endlein *et al.*, 2013). The adhesion performance of *L. caerulea* and *H. cinerea*, approximated by the falling angle α_{\perp} , is approximately constant up

to a roughness of $15\ \mu\text{m}$, showing that tree frogs are well able to adhere to substrates with a wide range of roughness. Also the adhesion F_{\perp} and tenacity σ_{\perp} barely differ on all tested substrates except the macrorough one. Such an insensitivity of adhesion towards substrate roughness is beneficial, as tree frogs encounter various roughness levels in their natural habitat, ranging from smooth to microrough leaves (e.g. $R_a \approx 0.5\text{--}100\ \mu\text{m}$; Koch *et al.*, 2008) to macrorough tree bark. In the following, we discuss the adhesion performance of the toe pads for the different roughness levels, from smooth over micro- to macrorough substrates. As the friction data are largely confounded by the contact of belly and other body portions, we discuss these only where helpful.

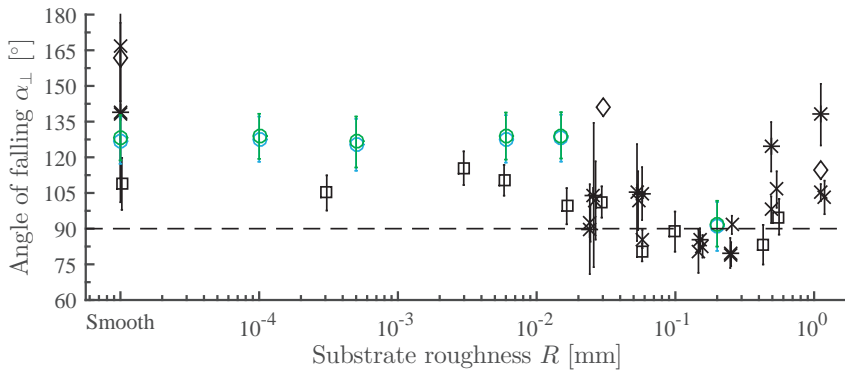


Figure 5.6 Adhesion performance of tree frogs as a function of (nominal) substrate roughness, indicated by the falling angles measured in this study (circles; means and 95% confidence intervals predicted from a linear mixed-effects model, *Litoria caerulea* [blue], *Hyla cinerea* [green]) and reported in literature (asterisks from Fig. 5 by Barnes (1999), *Hyla microcephala*; crosses from Fig. 8a by Barnes *et al.* (2002), *Colostethus trinitatis*; diamonds from Fig. 3b by Endlein *et al.* (2013), *Rhacophorus pardalis*; squares from Fig. 1B by Crawford *et al.* (2016), *Litoria caerulea*). For smooth substrates, $R = 10\ \text{nm}$ is assumed. Falling angles below 90° (dashed line) indicate full adhesive failure. Due to only small interspecific differences, the blue and green circles are almost overlapping.

The falling angles of *L. caerulea* and *H. cinerea* measured on the smooth substrate fall within the range of $100\text{--}180^\circ$ reported in literature (Fig. 5.6). This large range arises from several causes. Most importantly, the attachment performance of tree frogs scales intra- and interspecifically with body size: As reported in this study and elsewhere (Barnes, 1999; Smith *et al.*, 2006a,b), falling angles scale negatively with body mass. The correction for body mass in the linear mixed-effects model removes this size effect, resulting in $\alpha_{\perp} \approx 127.5^\circ$. Whereas the superficial morphology of the adhesive pad does not seem to differ between the two species (see Fig. 5.SI.9; Barnes *et al.*, 2006; Endlein *et al.*, 2013), interspecific differences in animal behaviour, in the chemistry of the secreted mucus, or in the internal morphology of the toe pads (Langowski *et al.*, 2018b) may explain the interspecific differences in attachment performance. Also, differences in substrate properties other than roughness should be considered. In this study, a hydrophilic epoxy resin with—compared to glass—relatively low free surface energy was used. We are not aware of extensive experimental studies on the effects

of variations of free surface energy on tree frog attachment (Langowski *et al.*, 2018a), and differences in free surface energy and hence in adhesion performance between the different studies (e.g. glass and aluminium oxide polishing paper in Crawford, 2016) cannot be excluded.

On microrough substrates (i.e. $0.1 \mu\text{m} < R < 15 \mu\text{m}$), the adhesion performance does not differ compared to the smooth substrate, as shown by the linear mixed-effects model for falling angles, and by the transformation of falling angles to adhesion forces or tenacities. Only for *H. cinerea*, tenacities are significantly higher on the $0.1 \mu\text{m}$ and the $15 \mu\text{m}$ substrate compared to the smooth one. These results are only partially in line with the findings of Crawford *et al.* (2016), who described for single pads of *L. caerulea* significantly higher tenacities for $R = 0.3\text{--}16 \mu\text{m}$, if compared to a smooth substrate. Presumably, this disagreement between rotation platform experiments and single pad studies arises from differences in pad loading. Normal as well as shear loading have been shown to be important factors in determining the attachment performance of tree frog toe pads (Endlein *et al.*, 2017; Hanna & Barnes, 1991), which is discussed in more detail in Section 5.4.3.

In general, adhesion performance changes only little with an increasing substrate roughness from smooth to ca. $40 \mu\text{m}$ (Fig. 5.6). Neither does adhesion performance increase abruptly with increasing roughness, as expected for biological attachment systems using mechanical interlocking [e.g. the claws of the beetles *Gastrophysa viridula* (Bullock & Federle, 2011) and *Pachnoda marginata* (Dai *et al.*, 2002), or of the may fly larva *Epeorus assimilis* (Ditsche-Kuru *et al.*, 2012)], nor does it drop suddenly, as hypothesised when the substrate asperities become too large to allow mechanical interlocking with the nano- to microscopic features of the ventral pad surface (Ernst, 1973b). Importantly, the toe pads of tree frogs are very soft (with an effective elastic modulus of ca. $20\text{--}50 \text{ kPa}$; Barnes *et al.*, 2013, 2011; Kappl *et al.*, 2016), potentially allowing a close conformation to a rough substrate, an increase in the effective contact area, and as a result enhanced van der Waals forces (e.g. Purtov *et al.*, 2013). Therefore, one cannot exclude that at different roughness levels the effects of mechanical interlocking and other possibly involved attachment mechanisms cancel each other, leading to a constant attachment performance with increasing roughness. For further studies of the pad conformability, we suggest the visualisation of the pad-substrate contact for varying roughness levels. A detailed interpretation of the effects of variations in the complex phenomenon roughness (Persson *et al.*, 2005) on tree frog attachment is challenging, also because of the presence of mucus in the contact area. Based on a discussion of the roughness parameters computed from the bearing area curves of the used substrates (see Section 5.SI.2.1), one can conclude that the adhesion performance of tree frogs does not change despite a continuous increase in total roughness height S_{tot} up to ca. $4 \mu\text{m}$ and in reduced peak height S_{pk} up to almost $3 \mu\text{m}$ between the smooth and the $15 \mu\text{m}$ substrate. As asperities are a primary prerequisite for mechanical interlocking, this speaks against an appreciable contribution of mechanical interlocking to tree frog attachment.

A comparison with the attachment performance of other bioadhesive systems from

various clades on rough substrates helps to further explore the fundamentals of tree frog attachment. For example, the hairy toe pads of insects (e.g. *G. viridula*, Bullock & Federle, 2011; *Leptinotarsa decemlineata*, Voigt *et al.*, 2008), arachnids (*Phlo-dromus dispar*, Wolff & Gorb, 2012), and geckos (*Gekko gekko*, Huber *et al.*, 2007) perform worse on microrough substrates (typically in a range of 0.3–1.0 μm) than on smooth ones, which is generally explained by a loss of effective contact area for dry adhesion. Similar observations were made for the smooth adhesive pads of insects (*Cydia pomonella*, Al Bitar *et al.*, 2010) and arachnids (*Ixodes ricinus*, Voigt & Gorb, 2017). Such a decline in attachment performance is clearly not observed for tree frogs in the microrough regime. This may be explained by the high pad conformability, which presumably facilitates a close pad-substrate contact and vdW force generation (Fig. 5.SI.10) on microrough substrates, as proposed by Crawford *et al.* (2016). Independence of the attachment performance on roughness variations in between 0 μm and 12 μm has also been reported for the hairy adhesive pads on the prey-capture apparatus of beetles in the genus *Stenus* (Koerner *et al.*, 2012). The authors related this independence partially to the small tip diameter (0.17–0.24 μm) of the hairy structures, which may widen the range of substrate roughness which the pads can conform to. The nanopillars on tree frogs' toe pads have a similar size (diameter \approx 0.3 μm , Scholz *et al.*, 2009), possibly indicating a functional analogy. Alternatively, the compensatory action of capillary adhesion may explain these findings, as suggested by the increase in tree frog adhesion on rough substrates when adding liquid (Barnes, 1999; Barnes *et al.*, 2002; Endlein *et al.*, 2013).

On macrorough substrates (i.e. $R > 40 \mu\text{m}$), adhesion decreases gradually from $R \approx 40 \mu\text{m}$ to a local minimum at $R \approx 200 \mu\text{m}$, suggesting a gradually progressing failure of the involved attachment mechanism(s) with increasing roughness. Such failure could be the cavitation of the liquid meniscus and hence the loss of capillary adhesion (Barnes, 1999; Barnes *et al.*, 2002; Crawford *et al.*, 2016). Alternatively, a gradual loss of effective contact area and of vdW forces with increasing roughness may lead to adhesive failure, as aforementioned at lower roughness levels for the pads of lizards, insects, and arachnids. For $R > 200 \mu\text{m}$, adhesion seemingly increases again. This may indicate mechanical interlocking of the whole toe pad with macroscopic surface asperities (Barnes *et al.*, 2002). Here, the distal phalanx, which in many species is pointy (with a tip diameter of ca. 60 μm in *H. cinerea*; Langowski *et al.*, 2018b) and extends distally into the subepidermal pad space (Manzano *et al.*, 2007), may act as 'internal claw'. Also, Huber *et al.* (2007) suggested for geckos that individual attachment units (i.e. setae) can conform to the tops or sides of macroscopic substrate asperities. A similar mechanism could apply to the individual epidermal cells on tree frogs' toe pads (Fig. 5.SI.10).

Further work is required for an explanation of the attachment performance of tree frogs on rough substrates. In order to test for the potential role of vdW forces, we suggest the direct quantification of the conformability of tree frog toe pads to micro- to macrorough substrates. Furthermore, a detailed analysis of the meniscus geometry for different roughness levels is needed to illuminate the role of capillary adhesion in tree frog attachment on rough substrates. Little is known about the substrates and

roughness levels which tree frogs experience in their natural habitats (Moen *et al.*, 2013). As increasingly emerging in the field of gecko adhesion (Collins *et al.*, 2015; Elstrott & Irschick, 2004), we propose ecomorphological analyses of tree frogs' toe pads in order to explore correlations between parameters of pad morphology (e.g. of the superficial epidermal cells; Smith *et al.*, 2006b), ecology and natural substrate properties, and attachment performance.

5.4.2 Maximum attachment performance of tree frogs

Using whole-animal rotation platform experiments, we measured mean tenacities of approximately 2.5 mN mm^{-2} and a peak tenacity of 8.8 mN mm^{-2} . These values are considerably higher than the tenacities of around 1 mN mm^{-2} measured in previous rotation platform studies (Barnes *et al.*, 2006; Emerson & Diehl, 1980; Hanna & Barnes, 1991; Smith *et al.*, 2006a,b). However, our results agree well with peak tenacities of up to ca. 8 mN mm^{-2} that were recently reported for single pads adhering to a microrough substrate (Crawford *et al.*, 2016). The deviation in tenacity from earlier studies presumably relates to several factors. Most importantly, we measured the instantaneous contact area before detachment of only the toe pads in contact, which is smaller than the total surface area of all pads considered in previous studies. For example, we found that tree frogs can generate sufficient adhesion with only two limbs in contact, approximately doubling the tenacity compared to a situation where all limbs are in contact. The falling angle measured here exceeds the values reported in most other studies (Fig. 5.6). This deviation may relate to the used setup, substrates, and the experimental animals. We specifically designed a stiff rotation platform to reduce vibrations, the induction of stress, and hence the chance of 'premature detachment' because of jumping of the animals. Moreover, we used frogs from a laboratory population that were accustomed to handling and the setup in pilot trials. Other studies (Barnes *et al.*, 2006; Smith *et al.*, 2006a,b) relied on wild-caught animals, which possibly are more susceptible towards stress during experimental handling.

Sometimes, the frogs swing backwards upon detachment of the forelimbs (Fig. 4), which results in inertial forces acting in addition to the static body weight on the pad-substrate interface. To estimate the magnitude of these inertial forces, the backwards swinging frog may be simplified as an oscillating pendulum. The maximum tension acting in the string of a pendulum is three times its weight (Beléndez *et al.*, 2010). Assuming the swinging frog as pendulum, we estimate that the toe pads can withstand a maximum load of around 26 mN mm^{-2} , which lies close to the peak tenacity of 22 mN mm^{-2} measured by Endlein *et al.* (2017). Assuming free fall of the animals, inertial forces may be even higher, as indicated by peak forces of 130 mN (*Osteopilus septentrionalis*, Hanna & Barnes, 1991) and 1270 mN (estimated from landing kinematics in *Trachycephalus resinifictrix*; Bijma *et al.*, 2016) generated by single pads and limbs during dynamic events.

In order to determine the 'true' maximum attachment performance of tree frogs in whole-animal measurements, an accurate quantification of the inertial loads acting

on the toes during dynamic events by a full inverse dynamics analysis is required. Moreover, rather than studying the average attachment performance—as done here and in previous work—we suggest for future studies a focus on an in-depth analysis of peak performance situations (e.g. the peak performance for each individual on each substrate), which was not possible here due to a too low sample number ($n = 4$). In combination with whole-animal studies, we suggest the execution of single pad force measurements under specified dynamic loading conditions, as done by Endlein *et al.* (2017).

Overall, the results of this study indicate that the attachment performance of tree frogs may be at least one order of magnitude higher than reported in earlier works. This makes tree frogs an interesting model system for the development of biomimetic high-performance adhesives in a wet environment. However, several questions remain unanswered: What is the real maximum attachment performance of tree frogs? Which mechanisms do explain the generation of the high attachment forces? Addressing these questions is relevant for the future design of biomimetic adhesives inspired by tree frog toe pads. For example, Drotlef *et al.* (2013) measured for a tree-frog-inspired PDMS surface covered with hexagonal micropillars tenacities of around $2\text{--}4\text{ mN mm}^{-2}$. Such technical adhesives may benefit significantly from a better understanding of the mechanisms determining the maximum attachment performance of tree frogs.

5.4.3 Problems and perspectives

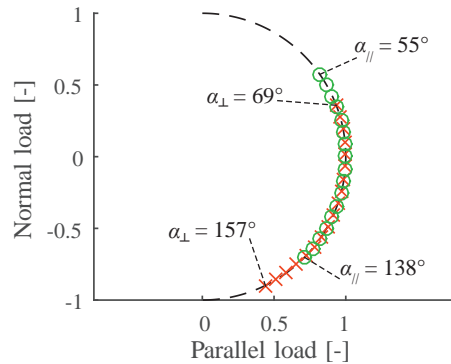
In this study, we used the rotation platform approach, which allows the collection of relatively large data sets. Also, attachment can be studied for a relatively natural body posture, because the artificial fixation of body parts performed in single pad studies (Crawford *et al.*, 2016; Endlein *et al.*, 2017; Federle *et al.*, 2006) is not required. However, rotation platform experiments also have drawbacks, which we discuss below.

Friction and adhesion are computed from the angles of falling and sliding (see Equations 5.1a and 5.1b), respectively. This approach allows a quick and easy quantification of whole-animal adhesion and friction. However, the two forces are inherently coupled due to the performed vector composition of the body weight. Hence, the normal load pulling the animal off the substrate (which equals adhesion at the moment of detachment) cannot be controlled independently of the parallel load dragging the frog along the substrate (which equals static friction at the onset of sliding; Fig. 5.7), and vice versa. For example, sliding occurred at a range of angles, for which the normal load was compressive as well as tensile, and at angles just before falling parallel loads varied by approximately 50% of the body weight (Fig. 5.7). In tree frogs, adhesion depends on the amount of the shear load before detachment (Barnes *et al.*, 2008; Endlein *et al.*, 2017), and—although to our knowledge not substantiated by measurements—friction also depends on normal loading [e.g. in Coulomb friction (Israelachvili, 2011) or in lubricated systems (Pitenis *et al.*, 2014)]. Therefore, the interdependency of



normal and shear loading in rotation platform experiments presumably leads to an artificially increased variation of the measured forces.

Figure 5.7 Interdependency of body-weight-normalised loads acting on a toe pad normal and parallel to the substrate in rotation platform experiments for the sliding (α_{\parallel} , green circles) and falling (α_{\perp} , red crosses) angles measured in this study.



For evaluation of the adhesive whole-animal performance of tree frogs, we measured the instantaneous contact area of only the toe pads making contact with the substrate just before detachment. In previous works (Barnes, 1999; Hanna & Barnes, 1991; Smith *et al.*, 2006a,b), it was assumed that the contact area is formed by the ventral surface areas of all toes of an individual, which presumably has led to an underestimation of the tenacity of tree frogs. Therefore, this study is an important step towards a more accurate quantification of the attachment performance, and an understanding of the fundamental attachment mechanisms of these animals. Such an understanding requires a detailed analysis of the fractions of the overall contact area, which are effective in the generation of wet and dry contact forces, respectively, and of the effective contact area on rough substrates. Such an analysis cannot be achieved with the FTIR technique used here. In future studies, optical methods (e.g. interference reflection microscopy; Crawford *et al.*, 2016; Federle *et al.*, 2006) or mechano-sensitive substrate coatings (Neubauer *et al.*, 2016) could be used to measure the detailed characteristics of the contact area.

The quantification of the frictional performance of tree frog toe pads is confounded by several factors. During sliding, large fractions of the contact area are formed by the belly and other body portions, which has also been shown elsewhere (Endlein *et al.*, 2013, 2017). As the belly and other body portions can contribute considerably to the attachment of tree frogs (Endlein *et al.*, 2013), the rotation platform is inappropriate for the analysis of the frictional performance of tree frogs' toe pads. Also, when analysing sliding at angles of around 90° , it seemed that individuals of *H. cinerea* started sliding with their frontlimbs but could still resist sliding with their hindlimbs. This observation indicates that the assumption of equal loading of all toes is not fulfilled, as to be expected for the required moment balance during steady attachment (Langowski *et al.*, 2018b). Such an unequal load distribution may also occur at the angle of falling, reducing the effective measured adhesion. Differences in the sliding of single toes may also explain the larger variation in sliding angles compared to the measured falling angles. Lastly, it is difficult—if not impossible—to quantify the

willingness of a tree frog to attach to a substrate. We found a relatively large variation of the falling angles per substrate and species, and of the number of successful trials per individual. In future rotation platform experiments, such behavioural differences among individuals may be considered, for example by including individual variability as random effect in the statistical model, as done in this study.

Statistical models such as the linear mixed-effects model used here may help to cope with the large variation in rotation platform studies. Temperature and relative air humidity should be controlled to test for the effects of variations of these parameters on tree frog attachment. Complementarily, single pad measurements with controlled shear loads in adhesion measurements and vice versa, as in (Barnes *et al.*, 2008; Endlein *et al.*, 2017), will help to deepen the understanding of tree frog attachment.

5.5 Conclusions

What is the maximum attachment performance of tree frogs on rough substrates? We address this question by measuring the whole-animal attachment performance of the tree frog species *Litoria caerulea* and *Hyla cinerea* on smooth, micro-, and macrorough substrates using a rotation platform setup. The adhesive performance of the toe pads of tree frogs is insensitive towards variations in substrate roughness up to a nominal roughness of ca. 40 μm . At higher roughness levels up to $R \approx 200 \mu\text{m}$, adhesion decreases significantly compared to lower roughness levels. The absence of a sudden increase in attachment performance when increasing the roughness from smooth to microrough, and the absence of a stepwise decline in attachment performance when further increasing the roughness negate a contribution of mechanical interlocking to tree frog attachment. Further work is required to elucidate if variations in substrate roughness affect attachment force generation by capillary adhesion or by vdW interactions (or by both mechanisms). Tree frogs were able to remain attached with only two limbs in contact with an overhanging substrate. In agreement with recent studies, the tenacity of the toe pads reaches peak values of up to 8.8 mN mm^{-2} , which is almost one order of magnitude higher than reported previously. Inertial forces have to be considered in the quantification of the maximum attachment performance, and we estimate that the maximum tenacity of tree frogs' toe pads may be as much as 26 mN mm^{-2} .



5.SI Supporting information

5.SI.1 Symbols and abbreviations

5.SI.1.1 List of symbols

Table 5.SI.1 List of Roman (top) and Greek (bottom) symbols in alphabetical order. a.u. arbitrary unit.

Symbol	Unit	Description
A	m^2	Contact area
CI	var.	Confidence interval
DF	-	Degrees of freedom
F	-	F-statistic
F_g	N	Body weight
F_{\perp}	N	Adhesion
F_{\parallel}	N	(Static) friction
H	%	Relative air humidity
ℓ_{SV}	m	Snout-vent-length
m	kg	Body mass
n	-	Number of measurements
p	-	p-value
R	m	Nominal roughness
R_a	m	Arithmetic average roughness
RMS	m	Root mean squared roughness
S	m	Total roughness height
S_k	m	Core roughness depth
S_{pk}	m	Reduced peak height
S_{vk}	m	Reduced valley depth
SE	var.	Standard error
T	$^{\circ}\text{C}$	Air temperature
t	-	t-statistic
α	-	Significance level
α_{\perp}	$^{\circ}$	Falling angle
α_{\parallel}	$^{\circ}$	Sliding angle
γ	J m^{-2}	Free surface energy
γ_d	J m^{-2}	Dispersive surface energy component
γ_p	J m^{-2}	Polar surface energy component
σ_{\perp}	N m^{-2}	Tenacity

5.SI.1.2 List of abbreviations

Table 5.SI.2 List of abbreviations.

Abbreviation	Description
FTIR	Frustrated total internal reflection
LED	Light-emitting diode
OWRK	Owens-Wendt-Rable-Kaelble
PDMS	Polydimethylsiloxane
vdW	van der Waals
WUR	Wageningen University & Research

5.SI.2 Substrate characterisation

5.SI.2.1 Surface roughness

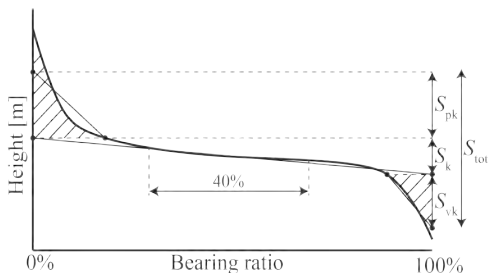
To characterise the height profiles and roughness of the used substrates, we used a VR-3100 3D measuring macroscope for the macrorough substrate (Keyence, Japan) and a New View 6000 white light interferometer for the smooth, 0.1 μm , 0.5 μm , 6 μm , and 15 μm substrates (Zygo, USA), respectively. Fig. 5.SI.2 shows characteristic examples of the surface profiles of these substrates. For white light interferometry, the analysed areas are 1.4·1.05 mm² and 0.14·0.11 mm² for 5 \times and 50 \times magnification, respectively. For the profilometer, areas of 24.13 · 18.10 mm² and 2.53 · 1.90 mm² were analysed for 12 \times and 120 \times magnification, respectively.

Per substrate, the height profile characteristics of the analysed patches varied only slightly with scanning location, as shown by the good overlap of the bearing area curves (Figs. 5.SI.3,5.SI.4), which were measured per substrate at 10 randomly distributed locations. Also the core roughness depth S_k , the reduced peak height S_{pk} , and the reduced valley depth S_{vk} , which were computed from these curves following ISO 13565-2:1996 (see Fig. SI.5.SI.1), varied only little among the 10 measurements per substrate (Fig. 5.SI.5).

The general increase in variation of the bearing area curve parameter values of the 6 μm and the 15 μm substrate with increasing magnification is explained by the averaging of irregular surface patches at lower magnification. At higher magnification, the probability of capturing such irregularities is higher. Unless mentioned otherwise, we report values at low magnification.

The smooth substrate has roughness parameters below 100 nm. A reduced valley depth S_{vk} of 73.3 \pm 22.4 nm indicates the presence of dimples, which are also seen in Fig. 5.SI.2. These dimples presumably originate from the entrapment of air bubbles during the manufacturing process. When scanning the smooth patches between these dimples at high magnification, S_{vk} drops to 3.1 \pm 0.6 nm. The smooth surface does not bear protruding structures (S_{pk} = 4.7 \pm 2.1 nm at 50 \times magnification).

Figure 5.SI.1 Analysis of the bearing area curve. To determine the core roughness depth S_k , a linear fit is applied to the data over a range of 40% of bearing ratio. By shifting this 40%-window, the most horizontal curve (i.e. highest slope) is identified. S_k is the difference in height between the points where this fitted line intercepts the verticals drawn through 0% and 100% of bearing ratio (i.e. the core region). The reduced peak height S_{pk} is determined as follows: First, the area under the bearing area curve between 0% and the bearing ratio of the top edge of the core region is computed. Then, an area-equivalent triangle is created. S_{pk} is the height of that triangle. The reduced valley depth S_{vk} is computed analogously for the lower edge of the core region. The total roughness height S_{tot} is the sum of S_k , S_{pk} , and S_{vk} .



The 0.1 μm and the 0.5 μm substrate have a core roughness depth S_k of $1.52 \pm 0.08 \mu\text{m}$ and $1.72 \pm 0.05 \mu\text{m}$, respectively, which is higher than for the 6 μm ($0.82 \pm 0.06 \mu\text{m}$) and the 15 μm substrate ($0.80 \pm 0.05 \mu\text{m}$), indicating a more gradual increase of bearing ratio with a change in height, and hence a less rapid transition between peak and core region for the two less rough substrates. The peaks of the 0.1 μm and the 0.5 μm substrate are $0.35 \pm 0.04 \mu\text{m}$ and $0.44 \pm 0.06 \mu\text{m}$ high, the valleys are $0.55 \pm 0.03 \mu\text{m}$ and $0.33 \pm 0.01 \mu\text{m}$ deep. The steeper bearing area curve (and accordingly the higher core roughness depth) of the 0.5 μm substrate compared to the 0.1 μm substrate may explain why the 0.1 μm substrate has a lower reduced peak height S_{pk} than the 0.5 μm substrate.

The low core roughness depth of the 6 μm and 15 μm substrate can also be seen in Fig. 5.SI.2, where the greenish regions represent the approximate core roughness regions. These two substrates carry higher asperities than the 0.1 μm and 0.5 μm substrate ($S_{pk} = 1.66 \pm 0.04 \mu\text{m}$ and $2.67 \pm 0.32 \mu\text{m}$). As the slopes around the asperities could not get measured properly with white light interferometry, the peak height presumably is underestimated. Interestingly, the valleys are less distinct than for the 0.1 μm and 0.5 μm substrate ($S_{vk} = 0.24 \pm 0.02 \mu\text{m}$ and $0.24 \pm 0.02 \mu\text{m}$). This may be explained by the structure of the original polishing papers. These are made from diamond particles coated on a polyester backing layer. Whereas for the 0.1 μm and 0.5 μm substrate these particles completely cover the backing layer, for the 6 μm and 15 μm substrate the backing layer may partially lie open, resulting in a relatively smooth base surface.

5.SI.2.2 Free surface energy

To determine the free surface energy—including the polar and non-polar dispersive free surface energy component—of the used substrate material, five samples were cut after animal experimentation from the smooth substrate, cleaned with 100% ethanol and demineralised water, and dried with pressurised air. Per sample, five

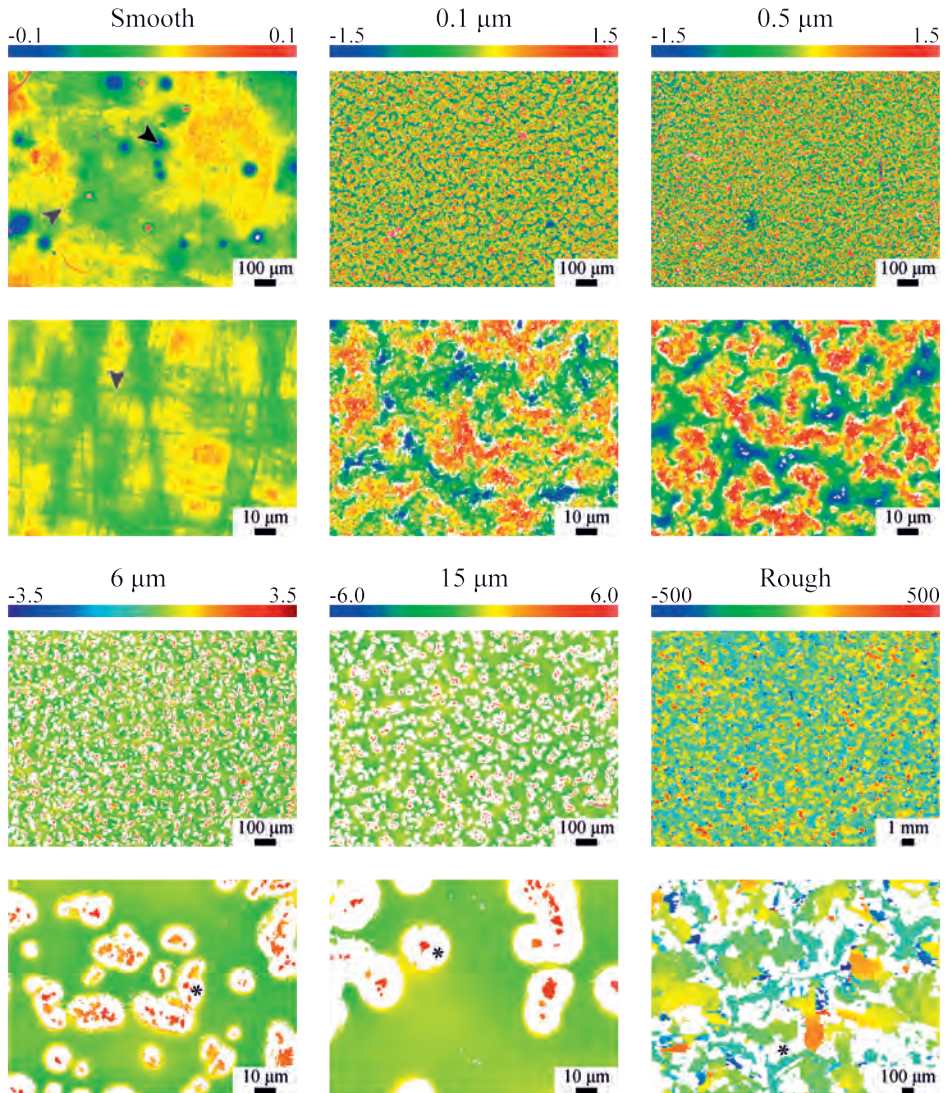


Figure 5.SI.2 Characteristic height profiles of the test substrates measured with white-light-interferometry (smooth, 0.1 μm , 0.5 μm , 6 μm , 15 μm ; top rows: 5 \times magnification; bottom rows: 50 \times magnification) and with profilometry (macrorough; top: 12 \times magnification; bottom: 120 \times magnification). The surface profiles are corrected for a cylindrical base surface. Colorbars indicate the profile height in μm . Black arrowheads: Nanoscopic dimples in the smooth substrate. Grey arrowheads: Scratches in the smooth substrate. Stars: Slopes of surface asperities and deep valleys (rough substrate) that could not get measured with the available methods.

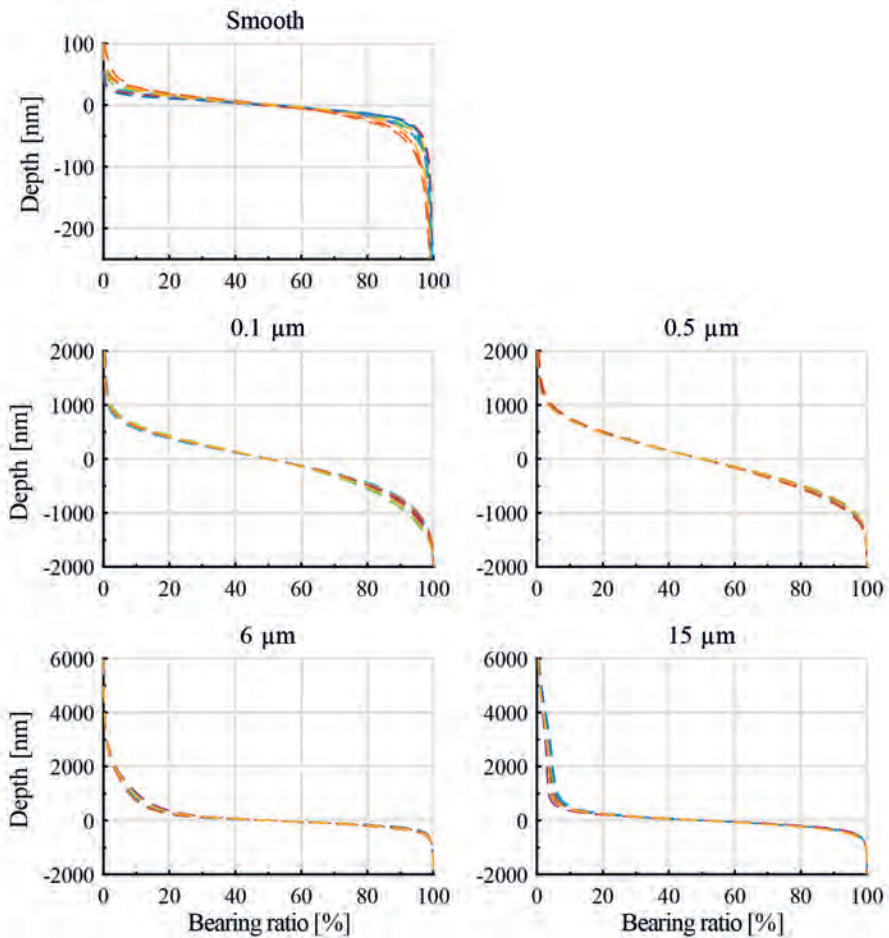


Figure 5.SI.3 Bearing area curves (also termed Abbot-Firestone curves) for the substrates analysed with white light interferometry ($5\times$ magnification). Per substrate, the bearing area curve was measured at 10 different, randomly distributed locations on the substrate surface (indicated by the different colours of the curves).

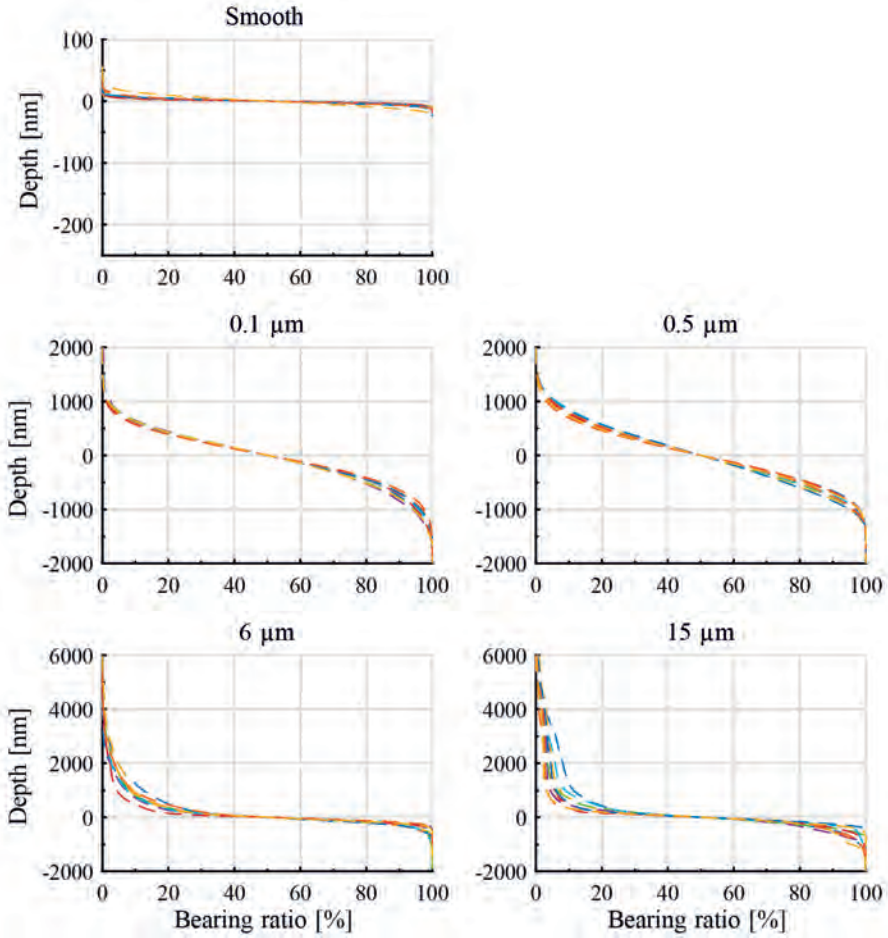


Figure 5.SI.4 Bearing area curves for the substrates analysed with white light interferometry (50× magnification).

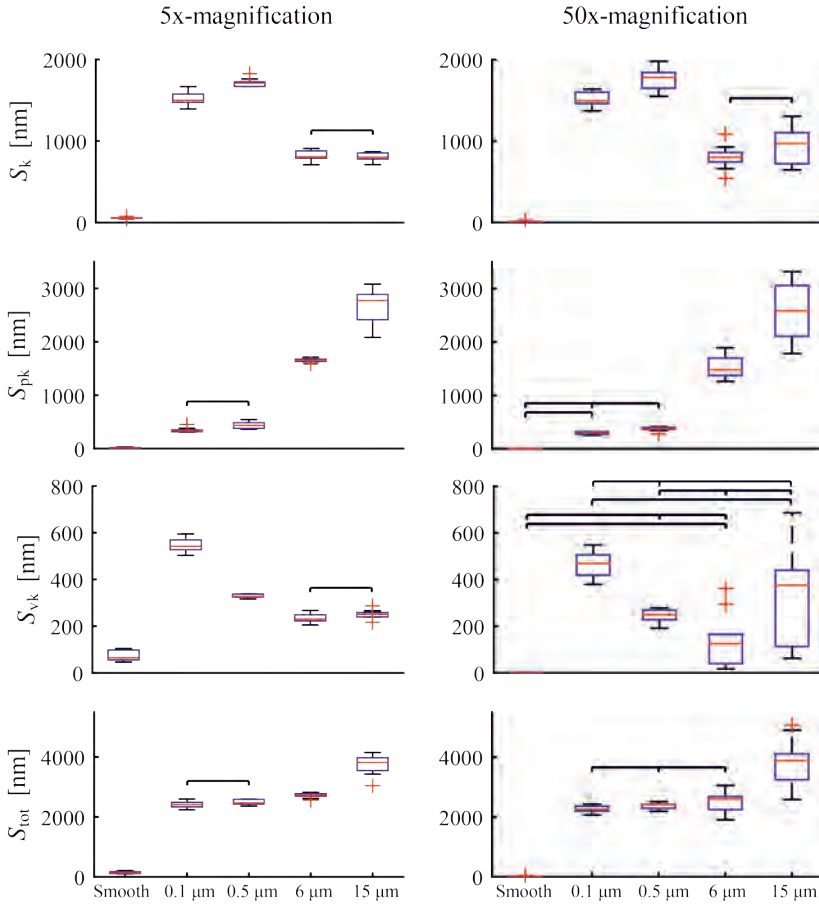


Figure 5.SI.5 Characteristic parameters of the bearing-ratio-curves shown in Figs. 5.SI.3 and 5.SI.4 analysed according to ISO 13565-2:1996. Boxes indicate median and 25th and 75th percentiles ($n = 10$ per boxplot). Values that are located more than 1.5 times the interquartile range above or below the boxes are shown as outliers. Horizontal lines indicate combinations of roughness parameter values that are not significantly different from each other. S_k core roughness depth, S_{pk} reduced peak height, S_{vk} reduced valley depth, S_{tot} total roughness height.

contact angle measurements with 2 μL drops of each water, diiodomethane, and ethylene glycol were performed using an OCAH 200 contact angle measuring system (DataPhysics Instruments, Germany; Table 5.SI.3). Using the sessile drop approach (drop dosage rates of $0.5 \mu\text{L s}^{-1}$ for water and $0.59 \mu\text{L s}^{-1}$ for diiodomethane and ethylene glycol) and surface tensions of the liquids according to Busscher *et al.* (1984) and Birdi (2009), we computed a free surface energy of $\gamma = 39.2 \text{ mJ m}^{-2}$ (dispersive component $\gamma_d = 30 \text{ mJ m}^{-2}$, polar component $\gamma_p = 9.2 \text{ mJ m}^{-2}$) with the Owens, Wendt, Rable, and Kaelble (OWRK) method (Owens & Wendt, 1969) using SCA 20 (Vers. 3.12.11, DataPhysics Instruments). The measured surface energies are in good agreement with values for polyurethanes reported in literature (e.g. Busscher *et al.*, 1983: $\gamma = 39 \text{ mJ m}^{-2}$, $\gamma_d = 32 \text{ mJ m}^{-2}$; Vargo *et al.*, 1991: $\gamma = 37.8 \text{ mJ m}^{-2}$, $\gamma = 35.1 \text{ mJ m}^{-2}$).

5.SI.3 Measurement of the instantaneous contact area

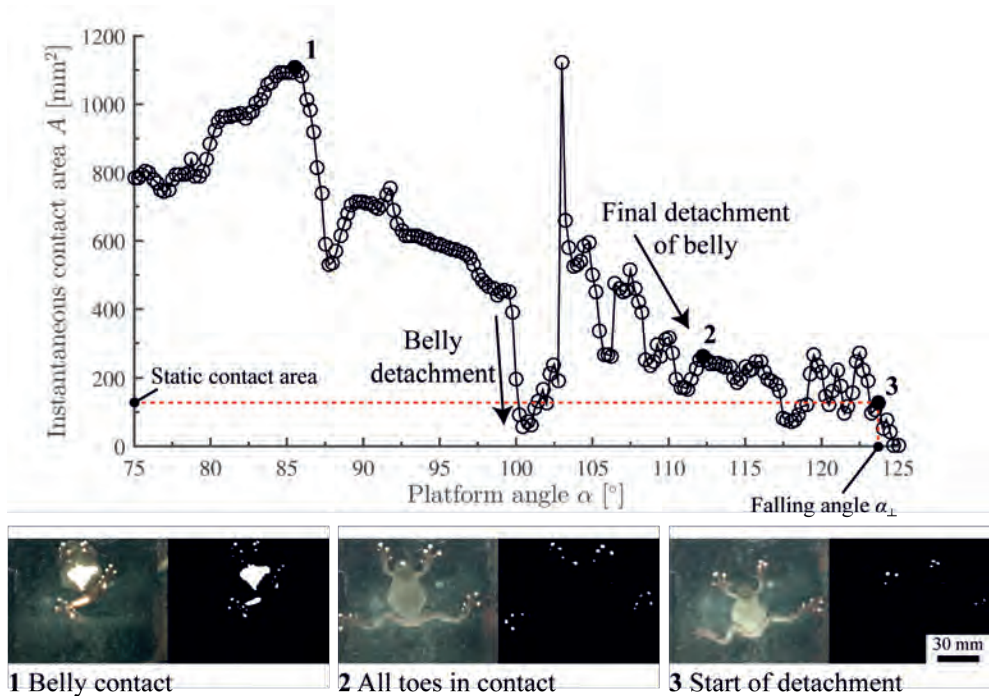


Figure 5.SI.6 Exemplary dynamics of the instantaneous contact area as a function of platform angle, and definition of the static contact area before detachment.

Table 5.SI.3 Overview of the static contact angle measurements. *n* number of measurements.

Sample	<i>n</i>	Average of left and right contact angle [°]		
		Diiodomethane	Water	Ethylene glycol
1	1	43.72	74.49	47.83
	2	42.88	74.54	46.38
	3	41.57	75.22	46.08
	4	39.28	73.43	47.97
	5	41.33	73.16	47.20
	mean [°]	41.75	74.17	47.09
	standard deviation [°]	1.69	0.85	0.84
standard deviation [%]	4.05	1.15	1.79	
2	1	37.25	74.16	51.68
	2	35.77	74.85	49.89
	3	35.78	73.52	48.90
	4	36.12	74.36	48.96
	5	37.03	73.58	48.59
	mean [°]	36.39	74.09	49.60
	standard deviation [°]	0.70	0.56	1.26
standard deviation [%]	1.93	0.75	2.54	
3	1	37.54	70.63	47.78
	2	38.67	68.92	48.05
	3	38.26	68.21	47.43
	4	37.94	70.94	47.93
	5	38.23	70.59	49.27
	mean [°]	38.13	69.86	48.09
	standard deviation [°]	0.42	1.21	0.70
standard deviation [%]	1.10	1.73	1.45	
4	1	39.91	72.90	44.32
	2	39.00	70.95	47.32
	3	39.58	69.84	45.54
	4	37.30	70.55	47.17
	5	38.23	71.66	48.24
	mean [°]	38.80	71.18	46.52
	standard deviation [°]	1.05	1.16	1.57
standard deviation [%]	2.72	1.64	3.37	
5	1	38.30	70.83	46.75
	2	39.01	71.43	46.43
	3	37.74	69.98	47.09
	4	37.76	69.79	48.16
	5	37.70	69.59	47.59
	mean [°]	38.10	70.32	47.20
	standard deviation [°]	0.56	0.78	0.69
standard deviation [%]	1.48	1.11	1.45	
Average over samples	mean [°]	38.64	71.92	47.70
	standard deviation [°]	1.96	2.07	1.20
	standard deviation [%]	5.07	2.88	2.52

5.SI.4 Model diagnostics

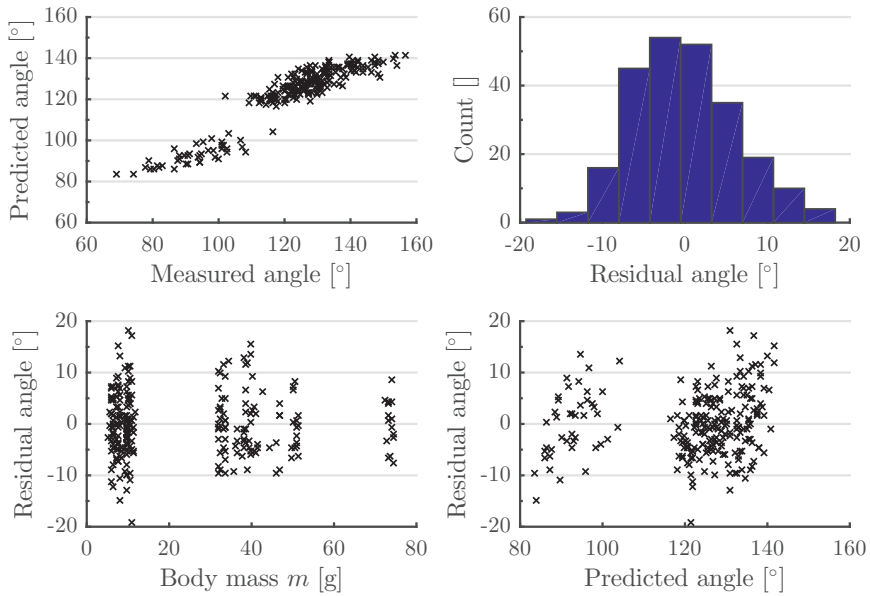


Figure 5.SI.7 (A) Predicted versus measured falling angle α_{\perp} . (B) Distribution of residuals of linear mixed-effects model. (C) Dependency of residuals on body mass m . (D) Dependency of residuals on predicted falling angle α_{\perp} .

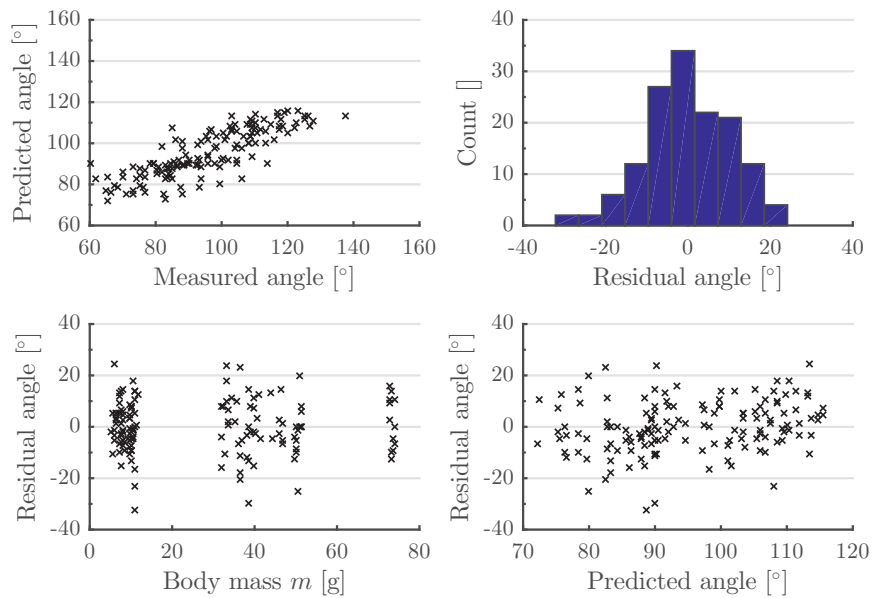


Figure 5.SI.8 (A) Predicted versus measured sliding angle $\alpha_{||}$. (B) Distribution of residuals of linear mixed-effects model. (C) Dependency of residuals on body mass m . (D) Dependency of residuals on predicted sliding angle $\alpha_{||}$.

5.SI.5 Interspecific comparison of the adhesive surface patterns on the digital pads of tree frogs

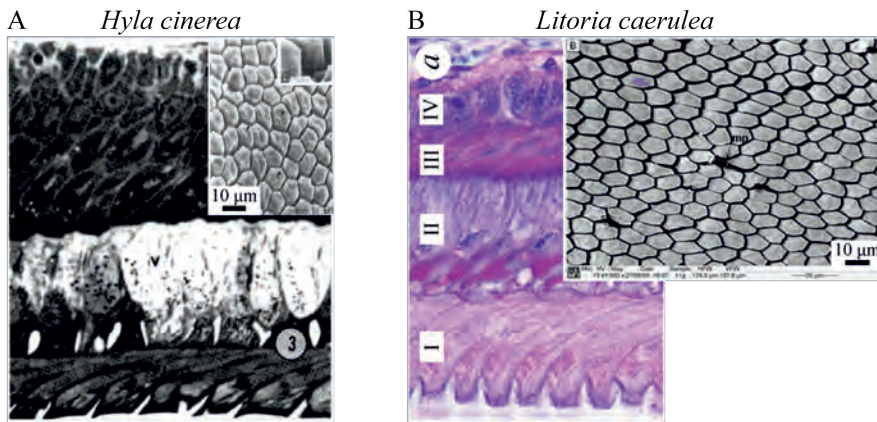


Figure 5.SI.9 Comparison of the adhesive surface structures formed by the ventral epidermis in the digital pads of the tree frogs (A) *Hyla cinerea* and (B) *Litoria caerulea*. Per species, the main image shows a sagittal section through the ventral epidermal cell layers, with the most apical layer forming the adhesive surface pattern. The insets are scanning electron micrographs showing the ventral pad surface. (A): Ernst, 1973a; inset: modified after Linnenbach (1985). (B): Nakano & Saino, 2016; inset: modified after Nokhbatolfoghahai (2013).

5.SI.6 Explanatory model

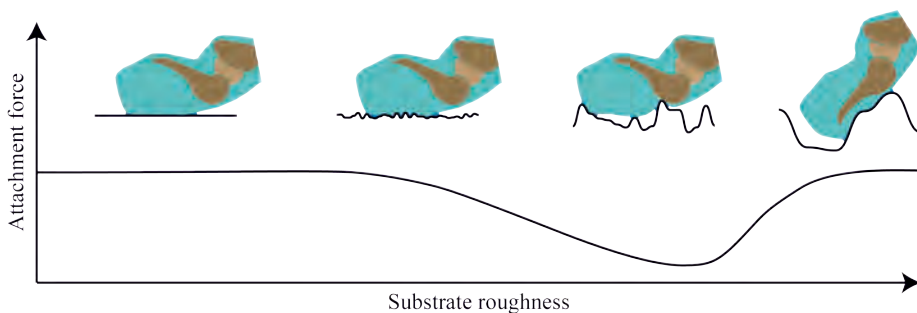


Figure 5.SI.10 Hypothesised explanatory model of the attachment of a tree frog's toe pad (turquoise, soft pad; dark brown, phalanges; light brown, intercalary element; blue, secreted mucus) to smooth and rough substrates. The pad can conform closely to a smooth substrate, hence allowing the generation of 'dry' van der Waals forces in addition to 'wet' attachment forces such as capillary or hydrodynamic adhesion. On microrough substrates, the low pad stiffness of the pad and the micro- and nanoscopic structures on the pad surface help—in addition to mucus secreted by tree frogs filling gaps in between pad and substrate—to avoid attachment failure. At an intermediate roughness ($R \approx 200 \mu\text{m}$), these mechanisms largely fail and attachment forces are minimal. At even higher macroscopic roughness levels, the pad may be able to conform to parts of the substrate asperities, potentially 'reenabling' dry and wet attachment mechanisms. Additionally, mechanical interlocking of the whole digital tip may contribute to attachment.



*With magic, you can turn a frog into a prince.
With science, you can turn a frog into a Ph.D.
and you still have the frog you started with.*

T. Pratchett, 2002

CHAPTER 6

General discussion

In this thesis, I attempt to provide an integrative analysis of the attachment apparatus of tree frogs, hence contributing to the understanding of nature's adhesive systems, and of anuran biology. Furthermore, I aim to provide input for the design of novel biomimetic adhesives inspired by tree frogs. The attachment apparatus of tree frogs and its underlying attachment mechanisms are a complex area with contributions from biology, physics, material sciences, chemistry, and related fields. The ability of tree frogs to attach after jumping to smooth substrates such as glass has fascinated researchers for centuries (Gatesby, 1743; Rösel von Rosenhof, 1758), and recently inspired the design of biomimetic adhesives emulating the digital pads of tree frogs. Most previous studies focused on the epidermal surface of the pads, providing an extensive body of literature on the role of surface structuring in tree frog attachment (see CHAPTER 2 for a review). However, a comprehensive explanation of the mechanisms of tree frog attachment and of the factors that affected the evolutionary development of the adhesive system of these animals is still unavailable, which may be partially due to a gap of knowledge on the internal pad architecture.

To deepen the understanding of tree frog attachment, I studied the digital pads of tree frogs and their attachment performance from different perspectives. In CHAPTER 2, I provided a synthesis of the *status quo* of knowledge on tree frog attachment, ranging from the functional pad morphology to experimental findings in support of the various hypothesised mechanisms of tree frog attachment, and identified gaps in the existing knowledge. The outcomes of this review stimulated the research presented in the subsequent chapters. To analyse the functional morphology of subepidermal structures and the pathways of force transmission between adhesive epidermis and internal skeleton, I studied the internal pad morphology in 3D and—with the help of numerical optimisation—provided a functional interpretation of the identified collagenous and muscular structures of force transmission (CHAPTER 3). As the digital mucus has been repeatedly hypothesised to facilitate 'wet adhesion' (e.g. Barnes *et al.*, 2011; Emerson & Diehl, 1980; Hanna & Barnes, 1991; Nachtigall, 1974), I investigated

in CHAPTER 4 the mucus chemistry and the morphology of the glands secreting it, aiming for a functional understanding of these components of the adhesive system. Finally, I tested a hypothesised contribution of mechanical interlocking to the attachment of tree frogs by systematically analysing the effects of variations in substrate roughness on the attachment performance of tree frogs (CHAPTER 5).

In the following discussion, I put the findings of my PhD research into a wider context. For a discussion of arguments for and against the various mechanisms of tree frog attachment suggested in the last two centuries, I integrate in Section 6.1 the most important findings of CHAPTERS 2 to 5 with the existing literature on the attachment of tree frogs and tree-frog-inspired adhesives. Phylogenetic arguments are largely missing in the research on tree frog attachment. As such arguments help to understand the functioning of a bioadhesive system (e.g. Irschick *et al.*, 1996), I illuminate in Section 6.2 the findings of this thesis and of previous works in the context of evolution and phylogenetics. In particular, I address the previously hypothesised convergent evolution of the digital pads of tree frogs. In Section 6.3, I provide an outlook on the design of novel tree-frog-inspired adhesives based on the findings of this thesis. Finally, I address the key questions arising from the discussion of bioadhesion, evolutionary history, and biomimetics of tree frog attachment, and discuss steps required to answer these questions, as well as challenges in doing so (Section 6.4).

6.1 How do tree frogs attach?

A number of hypothesised mechanisms recurred in previous research on tree frogs to explain the attachment of these animals (Fig. 6.1). Most of these mechanisms were under debate already in the 19th century. To my knowledge, suction generated by the whole digital pad is the earliest theory of tree frog attachment (Gatesby, 1743). The freestanding epidermal cells on the ventral pad surface were proposed to facilitate mechanical interlocking with substrate asperities (Ernst, 1973a; Leydig, 1868). Moreover, the concept of ‘adhesion’ of the ventral epidermal cells to a substrate was put forward (Schuberg, 1891), which later was rephrased as the action of van der Waals (vdW) forces (Emerson & Diehl, 1980). The mucus secreted onto the surface of the digital pads of tree frogs has been proposed quite early to facilitate wet adhesion, both in the form of capillary (Nachtigall, 1974; v. Wittich, 1854) and hydrodynamic (Emerson & Diehl, 1980) forces. Nowadays, wet adhesion is the commonly used explanation of tree frog attachment (e.g. Crawford, 2016; Endlein & Barnes, 2015; Kappl *et al.*, 2016), which, however, is not sufficiently supported by experimental data (CHAPTER 2).

6.1.1 Mechanical interlocking

Mechanical interlocking has been hypothesised to occur between asperities of rough substrates and individual superficial cells of the ventral pad epidermis (Crawford



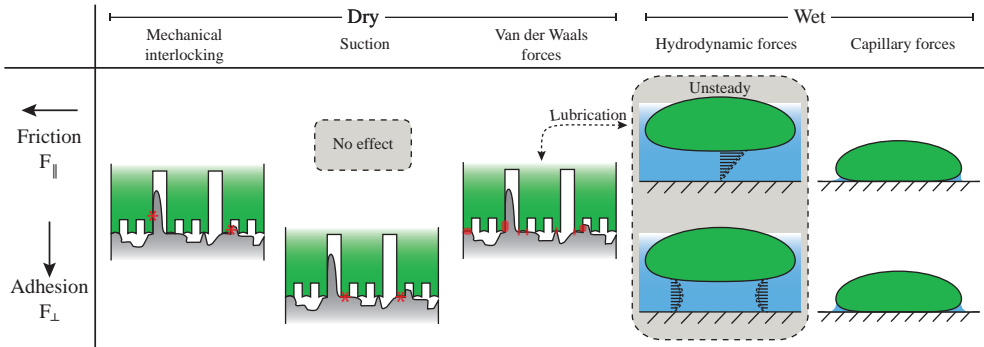


Figure 6.1 Schematic depictions of the mechanisms proposed previously to explain tree frog attachment. The mechanisms are classified by the need for liquid as attachment agent ('dry' vs. 'wet') and by the predominant orientation of the generated attachment force with respect to the substrate (adhesion normal to the substrate vs. friction parallel to the substrate).

et al., 2016; Emerson & Diehl, 1980) or individual nanopillars, respectively (Komnick & Stockem, 1969). Hence, the superficial epidermal structures were suggested to function—alogously to claws in lizards (Russell, 1975) or insects (e.g. Bullock & Federle, 2011; Dai *et al.*, 2002)—as micro- and nanoscopic hooks (Fig. 6.1; CHAPTER 2). Our experimental quantification of the effects of variations in substrate roughness on tree frog attachment performance (CHAPTER 5) shows that tree frogs adhere equally well to nano- and microrough substrates as to smooth ones. This observation disagrees with the expected increase in attachment performance when roughness exceeds a critical threshold, which has been observed in various other biological systems using mechanical interlocking (Bullock & Federle, 2011; Dai *et al.*, 2002; Ditsche-Kuru *et al.*, 2012). Moreover, with an effective elastic modulus in the order of 10 kPa (CHAPTER 2), the digital pads of tree frogs arguably are not stiff enough to maintain the adductive contact with the asperities of a rough substrate required for interlocking (Cartmill, 1974). Based on these considerations, I reject a contribution of mechanical interlocking to tree frog attachment.

6.1.2 Suction

Suction has been suggested to occur on the level of the whole digital pad (Gatesby, 1743), of single epidermal cells (Leydig, 1868), and of individual nanopillars (Scholz *et al.*, 2009). The attachment performance of tree frogs is not affected detrimentally by a reduction of the environmental pressure (Emerson & Diehl, 1980; Schuberg, 1891), disagreeing with a contribution of suction to tree frog attachment. Also, biological suction systems typically are soft, have a concave adhesive surface, show modifications of the outer perimeter of the adhesive surface for effective sealing of the suction volume, and contain muscular structures to generate suction (e.g. Ditsche & Summers, 2014; Gorb, 2008; Kier & Smith, 2002). Whereas the digital pads of tree frogs are soft, the pads appear convex in an unloaded state (CHAPTER 2), I am not aware of a

deviation from the ‘regular’ surface patterning towards the perimeter of the ventral pad surface, and the pads do not contain active structures suitable for the creation of suction pressure (CHAPTER 3). Arguably, one would expect such structures to connect approximately centrally and axial-symmetrically to the adhesive surface to avoid local stress concentrations at the interface. A collagenous septum is the only structure connecting roughly centrally to the ventral epidermis (CHAPTER 3). However, the septum spans the full width of the pad and presumably stresses the perimeter of the contact surface when loaded, hence compromising the speculated partial vacuum. Finally, I did not find muscular structures that would allow targeted lifting of the apical surfaces of individual epidermal cells or nanopillars, excluding the local occurrence of suction. Overall, I conclude that suction is negligible in tree frog attachment.

6.1.3 Wet adhesion

6.1.3.1 Hydrodynamic adhesion

Hydrodynamic adhesion describes the generation of normal attachment forces based on the creation of flow of a viscous liquid between adhesive and substrate (Stefan, 1874). Several observations suggest that tree frogs do not employ hydrodynamic adhesion for attachment (CHAPTER 2): Hydrodynamic adhesive forces typically scale with the contact area squared, whereas in tree frogs adhesion tends to scale with contact area (Smith *et al.*, 2006b). Furthermore, hydrodynamic adhesion is a function of detachment velocity (Stefan, 1874), potentially non-Newtonian mucus viscosity (CHAPTER 4), and viscoelastic properties of the digital pad (Barnes *et al.*, 2011; Scholz *et al.*, 2009), and hence highly rate-dependent. A sophisticated neuromuscular control system would be required to modulate the generated adhesion. Such a system would have to function rapidly to enable quick attachment (and detachment) of tree frogs during dynamic events such as jumping. To my knowledge, such a system is unreported in tree frogs. Importantly, hydrodynamic forces act against the direction of movement of an adhesive (CHAPTER 2). This counteracts rapid detachment manoeuvres, for example to escape a predator, and hinders the formation of close contact and the generation of vdW forces between pad and substrate.

These considerations render hydrodynamic adhesion a disadvantage rather than an evolutionary benefit in tree frog attachment. In fact, experiments on bioinspired micropatterned surfaces (Dhong & Fréchet, 2015; Gupta & Fréchet, 2012) suggest that the micro- to nanoscopic pillar-channel pattern on the ventral pad epidermis promotes drainage of interstitial mucus. The convex pad surface also helps to reduce repulsive hydrodynamic force during contact formation in a submerged pad (CHAPTER 2). For a rigid adhesive under constant load, drainage not only supports the formation of close contact when approaching the substrate (CHAPTER 2), but also reduces the hydrodynamic adhesion during detachment. A modification of the interstitial gap geometry after contact formation would be required to facilitate hysteretic hydrodynamic forces, with weak repulsion during approach and strong adhesion during detachment (Persson, 2007). To my knowledge, such a mechanism is unreported

in frog pads. Overall, the functional morphology of the pad appears to counteract hydrodynamic adhesion, hence disagreeing with an important role of this mechanism in tree frog attachment.

6.1.3.2 Capillary adhesion

A contribution of capillary adhesion to tree frog attachment has been proposed previously based on several observations (CHAPTER 2): (i) A mucus meniscus is present in between digital pad and substrate (Emerson & Diehl, 1980); (ii) a simplified experimental model of capillary adhesion between two glass plates shows similar adhesive tenacities as measured for tree frogs (Nachtigall, 1974); (iii) tree frog adhesion scales linearly with the contact area as predicted by a simplified analytical model of capillary adhesion (Emerson & Diehl, 1980); (iv) on rough substrates, the addition of water prevents a decrease in attachment performance, which may be explained by preservation of the liquid meniscus (Barnes, 1999). None of these observations, however, unambiguously supports a contribution of capillary adhesion (CHAPTER 2).

The volume of available mucus, which determines the size of the contact area covered by the meniscus, and the mucus chemistry, which governs the effective surface tension of the capillary bridge, are important parameters in the analysis of capillary adhesion in tree frogs. As shown in CHAPTER 4, the ventral digital mucus glands of the tree frog *Hyla cinerea* have a total volume of 38 nL per pad, which is sufficient for the formation of a capillary bridge covering the whole ventral pad surface. However, we also detected lipid-like constituents of tree frog mucus (CHAPTER 4). Such molecules likely act as surfactants—indicated also by the low contact angles of tree frog mucus on various substrates (Drotlef *et al.*, 2013)—that reduce the effective surface tension and the generated capillary adhesion (see Equations 1 and 2 in CHAPTER 2).

A discussion of analogies between existing tree-frog-inspired adhesives and the digital pads of tree frogs provides further insight into the capillary adhesion of these animals. The ‘wet’ adhesion of tree-frog-inspired micropatterned adhesives bearing hexagonal micropillars similar in size to the epidermal cells covering the ventral pad surface (see Fig. 6.4 for examples) is comprised of a long-range component (i.e. capillary adhesion) and a short-range component (i.e. vdW forces; Drotlef *et al.*, 2013; Li *et al.*, 2018a). In full wetting, which is expected for the pads of tree frogs given the presence of surfactant-like molecules in their mucus (CHAPTER 4), capillary forces account for ca. 45% of the total adhesion (Li *et al.*, 2018a), suggesting that capillary adhesion is not the prevailing adhesion mechanism. Interestingly, micropatterning was found to reduce the ‘long range’ of capillary forces, as the liquid forming the capillary bridge is distributed in the inter-pillar channel network (Drotlef *et al.*, 2013). Accordingly, micropatterning may counteract the proposed capillary adhesion of tree frogs.

Overall, a contribution of capillary adhesion in tree frog attachment cannot be excluded. Analyses of the chemical mucus composition, physical mucus properties, and the capillary pressure in the pad-substrate gap are needed to illuminate the exact size of the contribution of capillary adhesion. Whereas capillary adhesion may generate a



part of the adhesion of tree frogs, capillary forces do not explain the friction (and the measured shear-dependence of the adhesion; Endlein *et al.*, 2017) of frog pads (Federle *et al.*, 2006; CHAPTER 2), indicating the action of other attachment mechanisms such as vdW forces.

6.1.4 Van der Waals forces

Antithetically to wet adhesion, the presence of a mucus film between digital pad and substrate has been proposed to prohibit a contribution of vdW forces to tree frog attachment (Emerson & Diehl, 1980; CHAPTER 2). We showed with a simple analytical model that liquid in the pad-substrate gap does not *per se* impede vdW interactions, given a sufficiently low gap width of less than 2.5–6.7 nm and a homogeneous distribution of mechanical stress across the contact area (CHAPTER 2).

Federle *et al.* (2006) measured gap widths ≤ 5 nm for a considerable fraction ($\sim 40\%$) of the ventral pad surface of *Litoria caerulea* in contact with a smooth glass slide, supporting fulfillment of the first aforementioned condition. Close enough contact for the generation of vdW forces presumably is facilitated by drainage of interstitial liquid through the channel network between the freestanding epidermal cells and nanopillars. Drainage also occurs in tree-frog-inspired adhesives, especially on hydrophilic substrates (e.g. Chen *et al.*, 2015; Drotlef *et al.*, 2013; Iturri *et al.*, 2015). As a result, vdW forces can contribute significantly to adhesion in a wet environment (ca. 55% of the total adhesion; Li *et al.*, 2018a).

A functional analysis of the internal pad morphology (CHAPTER 3) suggests fulfillment of the second condition as well. If present, vdW forces are likely to occur between the apical portions of the ventral pad surface and the substrate. In *H. cinerea*, the ventral pad surface is mechanically linked with the middle phalanx via a sequence of tonofilament bundles that reinforce individual nanopillars, traverse the epidermis, and connect to dermal collagen fibres. When loaded during attachment, this sequence of force-transmitting structures may support the equalisation of contact stresses across the pad surface (CHAPTER 3), thus supporting the used model of vdW interactions. An analogous mechanism has been demonstrated in micropatterned adhesives bearing composite micropillars, which mimic the epidermal cells of tree frogs and the tonofilaments therein (Xue *et al.*, 2017). The enhanced attachment performance of a fibre-reinforced adhesive is explained by (i) a hindered crack initiation resulting from reduction and homogenisation of contact stresses, and (ii) crack arresting due to the staggered arrangement of the nanofilaments within a pillar (Xue *et al.*, 2017). These mechanisms may also occur in frog pads, albeit in an altered form, as the epidermal cells and tonofilaments therein are skewed (CHAPTER 3). Characterisation of the spatial distribution of contact stresses at the level of single nanopillars, epidermal cells, and the whole pad surface is required for the validation of a mechanism of contact stress equalisation in tree frog pads (Section 6.3).

Further support for a contribution of vdW forces to tree frog attachment is found in the functional morphology and chemistry of the digital pads:

- As mentioned above, vdW forces would be expected to occur primarily between the apical surfaces of individual nanopillars and the substrate. The observation of the tonofilaments—and hence of the primary pathways of force-transmission—connecting to the apical nanopillar surfaces (CHAPTER 3) indicates the local generation of attachment forces, possibly via vdW interactions.
- A thin layer of electron dense material lines the apical membrane of the nanopillars, possibly enhancing the Hamaker constant of the pad-substrate complex (CHAPTER 2).
- The presence of lipid-like surfactants in tree frog mucus (CHAPTER 4) arguably stabilises the interstitial mucus film with sub- μm -thickness and hence reduces the amount of generated vdW forces, as shown in a technical system (Li *et al.*, 2018b). Tree frogs may actively alter the concentration of surfactants in the mucus to modulate attachment strength.

Next to considerations of the functional pad morphology, several experimental observations provide support for the action of vdW forces:

- The approximately linear scaling of friction with body mass—and thereby with normal load—agrees with dry friction and hence with vdW forces (CHAPTER 2).
- Adhesion and friction of tree frog pads increase when pulling the pads proximally (Endlein *et al.*, 2017; Personal communication, W. Federle). Such pulling movements presumably facilitate drainage of interstitial mucus, hence decreasing the pad-substrate gap width (Hutt & Persson, 2016), increasing the generated vdW forces, and explaining the measured rise in attachment forces. Proximal pad pulling is also observed in unrestrained frogs (CHAPTER 3).
- Adding detergent to the mucus of an attaching frog causes the total failure of attachment (i.e. 0 mN attachment force; Green, 1981). The added surfactants may strengthen the interstitial mucus film against collapse (Li *et al.*, 2018b), hence causing the loss of vdW forces, and attachment failure.

In conclusion, vdW forces can, in theory, contribute significantly to tree frog attachment, which is supported by interpretations of the functional pad morphology and of experimental observations on tree frogs and the artificial adhesives inspired thereof. However, elaborate analytical, experimental, and computational methods are needed to test for the role of vdW forces in tree frog attachment (see Section 6.3). In future studies, vdW forces should not be considered independently, but in interaction with viscous friction and lubrication (CHAPTER 2).

6.1.5 Concluding remarks

Based on the antecedent discussion, I conclude that suction and mechanical interlocking are negligible in tree frog attachment. A contribution of hydrodynamic adhesion cannot be excluded, but, if present, presumably is a consequence of having a wet skin rather than a primary attachment mechanism. Capillary adhesion and vdW



forces appear to be the most significant known mechanisms of tree frog attachment. Overall, I hypothesise that tree frog attachment relies on a combination of wet and dry adhesion, with dry adhesion as primary mechanism, and with potential contributions of yet unknown mechanisms (CHAPTER 2).

6.2 Evolutionary aspects of tree frog attachment

In addition to the aforementioned arguments regarding biomechanics and bioadhesion, phylogenetic and evolutionary arguments contribute to an understanding of the fundamentals of tree frog attachment. Exploring the phylogeny of amphibians helps to examine the proposed convergent evolution of the digital pads of tree frogs (e.g. Barnes *et al.*, 2013; Green, 1979) and, if present, to identify pad components that evolved convergently. Identifying these components as well as the constraints and requirements that shaped their evolutionary history is also beneficial for biomimetics, as evolutionary convergence may indicate an ‘optimal’ design useful for the development of biomimetic adhesives (Barnes, 2012).

6.2.1 The digital pads of tree frogs, a convergent system?

Although the phylogenetic relationships among anuran clades are not entirely solved (e.g. Faivovich *et al.*, 2005; Frost *et al.*, 2006, 2008; Pyron & Wiens, 2011; Wells, 2007; Wiens, 2007), it appears that adhesive digital pads are found in different, only distantly related anuran groups. Species with enlarged pads were identified within the globally distributed neobatrachian superfamilies Hyloidae, Ranoidae, and Microhyloidae (Barnes *et al.*, 2013; Emerson & Diehl, 1980; Federle *et al.*, 2006; Liem, 1970; Manzano *et al.*, 2007; Wells, 2007). All three superfamilies also include species with digital surface patterning on a cellular level (i.e. freestanding epidermal cells) and on a subcellular level (i.e. nanopillars; Fig. 6.2). The distribution of adaptations towards an arboreal lifestyle over a wide range of neobatrachian species has been interpreted as a sign of convergent evolution (Barnes *et al.*, 2013, 2011; Hertwig & Sinsch, 1995; Liem, 1970; Scholz *et al.*, 2009).

As shown in CHAPTERS 3 and 4, the internal pad morphology has important functions too, such as the transmission of generated attachment forces and the secretion of mucus. A discussion of the distribution of the morphological elements identified and discussed in CHAPTER 3 (distal lymph space, collagen ridges, pad-intrinsic muscle fibres) across anurans is hindered by the small number of observations (Table 6.1). In contrast, the digital mucus gland cluster described in CHAPTER 4 has been reported or depicted in a surprisingly large number of references (although rarely mentioned explicitly; Fig. 6.3). We identified a digital mucus macrogland in 10 neobatrachian families, distributed across all three aforementioned superfamilies (see Table 4.SI.6 in CHAPTER 4). The presence of a proximal gland cluster may be correlated with a



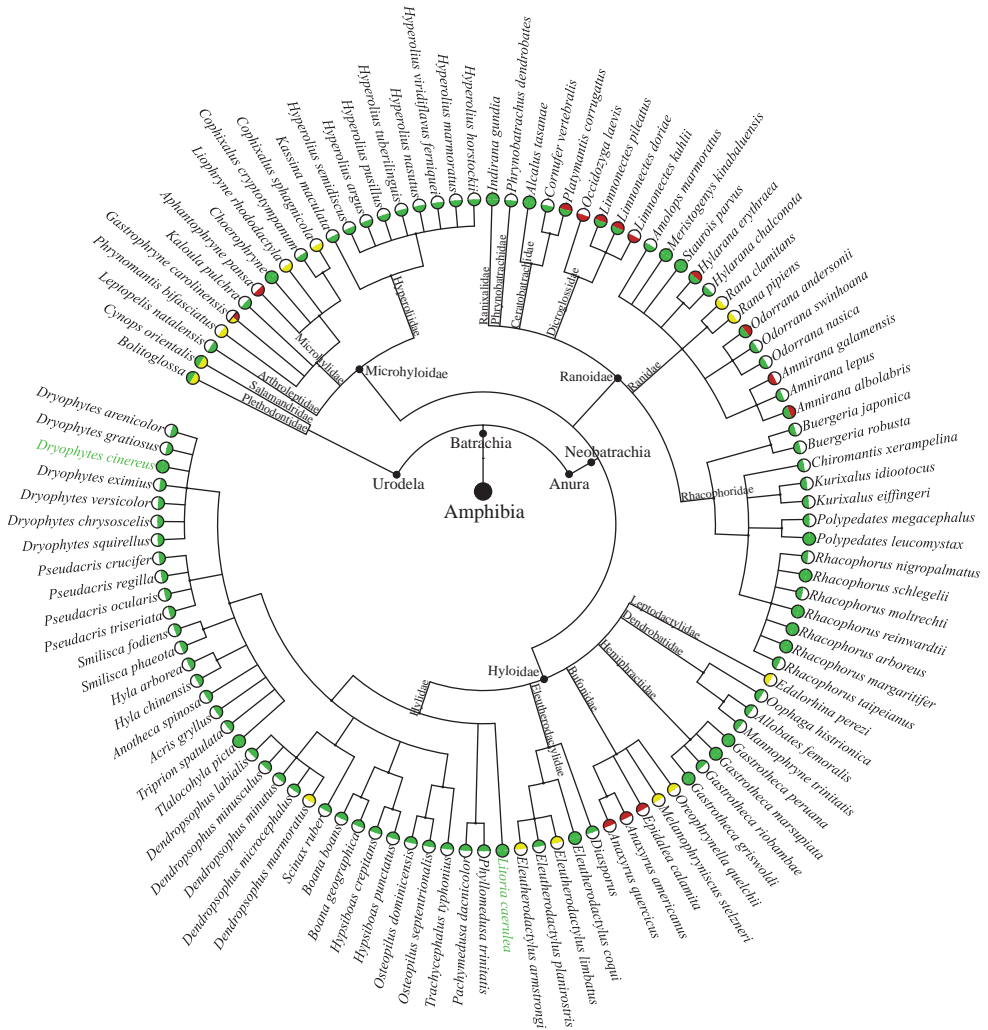


Figure 6.2 The occurrence of surface patterning of the ventral digital epidermis in batrachians. The colouring of the circles indicates the presence of surface patterning on the cellular level (i.e. polygonal surface cells separated by intercellular channels; inner halves of the circles) and on the subcellular level (i.e. ‘nanopillars’; outer halves of the circles). Green: patterning present, Yellow: moderate patterning present, Red: patterning not present, White: not reported. The phylogenetic tree was generated using `phylot.biobyte.de` based on the taxonomy database of the National Center for Biotechnology Information (NCBI) of the USA. *Litoria caerulea* and *Hyla cinerea* (reclassified as *Dryophytes cinereus*; Duellman *et al.*, 2016), the main study species in this thesis, are indicated by green lettering. The following references were used for the different families, in clockwise order: [... Continued on the next page.]

Figure 6.2 [...Continued from the previous page.] Plethodontidae (Green & Alberch, 1981), Salamandridae (Wang *et al.*, 2016), Arthropletidae (McAllister & Channing, 1983), Microhylidae (Emerson & Diehl, 1980; Green, 1979; Green & Simon, 1986; McAllister & Channing, 1983), Hyperoliidae (McAllister & Channing, 1983), Ranixalidae (Ohler, 1995), Phrynobatrachidae (Noble & Jaeckle, 1928), Ceratobatrachidae (Ohler, 1995), Dicroglossidae (Ohler, 1995), Ranidae (Drotlef *et al.*, 2014; Green, 1979; Lee *et al.*, 2001; Ohler, 1995), Rhacophoridae (Barnes, 2007b; Emerson & Diehl, 1980; Green, 1979; Lee *et al.*, 2001; McAllister & Channing, 1983; Mizuhira, 2004; Noble & Jaeckle, 1928; Ohler, 1995; Siedlecki, 1910; Welsch *et al.*, 1974), Leptodactylidae (Green, 1979), Dendrobatidae (Barnes, 2007b; Emerson & Diehl, 1980; Green, 1979), Hemiphractidae (Hertwig & Sinsch, 1992), Bufonidae (Emerson & Diehl, 1980; Green, 1979), Eleutherodactylidae (Emerson & Diehl, 1980; Green, 1979; Noble & Jaeckle, 1928), Hylidae (Ba-Omar *et al.*, 2000; Barnes, 2007b; Emerson & Diehl, 1980; Ernst, 1973a; Federle *et al.*, 2006; Green, 1979; Green & Carson, 1988; Hanna & Barnes, 1991; Lee *et al.*, 2001; Leydig, 1868; Linnenbach, 1985; Noble & Jaeckle, 1928; Smith *et al.*, 2006b).

distal subdermal lymph space, which has been identified in 4 neobatrachian families (Table 6.1).

Overall, the wide distribution of pad expansion, ventral surface patterning, and gland clustering in the digital pads of neobatrachians suggests that the whole digital tip acts as a functional unit that may have evolved convergently in arboreal frog species. However, the occurrence of surface patterning in the digital epidermis in min. 15 out of ca. 20 neobatrachian families (Frost *et al.*, 2006) raises the question, whether these structures developed independently, or originate from a common ancestor and got lost independently in the course of evolution. The latter is supported by a description of the loss of arboreal adaptations in *Gastrotheca* (Hertwig & Sinsch, 1995) and by indications that the adhesive digital apparatus of frogs arose before these animals became arboreal (Noble & Jaeckle, 1928). Modifications of the superficial epidermal cells occur also in the digits of the newt *Cynops orientalis* (Wang *et al.*, 2016) and of salamanders in the genus *Bolitoglossa* (Green & Alberch, 1981; Fig. 6.2). Both species are urodeles, which differentiated from lissamphibians (i.e. the common ancestors of modern urodeles and anurans) at least ca. 150 million years ago, adding further support for the presence of epidermal modifications in a common ancestor. Lastly, the

Table 6.1 Observations of subepidermal structures in the digital pads of neobatrachians.

Family	Species	Lymph space	Collagen ridges	Muscle fibres
Hylidae	<i>Hyla cinerea</i>	[1,2]	[1,2]	[1,2]
Hylidae	<i>H. arborea</i>	[3,4,5]	[3,5]	[3,5]
Hylidae	<i>Osteopilus septentrionalis</i>	[2]	[2]	[2]
Hylidae	<i>Acris gryllus</i>	—	—	—
Hylidae	<i>Litoria caerulea</i>	[6]	—	—
Phyllomedusidae	<i>Phyllomedusa sawagii</i>	[7]	—	[7]
Arthropletidae	<i>Lepoptelis karissimbensis</i>	[8]	—	—
Rhacophoridae	<i>Rhacophorus reinwardtii</i>	[9]	[9]	[9]

[1] (Langowski *et al.*, 2018b), [2] (Noble & Jaeckle, 1928), [3] (Leydig, 1876), [4] (Dewitz, 1883), [5] (Schuberg, 1891), [6] (Nakano & Saino, 2016), [7] (Fabrezi *et al.*, 2017), [8] (Drewes, 1984), [9] (Siedlecki, 1909)

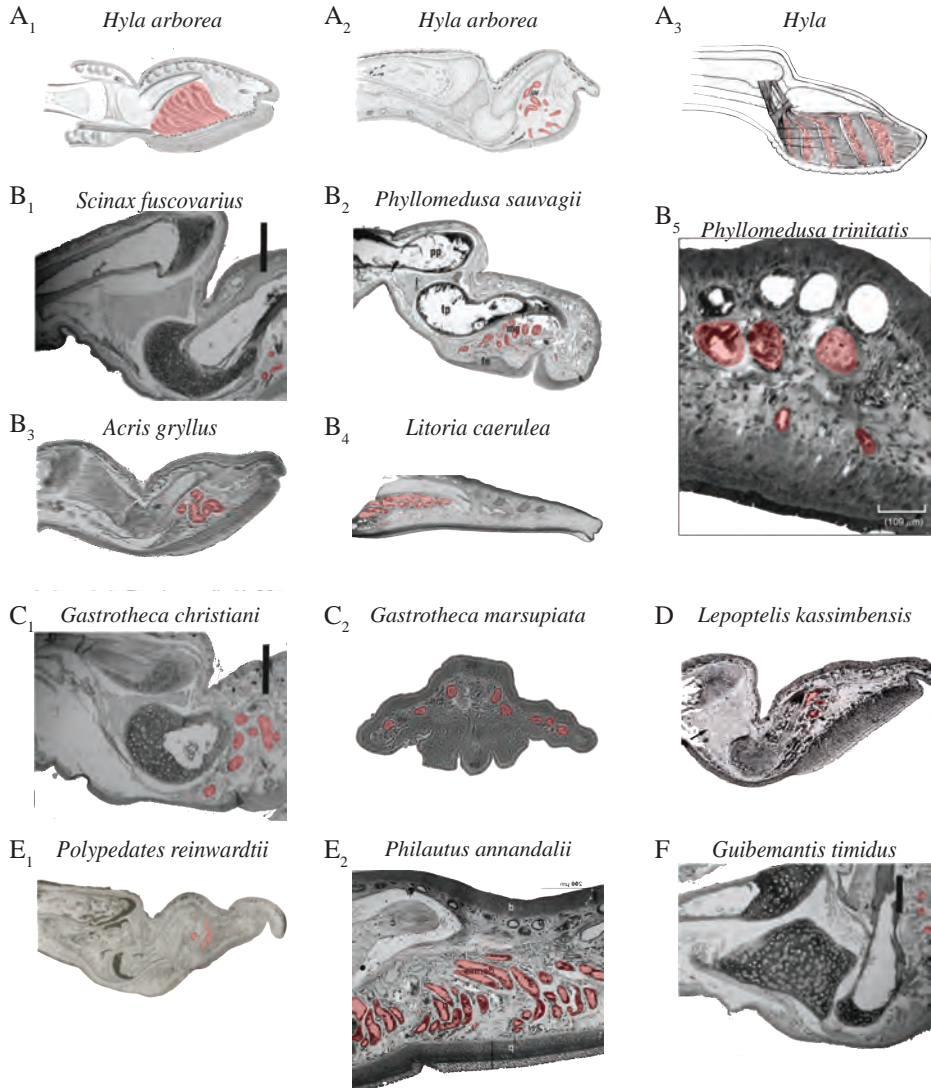


Figure 6.3 Depictions of gland clusters in the digital pads of various neobatrachian clades (presumptive ventral glands indicated in red). (A) *Hyla*, (B) other Hylidae, (C) Hemiphraactidae, (D) Hyperoliidae, (E) Rhacophoridae, and (F) Mantellidae. All sections are sagittal, with exception of transverse sections in B₅ and C₂. Subfigures modified after the following references: A₁ (Leydig, 1868); A₂ (Schuberg, 1891); A₃, B₃ (Noble & Jaeckle, 1928); B₁, C₁, F (Manzano *et al.*, 2007); B₂ (Fabrezi *et al.*, 2017); B₄ (Nakano & Saino, 2016) [Credit: M. Nakano]; B₅ (Ba-Omar *et al.*, 2000); C₂ (Hertwig & Sinsch, 1995) [Credit: American Society of Ichthyologists and Herpetologists]; D (Drewes, 1984) [Credit: R. Drewes]; E₁ (Siedlecki, 1910); E₂ (Chakraborti *et al.*, 2012). All figures reproduced with permission.

similarity in the general mucus chemistry of anurans, if compared between arboreal and terrestrial species within the Hyloidae and Ranoidae (CHAPTER 4), also supports the descent from a common ancestor.

To further examine the convergent evolution of the digital pads of tree frogs, a systematic approach, based on frequency and strength of convergence and specifying the considered level of the convergent system (e.g. individual pad components or whole digital morphology) rather than simply highlighting cases of convergence is required (Speed & Arbuckle, 2017). Here, the digital macroglands, which to my knowledge are not considered in current phylogenetic analyses (e.g. Frost *et al.*, 2006), may serve as important character in addition to traditional ones, which mostly relate to osteology and myology (e.g. Blotto *et al.*, 2017; Burton, 2004; Kamermans & Vences, 2009; Liem, 1970).

Overall, I conclude that the convergent evolution of the digital pads of tree frogs is still uncertain. If the digital pads evolved convergently, they presumably did so as a functional unit and under a generic selective pressure not exclusively related to an arboreal lifestyle. Evolutionary conservatism and the descent from a common ancestor is a valid alternative hypothesis (e.g. Moen *et al.*, 2013).

6.2.2 A tentative evolutionary history of the digital pads of tree frogs

Modern amphibians (Anura, Urodela, and Apoda) and reptiles originate from the ca. 400 million years old Tetrapodomorpha, which made the step from shallow waters to land (Haslam *et al.*, 2014). In contrast to their aquatic cousins, the skin of early amphibian ancestors (Temnospondyls, ca. 300–360 million years ago) lacked scales (Haslam *et al.*, 2014), which presumably facilitated the subsequent development of the cutaneous respiration present in modern amphibians (Haslam *et al.*, 2014; Wells, 2007). The adaptation towards cutaneous respiration may explain the lack of keratin-associated proteins and lipogenic substances (found in modern reptiles and their ancestors) in the amphibian epidermis, as such substances would hinder cutaneous gas exchange (Haslam *et al.*, 2014).

Cutaneous respiration requires a hydrophilic, slightly moist skin (Clarke, 1997). Arguably, a liquid layer between the appendicular cutis and the substrate leads to lubrication and a reduction in skin friction, especially on smooth substrates. Consequently, the appendicular cutis of early amphibian ancestors presumably was exposed to opposite functional demands, with skin wetting facilitating cutaneous respiration on the one hand and reducing locomotory efficiency (i.e. the range of travel for a given input of energy; Radhakrishnan, 1998) on the other hand. Friction also is crucial for the saltatorial locomotion (Fahrenbach & Knutson, 1975), which has been assigned to ca. 200 million year old amphibians (Shubin & Jenkins Jr., 1995). Besides a sufficient power output of the muscular-skeletal system (Astley & Roberts, 2012), friction between the limbs and the substrate is an important prerequisite in jumping, as friction determines the minimum possible take-off angle and hence the ability to jump forward (Clemente *et al.*, 2017). Enhanced friction between an arbitrary surface and a

substrate can be reached by micropatterning the surface, which enables drainage of interstitial liquids (Dhong & Fréchet, 2015; Gupta & Fréchet, 2012), closure of the pad-substrate gap, and the generation of vdW forces (CHAPTER 2). Accordingly, heightening of the ventral epidermal cells in amphibian digits, which previously was interpreted as adaptation towards an arboreal lifestyle (Green, 1979), presumably represents an adaptation towards a terrestrial lifestyle (Noble & Jaeckle, 1928), as it may have reduced the metabolic costs during the exploration of terrestrial habitats and facilitated the development of saltatorial locomotion in frogs. I hypothesise that not only the epidermal topography but also more basal structures such as the epidermal tonofilaments and dermal collagenous fibres described in CHAPTER 3 changed, reinforcing the soft epidermis against inertial mechanical loads occurring during jumping.

The morphological pad modifications enhancing friction on a horizontal substrate may also have promoted the initial exploration of habitats with inclined surfaces. Climbing vertical surfaces such as a tree stem requires predominantly frictional forces to counteract gravity, and some adhesion generated by the forelimbs to maintain moment balance (Cartmill, 1974). Increasing contact to vertical structures may have promoted a gradual gain in micropatterning of the digital pads of frogs (Green, 1979), which finally resulted in the sophisticated surface patterns found in the digital pads of modern tree frogs (CHAPTER 2). Hence, successive modifications of the epidermal cell morphology may have facilitated the step from a frictional pad to an attachment pad that generates friction and adhesion (Green, 1979). The appearance of the intercalary element (see CHAPTER 2) presumably represents the latest adaptation towards an arboreal lifestyle (Green, 1979; Noble & Jaeckle, 1928), which possibly occurred early in the neobatrachian line (Manzano *et al.*, 2007). As pointed out by Green (1979), the hypothesised phylogenetic development of the ventral pad epidermis is supported by the observation of similar stages in the ontogenetic pad development in tree frogs during post-amputatory regeneration (Richards *et al.*, 1977).

In conclusion, it appears that the evolution of the anuran digital epidermis is dominated by the presence of liquid, emphasising the relevance of drainage, friction, and vdW forces in tree frog attachment, which agrees with the foregoing discussion of the bioadhesion of tree frogs (Section 6.1).

6.2.3 Attachment systems bearing micropillars in non-amphibian clades

Adhesive organs covered with micropatterns of polygonal pillars have also been identified in non-amphibian species. Microscopic polygonal papillae packed with filaments coat the margin of the suction disc of *Gobiesox maeandricus* (Northern clingfish; Ditsche *et al.*, 2014). Analogously to tree frogs, these structures may promote drainage and the formation of close contact, hence sealing off the suction cup. Polygonal—primarily hexagonal—microstructures also cover the tarsal pads of the orthopterans *Tettigonia viridissima* (Great green bush-cricket; Gorb *et al.*, 2000) and *Acanthop-*



roctus diadematus (Nara cricket; Grohmann *et al.*, 2015). These microstructures are able to conform to rough substrates, thus enhancing the effective contact area and attachment forces (Perez Goodwyn *et al.*, 2006). Interestingly, *Locusta migratoria* (Migratory locust), another orthopteran species, does not show surface patterning (Perez Goodwyn *et al.*, 2006). *L. migratoria* lives in dry habitats, whereas *T. viridissima* lives in humid grass lands (Perez Goodwyn *et al.*, 2006), possibly hinting to a drainage-related function of polygonal microstructures in orthopterans as well.

Finally, one has to consider geckos and other lizards, the closest non-amphibian bio-adhesive cousins of tree frogs. Accompanying the increasing independence of reptilian ancestors from water for cutaneous respiration and for reproduction, their amniote epidermal cells progressively became keratinised and lipidised (Alibardi, 2006). In contrast, in the amphibian epidermis only a corneous layer is found, which is shed regularly to maintain cutaneous respiration (Alibardi, 2006). Hence, I hypothesise that the adaptation to a life with a wet skin not only explains the importance of drainage in frog pads, but also the different micropatterns found in the digital pads of geckos and tree frogs. Whereas amphibian epidermis is wet and only little keratinised (i.e. soft), requiring adaptations towards drainage and prohibiting the development of high-aspect-ratio microstructures (aspect ratio of epidermal cells and nanopillars in tree frogs ≈ 1 ; CHAPTER 2), the reptilian epidermis is dry and strongly keratinised (i.e. stiff), allowing the development of ca. 100 μm long and ca. 5 μm thick keratinous setae (aspect ratio ≈ 20), that branch at their tips into numerous nanoscopic spatulae (also with aspect ratios > 1 ; Autumn & Peattie, 2002) and enable the remarkable attachment of geckos.

6.3 Inspiration for the design of biomimetic adhesives

The versatile attachment of tree frogs stirred quite early the interest of researchers, who hoped to utilise the principles of tree frog attachment for the design of biomimetic technologies (Barnes, 1999; Barnes *et al.*, 2002). In the last decade, biomimetic research on tree frog attachment resulted in a number of meso- to microscopic reconstructions of the epidermal surface of the digital pads of tree frogs using homogeneous and isotropic materials (Fig. 6.4).

Sections 6.1 and 6.2 highlight the importance of epidermal micropatterning for the drainage of interstitial liquids, the formation of ‘dry’ contacts, and the generation of vdW forces. This principle has been successfully utilised to enhance the frictional and adhesive performance of current tree-frog-inspired adhesives (Fig. 6.4). However, the attachment performance of these adhesives presumably can be further improved by mimicking the hierarchical micro- to nanoscopic surface patterning in tree frog pads. In particular, the addition of nanopillars might help to reduce the force (and time) required to reach a gap-width in the single-digit nanometer range (Persson, 2007). Current experimental studies report contradictory trends on the optimal micropattern geometry for maximum attachment forces in a wet environment (Drotlef *et al.*,

2013; Xie *et al.*, 2018). A better understanding of the drainage performance of micropatterned adhesives may be obtained by a combination of parametric analyses of the effects of variations of the pillar geometry on attachment performance, analytical models (e.g. adequate hydrodynamic boundary conditions; Pilkington *et al.*, 2016), and numerical methods (e.g. computational fluid dynamics considering fluid-structure interactions).

Internal structures are important in the design of bioinspired adhesives with strong attachment, too. Most current tree-frog-inspired adhesives consist of a micropillar pattern that connects via a soft homogeneous base layer to a stiff support (e.g. Drotlef *et al.*, 2013). Mechanical loading of adhesives mounted in such a way can cause structural damage of the base layer and a reduction in friction (Xue *et al.*, 2017). In the digital pads of tree frogs, fibrous structures connect the adhesive pad epidermis with the skeleton (CHAPTER 3). The skewed tonofilaments traversing the epidermal cells presumably reinforce the pad surface against local stress concentrations. Furthermore, bundling of the tonofilaments in the basal cell regions, and strong interconnections between the epidermal cells (Ernst, 1973a) may enable the transmission of mechanical stresses between individual nanopillars (as shown for a technical system; Xue *et al.*, 2017) and superficial cells, respectively, hence avoiding local stress concentrations and impeding detachment (CHAPTER 3). The presence of stiff fibrous structures presumably causes anisotropic material behaviour. In compression, the low effective elastic modulus of frog pads (CHAPTER 2) allows a close conformation to rough substrates, thus enlarging the contact area effective for the generation of vdW forces. During tensile loading however, the internal fibrous structures stiffen the

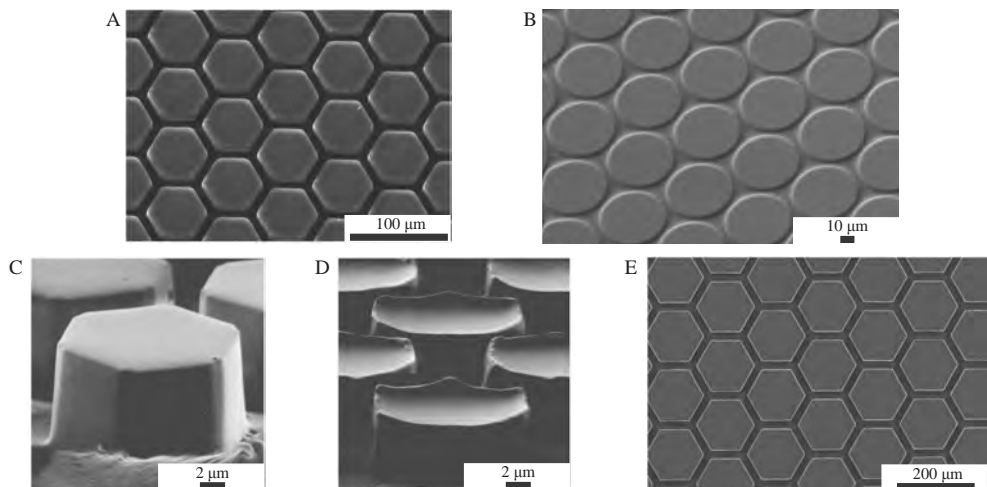


Figure 6.4 Tree-frog-inspired adhesives. (A) Hexagonal PDMS surface pattern for tunable friction on dry substrates (Murarash *et al.*, 2011), (B) Circular SU-8 surface pattern with reduced hydrodynamic contact forces (Gupta & Fréchet, 2012), (C) Hexagonally micropatterned PDMS surface with flat pillar tips for wet adhesion (Drotlef *et al.*, 2013), (D) Hexagonally micropatterned PDMS surface with concave pillar tips for wet adhesion (Drotlef *et al.*, 2013), (E) Hexagonal PDMS surface for friction in a wet environment (Chen *et al.*, 2015).

pad, and thus may allow the spatial distribution of contact stresses and impede crack formation. The benefit of a low stiffness during contact formation and a high stiffness during tensile loading has been formulated in a generalised scaling law ($F \propto \sqrt{AK}$; with attachment force capacity F , contact area A , and stiffness K of the adhesive; Bartlett *et al.*, 2012b), which explains the scaling of F of various biological and technical systems for a considerable range of variations (up to factors $\sim 10^{10}$) of A and K (Bartlett *et al.*, 2012a,b; Gilman *et al.*, 2015). Although the underlying physics are still under debate (Mojdehi *et al.*, 2017), the presence of fibrous elements in the surface region of the adhesive organs of geckos (e.g. Autumn & Peattie, 2002), insects (Gorb & Beutel, 2001), and tree frogs (CHAPTER 3) emphasises the importance of these structures for the design of bioinspired adhesives, particularly for applications where high mechanical loads are occurring (e.g. soft heavy duty grippers or dynamic bioinspired robots).

The digital pads of tree frogs contain several units of smooth muscle fibre bundles, which may allow these animals to modulate the generated attachment strength (CHAPTER 3). To my knowledge, the hypothesised functionality of these structures has not yet been transferred into technical systems. In existing actuated micropatterned adhesives, switchable adhesion mostly is achieved by modulations of the pillar geometry using external stimuli such as temperature (Cui *et al.*, 2012; Reddy *et al.*, 2007) or magnetism (Drotlef *et al.*, 2014; Northen *et al.*, 2008). Furthermore, switchable adhesion by modification of the overall contact surface topology was accomplished using pneumatic (Nadermann *et al.*, 2010) and electric (Shivapooja *et al.*, 2013) stimuli. Other solutions utilise a hysteresis in the buckling of micropillars (Paretkar *et al.*, 2011; Purtoev *et al.*, 2015), or the anisotropy of gecko-inspired adhesives (i.e. ‘frictional adhesion’; Modabberifar & Spenko, 2018) to switch between adhesive and non-adhesive state. All these solutions rely on modifications of the topology of the adhesive surface, which limits the freedom in the superficial and internal design of the micropatterns, thus reducing the aforementioned potential for drainage and control of contact stress distribution. Moreover, these adhesives are switchable rather than controllable. The tree-frog-inspired implementation of contractile elements in the base layer of a micropatterned adhesive could allow the gradual control of attachment via modification of the adhesive’s stiffness and contact area while maintaining freedom in the design of the surface pattern.

A simpler method of attachment control may be inspired by the passive structures of force transmission in frog pads (CHAPTER 3). The adhesive pad surface connects via a ventral collagen layer and a dorsal-ventral septum to the digital phalanx. As discussed in CHAPTER 3, loading of the adhesive surface via either one of these structures arguably leads to a difference in the contact stress distribution across the ventral pad surface, with firm attachment when loading the collagen layer, and detachment when loading the septum. Analogously, in future biomimetic adhesives various load trains could get implemented to rapidly modulate attachment strength.



6.4 Tree frog attachment, quo vadis?

As shown in this thesis, getting a grip on tree frog attachment is a complex problem, whose solution requires an interdisciplinary approach with contributions from biology, physics, chemistry, and engineering. Although some of the proposed attachment mechanisms may be rejected based on the antecedent discussion, we are still far from a comprehensive understanding of tree frog attachment. Most notably, a theoretical framework modelling the adhesive and frictional contact of the wet, soft, viscoelastic, micropatterned, composite pads of tree frogs is still missing. Combined modelling of these pad ‘dimensions’, as presented for insect adhesion (Gernay *et al.*, 2016), is required to advance the field. Next to insights obtained from the reverse engineering of tree frog pads (Section 6.3), contributions from several lines of research may help to deepen the understanding of tree frog attachment.

6.4.1 Ecology, phylogenetics, and evolution of tree frog attachment

Besides constraints related to phylogeny or the fundamental mechanisms of attachment, the habitat presumably is an important driver in the evolutionary development of the morphology and function of the digital pads of tree frogs. Using an ecomorphological approach, one could relate specific morphological traits of the pads to parameters regarding the environment (e.g. roughness or free surface energy of the encountered substrates) and the lifestyle (e.g. level of arboreality) of individual frog species. Whereas such studies exist in the field of gecko attachment (e.g. Collins *et al.*, 2015; Elstrott & Irschick, 2004; Hagey *et al.*, 2017; Irschick *et al.*, 1996), the ecomorphology of tree frogs received little attention. In complement, I propose an analysis of the evolutionary history of tree frog attachment to answer the questions raised in Section 6.2: Under which constraints and selective pressures did the digital pads of modern tree frogs develop, and was this development convergent? Such a study requires a screening of character states of the superficial and internal pad morphology over a wide range of extant anurans, as well as evidence from fossil samples, for example preserved in amber (as reported for geckos; Bauer *et al.*, 2005).

As we have shown in CHAPTER 5, tree frogs presumably perform better in attachment than previously reported. Quantification of the maximum attachment performance is important, as the obtained values serve as reference against predictions from analytical models of attachment. Further investigations of the maximum attachment performance of whole animals require a computation of the dynamic loads acting on the pads during taking off or landing via high-speed-recordings of the 3D kinematics and inverse body dynamics (see for example Wang *et al.*, 2013). Such studies face the challenge that frog skin is moist, preventing the use of conventional markers for kinematics tracking. Moreover, we found interindividual differences in attachment performance that are not explained by physical body parameters (e.g. mass or size; CHAPTER 5), suggesting that behaviour is a point of attention in future force measurements on unrestrained animals.

6.4.2 Single pad observations

In this thesis, I elucidated the internal morphology of the digital pads of tree frogs and proposed potential functions of the identified structures (CHAPTER 3 and 4). To provide support for the hypothesised mechanisms, *in vivo* observations of movements and deformations of the internal structures are required. For example, dynamic high-resolution magnetic resonance imaging may be used to study the kinematics of bony, collagenous, and muscular structures during attachment, and the hypothesised secretory deformations of the digital gland cluster.

Physiological and nervous components of the adhesive apparatus of tree frogs are barely known. The ventral pad cutis is interspersed by a dense network of blood vessels (e.g. Barnes *et al.*, 2011; Siedlecki, 1910). An analysis of the 3D architecture of this network may help to conclude on potential functions in attachment, such as a hypothesised control over the ventral pad topography (Nokhbatolfoghahai, 2013) or over pad stiffness (Barnes *et al.*, 2011) by the closure of individual blood vessels. Presumably, the liquid-filled lymph space codetermines the viscous properties of frog pads, especially at large deformations. Studying the detailed geometry of the lymph space, as well as the fluid dynamics of the contained lymph during attachment (e.g. using μ -CT as Hedrick *et al.*, 2014) would allow to assess its functional relevance. The presence of smooth muscle fibres and of a cluster of digital glands ensheathed by myoepithelial cells implies the presence of a nervous system innervating these structures, possibly allowing tree frogs to modulate attachment strength (CHAPTER 3). Moreover, sensory mechanoreceptors may be located in the pads. A morphological analysis of the digital nervous system would be the first step to an understanding of the role of motory and sensory structures in tree frog attachment. A better understanding of the nervous system in the digital pads of tree frogs is also important in future biomechanical experiments, as it might allow to control active processes (e.g. stiffness modulation or mucus secretion), and to reduce variation in the measured parameters of attachment performance.

6.4.3 What is happening at the interface?

Next to the development of adequate theoretical models, experimental work is needed to further elucidate the functional principles of tree frog attachment. Most importantly, the simultaneous measurement of the three-dimensional contact force exerted by an unrestrained single pad, contact area, and pad deformation over a whole step cycle is still missing. Such a measurement may allow, for example, partitioning of the generated adhesion into contributions from capillary adhesion and from vdW forces, as shown for tree-frog-inspired adhesives (e.g. Drotlef *et al.*, 2013). Mechano-sensitive substrate coatings (Neubauer *et al.*, 2016) may be used to characterise the distribution of mechanical stress over the contact interface.

In restrained animals, a parametric study of the tribological pad properties with control of normal load, sliding speed, and gap width would help to characterise tree

frog friction (e.g. the conditions at which boundary and hydrodynamic lubrication occur). A comparison of the obtained Stribeck curve with curves of known materials and geometries may provide insights into the fundamental friction mechanisms. In such studies, the anisotropy of tree frog friction should be taken into account by measuring friction as a function of sliding direction.

As shown in previous work and in this thesis, systematic studies of the attachment performance of frog pads in dependence of substrate properties allow to narrow down the set of involved attachment mechanisms. Whereas the effects of variations in substrate roughness and environmental pressure on tree frog attachment have been studied extensively, other substrate properties such as free surface energy or elastic modulus remained untouched so far. Importantly, such studies should aim to rebut rather than confirm the action of specific attachment mechanisms (see for example Loskill *et al.*, 2013). In order to facilitate metaanalyses on the attachment performance of tree frogs and other adhesive organisms, the characterisation of fundamental substrate properties (i.e. roughness and free surface energy) is crucial.

To further examine the role of vdW forces in the attachment of tree frogs to natural substrates, I suggest the quantification of the conformability of frog pads to micro- to macro-rough substrates (and of the gap-width between the two). Moreover, simultaneous measurements of the elastic modulus, compliance, and attachment force as well as a quantification of the spatial contact stress distribution at the pad-substrate interface are needed to analyse the shear stiffening of the digital pads of tree frogs.

Finally, further work is required on tree frog mucus. Whereas we could characterise in this thesis the general chemistry and the available volume of the mucus, its rheological properties are less well understood. The mucus has been shown to be roughly as viscous as water (Federle *et al.*, 2006), but its viscosity in the nanoscopic gap between hydrophilic pad and a substrate may be orders of magnitude higher (Ortiz-Young *et al.*, 2013).





Declarations

Authorship statements

Affiliation of co-authors

CHAPTER 2 to 5 of this thesis were written in collaboration with the following co-authors (sorted in order of appearance and alphabetically per research unit):

Frank T. van den Berg	FTvdB	<i>Experimental Zoology Group</i> <i>Department of Animal Sciences</i> <i>Wageningen University & Research</i> <i>De Elst 1</i> <i>6708 WD Wageningen</i> <i>The Netherlands</i>
Anne Blij	AB	
Dr. Sander W.S. Gussekloo	SWSG	
Prof. Dr. Johan L. van Leeuwen	JLvL	
Remco P.M. Pieters	RPMP	
Anne Rummenie	AR	<i>Department of</i> <i>Biomechanical Engineering</i> <i>Faculty of Mechanical, Maritime</i> <i>and Materials Engineering</i> <i>Delft University of Technology</i> <i>Mekelweg 2</i> <i>2628 CD Delft</i> <i>The Netherlands</i>
Henk Schipper	HS	
Dr. Dimitra Dodou	DD	<i>Physical Chemistry</i> <i>and Soft Matter</i> <i>Department of Agrotechnology</i> <i>and Food Sciences</i> <i>Wageningen University & Research</i> <i>Stippeneng 4</i> <i>6708 WE Wageningen</i> <i>The Netherlands</i>
Dr. Marleen Kamperman	MK	

Prof. Dr. Ali Dhinojwala	AD	<i>Prof. Ali Dhinojwala</i>
Sukhmanjot Kaur	SK	<i>Research Group</i>
Dr. Alex Nyarko	AN	<i>Department of Polymer Science</i>
Dr. Saranshu Singla	SS	<i>The University of Akron</i>
		<i>170 University Ave</i>
		<i>Ohio 44325-3909 Akron</i>
		<i>The United States of America</i>

		<i>Biomimicry Research & Innovation Center</i>
		<i>Departments of Biology and Polymer Science</i>
Dr. Henry C. Astley	HCA	<i>The University of Akron</i>
		<i>235 Carroll St.</i>
		<i>Ohio 44325-3908 Akron</i>
		<i>The United States of America</i>

		<i>Functional Morphology and Biomechanics</i>
		<i>Zoological Institute</i>
Prof. Dr. Stanislav N. Gorb	SNG	<i>Kiel University</i>
Dr. Alexander Kovalev	AK	<i>Am Botanischen Garten 1–9</i>
		<i>24118 Kiel</i>
		<i>Germany</i>

Author contributions

Julian K.A. Schöning-Langowski is abbreviated with JKAL. For abbreviations of the names of co-authors see the previous section.

CHAPTER 2

JKAL compiled the references, analysed the data, created the figures and drafted/revised the manuscript. DD, MK and JLvL commented and revised previous versions of the figures and the manuscript. All authors read and approved the final manuscript.

CHAPTER 3

Conception of the study: JKAL, HS, JLvL; data acquisition: JKAL, HS, AB, FTvdB, SWSG; data analysis: JKAL, HS; data interpretation: JKAL, JLvL, HS, SWSG; drafting of the manuscript and figures, literature analysis: JKAL; critical revision of the manuscript and the figures: JKAL, JLvL, SWSG, HS; final approval of the article: all authors.

CHAPTER 4

JKAL developed the initial study concept, which was revised together with JLvL. SWSG performed the μ -CT scan, which was analysed by JKAL. Histochemistry was

performed by HS and FTvdB, and analysed together with JKAL. SFG- and IR-measurements and -analyses were done by SS, AN, and SK. HCA provided the experimental animals and helped with mucus sampling. JKAL compiled the relevant literature and drafted the initial manuscript and figures, with contributions by SS and AN. All authors contributed to revising the manuscript, and approved the final manuscript.

CHAPTER 5

Conception of the study: AL, AR, JLvL; Development and testing of experimental setup: JKAL, RP, AR; Data collection: AR, JKAL; Data analysis: JKAL, AR; Data interpretation: JKAL, AR, JLvL; Drafting of the manuscript and figures: JKAL; Literature analysis: JKAL, SNG; Substrate preparation and characterisation methodology, and equipment: SNG, AK; Critical revision and approval: all authors.

Acknowledgements

CHAPTER 2

We thank D. Labonte, P. van Assenbergh and the journal club team of the Experimental Zoology Group, Wageningen University & Research, for helpful comments on the manuscript. We are grateful to W.J.P. Barnes, D. Labonte, T. Endlein and M. Kappl for constructive discussions on tree frog attachment. Also, we wish to express our gratitude towards D. Labonte for providing relevant literature from the 19th century.

CHAPTER 3

The authors acknowledge the Paul Scherrer Institut, Villigen, Switzerland, for provision of synchrotron radiation beamtime at the TOMCAT beamline X02DA of the SLS, and would like to thank C.M. Schlepütz for assistance as well as for helpful comments on the Materials and methods section of the manuscript. The authors are grateful to R.P.M. Pieters for assistance with logistics and for critical comments on the manuscript. The authors thank D. van de Pol, S. van Woudenberg, S. Visser and M. ter Veld from the CARUS research facility at Wageningen University & Research (WUR), Wageningen, The Netherlands, for setting up and taking care of the population of frogs used in this research. The authors are grateful to A. Rummenie and J. Jager for the support with sample collection, to B. Biemans for collecting the μ -CT data, to U. Cerkvenik and N. van Meer for assistance with the contrast-staining procedure and the segmentation of the μ -CT data, and to M. de Vries for preliminary analyses of the μ -CT data. The authors wish to express their gratitude towards the journal club team of the Experimental Zoology Group, WUR, for helpful comments on the manuscript, and towards D. Labonte, Imperial College London, UK, for providing relevant literature from the 19th century.

CHAPTER 4

The authors acknowledge the Paul Scherrer Institut, Villigen, Switzerland, for provision of synchrotron radiation beamtime at the TOMCAT beamline X02DA of the



SLS, and would like to thank C.M. Schlepütz for assistance. We are grateful to R.P.M. Pieters for assistance with logistics and for critical comments on the manuscript. The authors thank D. van de Pol, S. van Woudenberg, S. Visser and M. ter Veld from the CARUS research facility at WUR, for setting up and taking care of the population of frogs used in this research. We are grateful to A. Rummenie and J. Jager for the support with sample collection.

CHAPTER 5

We thank the following people for their valuable contributions. D. van de Pol, S. van Woudenberg, S. Visser, and M. ter Veld from the CARUS research facility at Wageningen University & Research (WUR), Wageningen, The Netherlands, set up and took care of the populations of frogs used in this research. J. Belgraver and H. Meijer from the Technical Development Studio, WUR, assisted with designing and manufacturing the experimental setup. A. Hagmayer and C. Voesenek, Experimental Zoology Group, WUR, helped with statistical analysis and with MATLAB scripting, respectively. W.J.P. Barnes, Institute of Molecular, Cell and Systems Biology, University of Glasgow, UK, provided helpful feedback on the experimental setup and animal housing. E.-J. Bakker, Biometris, WUR, provided advice on the statistical analysis, and R. Morssinkhof advised us on the housing of amphibians.

Ethical statements

CHAPTER 2

Not applicable.

CHAPTER 3

All animals used in this study were bought from legal vendors and were not killed for the purpose of this research. Therefore, this research is not considered as an animal experiment by the animal ethics committee of Wageningen University & Research (WUR).

CHAPTER 4

All frogs held at Wageningen University & Research (WUR) were bought from legal vendors and were not killed for the purpose of this research. Therefore, this research is not considered as an animal experiment by the animal ethics committee of WUR. All frogs held at the University of Akron were acquired from commercial vendors and experiments were conducted under IACUC protocol 16-08-17-AFD.

CHAPTER 5

All animals used in this study were bought from legal vendors. All procedures described were approved by the Animal Ethics Committee of Wageningen University & Research (permit number 2014126.d).

Funding

CHAPTER 2

This work is part of the research programme “Secure and gentle grip of delicate biological tissues” with project number 13353, which is financed by the Netherlands Organisation for Scientific Research (NWO).

CHAPTER 3

This work is part of the research programme “Secure and gentle grip of delicate biological tissues” with project number 13353, which is financed by the Netherlands Organisation for Scientific Research (NWO). The segmentation of the μ -CT data was supported by the National Institute of General Medical Sciences of the National Institutes of Health under grant number P41GM103545-18.

CHAPTER 4

This work is part of the research programme “Secure and gentle grip of delicate biological tissues” with project number 13353, which is (partly) financed by the Netherlands Organisation for Scientific Research (NWO). Further funding was provided by NSF-DMR 1610483 and NSF-IOS 1656645 (AN, AD, SS, SK).

CHAPTER 5

This work is part of the research programme “Secure and gentle grip of delicate biological tissues” with project number 13353, which is financed by the Netherlands Organisation for Scientific Research (NWO).



Competing interests

CHAPTER 2 to 5

All authors declare no competing interests.

Availability of data and materials

CHAPTER 2

The datasets used and analysed in this review are available in the cited literature and from the corresponding author on reasonable request.

CHAPTER 4

The datasets used and analysed in this article are provided in the article and the supplementary material, or will be made available from the corresponding author on reasonable request.



References

1. AFFERANTE, L., HEEPE, L., CASDORFF, K., GORB, S.N. & CARBONE, G. (2016). A theoretical characterization of curvature controlled adhesive properties of bio-inspired membranes. *Biomimetics* **1**, 1, p. 3.
2. AL BITAR, L., VOIGT, D., ZEBITZ, C. & GORB, S. (2010). Attachment ability of the codling moth *Cydia pomonella* L. to rough substrates. *Journal of Insect Physiology* **56**, 1966–1972.
3. ALIBARDI, L. (2006). Structural and immunocytochemical characterization of keratinization in vertebrate epidermis and epidermal derivatives. *International Review of Cytology* **253**, 177–259.
4. AMARPURI, G., ZHANG, C., DIAZ, C., OPELL, B.D., BLACKLEDGE, T.A. & DHINOJWALA, A. (2015). Spiders tune glue viscosity to maximize adhesion. *ACS Nano* **9**, 11, 11472–11478.
5. AMEY, A. & GRIGG, G. (1995). Lipid-reduced evaporative water loss in two arboreal hylid frogs. *Comparative Biochemistry and Physiology, Part A* **111**, 283–291.
6. ANIM-DANSO, E., ZHANG, Y., ALIZADEH, A. & DHINOJWALA, A. (2013). Freezing of water next to solid surfaces probed by infrared-visible sum frequency generation spectroscopy. *Journal of the American Chemical Society* **135**, 2734–2740.
7. ANTONIAZZI, M.M., NEVES, P.R., MAILHO-FONTANA, P.L., RODRIGUES, M.T. & JARED, C. (2013). Morphology of the parotoid macroglands in *Phyllomedusa* leaf frogs. *Journal of Zoology* **291**, 42–50.
8. ARISTOTLE (350 B.C.E., 1918). *Historia animalium*. Clarendon Press, Oxford, UK. Translated by Thompson, D.W. Clarendon.
9. ARZT, E., GORB, S. & SPOLENAK, R. (2003). From micro to nano contacts in biological attachment devices. *Proceedings of the National Academy of Sciences of the United States of America* **100**, 19, 10603–10606.
10. ASTLEY, H. & ROBERTS, T. (2012). Evidence for a vertebrate catapult: elastic energy storage in the plantaris tendon during frog jumping. *Biology Letters* **8**, 386–389.
11. ASTLEY, H.C., HARUTA, A. & ROBERTS, T.J. (2015). Robust jumping performance and elastic energy recovery from compliant perches in tree frogs. *Journal of Experimental Biology* **218**, 3360–3363.
12. AUTUMN, K., DITTMORE, A., SANTOS, D., SPENKO, M. & CUTKOSTY, M. (2006). Frictional adhesion: a new angle on gecko attachment. *Journal of Experimental Biology* **209**, 3569–3579.
13. AUTUMN, K., LIANG, Y.A., HSIEH, S.T., ZESCH, W., CHAN, W.P., KENNY, T.W., FEARING, R. & FULL, R.J. (2000). Adhesive force of a single gecko foot-hair. *Nature* **405**, 681–685.
14. AUTUMN, K. & PEATTIE, A.M. (2002). Mechanisms of adhesion in geckos. *Integrative and Comparative Biology* **42**, 6, 1081–1090.
15. AUTUMN, K., SITTI, M., LIANG, Y.A., PEATTIE, A.M., HANSEN, W.R., SPONBERG, S., KENNY, T.W., FEARING, R., ISRAELACHVILI, J.N. & FULL, R.J. (2002). Evidence for van der Waals adhesion in gecko setae. *Proceedings of the National Academy of Sciences of the United States of America* **99**, 19, 12252–12256.
16. BA-OMAR, T.A., DOWNIE, J.R. & BARNES, W.J.P. (2000). Development of adhesive toe-pads

- in the tree-frog (*Phyllomedusa trinitatis*). *Journal of Zoology* **250**, 267–282.
17. BANCROFT, J. & STEVENS, A., (eds.) (1996). *Theory and practice of histological techniques*. 4th edn. Churchill Livingstone, New York, USA.
 18. BARBEAU, T. & LILLYWHITE, H. (2005). Body wiping behaviors associated with cutaneous lipids in hylid tree frogs of Florida. *Journal of Experimental Biology* **208**, 2147–2156.
 19. BARNES, W.J.P. (1999). Tree frogs and tire technology. *Tire Technology International*, 42–47.
 20. ——— (2006). Dynamic adhesion in animals: mechanisms and biomimetic implications. *Journal of Comparative Physiology A* **192**, 1165–1168.
 21. ——— (2007a). Biomimetic solutions to sticky problems. *Science* **318**, 203–204.
 22. ——— (2007b). Functional morphology and design constraints of smooth adhesive pads. *Materials Research Society Bulletin* **32**, 479–485.
 23. ——— (2012). Adhesion in wet environments: Frogs. In: BHUSHAN, B., (ed.): *Encyclopedia of Nanotechnology*. Springer, 70–83.
 24. BARNES, W.J.P., BAUM, M., PEISKER, H. & GORB, S.N. (2013). Comparative cryo-SEM and AFM studies of hylid and rhacophorid tree frog toe pads. *Journal of Morphology* **274**, 1384–1396.
 25. BARNES, W.J.P., OINES, C. & SMITH, J.M. (2006). Whole animal measurements of shear and adhesive forces in adult tree frogs: insights into underlying mechanisms of adhesion obtained from studying the effects of size and scale. *Journal of Comparative Physiology A* **192**, 11, 1179–1191.
 26. BARNES, W.J.P., PEARMAN, J. & PLATTER, J. (2008). Application of peeling theory to tree frog adhesion, a biological system with biomimetic implications. *E-Newsletters for Science and Technology, Published by European Academy of Sciences (EAS)* **1**, 1, 1–2.
 27. BARNES, W.J.P., PEREZ GOODWYN, P.J., NOKHBATOLFOGHAAI, M. & GORB, S.N. (2011). Elastic modulus of tree frog adhesive toe pads. *Journal of Comparative Physiology A* **197**, 10, 969–978.
 28. BARNES, W.J.P., SMITH, J., OINES, C. & MUNDL, R. (2002). Bionics and wet grip. *Tire Technology International*, 56–60.
 29. BARRETT, A. (1971). The biochemistry and function of mucosubstances. *Histochemical Journal* **3**, 213–221.
 30. BARTLETT, M.D., CROLL, A.B. & CROSBY, A.J. (2012a). Designing bio-inspired adhesives for shear loading: From simple structures to complex patterns. *Advanced Functional Materials* **22**, 4985–4992.
 31. BARTLETT, M.D., CROLL, A.B., KING, D.R., PARET, B.M., J., I.D. & CROSBY, A.J. (2012b). Looking beyond fibrillar features to scale gecko-like adhesion. *Advanced Materials* **24**, 8, 1078–1083.
 32. BARTLETT, M.D. & CROSBY, A.J. (2014). High capacity, easy release adhesives from renewable materials. *Advanced Materials* **26**, 3405–3409.
 33. BAUER, A., BÖHME, W. & WEITSCHAT, W. (2005). An early Eocene gecko from Baltic amber and its implications for the evolution of gecko adhesion. *Journal of Zoology* **265**, 327–332.
 34. BELÉNDEZ, A., FRANCÉS, J., ORTUÑO, M., GALLEGO, S. & BERNABEU, J. (2010). Higher accurate approximate solutions for the simple pendulum in terms of elementary functions. *European Journal of Physics* **31**, 3, 65–70.
 35. BEUTEL, R. & GORB, S. (2001). Ultrastructure of attachment specializations of hexapods (Arthropoda): evolutionary patterns inferred from a revised ordinal phylogeny. *Journal of Zoological Systematics and Evolutionary Research* **39**, 177–207.
 36. ——— (2006). A revised interpretation of the evolution of attachment structures in Hexapoda with special emphasis on Mantophasmatodea. *Arthropod Systematics & Phylogeny* **64**, 1, 3–25.
 37. BIEWENER, A. (2008). *Collagen - Structure and Mechanics*, chap. 10: Tendons and Ligaments: Structure, Mechanical Behavior and Biological Function. Springer, New York, USA, 269–284.
 38. BIJMA, N.N., GORB, S.N. & KLEINTEICH, T. (2016). Landing on branches in the frog *Trachycephalus resinifictrix* (Anura: Hylidae). *Journal of Comparative Physiology A* **202**, 267–276.
 39. BIRDI, K., (ed.) (2009). *Handbook of Surface and Colloid Chemistry*. 3rd edn. CRC Press,

-
- Boca Raton, USA.
40. BLACKWALL, J. (1845). On the means by which various animals walk on the vertical surfaces of highly polished bodies. *Annals and Magazine of Natural History* **15**, 115–119.
 41. BLAYLOCK, L.A., RUIBAL, R. & PLATT-ALOIA, K. (1976). Skin structure and wiping behavior of phyllomedusine frogs. *Copeia* **1976**, 2, 283–295.
 42. BLOTTO, B., PEREYRA, M., FAIVOVICH, J. DOS SANTOS DIAS, P. & GRANT, T. (2017). Concentrated evolutionary novelties in the foot musculature of Odontophrynidae (Anura: Neobatrachia), with comments on adaptations for burrowing. *Zootaxa* **4258**, 5.
 43. BOGUE, R. (2008). Biomimetic adhesives: a review of recent developments. *Assembly Automation* **28**, 4, 282–288.
 44. BOTTOM, C., HANNA, S. & SIEHR, D. (1978). Mechanism of the Ninhydrin reaction. *Biochemical Education* **6**, 1, 4–5.
 45. BOVBJERG, A. (1963). Development of the glands of the dermal plicae in *Rana pipiens*. *Journal of Morphology* **113**, 2, 231–243.
 46. BREHM, A. (1892). *Brehms Tierleben: allgemeine Kunde des Tierreichs*, 7. 3rd edn. Bibliographisches Institut, Leipzig, Wien.
 47. BRIZZI, R., DELFINO, G., JANTRA, S., ALVAREZ, B. & SEVER, D. (2001). *Herpetologica Candiana*, chap. The amphibian cutaneous glands; some aspects of their structure and adaptive role. National Museum of Crete, Greece, 43–49.
 48. BRIZZI, R., DELFINO, G. & PELLEGRINI, R. (2002). Specialized mucous glands and their possible adaptive role in the males of some species of *Rana* (Amphibia, Anura). *Journal of Morphology* **254**, 328–341.
 49. BULLOCK, J.M.R., DRECHSLER, P. & FEDERLE, W. (2008). Comparison of smooth and hairy attachment pads in insects: friction, adhesion and mechanisms for direction-dependence. *Journal of Experimental Biology* **211**, 3333–3343.
 50. BULLOCK, J.M.R. & FEDERLE, W. (2011). The effect of surface roughness on claw and adhesive hair performance in the dock beetle *Gastrophysa viridula*. *Insect Science* **18**, 298–304.
 51. BURNHAM, K. & ANDERSON, D. (2002). *Model Selection and Multimodel Inference: A Practical Information-Theoretic Approach*. 2nd edn. Springer, New York.
 52. BURTON, T. (1998). Are the distal extensor muscles of the fingers of anurans an adaptation to arboreality? *Journal of Herpetology* **32**, 4, 611–617.
 53. ——— (2004). Muscles of the pes of hylid frogs. *Journal of Morphology* **260**, 209–233.
 54. BUSSCHER, H., VAN PELT, A., DE BOER, P., DE JONG, H. & ARENDS, J. (1984). The effect of surface roughening of polymers on measured contact angles of liquids. *Colloids and Surfaces* **9**, 319–331.
 55. BUSSCHER, H., VAN PELT, A., DE JONG, H. & ARENDS, J. (1983). Effect of spreading pressure on surface free energy determinations by means of contact angle measurements. *Journal of Colloid and Interface Science* **95**, 1, 23–27.
 56. BUTT, H.J., BARNES, W.J.P., DEL CAMPO, A., KAPPL, M. & SCHÖNFELD, F. (2010). Capillary forces between soft, elastic spheres. *Soft Matter* **6**, 5930–5936.
 57. BUTT, H.J. & KAPPL, M. (2009). Normal capillary forces. *Advances in Colloid and Interface Science* **146**, 48–60.
 58. VON BYERN, J. & GRUNWALD, I., (eds.) (2010). *Biological adhesive systems: From nature to technical and medical application*. Springer, Wien, New York.
 59. CAMPBELL, J., R.M., A., BERRZ, E. & HUF, E. (1967). Electrolytes in frog skin secretions. *Comparative Biochemistry and Physiology* **23**, 213–223.
 60. CARTMILL, M. (1974). *Primate locomotion*, chap. 2: Pads and claws in arboreal locomotion. Academic Press, New York, USA, 45–83.
 61. ——— (1985). *Functional vertebrate morphology*, chap. 5: Climbing. Harvard University Press, 73–88.
 62. CENTENO, F.C., ANTONIAZZI, M.M., ANDRADE, D.V., KODAMA, R.T., SCIANI, J.M., PIMENTA, D.C. & JARED, C.. (2015). Anuran skin and basking behavior: the case of the treefrog *Bokermannohyla alvarengai* (Bokermann, 1956). *Journal of Morphology* **276**, 1172–1182.
 63. CHAKRABORTI, S., DAS, D., DE, S.K. & NAG, T.C. (2012). Structural organization of the toe



- pads in the amphibian *Philautus annandalii* (Boulenger, 1906). *Acta Zoologica* **95**, 63–72.
64. CHAKRABORTI, S., NAG, T., DAS, D., SANYAL CHATTERJEE, T. & DE, S. (2014). Cytokeratin localization in toe pads of the anuran amphibian *Philautus annandalii* (Boulenger, 1906). *Tissue and Cell* **46**, 165–169.
65. CHEN, H., ZHANG, L., ZHANG, D., ZHANG, P. & HAN, Z. (2015). Bioinspired surface for surgical graspers based on the strong wet friction of tree frog toe pads. *ACS Applied Materials & Interfaces* **7**, 25, 13987–13995.
66. CHEN, X., CLARKE, M., WANG, J. & CHEN, Z. (2005). Sum frequency generation vibrational spectroscopy studies on molecular conformation and orientation of biological molecules at interfaces. *International Journal of Modern Physics B* **19**, 4, 691–713.
67. CLARKE, B. (1997). The natural history of amphibian skin secretions, their normal functioning and potential medical applications. *Biological Reviews* **72**, 365–379.
68. CLEMENTE, C.J., GOETZKE, H.H., BULLOCK, J.M.R., SUTTON, P.S., BURROWS, M. & FEDERLE, W. (2017). Jumping without slipping: leafhoppers (Hemiptera: Cicadellidae) possess special tarsal structures for jumping from smooth surfaces. *Journal of the Royal Society Interface* **14**, p. 20170022.
69. COLLINS, C.E., RUSSELL, A.P. & HIGHAM, T.E. (2015). Subdigital adhesive pad morphology varies in relation to structural habitat use in the Namib Day Gecko. *Functional Ecology* **29**, 66–77.
70. CONGDON, R., MUTH, G. & SPLITTGERBER, A. (1993). The binding interaction of Coomassie blue with proteins. *Analytical Biochemistry* **213**, 407–413.
71. COX, R.G. & BRENNER, H. (1967). The slow motion of a sphere through a viscous fluid towards a plane surface—II Small gap widths, including inertial effects. *Chemical Engineering Science* **22**, 1759–1777.
72. CRAWFORD, N., ENDLEIN, T. & BARNES, W.J.P. (2012). Self-cleaning in tree frog toe pads; a mechanism for recovering from contamination without the need for grooming. *Journal of Experimental Biology* **215**, 3965–3972.
73. CRAWFORD, N., ENDLEIN, T., PHAM, J., RIEHLE, M. & BARNES, W.J.P. (2016). When the going gets rough – studying the effect of surface roughness on the adhesive abilities of tree frogs. *Beilstein Journal of Nanotechnology* **7**, 2116–2131.
74. CRAWFORD, N.A. (2016). The biomechanics of tree frog adhesion under challenging conditions. PhD Thesis, University of Glasgow, Glasgow, UK.
75. CRETON, C. & GORB, S. (2007). Sticky feet: From animals to materials. *Materials Research Society Bulletin* **32**, 6, 466–472.
76. CUI, J., DROTLEF, D.M., LARRAZA, I., FERNÁNDEZ-BLÁZQUEZ, J., BOESEL, L., OHM, C., MEZGER, M., ZENTEL, R. & DEL CAMPO, A. (2012). Bioinspired actuated adhesive patterns of liquid crystalline elastomers. *Advanced Materials* **24**, 4601–4604.
77. CZOPEK, J. (1965). Quantitative studies on the morphology of respiratory surfaces in amphibians. *Acta Anatomica* **62**, 296–323.
78. DAI, Z., GORB, S. & SCHWARZ, U. (2002). Roughness-dependent friction force of the tarsal claw system in the beetle *Pachnoda marginata* (Coleoptera, Scarabaeidae). *Journal of Experimental Biology* **205**, 2479–2488.
79. DAPSON, R.W. (1969). Histochemistry of mucus in the skin of the frog, *Rana pipiens*. *The Anatomical Record* **166**, 4, 615–625.
80. DEWITZ, H. (1883). Ueber das verschiedene Aussehen der gereizten und ruhenden Drüsen im Zehenballen des Laubfrosches. *Biologisches Zentralblatt* **3**, 558–560.
81. DHONG, C. & FRÉCHETTE, J. (2015). Coupled effects of applied load and surface structure on the viscous forces during peeling. *Soft Matter* **11**, 1901–1909.
82. DIRKS, J.H. (2014). Physical principles of fluid-mediated insect attachment - shouldn't insects slip? *Beilstein Journal of Nanotechnology* **5**, 1160–1166.
83. DIRKS, J.H. & FEDERLE, W. (2011). Mechanisms of fluid production in smooth adhesive pads of insects. *Journal of The Royal Society Interface* **8**, 952–960.
84. DIRKS, J.H., LI, M., KABLA, A. & FEDERLE, W.A. (2012). In vivo dynamics of the internal fibrous structure in smooth adhesive pads of insects. *Acta Biomaterialia* **8**, 2730–2736.

-
85. DITSCHKE, P. & SUMMERS, A.P. (2014). Aquatic versus terrestrial attachment: Water makes a difference. *Beilstein Journal of Nanotechnology* **5**, 1, 2424–2439.
86. DITSCHKE, P., WAINWRIGHT, D. & SUMMERS, A. (2014). Attachment to challenging substrates – fouling, roughness and limits of adhesion in the northern clingfish (*Gobiesox maeandricus*). *Journal of Experimental Biology* **217**, 2548–2554.
87. DITSCHKE-KURU, P., BARTHLOTT, W. & KOOP, J.H. (2012). At which surface roughness do claws cling? investigations with larvae of the running water mayfly *Epeorus assimilis* (Heptageniidae, Ephemeroptera). *Zoology* **115**, 379–388.
88. DRECHSLER, P. & FEDERLE, W. (2006). Biomechanics of smooth adhesive pads in insects: influence of tarsal secretion on attachment performance. *Journal of Comparative Physiology A* **192**, 1213–1222.
89. DRECHSLER, P.H. (2008). Mechanics of adhesion and friction in stick insects and tree frogs. PhD Thesis, Julius-Maximilians-Universität Würzburg, Würzburg, Germany.
90. DREWES, R.C. (1984). A phylogenetic analysis of the Hyperoliidae (Anura): Treefrogs of Africa, Madagascar, and the Seychelles islands. *Occasional papers of the California Academy of Sciences* **139**, 1–70.
91. DROTLEF, D.M., APPEL, E., PEISKER, H., DENING, K., DEL CAMPO, A., GORB, S.N., & BARNES, W.J.P. (2015). Morphological studies of the toe pads of the rock frog, *Staurois parvus* (family: Ranidae) and their relevance to the development of new biomimetically inspired reversible adhesives. *Interface Focus* **5**, 1–11.
92. DROTLEF, D.M., BLÜMLER, P. & DEL CAMPO, A. (2014). Magnetically actuated patterns for bioinspired reversible adhesion (dry and wet). *Advanced Materials* **26**, 775–779.
93. DROTLEF, D.M., STEPIEN, L., KAPPL, M., BARNES, W.J.P., BUTT, H.J. & DEL CAMPO, A. (2013). Insights into the adhesive mechanisms of tree frogs using artificial mimics. *Advanced Functional Materials* **23**, 1137–1146.
94. DUELLMAN, W., MARIAN, A. & HEDGES, S. (2016). Phylogenetics, classification, and biogeography of the treefrogs (Amphibia: Anura: Arboranae). *Zootaxa* **4104**, 1, 1–109.
95. DUELLMAN, W.E. & TRUEB, L. (1994). *Biology of amphibians*. The Johns Hopkins University Press, Baltimore, USA.
96. ELS, W.J. & HENNEBERG, R. (1990). Histological features and histochemistry of the mucous glands in ventral skin of the frog (*Rana fuscigula*). *Histology and Histopathology* **5**, 343–348.
97. ELSTROTT, J. & IRSCHICK, D.J. (2004). Evolutionary correlations among morphology, habitat use and clinging performance in Caribbean *Anolis* lizards. *Biological Journal of the Linnean Society* **83**, 389–398.
98. EMERSON, S.B. (1978). Allometry and jumping in frogs: Helping the twain to meet. *Evolution* **32**, 3, 551–564.
99. ——— (1991). The ecomorphology of Bornean tree frogs (family Rhacophoridae). *Zoological Journal of the Linnean Society* **101**, 337–357.
100. EMERSON, S.B. & DIEHL, D. (1980). Toe pad morphology and mechanisms of sticking in frogs. *Biological Journal of the Linnean Society* **13**, 199–216.
101. ENDLEIN, T. & BARNES, W.J.P. (2015). Wet adhesion in tree and torrent frogs. In: BHUSHAN, B., (ed.): *Encyclopedia of Nanotechnology*. Springer, 1–20.
102. ENDLEIN, T., BARNES, W.J.P., SAMUEL, D.S., CRAWFORD, N.A., BIAW, A.B. & GRAFE, U. (2013). Sticking under wet conditions: The remarkable attachment abilities of the torrent frog, *Staurois guttatus*. *PLoS ONE* **8**, 9, 1–12.
103. ENDLEIN, T., JI, A., SAMUEL, D., YAO, N., WANG, Z., BARNES, W.J.P., FEDERLE, W., KAPPL, M. & DAI, Z. (2012). Sticking like sticky tape: tree frogs use friction forces to enhance attachment on overhanging surfaces. *Journal of The Royal Society Interface* **10**, 80, 1–11.
104. ENDLEIN, T., JI, A., YUAN, S., HILL, I., WANG, H., BARNES, W.J.P., DAI, Z. & SITTI, M. (2017). The use of clamping grips and friction pads by tree frogs for climbing curved surfaces. *Proceedings of the Royal Society B: Biological Sciences* **284**, 1–9.
105. ENGELMANN, T. (1872). Die Hautdrüsen des Frosches: Eine physiologische Studie. *Archiv für die gesammte Physiologie des Menschen und der Thiere* **5**, 498–537.
106. ERNST, V.V. (1973a). The digital pads of the tree frog, *Hyla cinerea*. I. The epidermis. *Tissue*



- and *Cell* **5**, 1, 83–96.
107. ——— (1973b). The digital pads of the tree frog, *Hyla cinerea*. II. The mucous glands. *Tissue and Cell* **5**, 1, 97–104.
 108. FABREZI, M., GOLDBERG, J. & CHULIVER PEREYRA, M. (2017). Morphological variation in anuran limbs: Constraints and novelties. *Journal of Experimental Zoology Part B: Molecular and Developmental Biology* **328**, 6, 546–574.
 109. FAHRENBACH, W.H. & KNUTSON, D.D. (1975). Surface adaptations of the vertebrate epidermis to friction. *The Journal of Investigative Dermatology* **65**, 1, 39–44.
 110. FAIVOVICH, J., HADDAD, C.F.B., GARCIA, P.C.A., FROST, D.R., CAMPBELL, J.A. & WHEELER, W.C. (2005). Systematic review of the frog family Hylidae, with special reference to Hylinae: phylogenetic analysis and taxonomic revision. *Bulletin of the American Museum of Natural History* **294**, 1–240.
 111. FAVI, P.M., SIJIA, Y., LENAGHAN, S.C., XIA, L. & ZHANG, M. (2014). Inspiration from the natural world: from bio-adhesives to bio-inspired adhesives. *Journal of Adhesion Science and Technology* **28**, 3–4, 290–319.
 112. FAYEMI, P.E., MARANZANA, N., AOUSSAT, A. & BERSANO, G. (2014). Bio-inspired design characterisation and its links with problem solving tools. In: MARJANOVIC, D., STORGA, M., PAVKOVIC, N. & BOJCETIC, N., (eds.): *Proceedings of the DESIGN 2014 13th International Design Conference*. 173–182.
 113. FEDERLE, W., BARNES, W.J.P., BAUMGARTNER, W., DRECHSLER, P. & SMITH, J.M. (2006). Wet but not slippery: boundary friction in tree frog adhesive toe pads. *Journal of The Royal Society Interface* **3**, 10, 689–697.
 114. FERRARO, D.P., TOPA, P.E. & HERMIDA, G.N. (2011). Lumbar glands in the frog genera *Pleurodema* and *Somuncuria* (Anura: Leiuperidae): histological and histochemical perspectives. *Acta Zoologica* **00**, 1–14.
 115. FILIPPOV, A. & GORB, S. (2015). Spatial model of the gecko foot hair: functional significance of highly specialized non-uniform geometry. *Interface Focus* **5**, 1–7.
 116. FISHER, M.C., GARNER, T.W. & WALKER, S.F. (2009). Global emergence of *Batrachochytrium dendrobatidis* and Amphibian Chytridiomycosis in space, time, and host. *Annual Review of Microbiology* **36**, 291–310.
 117. FLAMMANG, P. & SANTOS, R. (2015). Biological adhesives: from biology to biomimetics. *Interface Focus* **8**, 1–3.
 118. FONTANA, M., ASK, K., MACDONALD, R., CARNES, A. & STAUB, N. (2006). Loss of traditional mucous glands and presence of a novel mucus-producing granular gland in the plethodontid salamander *Ensatina eschscholtzii*. *Biological Journal of the Linnean Society* **87**, 469–477.
 119. FOWLER, J., KLEINTEICH, T., FRANZ, J., JAYE, C., FISCHER, D., GORB, S., WEIDNER, T. & BAIO, J. (2018). Surface chemistry of the frog sticky-tongue mechanism. *Biointerphases* **13**, 6, 1–7.
 120. FROST, D.R., GRANT, T., FAIVOVICH, J., BAIN, R.H., HAAS, A., HADDAD, C.F.B., DE SA, R.O., CHANNING, A., WILKINSON, M., DONNELLAN, S.C., RAXWORTHY, C.J., CAMPBELL, J.A., BLOTTO, B.L., MOLER, P., DREWES, R.C., NUSSBAUM, R.A., LYNCH, J.D., GREEN, D.M. & WHEELER, W.C. (2006). The amphibian tree of life. *Bulletin of the American Museum of Natural History* **297**, 1, 1–291.
 121. ——— (2008). Is the amphibian tree of life really fatally flawed? *Cladistics* **24**, 385–395.
 122. GADOW, H. (1909). *Amphibia and Reptiles*. MacMillan and Co., London, UK.
 123. GATESBY, M. (1743). *The natural history of Carolina, Florida and the Bahama Islands*, **2**.
 124. GAUPP, E. (1904). *A. Ecker's und R. Wiedersheim's Anatomie des Frosches auf Grund eigener Untersuchungen durchaus neu bearbeitet*. 2nd edn. Vieweg und Sohn, Braunschweig, Germany.
 125. GEBESHUBER, I.C. (2007). Biotribology inspires new technologies. *Nano Today* **2**, 5, 30–37.
 126. DE GENNES, P.G., BROCHARD-WYART, F. & QUÉRÉ, D. (2004). *Capillarity and Wetting Phenomena: Drops, Bubbles, Pearls, Waves*. Springer, New York, USA.
 127. GEORGIU, C., GRINTZALIS, K., ZERVOUDAKIS, G. & PAPAPOSTOLOU, I. (2008). Mechanism of Coomassie brilliant blue G-250 binding to proteins: a hydrophobic assay for nanogram

- quantities of proteins. *Analytical and Bioanalytical Chemistry* **391**, 1, 391–403.
128. GERNAY, S., FEDERLE, W., LAMBERT, P. & GILET, T. (2016). Elasto-capillarity in insect fibrillar adhesion. *Journal of the Royal Society Interface* **13**, p. 20160371.
129. GILMAN, C.A., IMBURGIA, M., J. BARTLETT, M.D., KING, D.R., CROSBY, A.J. & IRSCHICK, D.J. (2015). Geckos as springs: Mechanics explain across-species scaling of adhesion. *PLoS ONE* **10**, 9, 1–15.
130. GONIAKOWSKA-WITALIŃSKA, L. & KUBICZEK, U. (1998). The structure of the skin of the tree frog (*Hyla arborea arborea* l.). *Annals of Anatomy* **180**, 237–246.
131. GORB, S. (2001). *Attachment devices of the insect cuticle*. Kluwer Academic Publishers, New York, Boston, Dordrecht, London, Moscow.
132. ——— (2007). Visualisation of native surfaces by two-step molding. *Miscroscopy Today* **15**, 2, 44–47.
133. GORB, S. & BEUTEL, R. (2001). Evolution of locomotory attachment pads of hexapods. *Naturwissenschaften* **88**, 530–534.
134. GORB, S., JIAO, Y. & SCHERGE, M. (2000). Ultrastructural achitecture and mechanical properties of attachment pads in *Tettigonia viridissima* (Orthoptera Tettigoniidae). *Journal of Comparative Physiology A* **186**, 821–831.
135. GORB, S.N. (2008). Biological attachment devices: exploring nature’s diversity for biomimetics. *Philosophical Transactions of the Royal Society A* **366**, 1557–1574.
136. GREEN, D. & ALBERCH, P. (1981). Interdigital webbing and skin morphology in the neotropical salamander genus *Bolitoglossa* (Amphibia; Plethodontidae). *Journal of Morphology* **170**, 273–282.
137. GREEN, D.M. (1979). Treefrog toe pads: comparative surface morphology using scanning electron microscopy. *Canadian Journal of Zoology* **57**, 2033–2046.
138. ——— (1980). Size differences in adhesive toe-pad cells of treefrogs of the diploid-polyploid *Hyla versicolor* complex. *Journal of Herpetology* **14**, 1, 15–19.
139. ——— (1981). Adhesion and the toe-pads of treefrogs. *Copeia* **1981**, 790–796.
140. GREEN, D.M. & CARSON, J. (1988). The adhesion of treefrog toe-pads to glass: cryogenic examination of a capillary adhesion system. *Journal of Natural History* **22**, 131–135.
141. GREEN, D.M. & SIMON, M.P. (1986). Digital microstructure in ecologically diverse sympatric microhylid frogs, genera *Cophixalus* and *Sphenophryne* (Amphibia : Anura), from Papua New Guinea. *Australian Journal of Zoology* **34**, 135–45.
142. GROHMANN, C., HENZE, M.J., NØRGAARD, T. & GORB, S.N. (2015). Two functional types of attachment pads on a single foot in the Namibia bush cricket *Acanthoproctus diadematus* (Orthoptera: Tettigoniidae). *Proceedings of the Royal Society B: Biological Sciences* **282**, p. 20142976.
143. GU, Z., LI, S., ZHANG, F. & WANG, S. (2016). Understanding surface adhesion in nature: A peeling model. *Advanced Science* **3**, 1–13.
144. GUIGUI, K. & BEAUDOIN, A. (2007). The use of oil red O in sequence with other methods of fingerprint development. *Journal of Forensic Identification* **57**, 4, 550–581.
145. GUPTA, R. & FRÉCHETTE, J. (2012). Measurement and scaling of hydrodynamic interactions in the presence of draining channels. *Langmuir* **28**, 14703–14712.
146. HAGEY, T.J., HARTE, S., VICKERS, M., HARMON, L.J. & SCHWARZKOPF, L. (2017). There’s more than one way to climb a tree: Limb length and microhabitat use in lizards with toe pads. *PLoS ONE* **12**, 9, p. e0184641.
147. HANNA, G. & BARNES, W.J.P. (1991). Adhesion and detachment of the toe pads of tree frogs. *Journal of Experimental Biology* **155**, 1, 103–125.
148. HASLAM, I.S., ROUBOS, E.W., MANGONI, M.L., YOSHIKATO, K., VAUDRY, H., KLOEPPER, J.E., PATTWELL, D.M., MADERSON, P.F.A. & PAUS, R. (2014). From frog integument to human skin: dermatological perspectives from frog skin biology. *Biological Reviews* **89**, 618–655.
149. HEDRICK, M., HANSEN, K., WANG, T., LAURIDSEN, H., THYGESEN, J. & PEDERSEN, M. (2014). Visualising lymph movement in anuran amphibians with computed tomography. *Journal of Experimental Biology* **217**, 2990–2993.



150. HENNEBERT, E., GREGOROWICZ, E. & FLAMMANG, P. (2018). Involvement of sulfated biopolymers in adhesive secretions produced by marine invertebrates. *Biology Open* **7**, 1–11.
151. HERTWIG, I. & SINSCH, U. (1992). The digital pads of marsupial frogs (genus *Gastrotheca*). In: KORSÓS, Z. & KISS, I., (eds.): *Proceedings of the 6th Ordinary General Meeting of the Societas Europaea Herpetologica*. Budapest, Hungary, 225–229.
152. ——— (1995). Comparative toe pad morphology in marsupial frogs (genus *Gastrotheca*): Arboreal versus ground-dwelling species. *Copeia* **1995**, 1, 38–47.
153. HILL, I.D., DONG, B., BARNES, W.J.P., JI, A. & ENDLEIN, T. (2018). The biomechanics of tree frogs climbing curved surfaces: a gripping problem. *Journal of Experimental Biology* **221**, 1–10.
154. HOLDGATE, M. (1955). The wetting of insect cuticles by water. *Journal of Experimental Biology* **32**, 591–617.
155. HOLMGREN, S. & OLSSON, C. (2011). Autonomic control of glands and secretion: A comparative view. *Autonomic Neuroscience: Basic and Clinical* **165**, 102–112.
156. HOPKINS, J., BRENNER, L. & TUMOSA, C. (1991). Variation of the amide I and amide II peak absorbance ratio in human hair as measured by Fourier transform infrared spectroscopy. *Forensic Science International* **50**, 61–65.
157. HORNATOWSKA, J.: (2005). Visualisation of pectins and proteins by microscopy. Tech. rep., STFI-Packforsk.
158. HSU, P., GE, L., LI, X., STARK, A., WESEMIOTIS, C., NIEWIAROWSKI, P.H. & DHINOJWALA, A. (2011). Direct evidence of phospholipids in gecko footprints and spatula-substrate contact interface detected using surface-sensitive spectroscopy. *Journal of the Royal Society Interface* **9**, 69, 1–8.
159. HUBER, G., GORB, S., HOSODA, N., SPOLENAK, R. & ARZT, E. (2007). Influence of surface roughness on gecko adhesion. *Acta Biomaterialia* **3**, 607–610.
160. HUBER, G., GORB, S., SPOLENAK, R. & ARZT, E. (2005). Resolving the nanoscale adhesion of individual gecko spatulae by atomic force microscopy. *Biology Letters* **1**, 2–4.
161. HUTT, W. & PERSSON, B.N.J. (2016). Soft matter dynamics: Accelerated fluid squeeze-out during slip. *The Journal of Chemical Physics* **144**, p. 124903.
162. IRSCHICK, D.J., AUSTIN, C., PETREN, K., FISHER, R., LOSOS, J. & ELLERS, O. (1996). A comparative analysis of clinging ability among pad-bearing lizards. *Biological Journal of the Linnean Society* **59**, 21–35.
163. ISRAELACHVILI, J.N. (2011). *Intermolecular and surface forces*. 3rd edn. Elsevier, Amsterdam.
164. ITURRI, J., XUE, L., KAPPL, M., GARCÍA-FERNÁNDEZ, L., BARNES, W.J.P., BUTT, H.J. & DEL CAMPO, A. (2015). Torrent frog-inspired adhesives: Attachment to flooded surfaces. *Advanced Functional Materials* **25**, 10, 1499–1505.
165. JAGOTA, A. & HUI, C.Y. (2011). Adhesion, friction, and compliance of bio-mimetic and bio-inspired structured interfaces. *Materials Science and Engineering R* **72**, 253–292.
166. JARED, C., MAILHO-FONTANA, P.L., MARQUES-PORTO, R., SCIANI, J.M., CARVALHO PIMENTA, D., BRODIE JR., E.D. & ANTONIAZZI, M.M. (2018). Skin gland concentrations adapted to different evolutionary pressures in the head and posterior regions of the caecilian *Siphonops annulatus*. *Scientific Reports* **8**, 1–7.
167. JOHNSON, K.L., KENDALL, K. & ROBERTS, A.D. (1971). Surface energy and the contact of elastic solids. *Proceedings of the Royal Society of London. Series A, Mathematical and Physical Sciences* **324**, 1558, 301–313.
168. KAELBLE, D. (1970). Dispersion-polar surface tension properties of organic solids. *The Journal of Adhesion* **2**, 66–81.
169. KAMERMANS, M. & VENCES, M. (2009). Terminal phalanges in ranoid frogs: morphological diversity and evolutionary correlation with climbing habits. *Alytes* **26**, 1–4, 117–152.
170. KAMPERMAN, M., KRONER, E., DEL CAMPO, A., McMEEKING, R.M. & ARZT, E. (2010). Functional adhesive surfaces with “gecko” effect: The concept of contact splitting. *Advanced Engineering Materials* **12**, 335–348.
171. KANWAR, K. (1960). Note on the specificity of mercuric bromophenol blue for the cytochemical detection of proteins. *Experientia* **16**, 8, p. 355.

-
172. KAPPL, M., KAVEH, F. & BARNES, W.J.P. (2016). Nanoscale friction and adhesion of tree frog toe pads. *Bioinspiration & Biomimetics* **11**, 3.
173. KARPITSCHKA, S., DAS, S., VAN GORCUM, M., PERRIN, H., ANDREOTTI, B. & SNOELJER, J. (2015). Droplets move over viscoelastic substrates by surfing a ridge. *Nature Communications* **6**, 1–7.
174. KAVEH, F., ALLY, J., KAPPL, M. & BUTT, H.J. (2014). Hydrodynamic force between a sphere and a soft, elastic surface. *Langmuir* **30**, 11619–11624.
175. KENDALL, K. (1975). Thin-film peeling—the elastic term. *Journal of Physics D: Applied Physics* **8**, 1449–1452.
176. ——— (2004). *Molecular Adhesion and Its Applications - The Sticky Universe*. Kluwer Academic Publishers, New York, Boston, Dordrecht, London, Moscow.
177. KIER, W. & SMITH, A. (2002). The structure and adhesive mechanism of octopus suckers. *Integrative and Comparative Biology* **42**, 1146–1153.
178. KIERNAN, J. (2015). *Histological and Histochemical Methods: Theory and Practice*. 5th edn. Scion, Banbury, UK.
179. KIM, J. & SOMORJAI, G.A. (2003). Molecular packing of lysozyme, fibrinogen, and bovine serum albumin on hydrophilic and hydrophobic surfaces studied by infrared-visible sum frequency generation and fluorescence microscopy. *Journal of the American Chemical Society* **125**, 10, 3150–3158.
180. KITCHENER, A. & VINCENT, J.F. (1987). Composite theory and the effect of water on the stiffness of horn keratin. *Journal of Material Science* **22**, 1385–1389.
181. KLITTICH, M.R., WILSON, M.C., BERNARD, C., RODRIGO, R.M., KEITH, A.J., NIEWIAROWSKI, P.H. & DHINOJWALA, A. (2017). Influence of substrate modulus on gecko adhesion. *Scientific Reports* **7**, 1–10.
182. KOCH, K., BHUSHAN, B. & BARTHLOTT, W. (2008). Diversity of structure, morphology and wetting of plant surfaces. *Soft Matter* **4**, 1943–1963.
183. KOERNER, L., GORB, S. & BETZ, O. (2012). Adhesive performance of the stick-capture apparatus of rove beetles of the genus *Stenus* (Coleoptera, Staphylinidae) toward various surfaces. *Journal of Insect Physiology* **58**, 155–163.
184. KOMNICK, H. & STOCKEM, W. (1969). Oberfläche und Verankerung des Stratum corneum an mechanisch stark beanspruchten Körperstellen beim Grasfrosch. *Cytobiologie: Zeitschrift für experimentelle Zellforschung* **1**, 1, 1–16.
185. KURIAN, A., PRASAD, S. & DHINOJWALA, A. (2010). Direct measurement of acid-base interaction energy at solid interfaces. *Langmuir* **26**, 23, 17804–217807.
186. LABONTE, D., CLEMENTE, C.J., DITTRICH, A., KUO, C.Y., CROSBY, A.J., IRSCHICK, D.J. & FEDERLE, W. (2015). Extreme positive allometry of animal adhesive pads and the size limits of adhesion-based climbing. *Proceedings of the National Academy of Sciences of the United States of America* **113**, 5, 1297–1302.
187. LABONTE, D. & FEDERLE, W. (2015a). Rate-dependence of ‘wet’ biological adhesives and the function of the pad secretion in insects. *Soft Matter* **11**, 8661–8673.
188. ——— (2015b). Scaling and biomechanics of surface attachment in climbing animals. *Philosophical Transactions of the Royal Society B* **370**, 1–17.
189. LANDAU, L. & LIFSHITZ, E. (1987). *Fluid mechanics*. 2nd edn. Pergamon, Oxford.
190. LANGOWSKI, J.K.A., DODOU, D., KAMPERMAN, M. & VAN LEEUWEN, J.L. (2018a). Tree frog attachment: mechanisms, challenges, and perspectives. *Frontiers in Zoology* **15**, 1–21.
191. LANGOWSKI, J.K.A., RUMMENIE, A., PIETERS, R.P., KOVALEV, A., GORB, S.N. & VAN LEEUWEN, J.L. (2019). Estimating the maximum attachment performance of tree frogs on rough substrates. *Bioinspiration & Biomimetics* **14**, 2, p. 025001.
192. LANGOWSKI, J.K.A., SCHIPPER, H., BLIJ, A., VAN DEN BERG, F.T., GUSSEKLOO, S.W.S. & VAN LEEUWEN, J.L. (2018b). Force-transmitting structures in the digital pads of the tree frog *Hyla cinerea*: a functional interpretation. *Journal of Anatomy* **233**, 478–495.
193. LE QUANG TRONG, Y. (1971). Étude de la peau et des glandes cutanées de quelques amphibiens du genre *Phrynobatrachus*. *Bulletin de l'Institut français d'Afrique noire, Série A* **33**, 987–1025.



194. LEE, W.J., LUE, C.H. & LUE, K.Y. (2001). The SEM comparative study on toe pads among 11 species of tree frogs from Taiwan. *BioFormosa* **36**, 27–36.
195. LEPORA, N.F., VERSCHURE, P. & PRESCOTT, T.J. (2013). The state of the art in biomimetics. *Bioinspiration & Biomimetics* **8**, 1–11.
196. LEROY, S. & CHARLAIX, E. (2011). Hydrodynamic interactions for the measurement of thin film elastic properties. *Journal of Fluid Mechanics* **674**, 389–407.
197. LEV, R. & SPICER, S. (1964). Specific staining of sulphate groups with Alcian blue at low pH. *Journal of Histochemistry & Cytochemistry* **12**, 4, p. 309.
198. LEYDIG, F. (1868). *Ueber Organe eines sechsten Sinnes*. E. Blochmann & Sohn, Dresden, Germany.
199. ——— (1876). Die Hautdecke und Hautsinnesorgane der Urodelen. *Morphologisches Jahrbuch* **2**, 3, 287–319.
200. LI, M., XIE, J., DAI, Q., HUANG, W. & WANG, X. (2018a). Effect of wetting case and softness on adhesion of bioinspired micropatterned surfaces. *Journal of the Mechanical Behavior of Biomedical Materials* **78**, 266–272.
201. LI, M., XIE, J., SHI, L., HUANG, W. & WANG, X. (2018b). Controlling direct contact force for wet adhesion with different wedged film stabilities. *Journal of Physics D: Applied Physics* **51**, 1–7.
202. LI, Y., KRAHN, J. & MENON, C. (2013). Bioinspired dry adhesive materials and their application in robotics: A review. *Journal of Bionic Engineering* **13**, 181–199.
203. LIEM, S.S. (1970). The morphology, systematics, and evolution of the old world treefrogs (Rhacophoridae and Hyperoliidae). In: WILLIAMS, P.M., (ed.): *Fieldiana: Zoology*, **57**, *Zoological Series*. Field Museum of Natural History, Chicago, USA.
204. LILLIE, R. & ASHBURN, L. (1943). Supersaturated solutions of fat stains in dilute isopropanol for demonstration of acute fatty degeneration not shown by Herxheimer's technique. *Archives of Pathology & Laboratory Medicine* **36**, 432–440.
205. LILLYWHITE, H. (1971). Thermal modulation of cutaneous mucus discharge as a determinant of evaporative water loss in the frog, *Rana catesbeiana*. *Zeitschrift für vergleichende Physiologie* **73**, 84–104.
206. LILLYWHITE, H. & LICHT, P. (1975). A comparative study of integumentary mucous secretions in amphibians. *Comparative Biochemistry and Physiology* **51A**, 937–941.
207. LILLYWHITE, H., MITTAL, A., GARG, T. & AGRAWAL, N. (1997). Integumentary structure and its relationship to wiping behaviour in the common indian tree frog, *Polypedutes muculatus*. *Journal of Zoology* **243**, 675–687.
208. LINNENBACH, M. (1985). Zum Feinbau der Haftscheiben von *Hyla cinerea* (Schneider, 1799) (Salientia: Hylidae). *Salamandra* **21**, 1, 81–85.
209. LOSKILL, P., PUTHOFF, J., WILKINSON, M., MECKE, K., JACOBS, K. & AUTUMN, K. (2013). Macroscale adhesion of gecko setae reflects nanoscale differences in subsurface composition. *Journal of The Royal Society Interface* **10**, 1–8.
210. LUNA, L., (ed.) (1968). *Manual of histological staining methods of the armed forces institute of pathology*. 3rd edn. McGraw-Hill, New York, USA.
211. MANZANO, A.S., ABDALA, V. & HERREL, A. (2008). Morphology and function of the forelimb in arboreal frogs: specializations for grasping ability? *Journal of Anatomy* **213**, 296–307.
212. MANZANO, A.S., FABREZI, M. & VENCES, M. (2007). Intercalary elements, treefrogs, and the early differentiation of a complex system in the Neobatrachia. *The Anatomical Record* **290**, 12, 1551–1567.
213. MANZANO, A.S., FONTANARROSA, G., PRIETO, Y. & ABDALA, V. (2017). *Morfología de Vertebrados: Conceptos, métodos y grupos de investigación en Argentina*, chap. La prensilidad en anfibios y reptiles: perspectivas evolutivas basadas en la anatomía y la función. 59–82.
214. McALLISTER, W. & CHANNING, A. (1983). Comparison of toe pads of some southern African climbing frogs. *South African Journal of Zoology* **18**, 2, 110–114.
215. METSCHER, B.D. (2009). Microct for comparative morphology: simple staining methods allow high-contrast 3D imaging of diverse non-mineralized animal tissues. *BMC Physiology* **9**, 11, 1–14.

-
216. MILLS, J. & PRUM, B. (1984). Morphology of the exocrine glands of the frog skin. *The American Journal of Anatomy* **171**, 91–106.
217. MIZUHIRA, V. (2004). The digital pads of rhacophorid tree-frogs. *Journal of Electron Microscopy* **53**, 1, 63–78.
218. MODABBERIFAR, M. & SPENKO, M. (2018). A shape memory alloy-actuated gecko-inspired robotic gripper. *Sensors and Actuators A: Physical* **276**, 76–82.
219. MOEN, D., IRSCHICK, D.J. & WIENS, J. (2013). Evolutionary conservatism and convergence both lead to striking similarity in ecology, morphology and performance across continents in frogs. *Proceedings of the Royal Society B: Biological Sciences* **280**, 1–9.
220. MOHNIKE, O. (1879). Ueber das Vermögen verschiedener Säugethiere sich mittels des atmosphärischen Druckes an glatten, mehr oder weniger senkrechten Flächen festhalten und aufwärts bewegen zu können. *Zeitschrift für wissenschaftliche Zoologie* **32**, 388–406.
221. MOJDEHI, A.R., HOLMES, D.P. & DILLARD, D.A. (2017). Revisiting the generalized scaling law for adhesion: role of compliance and extension to progressive failure. *Soft Matter* **13**, 7529–7536.
222. MULISCH, M. & WELSCH, U., (eds.) (2010). *Romeis - Mikroskopische Technik*. 18th edn. Springer Spektrum, Heidelberg, Germany.
223. MURARASH, B., ITOVICH, Y. & VARENBERG, M. (2011). Tuning elastomer friction by hexagonal surface patterning. *Soft Matter* **7**, 5553–5557.
224. MURPHY, M., AKSAK, B. & SITTI, M. (2007). Adhesion and anisotropic friction enhancements of angled heterogeneous micro-fiber arrays with spherical and spatula tips. *Journal of Adhesion Science and Technology* **21**, 12–13, 1281–1296.
225. NACHTIGALL, W. (1974). *Biological Mechanisms of Attachment: The Comparative Morphology and Bioengineering of Organs for Linkage, Suction, and Adhesion*. 1st edn. Springer Verlag, Berlin, Heidelberg, New York.
226. NADERMANN, N., NING, J., JAGOTA, A. & HUI, C.Y. (2010). Active switching of adhesion in a film-terminated fibrillar structure. *Langmuir* **26**, 15464–15471.
227. NAKANO, M. & SAINO, T. (2016). Light and electron microscopic analyses of the high deformability of adhesive toe pads in White's tree frog, *Litoria caerulea*. *Journal of Morphology* **277**, 1509–1516.
228. NAUWELAERTS, S. & AERTS, P. (2006). Take-off and landing forces in jumping frogs. *Journal of Experimental Biology* **209**, 66–77.
229. NEUBAUER, J.W., XUE, L., ERATH, J., DROTLEF, D.M., DEL CAMPO, A. & FERY, A. (2016). Monitoring the contact stress distribution of gecko-inspired adhesives using mechano-sensitive surface coatings. *ACS Applied Materials & Interfaces* **8**, 17870–17877.
230. NIEWIAROWSKI, P.H., STARK, A.Y. & DHINOJWALA, A. (2016). Sticking to the story: outstanding challenges in gecko-inspired adhesives. *Journal of Experimental Biology* **219**, 7, 912–919.
231. NOBLE, G. & JAECKLE, M. (1928). The digital pads of the tree frogs. A study of the phylogenesis of an adaptive structure. *Journal of Morphology and Physiology* **45**, 1, 259–292.
232. NOKHBATOLFOGHAI, M. (2013). Toe-pad morphology in White's tree frog, *Litoria caerulea* (family Hylidae). *Iranian Journal of Science & Technology* **37**, 4, 491–499.
233. NORTHEN, M., GREINER, C., ARZT, E. & TURNER, K. (2008). A gecko-inspired reversible adhesive. *Advanced Materials* **20**, 3905–3909.
234. OHLER, A. (1995). Digital pad morphology in torrent-living ranid frogs. *Asiatic Herpetological Research* **6**, 85–96.
235. OMOIKE, A., & CHOROVER, J. (2004). Spectroscopic study of extracellular polymeric substances from *Bacillus subtilis*: Aqueous chemistry and adsorption effects. *Biomacromolecules* **5**, 1219–1230.
236. ORTIZ-YOUNG, D., CHIU, H.C., KIM, S., VOÏTCHOVSKY & RIEDO, E. (2013). The interplay between apparent viscosity and wettability in nanoconfined water. *Nature Communications* **4**.
237. OWENS, D. & WENDT, R. (1969). Estimation of the surface free energy of polymers. *Journal of Applied Polymer Science* **13**, 1741–1747.



238. PAGANIN, D., MAYO, S., GUREYEV, T., MILLER, P. & WILKINS, S. (2002). Simultaneous phase and amplitude extraction from a single defocused image of a homogeneous object. *Journal of Microscopy* **206**, 33–40.
239. PARETKAR, D., KAMPERMAN, M., SCHNEIDER, A.S., MARTINA, D., CRETON, C. & ARZT, E. (2011). Bioinspired pressure actuated adhesive system. *Materials Science and Engineering C* **31**, 1152–1159.
240. PARSEGHIAN, V.A. (2006). *Van der Waals forces*. Cambridge University Press, New York, USA.
241. PAUKSTIS, G. & BROWN, L. (1991). Evolutionary trends in the morphology of the intercalary phalanx of anuran amphibian. *Canadian Journal of Zoology* **69**, 1297–1301.
242. PEATTIE, A.M. (2009). Functional demands of dynamic biological adhesion: an integrative approach. *Journal of Comparative Physiology B* **179**, 231–239.
243. PEREIRA, K.E., CROTHER, B.I., SEVER, D.M., FONTENOT, JR, C.L., POJMAN, SR, J.A., WILBURN, D.B. & WOODLEY, S.K. (2018). Skin glands of an aquatic salamander vary in size and distribution and release antimicrobial secretions effective against chytrid fungal pathogens. *Journal of Experimental Biology* **221**.
244. PEREZ GOODWYN, P., PERESSADKO, A., SCHWARZ, H., KASTNER, W. & GORB, S. (2006). Material structure, stiffness, and adhesion: why attachment pads of the grasshopper (*Tettigonia viridissima*) adhere more strongly than those of the locust (*Locusta migratoria*) (Insecta: Orthoptera). *Journal of Comparative Physiology A* **192**, 1233–1243.
245. PERSSON, B.N.J. (2007). Wet adhesion with application to tree frog adhesive toe pads and tires. *Journal of Physics: Condensed Matter* **19**, 37, 1–16.
246. PERSSON, B.N.J., ALBOHR, O., TARTAGLINO, U., VOLOKITIN, A.I. & TOSATTI, E. (2005). On the nature of surface roughness with application to contact mechanics, sealing, rubber friction and adhesion. *Journal of Physics: Condensed Matter* **17**, 1, 1–62.
247. PESIKA, N.S., TIAN, Y., ZHAO, B., ROSENBERG, K., ZENG, H., MCGUIGGAN, P., I.J.N. & AUTUMN, K.: (2006). Peel zone model of tape peeling based on the gecko adhesive system. Tech. rep., Department of Chemical Engineering, University of California Santa Barbara, Santa Barbara, USA.
248. PILKINGTON, G.A., GUPTA, R. & FRÉCHETTE, J. (2016). Scaling hydrodynamic boundary conditions of microstructured surfaces in the thin channel limit. *Langmuir* **23**, 2360–2368.
249. PITENIS, A.A., URUEÑA, J.M., SCHULZE, K.D., NIXON, R.M., DUNN, A.C., KRICK, B.A., SAWYER, W.G. & ANGELINI, T.E. (2014). Polymer fluctuation lubrication in hydrogel gemini interfaces. *Soft Matter* **10**, 8955–8962.
250. POPOV, V. (2010). *Contact Mechanics and Friction: Physical Principles and Applications*. Springer, Heidelberg, Dordrecht, London, New York.
251. PRATES, I., ANTONIAZZI, M.M., SCIANI, J.M., PIMENTA, D.C., TOLEDO, L.F., HADDAD, C.F.B. & JARED, C. (2012). Skin glands, poison and mimicry in dendrobatid and leptodactylid amphibians. *Journal of Morphology* **273**, 279–290.
252. PROBST, J., HAUSER, F., JOBA, W. & HOFFMANN, W. (1992). The polymorphic integumentary mucin B.1 from *Xenopus Laevis* contains the short consensus repeat. *The Journal of Biological Chemistry* **267**, 9, 6310–6316.
253. PURTOV, J., FRENSEMEIER, M. & KRONER, E. (2015). Switchable adhesion in vacuum using bio-inspired dry adhesives. *ACS Applied Materials & Interfaces* **7**, 24127–24135.
254. PURTOV, J., GORB, E., STEINHART, M. & GORB, S. (2013). Measuring of the hardly measurable: adhesion properties of anti-adhesive surfaces. *Applied Physics A* **111**, 1, 183–189.
255. PUTHOFF, J.B., PROWSE, M.S., WILKINSON, M. & AUTUMN, K. (2010). Changes in materials properties explain the effects of humidity on gecko adhesion. *Journal of Experimental Biology* **213**, 3699–3704.
256. PYRON, R. & WIENS, J. (2011). A large-scale phylogeny of Amphibia including over 2800 species, and a revised classification of extant frogs, salamanders, and caecilians. *Molecular Phylogenetics and Evolution* **61**, 573–583.
257. RABEL, W. (1971). Einige Aspekte der Benetzungstheorie und ihre Anwendung auf die Untersuchung und Veränderung der Oberflächeneigenschaften von Polymeren. *Farbe und Lack* **77**, 997–1005.
258. RADHAKRISHNAN, V. (1998). Locomotion: Dealing with friction. *Proceedings of the National*

- Academy of Sciences of the United States of America* **95**, 5448–5455.
259. RAPPAY, G. (1963). Blocking the Ninhydrin-Schiff reaction with copper ions. *Nature* **200**, 4903, 274–275.
 260. REDDY, S., ARZT, E. & DEL CAMPO, A. (2007). Bioinspired surfaces with switchable adhesion. *Advanced Materials* **19**, 3833–3837.
 261. REGUEIRA, E., DÁVILA, C. & HERMIDA, G. (2016). Morphological changes in skin glands during development in *Rhinella Arenarum* (Anura: Bufonidae). *The Anatomical Record* **299**, 141–156.
 262. REYNOLDS, O. (1886). On the theory of lubrication and its application to Mr. Beauchamp Tower's experiments, including an experimental determination of the viscosity of olive oil. *Philosophical Transactions of the Royal Society of London* **177**, 157–234.
 263. RICHARDS, C.M., CARLSON, B.M., CONNELLY, T.G., ROGERS, S.L. & ASHCRAFT, E. (1977). A scanning electron microscopic study of differentiation of the digital pad in regenerating digits of the Kenyan reed frog, *Hyperolius viridiflavus ferniquei*. *Journal of Morphology* **153**, 387–396.
 264. RISKIN, D. & RACEY, P. (2010). How do suckerfooted bats hold on, and why do they roost headup? *Biological Journal of the Linnean Society* **99**, 233–240.
 265. RIVERO, J., OLIVER, L. & DE LOS ANGELES IRIZARRY, M. (1987). Los discos digitales de tres *Eleutherodactylus* (Anura, Leptodactylidae) de Puerto Rico, con anotaciones sobre los mecanismos de adhesión en las ranas. *Caribbean Journal of Science* **23**, 2, 226–237.
 266. ROMEIS, B. (1968). *Mikroskopische Technik*. 16th edn. R. Oldenbourg, München, Germany.
 267. ROSENBERG, H. & ROSE, R. (1999). Volar adhesive pads of the feathered glider, *Acrobates pygmaeus* (Marsupialia; Acrobatidae). *Canadian Journal of Zoology* **77**, 233–248.
 268. RÖSEL VON ROSENHOF, A.J. (1758). *Die natürliche Historie der Frösche hiesigen Landes, worinnen alle Eigenschaften und ihre Fortpflanzung beschrieben*. Nürnberg, Germany.
 269. RUSSELL, A.P. (1975). A contribution to the functional analysis of the foot of the tokay, *Gekko gecko* (Reptilia : Gekkonidae). *Journal of Zoology* **176**, 437–476.
 270. ——— (1986). The morphological basis of weight-bearing in the scensors of the tokay gecko (Reptilia: Sauria). *Canadian Journal of Zoology* **64**, 4, 948–955.
 271. SAHNI, V., CHEN, T.M.K., JAIN, D., BLAMIRE, S.J., BLACKLEDGE, T.A. & DHINOJWALA, A. (2014). Direct solution of glycoproteins by salts in spider silk glues enhances adhesion and helps to explain the evolution of modern spider orb webs. *Biomacromolecules* **15**, 1225–1232.
 272. SCHOLZ, I., BARNES, W.J.P., SMITH, J.M. & BAUMGARTNER, W. (2009). Ultrastructure and physical properties of an adhesive surface, the toe pad epithelium of the tree frog, *Litoria caerulea* White. *Journal of Experimental Biology* **212**, 155–162.
 273. SCHUBERG, A. (1891). Über den Bau und die Funktion der Haftapparate des Laubfrosches. *Arbeiten aus dem Zoologisch-Zoatomischen Institut in Würzburg* **10**, 1, 57–119.
 274. SELDIN, J. & HOSHIKO, T. (1966). Ionic requirement for epinephrine stimulation of frog skin gland secretion. *Journal of Experimental Zoology* **163**, 111–114.
 275. SHIVAPOOJA, P., WANG, Q., ORIHUELA, B., RITTSCHOF, D., LÓPEZ, G. & ZHAO, X. (2013). Bioinspired surfaces with dynamic topography for active control of biofouling. *Advanced Materials* **25**, 1430–1434.
 276. SHUBIN, N.H. & JENKINS JR., F.A. (1995). An early jurassic jumping frog. *Letters to Nature* **377**, 49–52.
 277. SIEDLECKI, M. (1909). Zur Kenntnis des javanischen Flugfrosches. *Biologisches Centralblatt* **29**, 704–715.
 278. ——— (1910). Die Haftballen des javanischen Flugfrosches. *Bulletin of the Academy of Sciences, Krakow (B)*, 593–606.
 279. SINGLA, S., AMARPURI, G., DHOPATKAR, N., BLACKLEDGE, T.A. & DHINOJWALA, A. (2018). Hygroscopic compounds in spider aggregate glue remove interfacial water to maintain adhesion in humid conditions. *Nature Communications* **9**, 1–8.
 280. SKALLI, O., ROPRAZ, P., TRZECIAK, A., BENZONANA, G., GILLESSEN, D. & GABBIANI, G. (1986). A monoclonal antibody against α -smooth muscle actin: A new probe for smooth muscle differentiation. *The Journal of Cell Biology* **103**, 2787–2796.



281. SKOGLUND, C. & SJÖBERG, E. (1977). In vivo studies of individual mucus glands in frogs. *Acta Physiologica Scandinavica* **100**, 471–484.
282. SMITH, A. (2010). *Biological adhesives: from Nature to Technical and Medical Application*, chap. 4: Gastropod Secretory Glands and Adhesive Gels. Springer, 41–51.
283. SMITH, A., (ed.) (2016). *Biological adhesives*. 2nd edn. Springer, Cham, Switzerland.
284. SMITH, J.M., BARNES, W.J.P., DOWNIE, J.R. & RUXTON, G.D. (2006a). Adhesion and allometry from metamorphosis to maturation in hyloid tree frogs: a sticky problem. *Journal of Zoology* **270**, 372–383.
285. ——— (2006b). Structural correlates of increased adhesive efficiency with adult size in the toe pads of hyloid tree frogs. *Journal of Comparative Physiology A* **192**, 11, 1193–1204.
286. SPEED, M. & ARBUCKLE, K. (2017). Quantification provides a conceptual basis for convergent evolution. *Biological Reviews* **92**, 815–829.
287. STARK, A.Y., BADGE, I., WUCINICH, N.A., SULLIVAN, T.W., NIEWIAROWSKI, P.H. & DHINOJWALA, A. (2013). Surface wettability plays a significant role in gecko adhesion underwater. *Proceedings of the National Academy of Sciences of the United States of America* **110**, 16, 6340–6345.
288. STEBBINS, R.C. & COHEN, N.W. (1995). *A natural history of amphibians*. Princeton University Press, Princeton, USA.
289. STEFAN, J. (1874). Versuche über die scheinbare Adhäsion. *Anzeiger der Kaiserlichen Akademie zu Wien* **12**, 316–318.
290. SUBRAMONIAM, T. (1982). Manual of research methods for marine invertebrate reproduction. *Central marine fisheries research institute (CMFRI) special publication* **9**.
291. SURESH, K. (2013). Efficient generation of large-scale pareto-optimal topologies. *Structural and Multidisciplinary Optimization* **1**, 49–61.
292. SUSTAITA, D., POUYDEBAT, E., MANZANO, A., ABDALA, V., HERTEL, F. & HERREL, A. (2013). Getting a grip on tetrapod grasping: form, function, and evolution. *Biological Reviews* **88**, 380–405.
293. TANAKA, Y. (1976). Architecture of the marrow vasculature in three amphibian species and its significance in hematopoietic development. *American Journal of Anatomy* **145**, 4, 485–497.
294. THOMAS, E.O., TSANG, L. & LIGHT, P. (1993). Comparative histochemistry of the sexually dimorphic skin glands of anuran amphibians. *Copeia* **1993**, 1, 133–143.
295. TOLEDO, R. & JARED, C. (1993). Cutaneous adaptations to water balance in amphibians. *Comparative Biochemistry and Physiology Part A: Physiology* **105**, 4, 593–608.
296. ——— (1995). Cutaneous granular glands and amphibian venoms. *Comparative Biochemistry and Physiology* **111A**, 1–29.
297. TRACY, C.R., LAURENCE, N. & CHRISTIAN, K.A. (2011). Condensation onto the skin as a means for water gain by tree frogs in tropical Australia. *The American Naturalist* **178**, 4, 553–558.
298. TSIPENYUK, A. & VARENBERG, M. (2014). Use of biomimetic hexagonal surface texture in friction against lubricated skin. *Journal of The Royal Society Interface* **11**, 1–13.
299. TULCHINSKY, A. & GAT, A. (2015). Viscous-poroelastic interaction as mechanism to create adhesion in frogs' toe pads. *Journal of Fluid Mechanics* **775**, 288–303.
300. TYLER, M. (1968). Papuan hyloid frog of the genus *Hyla*. *Zoologische Verhandelingen* **96**, 4–203.
301. TYLER, M.J. & DAVIES, M. (1993). *Fauna of Australia*, **2A**, chap. Family Hylidae. Australian Government Publishing Service, Canberra, Australia, 1–15.
302. TYLER, M.J., STONE, D.J.M. & BOWIE, J.H. (1992). A novel method for the release and collection of dermal, glandular secretions from the skin of frogs. *Journal of Pharmacological and Toxicological Methods* **28**, 199–200.
303. VAKIS, A., YASTREBOV, V., SCHEIBERT, J., MINFRAY, C., NICOLA, L., DINI, D., ALMQVIST, A., PAGGI, M., LEE, S., LIMBERT, G., MOLINARI, J., ANCIAUX, G., AGHABABAEI, R., RESTREPO, S.E., PAPANGELO, A., CAMMARATA, A., NICOLINI, P., PUTIGNANO, C., CARBONE, G., CIAVARELLA, M., STUPKIEWICZ, S., LENGIEWICZ, J., COSTAGLIOLA, G., BOSIA, F., GUARINO, R., PUGNO, N. & MÜSER, M. (2018). Modeling and simulation in tribology across scales: An

-
- overview. *Tribology International* **125**, 1–84.
304. VANDEBERGH, W., MAEX, M., BOSSUYT, F. & VAN BOCXLAER, I. (2013). Recurrent functional divergence of early tetrapod keratins in amphibian toe pads and mammalian hair. *Biology Letters* **9**, 1–4.
305. VARGO, T., HOOK, D., GARDELLA JR., J., EBERHARDT, M., MEYER, A. & BAIER, R. (1991). A multitechnique surface analytical study of a segmented block copolymer poly (ether-urethane) modified through an H₂O radio frequency glow discharge. *Journal of Polymer Science: Part A Polymer Chemistry* **29**, 535–545.
306. VDI-DEPARTMENT BIOMIMETICS (2012). *VDI manual Biomimetics*, chap. Guideline VDI 6220 - Biomimetics - Conception and strategy - Differences between biomimetic and conventional methods/products. The Association of German Engineers - Society Technologies of Life Sciences, Düsseldorf, Germany. Guideline.
307. VINCENT, J.F. & WEGST, U.G. (2004). Design and mechanical properties of insect cuticle. *Arthropod Structure & Development* **33**, 187–199.
308. VOIGT, D. & GORB, S. (2017). Functional morphology of tarsal adhesive pads and attachment ability in ticks *Ixodes ricinus* (Arachnida, Acari, Ixodidae). *Journal of Experimental Biology* **220**.
309. VOIGT, D., SCHUPPERT, J., DATTINGER, S. & GORB, S. (2008). Sexual dimorphism in the attachment ability of the Colorado potato beetle *Leptinotarsa decemlineata* (Coleoptera: Chrysomelidae) to rough substrates. *Journal of Insect Physiology* **54**, 765–776.
310. WANG, H., WANG, L., SHAO, J., LIU, T. & Z., D. (2013). Long hindlimbs contribute to air-righting performance in falling tree frogs. *Journal of Mechanics in Medicine and Biology* **13**, p. 1340023.
311. WANG, J., BUCK, S. & CHEN, Z. (2002). Sum frequency generation vibrational spectroscopy studies on protein adsorption. *Journal of Physical Chemistry B* **106**, 11666–11672.
312. WANG, S., LI, M., HUANG, W. & WANG, X. (2016). Sticking/climbing ability and morphology studies of the toe pads of Chinese fire belly newt. *Journal of Bionic Engineering* **13**, 1, 115–123.
313. WANNINGER, M., SCHWAHA, T. & HEISS, E. (2018). Form and function of the skin glands in the Himalayan newt *Tylosotriton verrucosus*. *Zoological Letters* **4**, 2–10.
314. WARBURG, M., ROSENBERG, M., ROBERTS, J. & HEATWOLE, H. (2000). Cutaneous glands in the Australian hyliid *Litoria caerulea* (Amphibia, Hylidae). *Anatomy and Embryology* **201**, 5, 341–348.
315. WEHNER, R. & GEHRING, W., (eds.) (2007). *Zoologie*. 24th edn. Thieme, Stuttgart, Germany.
316. WELLS, K.D. (2007). *The ecology & behaviour of amphibians*. The University of Chicago Press, Chicago, USA.
317. WELSCH, U., STORCH, V. & FUCHS, W. (1974). The fine structure of the digital pads of rhacophorid tree frogs. *Cell and tissue research* **148**, 3, 407–416.
318. WEXLER, J.S., HEARD, T.M. & STONE, H.A. (2014). Capillary bridges between soft substrates. *Physical Review Letters* **112**, 066102–1–5.
319. WIENS, J. (2007). Book review: The amphibian tree of life. *The Quarterly Reviews of Biology* **82**, 55–56.
320. v. WITTICH (1854). Der Mechanismus der Haftzehen von *Hyla arborea*. *Archiv für Anatomie, Physiologie und Wissenschaftliche Medizin*, 170–184.
321. WOLFF, J. & GORB, S. (2012). Surface roughness effects on attachment ability of the spider *Philodromus dispar* (Araneae, Philodromidae). *Journal of Experimental Biology* **215**, 179–184.
322. WOLFF, J.O. & GORB, S. (2016). Attachment structures and adhesive secretions in arachnids. In: GORB, S., (ed.): *Biologically-Inspired Systems*, **7**. Springer, Cham, Switzerland.
323. WU, N.C., CRAMP, R.L. & FRANKLIN, C.E. (2017). Living with a leaky skin: upregulation of ion transport proteins during sloughing. *Journal of Experimental Biology* **220**, 2026–2035.
324. XIE, J., LI, M., DAI, Q., HUANG, W. & WANG, X. (2018). Key parameters of biomimetic patterned surface for wet adhesion. *International Journal of Adhesion and Adhesives* **82**, 72–78.



325. XUE, L., ITURRI, J., KAPPL, M., BUTT, H.J. & DEL CAMPO, A. (2014). Bioinspired orientation-dependent friction. *Langmuir* **30**, 11175–11182.
326. XUE, L., SANZ, B., LUO, A., TURNER, K.T., WANG, X., TAN, D., ZHANG, R., DU, H., STEINHART, M., MIJANGOS, C., GUTTMANN, M., KAPPL, M. & DEL CAMPO, A. (2017). Hybrid surface patterns mimicking the design of the adhesive toe pad of tree frog. *ACS Nano* **11**, 10, 9711–9719.
327. ZHANG, L., CHEN, H., ZHANG, P. & ZHANG, D. (2016). Boundary friction force of tree frog's toe pads and bio-inspired hexagon pillar surface. *Chinese Science Bulletin* **61**, 2596–2604.
328. ZHU, H. & DHINOJWALA, A. (2015). Thermal behavior of long-chain alcohols on sapphire substrate. *Langmuir* **31**, 23, 6306–6313.



Summaries

Summary

Tree frogs are versatile climbers that use their adhesive digital pads to attach to various substrates, even under challenging conditions. The pads are covered in mucus and can generate adhesive and frictional forces of up to several body weights per digit. For centuries, the remarkable attachment performance of tree frogs has fascinated scientists who aimed to unravel the fundamentals of tree frog attachment. Among the various mechanisms that have been discussed to explain tree frog attachment, capillary adhesion is the most commonly used one. Previous research was primarily directed at the role of the micropatterned pad surface in attachment, which resulted in the development of several tree-frog-inspired micropatterned adhesives. However, a comprehensive explanation of the mechanisms of tree frog attachment is still unavailable, and the role of internal pad structures in attachment is barely understood. In this thesis, I present an interdisciplinary analysis of the attachment apparatus of tree frogs with focus on subepidermal structures, hence contributing to the understanding of nature's adhesive systems, and providing input for the design of biomimetic adhesives inspired by tree frogs.

In CHAPTER 2, we provided a synthesis of the *status quo* of knowledge on tree frog attachment—ranging from the functional pad morphology to experimental findings in support of the various hypothesised mechanisms of tree frog attachment—and identified gaps in the existing knowledge. An account of the functional morphology highlights the need for an exploration of the internal pad morphology and of the chemistry of the secreted mucus in order to deepen the understanding of tree frog attachment. By revisiting current analytical models, reported data, and observations, we show that the hypothesis of wet adhesion as primary mechanism in tree frog attachment is not sufficiently supported. Van der Waals forces, which were for a long time believed to play only a minor role due to mucus covering the pad surface, may well be involved in tree frog attachment.

In CHAPTER 3, we combined histochemistry and synchrotron micro-computer-tomography to characterise the internal morphology of the digital pads of the tree frog *Hyla cinerea* in 3D, with a focus on mechanical links between the adhesive pad surface and the internal digital skeleton. The ventral pad surface connects to the skeleton via several pathways of force transmission. A collagenous septum runs from the ventral cutis to the tip of the distal phalanx and compartmentalises the subcutaneous pad volume into a distal lymph space and a proximal space filled with mucus glands. Moreover, a collagen layer runs from the ventral cutis via interphalangeal ligaments to the middle phalanx. The fibres constituting this layer run in trajectories curved around the transverse pad-axis and form laterally separated ridges below the gland space. Using finite element analysis and numerical optimisation of a shear-loaded pad model, we show that the collagen fibres are presumably oriented along the trajectories of the maximum principal stresses, and the optimisation also results in ridge-formation, suggesting that the collagen layer is adapted towards a high stiffness during shear loading. Finally, immunohistochemical staining reveals the presence of several units



of smooth muscle fibres in frog pads. These active structures may provide tree frogs with the ability to control the distribution of mechanical stresses across the ventral pad surface, hence facilitating modulation of the attachment strength.

CHAPTER 4 addresses the morphology of the digital mucus glands and the chemistry of the secreted mucus. In *H. cinerea*, the mucus glands opening to the ventral pad surface form a macrogland and thus differ significantly in their morphology from the ones opening to the dorsal (non-adhesive) pad surface. We identified a digital mucus macrogland in min. 10 neobatrachian families that are not exclusively arboreal, indicating that the macrogland morphology is determined by generic functional requirements arising from ‘ground contact’ (e.g. lubrication and compensation of mucus loss) as well as by specific requirements for climbing and attachment. Using cryo-histochemistry as well as infrared and sum frequency generation spectroscopy, we show that—in contrast to the gland morphology—the general mucus chemistry varies only little between different body locations in the tree frogs *H. cinerea* and *Osteopilus septentrionalis*, as well as between arboreal and non-arboreal (*Ptychocheilus adsperus* and *Ceratophrys cranwelli*) frog species. This observation suggests conservation of the mucus chemistry in the course of anuran evolution and does not support a specialisation of the mucus towards attachment.

In CHAPTER 5, we experimentally measured the attachment performance of the tree frogs *H. cinerea* and *Litoria caerulea* using a rotation platform setup. By analysing the effects of variations in nominal substrate roughness on attachment performance, we investigated the role of the previously proposed mechanism of mechanical interlocking in tree frog attachment. Tree frogs attach as well to nano- and microrough substrates as to a smooth substrate. Attachment performance only decreases above a nominal substrate roughness of 15 μm . These observations disagree with the expected variation of attachment performance with substrate roughness if interlocking were present, hence indicating that mechanical interlocking is negligible in tree frog attachment. Furthermore, observations of detaching frogs with our updated rotation platform setup show that tree frogs are able to withstand substantial inertial loads with only two attached limbs, suggesting that the maximum attachment performance of tree frogs is higher than reported previously.

Finally, I put in CHAPTER 6 the findings of this thesis in a wider scientific context. By integrating the outcomes of the review on tree frog attachment with the results of the experimental chapters and with insights obtained on tree-frog-inspired adhesives, I discuss the importance of the previously proposed mechanisms of tree frog attachment. I conclude that suction and mechanical interlocking are negligible. A contribution of hydrodynamic adhesion cannot be excluded, but seems to be a consequence of having a wet skin rather than a primary attachment mechanism. Whereas capillary adhesion was previously mentioned as primary adhesion mechanism, an integration of the available knowledge suggests that capillary adhesion acts together with van der Waals forces, with the latter as dominant attachment mechanism. To explore the hypothesised convergent evolution of the digital pads of tree frogs, I provide an account of what is known from this thesis and earlier works on the phylogeny of the



adhesive pads. Overall, several morphological features (e.g. the micropatterned pad surface and the digital gland cluster) are widely distributed over anuran families, suggesting that the whole pad is a functional unit and raising the question if the pads evolved convergently or if they are derived from a common ancestor. In agreement with the antecedent sections, a tentative discussion of the evolutionary history of frog pads emphasises the importance of drainage, friction generation, and van der Waals forces in tree frog attachment. Based on the outcomes of this thesis, I provide suggestions for the design of tree-frog-inspired adhesives. The drainage-capabilities of frog pads render these a good model for the development of technical adhesives in a wet environment. Further promising trends are the design of fibre-reinforced micropatterned adhesives for heavy duty applications, and the creation of actuated adhesives with controllable adhesion inspired by the muscular structures found in the biological model. Finally, I present an outlook on how the field of tree frog attachment may develop in the coming years.



Samenvatting

Boomkickers zijn veelzijdige klimmers die hun met slijm bedekte teen- en vingerkussens gebruiken om zich te hechten aan verscheidene substraten, zelfs onder uitdagende omstandigheden. De hechtkussens kunnen adhesie- en wrijvingskrachten genereren tot enkele malen het lichaamsgewicht van de kikker per teen. Al eeuwen trachten wetenschappers de fundamentele principes van de opmerkelijke aanhechtingsprestaties van boomkickers te ontrafelen. Van de verscheidene mechanismen die bediscussieerd zijn om de aanhechting van boomkickers te verklaren, is capillaire adhesie de meest gebruikte. Voorgaand onderzoek richtte zich voornamelijk op de rol van de microstructuur van het hechtkussenoppervlak op de aanhechting. Dit resulteerde in de ontwikkeling van verschillende boomkikker-geïnspireerde adhesieven. Een overtuigende verklaring van de aanhechtingsmechanismen is hier echter niet uit voortgekomen. Daarnaast wordt de rol van de interne structuur van de hechtkussens in de aanhechting onvoldoende begrepen. In dit proefschrift presenter ik een interdisciplinaire analyse van het aanhechtingsapparaat van boomkickers met de focus op sub-epidermale structuren. Dit draagt niet alleen bij aan het begrijpen van natuurlijke aanhechtingsystemen maar verschaft tevens inspiratie voor het ontwerpen van biomimetische aanhechtingsmechanismen.

In HOOFDSTUK 2 presenteren wij een synthese van de *status quo* van de kennis van boomkikkeraanhechting—van de functionele morfologie van de hechtkussens tot experimentele bevindingen die voorgestelde mechanismen voor boomkikkeraanhechting wel of niet ondersteunen—en identificeren wij belangrijke kennislacunes van dit onderzoeksgebied. Onze revisie van de beschikbare analytische modellen, gerapporteerde data en observaties maakt duidelijk dat de eerder voorgestelde natte adhesie als primair mechanisme in de aanhechting niet afdoende ondersteund wordt. Vanderwaalskrachten, waarvan langdurig gedacht werd dat ze een geringe rol spelen doordat het hechtkussen met slijm bedekt is, zijn mogelijk belangrijk in boomkikkeraanhechting. Onze literatuuranalyse laat zien dat een beter begrip van de functionele morfologie van de interne structuur van de hechtkussens en van de chemische samenstelling van het afgescheiden slijm noodzakelijk is om het mechanisme van aanhechting te ontrafelen.

In HOOFDSTUK 3 combineren wij histochemie en synchrotron micro-computer-tomografie om de interne morfologie van de hechtkussens van de boomkikker *Hyla cinerea* in 3D te karakteriseren. Daarbij richten wij ons op de mechanische verbindingen tussen het hechtkussenoppervlak en het interne vinger- en teenskelet. De ventrale zijde van het hechtkussen is door verschillende krachttransmissiestructuren verbonden met het skelet. Een bindweefselschot loopt van de ventrale huid tot het uiteinde van de distale falanx en verdeelt het onderhuidse hechtkussenvolume in een distale lymferuimte en een met slijmklieren gevulde proximale ruimte. Bovendien loopt een collageene bindweefsellaag vanaf de ventrale lederhuid via de interfalangiale ligamenten tot de middelste falanx. De vezels die deel uit maken van deze laag lopen in gebogen banen om de transversale hechtkussenas en vormen lateraal gescheiden ri-



chels onder de klierruimte. Door gebruik te maken van eindige-elementenanalyse en numerieke optimalisatie van een met schuifkrachten belast hechtkussenmodel laten wij zien dat de collageenvezels vermoedelijk in de richting van de maximale trekspanning georiënteerd zijn. De optimalisatie resulteert ook in richelformatie als gevolg van de noodzakelijke aanwezigheid van de klierbuizen die uitmonden op de ventrale epidermis. Het collageenvezelverloop en de richels duiden erop dat de collageenlaag cruciaal is voor een effectieve krachttransmissie van huid naar distale falanx (inclusief de daarbij behorende hoge stijfheid) tijdens schuifkrachtbelasting, hetgeen overeenkomt met de waarneming dat de maximale afschuifkrachten aanzienlijk hoger zijn dan de maximale adhesiekrachten. Tenslotte onthulde onze immunohistochemische kleuring van het weefsel de aanwezigheid van verspreid voorkomende gladde spiervezelbundels in de kikkerhechkussens. Deze actieve structuren verschaffen boomkikkers waarschijnlijk de mogelijkheid om de verdeling van de mechanische spanning over de ventrale zijde van het hechtkussen te reguleren, en daarmee de uitgeoefende aanhechtingskracht.

HOOFDSTUK 4 adresseert de morfologie van de slijmklieren van de vinger- en teenkussens en de chemie van het afgescheiden slijm. In *H. cinerea* vormen de slijmklieren, die gezamenlijk uitmonden aan de ventrale zijde van het hechtkussenoppervlak, een macroklier. Daarmee verschillen ze morfologisch van de slijmklieren, welke uitmonden op het dorsale (niet-adhesieve) huidoppervlak. Wij hebben dergelijke ventrale vinger- en teenslijmmacroklieren geïdentificeerd in minstens 10 neobatrachiale families die niet exclusief arboreaal leven. Dit impliceert dat de macrokliermorfologie bepaald wordt door zowel algemene functionele vereisten die voortkomen uit ‘bodemcontact’ (e.g. smering en het compenseren van slijmverlies) als door specifieke vereisten voor klimmen en aanhechting. Door gebruik te maken van zowel cryo-histochemie als infrarood- en som-frequentie-generatie-spectroscopie laten wij zien dat—in contrast met de kliermorfologie—de algemene slijmchemie slechts weinig varieert tussen de lichaamslocaties in zowel de boomkikkers *H. cinerea* en *Osteopilus septentrionalis* als tussen arboreale en niet-arboreale (*Pyxicephalus adspersus* en *Ceratophrys cranwelli*) kikkersoorten. Deze waarnemingen suggereren dat de chemie van het slijm gedurende de evolutie grotendeels geconserveerd is en geen specialisatie laat zien van het slijm voor aanhechting.

In HOOFDSTUK 5 hebben wij de aanhechtingsprestatie van de boomkikkers *H. cinerea* en *Litoria caerulea* gemeten met behulp van een met videocamera’s uitgerust roterend platform waarop de kikkers werden geplaatst. Door de effecten van variatie in de nominale substraatruwheid op de aanhechtingsprestatie te analyseren onderzochten wij de rol van het eerder voorgestelde mechanisme van mechanisch in-elkaar-grijpen van substraat en aanhechtingskussen in de aanhechting. Boomkikkers hechten zowel aan nano- en microruwe substraten als aan een glad substraat. De aanhechtingsprestatie neemt pas af boven een nominale substraatruwheid van 15 μm . Deze waarnemingen komen niet overeen met de verwachte variatie in aanhechtingskracht met substraatruwheid bij aanwezigheid van een mechanisme van in-elkaar-grijpen. Dit geeft aan dat mechanisch in-elkaar-grijpen verwaarloosbaar is in boomkikkeraanhechting. Onze op video-waarnemingen gebaseerde analyses van aanhechtingsoppervlakken en lichaams-

bewegingen hebben duidelijk gemaakt dat boomkickers substantiële traagheidskrachten kunnen weerstaan met slechts twee aangehechte ledematen. Dit suggereert dat de maximale aanhechtingsprestatie van boomkickers beduidend hoger is dan voorheen werd gerapporteerd.

Tenslotte plaats ik in HOOFDSTUK 6 de eerdere bevindingen van dit proefschrift in een bredere wetenschappelijke context. Ik bespreek het belang van voorheen voorgestelde mechanismen van boomkikkeraanhechting door de uitkomsten van onze literatuuranalyse (hoofdstuk 2) te integreren met de resultaten van de experimentele hoofdstukken en de inzichten verkregen over boomkikker-geïnspireerde adhesieven. Ik concludeer dat aanzuiging en mechanisch in-elkaar-grijpen verwaarloosbaar zijn. Een bijdrage van hydrodynamische adhesie kan niet worden uitgesloten maar lijkt een onvermijdelijk gevolg te zijn van het hebben van een natte huid in plaats van een primair aanhechtingsmechanisme. Terwijl voorheen capillaire adhesie genoemd werd als primair adhesiemechanisme, suggereert integratie van de beschikbare kennis dat capillaire adhesie en Vanderwaalskrachten beiden bijdragen waarbij die laatste het dominante aanhechtingsmechanisme is. Ter verkenning van de gehypotheseerde convergente evolutie van boomkikkerhechtingskussens verschaf ik een overzicht van eerder werk over de fylogenie van de hechtkussens, aangevuld met nieuwe gegevens van mijn promotieonderzoek. Globaal bekeken zijn verscheidene morfologische kenmerken (e.g. het micro gestructureerde hechtkussenoppervlak en het klierencluster in de vinger en tenen) wijdverspreid over de kikkerfamilies. Dit suggereert dat het gehele hechtkussen een functionele eenheid is en roept de vraag op of hechtkussens convergent geëvolueerd zijn of dat zij afstammen van een algemene voorouder. Een voorlopige discussie omtrent de evolutionaire geschiedenis van kikkerhechtkussens benadrukt, in overeenstemming met de voorgaande secties, het belang van drainering, genereren van wrijving en Vanderwaalskrachten in boomkikkeraanhechting. Gebaseerd op de uitkomsten van dit proefschrift verschaf ik ontwerpsuggesties voor boomkikker-geïnspireerde-adhesieven. De draineringsmogelijkheden van kikkerhechtkussens maken dit een goed model voor de ontwikkeling van technische adhesieven in een natte omgeving. Veelbelovende trends zijn het ontwerp van vezel-versterkte adhesieven met microstructuren voor de transmissie van hoge mechanische belastingen en het maken van adhesieven met actief controleerbare adhesie, geïnspireerd door de spierstructuren die in het biologisch model aanwezig zijn. Tenslotte presenteer ik een vooruitzicht voor de komende jaren van de mogelijke ontwikkelingen van het onderzoek aan boomkikkeraanhechting.



Zusammenfassung

Baumfrösche sind vielseitige Kletterer. Mit Hilfe von Haftballen an ihren Fingern und Zehen können Baumfrösche sogar unter schwierigen Umständen an vielfältigen Oberflächen haften. Die Haftballen sind von einer Schleimschicht bedeckt und können pro Finger oder Zeh Adhäsions- und Reibungskräfte vom Mehrfachen des Körpergewichts dieser Tiere erzeugen. Die bemerkenswerten Hafteigenschaften der Baumfrösche faszinieren schon seit Jahrhunderten Wissenschaftler, die sich bemühten, die Grundlagen der Baumfroschhaftung zu ergründen. Unter den verschiedenen zur Erklärung der Baumfroschhaftung herangezogenen Mechanismen ist Kapillaradhäsion die am häufigsten genannte. Bisherige Untersuchungen konzentrierten sich vor Allem auf die Funktion der mikrostrukturierten Ballenoberfläche in der Haftung, was zu der Entwicklung von einigen Baumfrosch-inspirierten mikrostrukturierten Haftsystemen führte. Allerdings wurde stets noch keine umfassende Erklärung der Mechanismen der Baumfroschhaftung gefunden und die Rolle innerer Ballenstrukturen ist noch weitgehend unerforscht. In dieser Dissertation präsentiere ich eine interdisziplinäre Analyse des Haftapparates der Baumfrösche mit Schwerpunkt auf subepidermalen Strukturen, welche zum Verständnis natürlicher Haftsysteme sowie zur Entwicklung von bionischen, durch Baumfrösche inspirierten Haftsystemen beiträgt.

In KAPITEL 2 geben wir eine Synthese des *status quo* der Forschung über Baumfroschhaftung—von der funktionalen Morphologie der Ballen bis zu experimentellen Ergebnissen, welche die verschiedenen mutmaßlichen Mechanismen der Baumfroschhaftung unterstützen—und zeigen Lücken im Wissen über Baumfroschhaftung auf. Eine Übersicht der funktionalen Morphologie zeigt, dass Untersuchungen der inneren Morphologie der Haftballen sowie der Chemie des abgesonderten Schleimes notwendig sind, um das Verständnis der Baumfroschhaftung zu vertiefen. Die Auswertung aktueller analytischer Modelle sowie publizierter Daten und Beobachtungen ergibt, dass die Hypothese der Nasshaftung als primärer Mechanismus der Baumfroschhaftung nicht ausreichend belegt ist. Van der Waals Kräfte, denen aufgrund des Schleimes auf der Oberfläche der Haftballen lange Zeit nur eine geringe Rolle zugewiesen wurde, können sehr wohl eine wichtige Rolle in der Baumfroschhaftung spielen.

In KAPITEL 3 präsentieren wir eine 3D Analyse der inneren Ballenmorphologie des Baumfrosches *Hyla cinerea* mittels Histochemie und Synchrotron-Mikro-Computertomografie. Das Hauptaugenmerk liegt auf der mechanischen Verbindung zwischen der haftenden Ballenoberfläche und dem inneren Skelett des Zehs. Die ventrale Ballenoberfläche ist mit dem Skelett durch mehrere Wege der Kraftübertragung verbunden. Ein kollagenes Septum läuft von der ventralen Kutis bis zur Spitze der distalen Phalanx und teilt das subkutane Ballenvolumen in einen distalen Lymphraum und einen proximalen Raum, der mit Schleimdrüsen gefüllt ist. Zudem verbindet eine Kollagenschicht die ventrale Kutis über interphalangeale Ligamente mit der mittleren Phalanx. Die Fasern, welche diese Schicht bilden, verlaufen in um die Transversalachse der Ballen gekrümmten Trajektorien und formen unterhalb des Drüsenraumes lateral

getrennte Grate. Durch Finite-Elemente-Analyse und numerische Optimierung eines Ballenmodells unter Scherbelastung zeigen wir, dass die Kollagenfasern vermutlich entlang der mechanischen Hauptspannungsrichtungen verlaufen. Des Weiteren resultiert die Optimierung ebenfalls in Gratformung, was vermuten lässt, dass die Kollagenschicht an eine hohe Steifheit unter Scherbelastung angepasst ist. Schließlich enthüllt immunohistochemisches Färben mehrere Einheiten von glatten Muskelfasern in den Haftballen von Fröschen. Diese muskulären Strukturen könnten es dem Baumfrosch ermöglichen, die Verteilung der mechanischen Spannung auf der ventralen Haftballenoberfläche zu kontrollieren und somit die Haftstärke zu modulieren.

In KAPITEL 4 widmen wir uns der Morphologie der Schleimdrüsen in den Zehen und Fingern sowie der Chemie des abgesonderten Schleims. Bei *H. cinerea* formen die sich zur ventralen Ballenfläche hin öffnenden Schleimdrüsen eine Makrodrüse und weichen somit deutlich in ihrer Morphologie von den sich zur dorsalen (nicht-haftenden) Ballenoberfläche öffnenden Schleimdrüsen ab. Wir konnten in den Fingern und Zehen von mindestens 10—nicht ausschließlich arborealen—Familien der Neobatrachia Schleim-Makrodrüsen feststellen. Diese Beobachtung legt nahe, dass die Morphologie der Makrodrüsen sowohl durch allgemeine funktionale Anforderungen, die von ‘Bodenkontakt’ herrühren (z.B. Schmierung und der Ausgleich von Schleimverlust), als auch durch spezifische Anforderungen an Klettern und Haftung bestimmt ist. Mittels Kryohistochemie sowie Infrarot- und Summenfrequenzspektroskopie konnten wir zeigen, dass sich—im Gegensatz zur Drüsenmorphologie—die allgemeine Chemie des Schleims nur wenig zwischen verschiedenen Körperteilen innerhalb der Baumfroscharten *H. cinerea* und *Osteopilus septentrionalis* sowie zwischen arborealen und nicht-arborealen (*Pyxicephalus adspersus* und *Ceratophrys cranwelli*) Froscharten unterscheidet. Diese Beobachtung deutet auf die Bewahrung der chemischen Zusammensetzung des Schleims in der Evolution der Anura hin und spricht gegen eine Spezialisierung des Schleims zwecks Haftung.

In KAPITEL 5 haben wir die Haftstärke der Baumfrösche *H. cinerea* und *Litoria caerulea* mittels eines Drehtisch-Versuchsaufbaus experimentell gemessen. Durch die Messung des Effekts von Variationen in der nominellen Substrat-Rauheit auf die Haftung von Baumfröschen haben wir die Rolle des in vorangehender Forschung vorgeschlagenen Haftmechanismus der mechanischen Verklettung näher untersucht. Baumfrösche haften sicher auf nano- und mikrorauen sowie auf glatten Substraten. Erst ab einer nominellen Substrat-Rauheit von ca. 15 µm fällt die Haftstärke ab. Diese Beobachtung stimmt nicht mit der Variation der Haftstärke bei Änderung der Substrat-Rauheit überein, die bei Vorhandensein von mechanischer Verklettung zu erwarten wäre. Somit ist mechanische Verklettung in der Baumfroschhaftung vermutlich vernachlässigbar. Weiterhin zeigen Beobachtungen von sich in der Ablösung befindlichen Fröschen mit unserem Versuchsaufbau, dass Baumfrösche mit nur zwei haftenden Gliedmaßen beachtlichen Trägheitskräften widerstehen können. Dies deutet darauf hin, dass die maximale Haftstärke von Baumfröschen höher ist als bisher berichtet.

Schließlich ordne ich in KAPITEL 6 die Ergebnisse dieser Dissertation in den wissenschaftlichen Kontext ein. Durch Kombination der Resultate der Literaturanalyse zum



Thema Baumfroschhaftung, der Befunde der Forschungskapitel und der Erkenntnisse, die an Baumfrosch-inspirierten Haftsystemen gewonnen wurden, erörtere ich die Relevanz der bisher vorgeschlagenen Mechanismen der Baumfroschhaftung. Ich schlussfolgere, dass Saughaftung und mechanische Verklettung vernachlässigbar sind. Ein Beitrag von hydrodynamischer Adhäsion kann zwar nicht ausgeschlossen werden, scheint aber eher eine Folge der feuchten Froschhaut als ein primärer Haftmechanismus zu sein. Während Kapillaradhäsion bisher als primärer Adhäsionsmechanismus genannt wurde, deutet die Kombination der gewonnenen Einsichten darauf hin, dass Kapillaradhäsion zusammen mit van der Waals Kräften als vorrangigem Mechanismus wirkt. Des Weiteren verschaffe ich einen Überblick über die aus dieser und früheren Arbeiten gewonnenen Erkenntnisse über die Phylogenie der Haftballen der Baumfrösche, um die vermutete konvergente Evolution der Haftzehen und -finger der Baumfrösche zu erörtern. Mehrere morphologische Merkmale (z.B. die mikrostrukturierte Ballenoberfläche und die Makrodrüsen in Zehen und Fingern) sind in diversen Familien der Anura zu finden. Dies lässt vermuten, dass der gesamte Ballen eine funktionale Einheit bildet und wirft die Frage auf, ob die Ballen das Ergebnis konvergenter Evolution sind oder von einem gemeinsamen Vorfahren abstammen. Eine Diskussion der Evolutionsgeschichte der Haftballen stimmt mit der vorhergehenden Diskussion überein und hebt die Wichtigkeit von Flüssigkeitsabfuhr, Reibung, und van der Waals Kräften in der Baumfroschhaftung hervor. Basierend auf den Resultaten dieser Arbeit gebe ich Anregungen für die Gestaltung von Baumfrosch-inspirierten Haftsystemen. Die Fähigkeit zur Flüssigkeitsabfuhr zeichnet die Haftballen von Baumfröschen als hervorragendes Modell für die Entwicklung von technischen Nasshaftsystemen aus. Weitere vielversprechende Anwendungsgebiete sind das Design von faserverstärkten, mikrostrukturierten Haftsystemen für Schwerlasten sowie die Erzeugung von Haftsystemen mit kontrollierbarer Haftung inspiriert durch die muskulären Strukturen, welche wir im biologischen Modell gefunden haben. Schließlich präsentiere ich einen Ausblick auf mögliche Entwicklungen im Feld der Baumfroschhaftung in den kommenden Jahren.





And now for something completely different.

Monty Python

Acknowledgements

A PhD project is a team effort. My co-authors and a multitude of other people helped me with their thoughts and actions to finish this thesis, and to survive the past four years. Here, I would like to devote a few pages to thank all these people. Also, I would like to apologise to and thank all those who I might have forgotten.

First, I want to express my deep gratitude to my promoters. **Johan**, thank you for believing in me, and for taking me in at the *Experimental Zoology Group (EZO)*. From my first day in Wageningen on, you have been supporting me in my professional and private life. Despite your brimful agenda, there was always time for an emergency meeting. Your sharp eyes for logical gaps, and your experienced advice helped me to develop as a scientist. I appreciate very much that you gave me the freedom to turn the ‘tree-frog-project’ into ‘my own’, and I look forward to more late-afternoon-discussions in the coming years. **Dimitra**, without you there would be no project on tree frog attachment, and I might not have pursued a doctorate. Your positive attitude helped me tremendously to finish the infamous review on tree frog attachment, and from your feedback I learned a lot about scientific writing. I hope that we can continue the Wageningen-Delft collaboration on ‘Kermit’s sticky little fingers’. **Marleen**, you always had a friendly reply ready (or you knew someone who could help me) when I came up with yet another question on chemical issues. Thanks for opening the doors of *Physical Chemistry and Soft Matter* to me, and for inviting me to the adhesion club. I wish you all the best in the cold North, and hope that you will come back to Wageningen from time to time.

In the last four years, I received an incredible amount of support from the *EZO* staff. **Annemarie**, to new students I always introduce you as “the most important person of the group” and this is not a lie: You make sure that administrative processes run as smoothly as if they were coated with Teflon, you care for the wellbeing of mine (as well as of Annika and Sophie), and taught me circa 70% of the Dutch I am capable of. Dank je wel! **Henk**, I learned more from you about tissue sectioning and histology than I ever would have expected at the begin of this project. You helped me to rethink the morphology of frog pads and contributed a lot to this thesis. Thank you for all the advice related not only to work but also to the rest of life. I look forward to the nice pictures that we will work on in the future. **Remco** (a.k.a. ‘the man who makes

every setup work'), you always have a solution in mind for my experimental setups (even when I do not yet see the problem), and one or two hands free to realise them. I could not have done that without you. Also, thanks for arranging all the fancy lab equipment. **Karen**, although we do not work at the same project, you always have an open ear and a helping hand for lab-related and other issues. **Frank** and **Anne B**, you provided immense support during the morphological analyses, and without your help many of the figures in this thesis would not be half as nice as they got. **Frank**, I hope that we stay in touch, and wish you all the best with your studies. **Sander G**, thanks for introducing me to all the weird terminology of anatomists, and—more importantly—for the funny calendar bits that lightened up the coffee breaks. **Kas**, thank you for the help with the setups. **Florian**, you were the first to invite me to a social event in the Netherlands (Bouldering in Arnhem), and give a promising example on how academic life may look like a few years down the road. **Martin**, **Bart**, **Sander K**, and **Kees S**, thanks for answering all my questions on neurology, statistics, and evolution, and for your feedback on my work. **Leonardo**: Welcome in the group :).

The pages of this thesis are piled up on the backs of numerous students. **Lisa**, **Jorn**, **Anne R**, **Timo**, **Jos**, **Mark**, **Yani**, and **Nicky**, supervising you was a pleasure, and I learned a lot from your questions and from working with you. The projects were not always easy but I hope they helped preparing you for the future, for which I wish you all the best. **Noraly**, thanks for the help with μ -CT.

A number of people from *Wageningen University & Research (WUR)* helped me to explore different research lines (that unfortunately did not all make it into the chapters of this thesis), and to find my way. First of all, my gratitude goes to the *Carus*-team: **Menno**, **Sander**, **Debbie**, **Sabine**, **Aglaja**, **Linsey**, **Marleen**, and all the others, thank you for setting up and taking care of our frog population. I could always count on you. **Rob**, thanks for teaching me about animal welfare regulations. I hope I did a good job with our frogs. **Roy**, you gave us sound advice on the husbandry of tree frogs. I am thankful for the support from the *Technical Development Studio*. **Johan**, **Hans**, and **Eric**, sorry for disturbing so many of your lunch- and coffee-breaks with questions on the design of experimental setups. Johan, without you we would not have been able to build the most sophisticated rotation table setup of the world. **Jan-Evert** (*Biometris*), thank you for settings us on the right path in the statistical analysis. I received a lot of support at *Physical Chemistry and Soft Matter*: **Menno**, **Mieke**, and **Hanni**, thanks for introducing me to your setups, and for answering all the questions. **Sven**, **Aljoscha**, and the rest: I enjoyed discussing with you about adhesion-related topics. **Barend** and **Frank** (*Organic Chemistry*), unfortunately our pilot measurements did not make into this thesis, but I will certainly come back to you!

Of course, also people from outside Wageningen contributed to this thesis. **Peter**, **Paul**, and Dimitra (pun intended ;)), it was great to collaborate with *Biomechanical Engineering* at *TU Delft*. I learned a lot at our meetings, and I look forward to future developments of tree-frog-inspired surgical grippers. Peter, our interactions were as

easy-going as can be, and I enjoyed our trips to Potsdam, Akron, South Hadley, and of course Boston. All the best with finalising your thesis!!! I also would like to thank **Menno** from the *3ME Workshop*: I cannot count the number of mails and design iterations that we had on the 3D-force-transducer. Thanks for your creative solutions and steady fingers. Also the rest of the STW-team (or should I say TTW?) made sure that the project went smoothly: **Lise**, thanks for your swift support and insightful questions. I also would like to thank all the users and scientific advisers, that helped with their comments and questions to set this project on the right track. **Chris**, thank you for the support at the *Paul Scherrer Institut*, which allowed us to explore the morphology of frog pads in 3D. **Ali**, **Saranshu**, **Alex**, **Sukhmanjot**, and **Henry** (*The University of Akron*), thanks for inviting us over to your group, and for sharing our interest in frog mucus. Without your theoretical and practical support, CHAPTER 4 would be much less meaningful. I am sure that this was only the beginning of a fruitful collaboration. **Jon** (*University of Glasgow*), your works form a large part of the scientific fundament of this thesis. Our discussions and your kind comments helped me to find my way into the topic, and I will never forget your polite and friendly attitude, even though we did not always share the same views on tree frog attachment. **Stas** and **Alexander**, thank you for giving me the opportunity to visit your group on *Functional Morphology & Biomechanics* in Kiel, and to perform the roughness measurements. **Lars**, **Dennis**, and all the others: I am sure we will meet at one of the next SEB conferences. **Andor** and **Tom**, thank you for your efforts on the MRI of frog pads at *Radboud UMC*. Unfortunately, these results did not make it to publication, but let's see what the future brings. **David** (*Imperial College London*) and **Walter** (*University of Cambridge*), I learned a lot from our discussions on the fundamentals of bioadhesion. David, thanks for your feedback on my manuscripts, and for providing me some of the 'ancient' German literature on tree frogs, which led me to the discovery of further literary treasures. I hope to see you again (in Wageningen or elsewhere). **Rob** from *ZOO&ZO* and **José** from *Ouwehands Dierenpark Rhenen*, I am grateful for the tree frog samples that you provided so uncomplicatedly. **Mattias** (*RISE*), thank you for your enthusiasm and for working with us towards the generation of sophisticated substrate geometries.

Uroš and **Pim**, you are not only Leidensgenossen (only Germans could invent a term for 'fellow sufferers'), colleagues, office mates, and paranympths, but also good friends. Thank you for all the help in the last weeks and months!!! Uroš, I think we already noticed quite early that we are on the same wavelength. I enjoyed complaining with you about PhD life, science, and the world in general ('Shared loads are twice as heavy'). Thanks for letting me crush your couch so I could get a taste of the famous Wageningen nightlife, and, more importantly, for giving Sophie, Annika, and me a place in your life. You are one of the most diversely interested and scientifically well-rounded persons I know, and I wish you all the best in Belgium and beyond. Pim (a.k.a. 'the man who asks questions faster than his shadow'), I am glad that we ended up in the same office. From the first day on, you showed your heart of gold. You are one of the most approachable, friendly, and interested persons I know, and I am truly amazed how you always can come up with yet another question on any topic being



discussed. I will crash your couch one day, promised. Good luck with the finalisation of the largest x-ray fish database of the world!

EZO is a great place to work, and that is due to the amazing people working here. **Andres**, I am happy that you ended up living in Arnhem! Thanks for all the free advice on statistics, and for the free beer :). **Myrthe**, we live separated by half a country, but still you and Joeri always manage to join our parties. **Mike**, only one word: Doomsdayclock. I wish you and Suzanne all the best in Amersfoort. **Lana**, I am happy that you joined the best office of the campus. **Cees**...**Kees**...I mean Cornelis, thank you for your friendship and the approximately 3000 invites to morning coffee, lunch, and afternoon coffee breaks. Also, thanks for taking care of the office sound system (ACDC Friday!), and for being available for all kinds of software- and programming-related questions of mine and ‘my’ students. I wish you and Carmen all the best in Rotterdam. **Antoine**, thanks for organising all the movie nights. **Pulkit** or should I say ‘Chef *EZO*’: Thanks to you we have the best catering of the university. **Wouter**, I am thankful for the tech-advice, the feedback on my manuscripts, and all the bits of helpful information. **Elsa** (thanks for the frog :)), **Gauthier**, **Henri**, **Maurijn**, **Sebastian**, and **Sem**, I enjoyed working with you. Thank you all for the nice coffee break discussions (some of which I would like to forget again ;)), for the article-bashing during journal club, for the great PhD dinners, and for all the other events. If only there were a night bus Wageningen-Arnhem... A group is only as good as its members, and a wing only as good as its groups: **Anja**, **Annelieke**, **Carmen**, **Christine**, **Ellen**, **Esther**, **Éva**, **Hilda**, **Jules**, **Lieke**, **Loes**, **Marcella**, **Maria**, **Mark**, **Marloes**, **Mirelle**, **Mojtaba**, **Olaf**, **Paulina**, **Sylvia**, **Sam**, and all the others from *Cell Biology and Immunology* and *Host-Microbe Interactomics*, thank you for making the E-wing such a nice place to work, and for forming the best film industry between Hollywood and Bollywood. At this place I also wish to express my gratitude to all the members of the cleaning services, who helped me in various late-afternoon-discussions to improve my Dutch.

Viele Andere haben direkt und indirekt zu dieser Arbeit beigetragen. **Iris**, **Roel**, **Hilario**, **Peter** (I trust that Hilario is going to translate this for you), **Rodrigo** (You will have to use Google translate), **Anna**, **Liga** (You too ;)), **Anthony** und **Andres**: Danke für die tolle Zeit in Arnhem, für die Massnahmen zur Verschmelzung der deutschen und niederländischen Sprache (“Abbeugeln!”), und für die Betreuung von Annika, wenn ich mal wieder in Arbeit unterging. In Deutschland haben viele Freundschaften meine unregelmässigen Updates (und meine Abneigung gegen WhatsApp) ausgehalten: **Jonathan**, **Ilka**, **Moritz**, **Timo**, **Miri**, **Benny**, **Claudia**, **Andi** und alle Anderen — Danke dafür!

Mama und **Papa**, ohne euch hätte ich diese Arbeit schwerlich schreiben können! Danke für meine Kieler Kindheit, meine Einstellung zur Natur, zu ganzheitlichem Denken, und zu Wortspielereien. Ich konnte immer auf eure Unterstützung zählen. **Caro** und **Brakkies**: Dito. Best sister/brother/godparents/visitors ever! Unser Karaoke im Pegasus Pub bleibt unübertroffen. **Oma**, du warst immer für mich da und hast stets in mich geglaubt — Danke! Wir kommen immer wieder gerne nach Ber-

senbrück. **Eva** und **Norbert**, vielen Dank für die Unterstützung und die schönen Besuche in Essen. **Bianca**, **Jörg**, vielen Dank für Annika und dafür dass ihr mich in eure Familie aufgenommen habt. **Jule**, **Christian**, und **Marie**, viel Glück mit eurer eigenen kleinen Familie.

Annika und **Sophie**, diese Arbeit begann mit euch, sie soll auch mit euch enden. Annika, ich bin dir unendlich dankbar für deine Liebe, Unterstützung und Geduld. Die letzten Jahre waren nicht immer einfach, ich war zu oft mit Körper und/oder Kopf auf der Arbeit, und du hast durch unseren Umzug auf Vieles verzichtet. Trotz aller Schwierigkeiten hast du mich immer unterstützt. Du hast mich daran erinnert, dass Arbeit und Wissenschaft nicht alles sind, hast mich angetrieben, wenn ich zu träge war, abgebremst, wenn ich zu schnell war, warst mein Versuchskaninchen für Präsentationen, mein Tor zur Aussenwelt und vieles mehr. Dass diese Arbeit 'nur' 4 Jahre gedauert hat, ist dir zu verdanken. Jetzt sind wir verheiratet und haben die wundervollste Tochter der Welt. Für dieses Glück kann ich mich nicht genug bei dir bedanken. Fehlt nur noch ein Haus ;). Sophie, wenn du nur ein kleines bisschen von deiner Mutter abgekriegt hast, müssen wir uns über dich keine Sorgen machen. Du bist ein Wunder ohne Ausmaß (sogar im Vergleich zu Baumfröschen :)). Du bringst uns zum Staunen, Weinen und Lachen, alles an einem Tag. Ich freue mich auf die Zukunft mit dir und deiner Mutter.





Personalia

Curriculum vitae

Julian Karl André Schöning-Langowski (birth name: Langowski) was born on the 17th of August, 1987, in Eckernförde (Germany). He grew up in Kiel (Germany) close to the Baltic sea, where he was fascinated by the marine fauna already at a young age. He visited the *Kieler Gelehrtenschule* and obtained his higher education entrance qualification in 2007 with ‘very good’ grades. At the *Deutsche Schüler Akademie*, a talent fostering programme for adolescents, Julian heard for the first time about biomimetics and according higher education programmes. After secondary school, he did a year of civil service at the Altenzentrum St. Nicolai, Kiel.

In 2008, Julian enrolled for the international degree course (B.Sc.) *Biomimetics* at the *University of Applied Sciences Bremen* in Bremen (Germany). In the next 3.5 years, he immersed into the interdisciplinary world of biomimetics and studied various subjects, ranging from anatomy and evolutionary biology, over chemistry and physics, to material science and engineering. In 2012, Julian obtained his B.Sc. with the thesis entitled *Design, construction and test of a biomimetic Robot-Fish with an undulating propulsion system inspired by carangiform swimming* (supervised by Prof. Dr. Eize J. Stamhuis), which reflects his interests for biomimetics and marine animals.

Driven by his interest for biomimetics and organisms living in a wet environment, Julian continued in 2012 with the M.Sc. programme *Biomimetics / Locomotion in fluids* at the *University of Applied Sciences Bremen*. He specialised in experimental and numerical methods (e.g. wind tunnel measurements and computational fluid dynamics) that allow for fundamental analyses of the principles of swimming and flight in biological and technical systems. At the same time, Julian worked as wind tunnel engineer at *Deutsche WindGuard*, Bremerhaven (Germany), where he became acquainted with the aerodynamic design of wind turbine rotor blades. His M.Sc. thesis entitled *Do a humpback whale’s tubercles increase the efficiency of a wind turbine? Sinusoidal leading edge modifications as boundary layer fence on a horizontal axis wind turbine* (supervised by Prof. Dr. Albert Baars) was awarded with the highest grade, and Julian finished his studies as best of the year. Julian’s B.Sc. and M.Sc.

studies were supported by a scholarship from the *Heinrich Böll Foundation*.

For his PhD thesis entitled *Getting a grip on tree frog attachment: Mechanisms, structures, and biomimetic potential* (supervised by Prof. Dr. Johan L. van Leeuwen, Dr. Dimitra Dodou, and Prof. Dr. Marleen Kamperman) at the *Experimental Zoology Group (EZO), Wageningen University & Research*, Wageningen (The Netherlands), Julian focussed from 2015 onwards on another wet biological system: the mucus-covered adhesive toes of tree frogs. In the interdisciplinary research project *Secure and gentle grip of delicate biological tissues* (funded by the *Netherlands Organisation for Scientific Research*), he studied the fundamentals of tree frog attachment in order to advance—in collaboration with scientists from TU Delft—the development of soft gripping tools that function in a wet environment. He finished his thesis within approximately 4 years, and published all research chapters of his thesis in peer-reviewed renowned (Q1) journals.

Julian established international collaborations with Prof. Dr. Stanislav Gorb, *Functional Morphology and Biomechanics, Kiel University* (Germany), as well as with Prof. Dr. Ali Dhinojwala and his team members, *Department of Polymer Science, The University of Akron* (United States), to study the attachment of tree frogs in a comprehensive, interdisciplinary approach. Awarded with several travel grants, he presented his research at various conferences (e.g. *European Network of Bioadhesion Expertise, Society for Experimental Biology*, and *Gordon research conference: Science of adhesion*). Next to doing research, Julian supervised in total 12 student theses as well as other works, and assisted in the teaching of the M.Sc.-course *Functional Zoology*. Moreover, he joined various courses and summer schools to expand his disciplinary knowledge as well as to gain further competences in research and management. In addition, he organised the WIAS Science Day 2016 on research at the interface between nature and technology.

Since 2019, Julian works as postdoctoral researcher at *EZO*. Within the 4TU project *Soft Robotics*, he explores the biomimetic potential of soft biological gripping systems (e.g. the sticky toes of tree frogs) for the development of state-of-the-art soft grippers, for example for handling delicate agricultural products.

Julian is married and lives with his wife and daughter in Arnhem (The Netherlands). He publishes and communicates in the scientific community as “Julian K.A. Langowski”.



Publications

Journal publications

- [5] **Langowski, J.K.A.**, SINGLA, S., NYARKO, A., SCHIPPER, H., VAN DEN BERG, F.T., KAUR, S., ASTLEY, H.C., GUSSEKLOO, S.W.S., DHINOJWALA, A. & VAN LEEUWEN, J.L. (2019). Comparative and functional analysis of the digital mucus glands and secretions of tree frogs. *Frontiers in Zoology*. Accepted for publication.
- [4] **Langowski, J.K.A.**, RUMMENIE, A., PIETERS, R.P.M., KOVALEV, A., GORB, S.N. & VAN LEEUWEN, J.L. (2019). Estimating the maximum attachment performance of tree frogs on rough substrates. *Bioinspiration & Biomimetics* **14**, 025011.
- [3] VAN ASSENBERGH, P., FOKKER, M., **Langowski, J.K.A.**, VAN ESCH, J., KAMPERMAN, M. & DODOU, D. (2019). Pull-off and friction forces of micropatterned elastomers on soft substrates: the effects of pattern length scale and stiffness. *Beilstein Journal of Nanotechnology* **10**, 79–94.
- [2] **Langowski, J.K.A.**, SCHIPPER, H., BLIJ, A., VAN DEN BERG, F.T., GUSSEKLOO, S.W.S. & VAN LEEUWEN, J.L. (2018). Force-transmitting structures in the digital pads of the tree frog *Hyla cinerea*: a functional interpretation. *Journal of Anatomy* **233**, 478–495.
- [1] **Langowski, J.K.A.**, DODOU, D., KAMPERMAN, M. & VAN LEEUWEN, J.L. (2018). Tree frog attachment: mechanisms, challenges, and perspectives. *Frontiers in Zoology* **15**, 1–21.

Conference abstracts

International

- [5] **Langowski, J.K.A.**, H. SCHIPPER, F.T. VAN DEN BERG, A. BLIJ, S.W.S. GUSSEKLOO & J.L. VAN LEEUWEN (2018). Functional interpretation of the force-transmitting structures in a tree frog's toe pad. *SEB Annual Meeting*, Florence, Italy.
- [4] **Langowski, J.K.A.**, A. RUMMENIE & J.L. VAN LEEUWEN (2017). Exploring the role of mechanical interlocking and hydrodynamic friction in tree frog attachment. *SEB Annual Meeting*, Gothenburg, Sweden.
- [3] **Langowski, J.K.A.**, A. RUMMENIE & J.L. VAN LEEUWEN (2017). Exploring the roles of mechanical interlocking and hydrodynamic friction in tree frog attachment. *Gordon research conference: Science of adhesion*, South Hadley, USA.



[2] **Langowski, J.K.A.**, A. RUMMENIE & J.L. VAN LEEUWEN (2017). Attachment to rough substrates and friction scaling in tree frogs. *European Network of Bioadhesion Expertise: 1st General Action Participant Meeting*, Vienna, Austria.

[1] **Langowski, J.K.A.**, J. VROON, D. DODOU & J.L. VAN LEEUWEN (2016). Finite element modelling of the adhesive contact of tree frog toe pads. *Biological and Bioinspired Adhesion: From Macro- to Nanoscale: Beilstein Nanotechnology Symposium*, Potsdam, Germany.

National

[4] **Langowski, J.K.A.** & J.L. VAN LEEUWEN (2019). Getting a grip on tree frog attachment: Structures, mechanisms, and biomimetic potential. *WIAS Science Day*, Lunteren, The Netherlands.

[3] **Langowski, J.K.A.** & J.L. VAN LEEUWEN (2019). Biomimetics promoting conservation: a case study. *Wageningen graduate schools symposium*, Wageningen, The Netherlands.

[2] **Langowski, J.K.A.**, A. RUMMENIE & J.L. VAN LEEUWEN (2017). Kermit's sticky little fingers: Exploring tree frogs' toe pads as a biomimetic model for versatile attachment. *Wageningen graduate schools symposium*, Wageningen, The Netherlands.

[1] **Langowski, J.K.A.**, D. DODOU & J.L. VAN LEEUWEN (2016). Kermit's sticky little fingers: A biomimetic point of view on tree frog adhesion. *WIAS Science day*, Wageningen, The Netherlands.



Training and supervision plan

With the training and education activities listed below Julian K.A. Schöning-Langowski has complied with the requirements set by the Graduate School of the Wageningen Institute of Animal Sciences (WIAS) which comprises of a minimum total of 30 ECTS (1 ECTS equals a study load of 28 hours).



Activity	Year	ECTS
Scientific exposure		4
<u>Oral presentations</u>		
Society for experimental biology (SEB), <i>Gothenburg, Sweden</i>	2017	
Wageningen graduate schools symposium, <i>Wageningen, The Netherlands</i>	2017	
Society for experimental biology (SEB), <i>Florence, Italy</i>	2018	
Wageningen graduate schools symposium, <i>Wageningen</i>	2019	
WIAS science day, <i>Lunteren, The Netherlands</i>	2019	
<u>Poster presentations</u>		
WIAS science day, <i>Wageningen</i>	2016	
Beilstein nanotechnology symposium: "Biological and Bioinspired Adhesion: From Macro- to Nanoscale", <i>Potsdam, Germany</i>	2016	
Gordon conference: Science of adhesion, <i>South Hadley, USA</i>	2017	
European network of bioadhesion expertise (ENBA): 1st general action participant meeting, <i>Vienna, Austria</i>	2017	
<u>Outreach and guest lectures</u>		
Science Cafe, <i>Wageningen</i>	2015	
Prof. Ali Dhinojwala Research Group, <i>The University of Akron, USA</i>	2017	
100 years WUR - Recreating life and bioinspired design, <i>WUR, Wageningen</i>	2018	
Functional Morphology and Biomechanics, <i>Kiel University, Germany</i>	2018	
The basic package		3
WIAS introduction day, <i>WUR</i>	2015	
Philosophy of science, <i>WUR</i>	2015	
Essential skills, <i>WUR</i>	2015	
Disciplinary competences		12
Statistics for life sciences, <i>WUR</i>	2015	
Systems biology modelling, <i>WUR</i>	2015	
Experimental design, <i>WUR</i>	2015	
46th IFF spring school functional soft matter, <i>Forschungszentrum Jülich, Germany</i>	2015	
10th EXCITE summer school on biomedical imaging, <i>ETH Zürich, Switzerland</i>	2015	
Statutory courses		3
Laboratory Animal Sciences, <i>WUR</i>	2016	

Personalia

Activity	Year	ECTS
Professional competences		1.9
Scientific Publishing, <i>WUR</i>	2015	
High Impact Writing, <i>WUR</i>	2015	
Survival guide to peer review, <i>WUR</i>	2015	
Research skills		6.2
Literature review: "Tree frog attachment: mechanisms, challenges, and perspectives"	2017	
SEB Careers Day: "Adding value to your research experience; CV workshop", <i>Prague, Czech Republic</i>	2015	
Management skills		3.7
Organiser: WIAS Science Day 2016 "Nature <-> Technology", <i>WUR</i>	2016	
WGS PhD Carousel: "Managing your Supervisor; Finding and acquiring small grants; Communication in academia: basics, issues and solutions", <i>WUR</i>	2015	
Project & time management, <i>WUR</i>	2017	
Teaching competences		6
Supervision of 3 BSc theses	2015–17	
Supervision of 5 MSc theses	2015–19	
Supervision of 2 interns	2017–18	
Tutoring of 1 'Capita selecta'	2016	
Tutoring of 1 international internship	2017	
Lecture, Bionik presentation series, <i>Rhine-Waal University of Applied Sciences Kleve, Germany</i>	2017	
Teaching assistant in "Functional Zoology", <i>WUR</i>	2018	
	Total	39.9



This work is part of the research programme “Secure and gentle grip of delicate biological tissues” with project number 13353, which is (partly) financed by the Netherlands Organisation for Scientific Research (NWO).

Financial support from the Experimental Zoology Group (Wageningen University & Research) for printing this thesis is gratefully acknowledged.

Quotes on the artworks accompanying the chapter title-pages

CHAPTER 1: RÖSEL VON ROSENHOF, A. J. (1758). *Die natürliche Historie der Frösche hiesigen Landes, worinnen alle Eigenschaften und ihre Fortpflanzung beschrieben*. Frontispiece.

CHAPTER 2: translated from W. MOERS (2011). *Das Labyrinth der träumenden Bücher*. Albrecht Knaus, München, Germany, p. 296.

CHAPTER 3: translated from v. WITTICH (1854). *Der Mechanismus der Haftzehen von Hyla arborea*. Archiv für Anatomie, Physiologie und Wissenschaftliche Medicin, p. 170.

CHAPTER 4: J. BLACKWALL (1868). *On the means by which various animals walk on the vertical surfaces of highly polished bodies*. Annals and Magazine of Natural History, **15**, p. 118.

CHAPTER 5: translated from F. LEYDIG (1854). *Ueber Organe eines sechsten Sinnes*. E. Blochmann & Sohn, Dresden, Germany p. 170.

CHAPTER 6: T. PRATCHETT (2002). *The Science of Discworld*, Ebury press, London, UK.

PERSONALIA: MONTY PYTHON.

Layout and typesetting

by Julian K.A. Schöning-Langowski,
TeXlipse, Vers. 1.5.0.

Literature management

Docear, Vers. 1.1.1.

Printing

by Proefschriftmaken, The Netherlands,
on 115 g silk paper.

Design of cover and artworks accompanying the chapter title-pages

by Gaja Hanzel, Master of graphics (M.F.A.), Malina Design.

Illustration of cover and artworks accompanying the chapter title-pages

by Petra Grmek, Master of landscape and architecture (M.Sc.),
chapter artworks inspired by the frontispiece by RÖSEL VON ROSENHOF, A.J. (1758). *Die natürliche Historie der Frösche hiesigen Landes, worinnen alle Eigenschaften und ihre Fortpflanzung beschrieben*. Nürnberg, Germany.

